

ISBN 978-82-326-2772-1 (printed ver.)  
ISBN 978-82-326-2773-8 (electronic ver.)  
ISSN 1503-8181



Doctoral theses at NTNU, 2017:352

Magnus Moreau

# Ab Initio Studies of Functional Oxides for Thin Film Applications

 **NTNU**  
Norwegian University of  
Science and Technology

Doctoral theses at NTNU, 2017:352

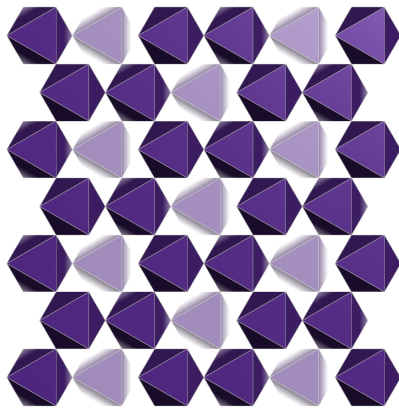
 NTNU

**NTNU**  
Norwegian University of Science and Technology  
Thesis for the Degree of  
Philosophiae Doctor  
Faculty of Information Technology and Electrical  
Engineering  
Department of Electronic Systems

 **NTNU**  
Norwegian University of  
Science and Technology

Magnus Moreau

# Ab Initio Studies of Functional Oxides for Thin Film Applications



Thesis for the Degree of Philosophiae Doctor

Trondheim, December 2017

Norwegian University of Science and Technology  
Faculty of Information Technology and Electrical Engineering  
Department of Electronic Systems



Norwegian University of  
Science and Technology

**NTNU**

Norwegian University of Science and Technology

Thesis for the Degree of Philosophiae Doctor

Faculty of Information Technology and Electrical Engineering  
Department of Electronic Systems

© Magnus Moreau

ISBN 978-82-326-2772-1 (printed ver.)  
ISBN 978-82-326-2773-8 (electronic ver.)  
ISSN 1503-8181

Doctoral theses at NTNU, 2017:2017:352

Printed by NTNU Grafisk senter

*Til William*

*Å se ansiktet ditt lyse opp når  
jeg kommer hjem fra en lang  
dag på kontoret får meg alltid til  
å glemme hvor sliten jeg er.*



---

## Summary

To continue the tremendous growth that the electronics industry has experienced over the last half-century, new energy efficient nanoscale devices are needed. One promising route towards this end is to introduce novel materials such as perovskite oxides. Perovskite oxides are known for their strong structure-property coupling and can host multiple device relevant properties, including magnetism and ferroelectricity. The strong structure-property coupling in these materials also enables controlling, enhancing and inducing such properties by external means, e.g. using a thin film geometry. However, as this coupling is often complex, and multiple phenomena occur simultaneously, theoretical studies are required to enable rational design of novel device concepts. Hence, in this thesis perovskite oxides are studied by density functional theory (DFT), with a focus on thin film applications. DFT is able to predict the atomic structure of materials with sub-ångström resolution. This includes the distortions of oxygen octahedra, which are central for the properties of perovskite oxides, but can be difficult to determine experimentally. Having established the ground state atomic structure, DFT can then predict several functional properties such as the ferroelectric polarization.

In this work, the focus is on *ordered oxygen vacancies* and the effect of the *crystallographic (111)-orientation* as avenues to control the properties of perovskite oxide thin films. Oxygen vacancies are known to have a strong impact on the properties of these materials. When the concentration of vacancies becomes large, they start to interact, and can form structures with alternating layers of octahedra and tetrahedra. These layered structures are interesting as they enforce anisotropic properties and can decouple the oxygen octahedra. Furthermore, the (111)-orientation, is interesting due its trigonal symmetry, which can induce novel topological properties, and has a different interface octahedral connectivity compared to other orientations, such as the (001). Here we investigate both the

effect of the strain from a (111)-substrate, and the effect of octahedral coupling at the (111)-interface.

In this work, it is found that oxygen vacancies in (La,Sr)MnO<sub>3</sub> thin films grown on (001)-oriented SrTiO<sub>3</sub> can accumulate close to the interface. These vacancies are initially disordered, but will order in a brownmillerite structure given time. Furthermore, it is found that the layering in the brownmillerite family of structures gives rise to different magnetic ordering patterns in the octahedral and tetrahedral layers, which are nearly decoupled from each other. In addition, the electronic band gap is larger in the tetrahedral layers, and the band structure is almost completely flat perpendicular to the layers. Hence, ordered anion vacancies in (La,Sr)MnO<sub>3</sub> enables spatially confined spin polarized conduction.

Investigating strain in the (111)-plane, we find that it is considerably different compared to strain in the (001)-plane. Using LaAlO<sub>3</sub> as a model system, we find an opposite splitting of in-plane and out-of-plane rotations compared to (001)-strain. Also in contrast to (001)-strain, there is no preferred in-plane rotation axis for (111)-strain, giving rise to Goldstone-like modes. Next, we analyse the strain-phonon coupling of twenty different perovskite oxides. We find that this coupling depends on the tolerance factor and the nominal charge of the A- and B-cations. This makes (111)-strained perovskite oxides interesting as it has multiple ways of engineering unstable phonons, while under (001)-strain the strain-phonon coupling is similar for all materials studied. Using this strain-phonon coupling, the crystal structure of LaFeO<sub>3</sub> when strained to SrTiO<sub>3</sub>(111) is determined, and found to coincide with the antiferromagnetic domain structure.

The octahedral coupling at (111)-oriented interfaces is established, and found to be significantly different compared to the coupling at (001)-oriented interfaces, due to the different interface symmetry. In the model system (La,Sr)MnO<sub>3</sub>/SrTiO<sub>3</sub> it is found that the coupling length is similar for the two orientations. However, the way octahedral rotations couple from the SrTiO<sub>3</sub> strongly depend on the facet of the interface. This difference in octahedral coupling can be used to control magnetic properties, as exemplified by the spatial distribution of the spin density. Finally we have shown that octahedral rotation mismatch between (111)-oriented LaFeO<sub>3</sub> and (La,Sr)MnO<sub>3</sub> has to reconstruct structurally. Concurrent with this octahedral reconstruction, an induced ferromagnetic moment in LaFeO<sub>3</sub> is found. This moment can again be related to changes in electron correlation strength due to the octahedral mismatch.

Using DFT, we have gained further insight into functional perovskite oxide thin films, on a level that would have been nearly impossible using experimental methods alone. Taken together, the results in this work show that both ordered oxygen vacancies and (111)-oriented interfaces are interesting avenues for tailoring material properties for novel electronic devices.

---

# Preface

*This dissertation is submitted in partial fulfillment of the requirements for the degree of Philosophiae Doctor (PhD) at the Norwegian University of Science and Technology (NTNU). The work was carried out at the Department of Electronic Systems (IES) with Professor Thomas Tybell as main supervisor. Associate Professor Sverre M. Selbach from Department of Materials Science and Engineering (IMA) has been the co-supervisor.*

## Acknowledgements

Although a PhD is considered an individual achievement, I could personally never have finished this thesis locked up alone in an office for four years. Hence, I would like to thank all the people making this work possible.

First I would like to thank my thesis advisor Thomas Tybell. Your unbounded positivity and infinite passion for oxides has been a guiding light for me these four years. I especially appreciate how I can come disillusioned to one of our meetings, but when I walk out again you have made me believe in what I do again. I would gladly do another PhD with you at the steering wheel. Especially now, when I know how to separate your crazy ideas from the actual plausible ones. To Sverre Selbach, my co-advisor, thank you for teaching me DFT, I learned so much from your DFT-bootcamp, and still do through the DFT-meetings. Your chemical intuition continues to baffle me, I also love your calm nerdy humour, although I often can't seem to figure it out.

Thanks to my office mates at A479 for holding out with me these four years. Fredrik Olsen, thanks for your good mood and excessive attention to detail, your proofreading has been invaluable! Also, thank you for bringing me with you on several trips to your cabin, and that we can discuss anything inside the walls of



our office. Ingrid Hallsteinsen, thanks for your down to earth rationalism when discussing Thomas' way too ambitious ideas. Sam Sløetjes, thanks for adding to theoretical community in A479. I love your Dutch feel-good-attitude and listening to your plans for a future wife. A special thanks also to Erik Folven for the great talks we have during the morning coffee; and thanks for letting your door always be open if I have some question, scientific or not. I would also like to thank the rest of the Oxide Electronics Group at IES, Torstein Bolstad, Ambjørn Dahle Bang, Kristoffer Kjærnes, Einar Digernes, Runar Dahl-Hansen, and Jostein Grepstad. Thanks for the numerous inspiring Monday-meetings and equally inspiring coffee breaks (or other beverages for people not into that kind of drug). I would also like to give a large thank to my name brother Magnus Nord, our group's satellite from the physics department. No one can be as excited for a TEM image as you, Magnus. In addition, I would like to thank my master students Sindre Tuset and Eirin Mærk Wehn, thanks for your patience when I try to pass on my DFT-knowledge. Furthermore, a thank you to my other colleagues, lunch- and lønnøl-mates at IES: Lukasz Paluchowski, Roger Birkeland, Nina Lundberg, Amund Gjersvik, Stein-Arne Askeland, Magnus Breivik, Johannes Reinertsen, Lars Martin Sandvik, Erlend Leirset, Kamal Raj Chapagain, Astrid Aksnes, Karolina Mileńko, Silje Skeide Fuglerud, Hans Olaf Hågenvik, Jens Abraham, Sebastian Arndt, Asgeir Bjørgan, Harald Garvik, Jens Høvik, Even Låte and Mohammed Sourouri.

Thanks to Ida Marie Høiaas for being my sidekick in our own television miniseries on NRK. It was great fun to do something so different! Also thanks to our Producer, Ketil Flatøy, for giving us the chance. These shows gave me hands on experience with disseminating science to the public, and I will remember it for the rest of my life. Furthermore, thanks to Johannes Skaar, Torbjörn Ekman, Tore Landsem, Erik Wessel-Berg and the crew down at the electronic prototyping lab; without your support, the experiments on the TV-shows and the follow up at "*Hvorfor det?*" would not have been nearly as interesting.

Also thanks to the people in the DFT-group, for sharing your results, ideas and feedback. Especially thanks to Astrid Marthinsen for teaching me about Phonopy, sharing your knowledge about (111)-strain, and for your iconic laughter. Furthermore, thank you Gerhard Henning Olsen for getting my DFT workstation up and running. Also thanks for sharing your passion about phonons; they have become my favourite quasiparticle too! Thank you Didrik René Småbråten for your dry ironic humour, we had such a great drive through Switzerland. Also thank you Sandra Helen Skjærvø, we went through DFT-bootcamp at the same time; and I appreciate that can always come by your office to chat about everything from convergence to babies, while enjoying an excellent cup of coffee.

I would also like to send a thanks to Eric Bousquet, Ulrich Aschauer and Nicola Spaldin meeting me and discussing my work at various points during my thesis.

A thank you also to Ingeborg-Helene Svenum, for sharing some CPU hours with me in my time of need.

Furthermore, I would also send thanks to Sigma Uninett 2 for providing computational resources. I estimate that I have spent approximately 3 million CPU hours during this thesis. If that were to be done on a single core, I would have spent around 350 years completing this thesis.

Finally, thanks to my family and parents for always believing in me. Special thanks in this regard goes out to my fiancée Janne-Lise A. Hegstad; without your endless support at home, I could never have completed this work. I hope not too long after I am done with this thesis, I can call you my wife.

Magnus Moreau  
Trondheim, Norway  
September 2017



---

# Contents

Summary	v
Preface	vii
Contents	xi
<b>I Background</b>	<b>1</b>
1 Introduction	3
<b>2 Properties of Perovskite Oxides</b>	<b>9</b>
2.1 Crystal Structure . . . . .	9
2.1.1 Octahedral Rotations . . . . .	11
2.1.2 Polar Distortions . . . . .	13
2.2 Orbital Structure . . . . .	14
2.3 Magnetic Structure . . . . .	15
2.4 Point Defects and Ordered Defect Structures . . . . .	18
2.4.1 Oxygen Vacancies . . . . .	18
2.4.2 Ordered Defect Structures . . . . .	20
2.5 Effects of a Thin Film Geometry . . . . .	23
2.5.1 Strain Engineering . . . . .	23
2.5.2 Interface Engineering . . . . .	27
2.6 Open Challenges and Opportunities . . . . .	34
<b>3 Methods</b>	<b>37</b>
3.1 First-Principles Background . . . . .	37

3.1.1	Many-Body Problem . . . . .	37
3.1.2	Density Functional Theory . . . . .	38
3.1.3	Approximate Exchange-Correlation Functionals . . . . .	40
3.1.4	Other Approximations . . . . .	42
3.2	DFT for Thin Films . . . . .	44
3.2.1	Homoepitaxial Strain Approach . . . . .	44
3.2.2	Heteroepitaxial Strain Approach . . . . .	45
3.3	Lattice Dynamics . . . . .	48
3.4	Calculation Details . . . . .	49
3.4.1	General . . . . .	50
3.4.2	Potentials . . . . .	50
3.4.3	Functional . . . . .	52
3.4.4	Structural Relaxations and Strain . . . . .	52
3.4.5	Lattice Dynamics . . . . .	53
3.4.6	Electronic Structure . . . . .	55
<b>II</b>	<b>Papers</b>	<b>57</b>
<b>4</b>	<b>Author's contribution</b>	<b>59</b>
<b>A</b>	<b>Structural phases driven by oxygen vacancies at the La<sub>0.7</sub>Sr<sub>0.3</sub>MnO<sub>3</sub> / SrTiO<sub>3</sub> hetero-interface</b>	<b>63</b>
	Supplementary Information . . . . .	69
<b>B</b>	<b>Spatially Confined Spin Polarization and Magnetic Sublattice Control in (La,Sr)MnO<sub>3-δ</sub> Thin Films by Oxygen Vacancy Or- dering</b>	<b>73</b>
	Supplementary Information . . . . .	84
<b>C</b>	<b>First-principles study of the effect of (111) strain on octahedral rotations and structural phases of LaAlO<sub>3</sub></b>	<b>95</b>
	Supplementary Information . . . . .	107
<b>D</b>	<b>Strain-phonon coupling in (111)-oriented perovskite oxides</b>	<b>111</b>
	Supplementary Information . . . . .	123
<b>E</b>	<b>Magnetic domain configuration of (111)-oriented LaFeO<sub>3</sub> epi- taxial thin films</b>	<b>139</b>
<b>F</b>	<b>Octahedral coupling in (111)- and (001)-oriented La<sub>2/3</sub>Sr<sub>1/3</sub>MnO<sub>3</sub> / SrTiO<sub>3</sub> heterostructures</b>	<b>149</b>

---

<b>G</b>	<b>Concurrent magnetic and structural reconstructions at the interface of (111)-oriented <math>\text{La}_{0.7}\text{Sr}_{0.3}\text{MnO}_3</math> / <math>\text{LaFeO}_3</math></b>	<b>175</b>
	Supplementary Information . . . . .	183
<b>III</b>	<b>Conclusion and Outlook</b>	<b>193</b>
<b>5</b>	<b>Conclusion</b>	<b>195</b>
<b>6</b>	<b>Outlook</b>	<b>199</b>
	<b>Bibliography</b>	<b>203</b>



**Part I**

**Background**





---

## Introduction

*"If the auto industry advanced as rapidly as the semiconductor industry, a Rolls Royce would get half a million miles per gallon, and it would be cheaper to throw it away than to park it."*

– Gordon Moore

The inventions of the first transistor in 1947 [1], and the first integrated circuit in 1958 [2], have enabled the entire semiconductor industry and the digital society that we live in today.<sup>1</sup> Gordon Moore first recognized the possibilities of the industry. He observed in 1965 that the number of components in an integrated circuit had been doubling every second year, and stated that this was something he could envision continuing for at least another decade [3]. The statement has later been known as Moore's law, and has been valid for over half a century, reaching 20 billion transistors in 2017 [4]. This is the main reason why computers and other electronic devices becomes faster and better every year. Moore's law has since become a self-fulfilling law; it is no longer a simple observation. The semiconductor industry has set the goal to fulfil Moore's law and the consumers are expecting that the device they buy today will be outdated in a couple of years [5].

What Moore realized in 1965 was that simply through scaling down the transistor size, one could produce more transistors at once, improve its performance, and reduce the cost per component [3]. Moore's recipe turned out successful, however after several years of downscaling, the semiconductor industry realized that at one point, some physical limit would hinder the development. Hence, to combine the efforts of the whole semiconductor industry, the semiconductor association established the *national technology roadmap for semiconductors* (NTRS) in 1992, which was expanded to the *international technology roadmap for semiconductors*

---

<sup>1</sup>Both inventions have later been recognized with Nobel prizes in physics.

(ITRS) in 1998 [6]. Still, a major roadblock for the transistor development came in 2005, where one realized the amount of heat generated by the chip limited the increase in processor clock frequency, which then plateaued at around 3 GHz [7]. Nonetheless, by employing various smart solutions such as straining the silicon [8], creating multi-gate transistors such as the finFET [9], scaling has continued until today. This is much further than one expected in the late 1990s [10], and the semiconductor industry started the production of the 10 nm generation of transistors for commercial use in late 2016 [11]. Despite their combined efforts, this trend is now nearing an end, as the semiconductor industry is now running out of tricks to improve the scaling of silicon-based transistors [12]. Hence, the ITRS decided that the 2015 roadmap would be the last, as for future generations of transistors completely *new physics* are needed to continue the visions of Moore and fulfil the expectations of the of the industry, as well as the consumers [5, 7, 12, 13].

One possibility to include such *new physics* is to introduce new materials such as functional oxides [14–16]. In many functional oxides, the electrons are strongly correlated, meaning that the motion of one electron depends on all the others. This correlation effect can make the charge, spin, orbital and lattice degrees of freedom of the electrons operate on a similar energy scale and can thus give rise to a strong structure-property coupling, as illustrated in Figure 1.1 [16]. As the electrons are correlated, they open up for a plethora of functional properties in these materials, such as magnetism, and superconductivity. The large structure-property coupling in these materials can also create a strong link between the atomic structure and functional properties such as ferroelectricity. Furthermore, as shown in Figure 1.1, the similar energy scale makes it such that minute changes e.g. in charge-transfer, strain, frustration, electrostatic coupling and symmetry breaking can significantly alter the properties [15]. One of the most used examples is the formation of a superconductive state at the just at interface between the band insulators  $\text{LaAlO}_3$  and  $\text{SrTiO}_3$ , which has been explained by charge transfer due to a polar discontinuity at the interface [17, 18].

Inspired by the ITRS, several researchers within the field of oxides established *The 2016 oxide electronic materials and oxide interfaces roadmap*, or for short, the oxide electronics roadmap (OER) [19]. This was done to communicate the possibilities but also the challenges, by employing oxide based materials for future electronic devices. Among the many avenues that the OER discusses to further advance the field of oxide electronics is the consequence of point defects in these materials, including oxygen vacancies, and heterostructures grown along novel crystallographic directions, such as the [111]. Oxygen vacancies are e.g. pointed out to be important for resistive switching, domain wall conductivity and possibly understanding the conductive state at the  $\text{LaAlO}_3/\text{SrTiO}_3$  interface

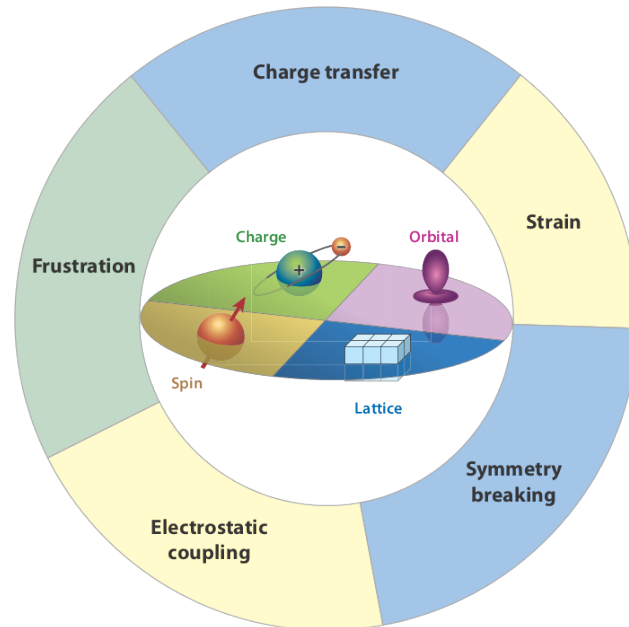


**Figure 1.1:** The strongly correlated electrons in perovskite oxides makes the charge, orbital, spin and lattice, all important for the physical properties, these can all again be tuned by e.g. local symmetry breaking, strain, charge transfer, strain, electrostatic coupling and frustration. Figure from [16].

[19]. While the (111)-interface is interesting because it enables control of orbital reconstruction, metal-to-insulator transitions and topologically nontrivial phases [19]. Due to the complexity of these materials, there is also need for precise electronic structure calculations in these systems [19]. Theoretical models that can help in this regard, as they can disentangle many of the coupled and intricate phenomena that necessarily occurs simultaneously in experiments [20].

Theoretical studies of solids based on density functional theory (DFT) is a field that has developed considerably the last decades, and has been of immense importance to understand the properties of perovskites. Examples include the seminal work of Cohen and Krakauer in the early 90s, which explained the microscopical mechanisms leading to ferroelectricity [21, 22]. More recent examples of DFT in action within functional oxides includes the discovery of hybrid improper ferroelectricity in  $\text{PbTiO}_3/\text{SrTiO}_3$  superlattices [23], polar metallic ground states in rare earth nickelates by straining in the (111)-plane [24], and the coupling between oxygen vacancies to structural domain walls in multiferroic  $\text{SrMnO}_3$  [25].

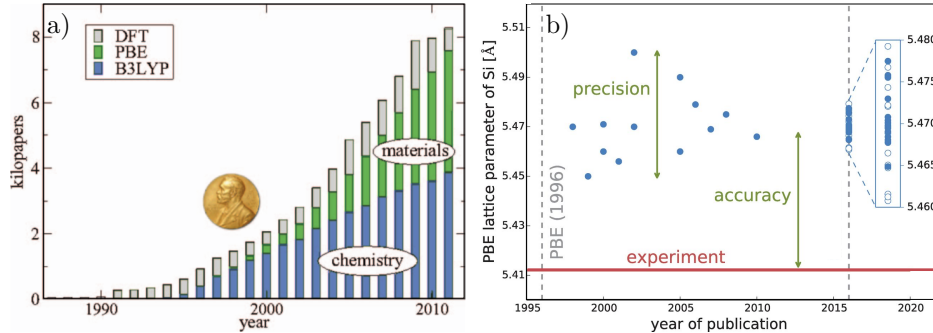


**Figure 1.2:** Developments within the field of density functional theory (DFT). a) The number of number citations per year resolved into chemistry and materials based on the citations on the B3LYP [29, 30] or PBE [27] functional. The Gold medal represents the Nobel prize in chemistry given to Walter Kohn and John Pople. Figure from [28]. b) Precision and accuracy of DFT calculation, here exemplified by the lattice parameter of silicon calculated by different DFT codes using the PBE functional. Large improvements in precision has been made over the 20 years since PBE was released, meaning that the calculations become more reproducible. The accuracy is determined by the details of the functional, as seen here PBE overestimates the lattice constant. Figure adapted from [26].

DFT has been an ever-growing field since Cohens work in the early 1990s, as illustrated in Figure 1.2 a) by the increase in the number of papers per year. Furthermore, in 2016 a major collaboration between developers of different DFT codes assessed the reliability of DFT calculations [26]. As illustrated in Figure 1.2 b), the reliability has improved much over the last two decades. This was shown by calculating the lattice parameter of silicon with multiple different codes, all supporting the Perdew-Burke-Ernzerhof (PBE) functional [27]. On the other hand, the accuracy, as defined by the difference between the calculated and the experimental value, has not improved. This is because it is related to the chosen approximations when establishing the specific functionals. As long as one is aware of these discrepancies, the results are still valuable [28]. The fact that the complex, parallelized DFT-codes, produced by different groups in different parts of the world with different approaches, converge around the same value, is very reassuring [26].

The goal of this thesis has first been to establish DFT as a tool in the Oxide Electronics group at Department of Electronic Systems at NTNU, and then use DFT to study how one can use thin film techniques to manipulate the structure of functional oxides. We focus on two different methods to control the structure of perovskites. First, we investigate how oxygen vacancies, illustrated in Figure

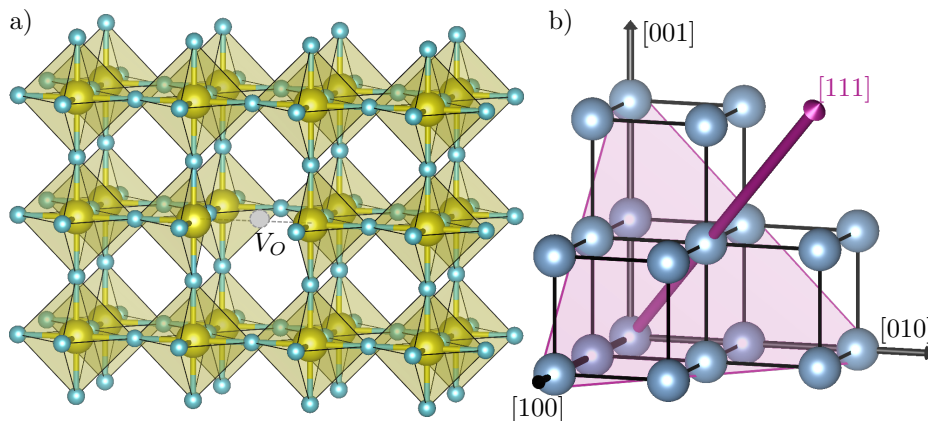


**Figure 1.3:** Illustration of avenues used to control the structure of perovskite oxides in this work. a) an oxygen atom is missing where the grey circle is, creating a vacancy  $V_O$ . b) the crystallographic directions  $[001]$ ,  $[010]$ ,  $[100]$  and  $[111]$  for a cubic crystal. The  $(111)$ -plane is shown in magenta.

1.3 a), can order in layered structures in perovskite thin films, and how this affects the magnetic and electronic properties. As has been pointed out in several perspectives [31, 32], understanding oxygen vacancies in perovskites is essential both to interpret experimental measurements correctly, but it is also a promising vista for controlling the functional properties. The second avenue we explore is how the  $(111)$ -orientation affects the structure and properties compared to bulk and the more common  $(001)$ -orientation. As illustrated in Figure 1.3 b), the  $[001]$ -direction is along the side of the edge of the cube, while the  $[111]$ -direction is along the body diagonal. In this work we focus on both the aspects of epitaxial strain in the  $(111)$ -plane, and how the structural distortions can couple across a  $(111)$ -oriented interface. A Nature Materials commentary [33] pointed out that the  $(111)$ -interface and strain was two of the most promising opportunities for further development within the field of oxide interfaces, due to the hexagonal symmetry and the ability to manipulate the oxygen octahedra. We further note that these goals are well in line with what is pointed out in the OER as important areas to further develop oxide electronics.

The thesis is structured as follows: Part I describes the background for the work and contains 2 chapters in addition to this one. Chapter 2 describes the physics of perovskite oxides with a focus on recent developments within thin film applications. Chapter 3 gives an introduction to density functional theory and describes the different calculation parameters used in this work. Part II contains the results, which are presented in seven papers, numbered from A–G. Papers A and B focus

on ordered oxygen vacancies. Papers C, D and E discuss the effect of strain in the (111)-plane, while papers F and G discuss the effect of (111)-interfaces. Part III ends the thesis with a conclusion and outlook. All atomic structure figures have been generated with VESTA [34].

---

# Properties of Perovskite Oxides

*“Quantum physics makes me so happy. It’s like looking at the universe naked.”*

– Sheldon Cooper

In this chapter, some of the main physics behind the properties of perovskite oxides are presented with an emphasis on thin film applications. We start with the perovskite crystal structure, and focus on which kind of distortions are common in this structure. Then the orbital and magnetic structure of perovskites are discussed, and how they are influenced by the perovskite structure. Furthermore, the effect of point defects is discussed with a focus on oxygen vacancies and the possibility for point defects to order in layered structures. Finally, how a thin film geometry can be used to tune, enhance and control the properties of perovskite oxides is presented.

## 2.1 Crystal Structure

As mentioned in chapter 1, perovskite oxides have a strong structure-property coupling. Hence, to understand their properties one must first understand their structure. Perovskite oxides have general formula  $ABO_3$ , and the name comes from the mineral perovskite  $CaTiO_3$  named after the Russian mineralogist Lev Perovski. The aristotype perovskite has a cubic structure with space group symmetry  $Pm\bar{3}m$ , as visualized in Figure 2.1. As shown, the B-cations are octahedrally coordinated by the oxygen atoms, and the oxygen octahedra share corners. The A-cations on the other hand are dodecahedrally coordinated, and fill up the octahedral voids. To assure charge neutrality, the sum of the cation valence must be +VI in stoichiometric materials. This leads to three main classes of perovskites, III-III, II-IV, and I-V, which correspond to the oxidation states of the A and B cation, respectively. The multiple possible oxidation states make the



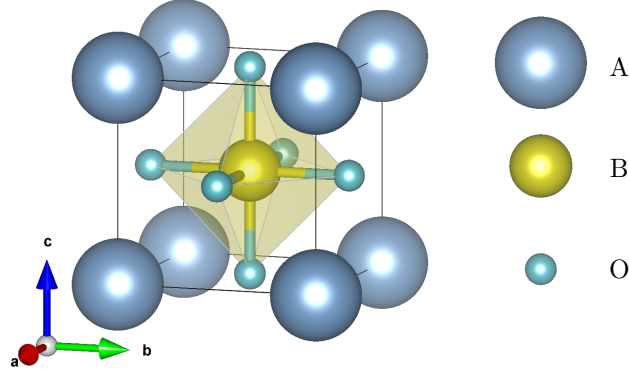


**Figure 2.1:** The cubic aristotype of the  $ABO_3$  perovskite structure.

perovskite structure chemically flexible, where different elements including alkali metals, rare earths and transition metals can occupy the A and B sites [35, 36].

The cubic  $Pm\bar{3}m$  structure is for most perovskites only stable at high temperatures, while at lower temperatures different distortional modes tend to condensate. The distortions likely to occur in a perovskite can often be rationalized based on the mismatch between the A and B cation sizes. The degree of size mismatch is often measured using the Goldschmidt tolerance factor, defined as [37]:

$$t = \frac{r_A + r_O}{\sqrt{2}(r_B + r_O)}, \quad (2.1)$$

where  $r_A$ ,  $r_B$  and  $r_O$  are the radii of the A, B and oxygen ions, respectively. If  $t = 1$  the cubic structure is likely to be stable. If  $t < 1$  the A cation is too small, and the most common way to mitigate this size mismatch is by reducing the A-site dodecahedral volume through octahedral rotations. The rotations can be either out-of-phase or in-phase with the next layer along the rotation axis as illustrated in Figure 2.2 a) and b), respectively. As shown, for in-phase rotations all the octahedra rotate in the same direction, while for the out-of-phase rotations, half of the octahedra rotate one way while the other half rotate the other way. On the other hand if  $t > 1$ , the B-cation is too small. The B-cation can then make some of the B-O bonds shorter by displacing away from the centre of the octahedra, hence creating a polar displacement as shown in Figure 2.2 c). Finally, if  $t$  deviates too much from unity, other kinds of crystal structures are preferred, such as the hexagonal perovskite polytypes [36]. However, the exact limit for when the perovskite structure becomes unstable depends on the specific material, and can e.g. be tuned through thin film growth techniques [38–40].

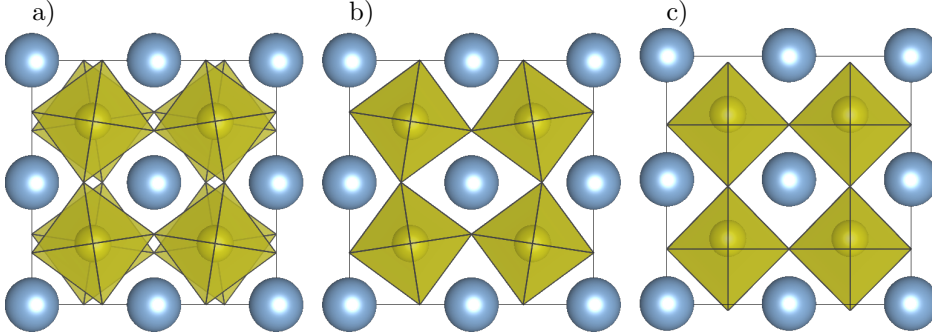


**Figure 2.2:** Typical distortions occurring in perovskite oxides illustrated in  $2 \times 2 \times 2$  supercells of the simple cubic cell. a) out-of-phase octahedral rotations, b) in-phase octahedral rotations c) Polar displacements of the B-cation. The rotations shown in a) and b) are most common for materials with  $t < 1$ , while the displacements in c) are commonly stabilized when  $t > 1$ .

In the following sections, the distortions shown in Figure 2.2 are discussed in more detail.

### 2.1.1 Octahedral Rotations

Octahedral rotations are essential for the properties of perovskite oxides, as they change the B–O–B bond angles, and hence how the different orbitals overlap. As discussed in the previous section, there are two different types of octahedral rotations. Each consecutive layer can rotate in opposite directions, known as out-of-phase rotations (Figure 2.2 a) or each layer along the rotation axis can rotate in the same direction, known as in-phase rotations (Figure 2.2 b). Each of these types of rotations can again happen around each of the three pseudocubic axes. Glazer found that there are 23 different rotation patterns<sup>1</sup> that ensures octahedral corner connectivity. I.e., since an oxygen atom can only be at one place at the same time, all octahedra have to be connected. Glazer also provided a notation for describing the rotations [42, 43]. Glazer notation is written as  $a^\#b^\#c^\#$ , where the Latin letters describes the rotations around each pseudocubic direction, respectively. While the superscripts indicate whether the rotations are out-of-phase, denoted with a  $-$ , in-phase, denoted with a  $+$ , or not at all, denoted with a  $0$ . If two Latin letters are the same, it indicates that the magnitude of these octahedral rotations are the same. A group theoretical analysis assuming rigid octahedra, revealed the group-subgroup relationships between the different tilt patterns as shown in Figure 2.3 [41].

<sup>1</sup>Later reduced to 15 as some of them are equivalent due to symmetry [41].

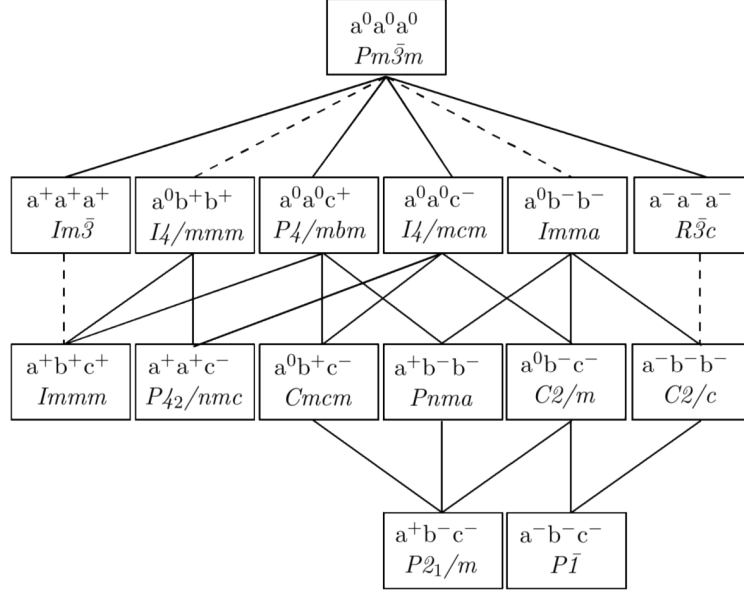


**Figure 2.3:** Diagram indicating the group-subgroup relationships between the 15 different octahedral rotation patterns. The dashed lines indicate that the corresponding phase transition is required to be first order by Landau theory. Figure from [41].

It has been shown for perovskite oxides that out-of-phase rotations are energetically favoured over in-phase rotations. This is because out-of-phase rotations minimize electrostatic interactions, improve the bond valence of the A-site and enhance the covalency of the A–O bonds, while still maintaining the highest number of equivalent sites [44–46]. From this argument, one could naively assume that the most common perovskite structure is  $R\bar{3}c$  with tilt pattern  $a^- a^- a^-$ . However, the most common crystal structure for perovskite oxides is instead  $Pnma$ , with tilt pattern  $a^+ b^- b^-$  [45, 47]. The reason for this, is that the  $a^+ b^- b^-$ , tilt pattern also allows for shifts of the A-cations to further increase their covalency, thus maximizing electrostatic attraction for small  $t$ . However, these shifts of the A-cations are forbidden by symmetry in the  $R\bar{3}c$  space group. For this reason, the  $Pnma$  structure is found almost exclusively when the tolerance factor is lower than 0.975 or when the A-site is relatively electronegative [45]. On the other hand, having a  $6s^2$  lone pair on the A-site can stabilize different structures, even for low  $t$ . A prominent example here is  $\text{BiFeO}_3$ , which has  $t = 0.913$  [48], but is stable in the polar  $R\bar{3}c$  structure with tilt pattern  $a^- a^- a^-$  [49].

Another way of describing the stability of perovskite oxides which possess octahe-

dral rotations is by the polyhedral volume ratio,  $V_A/V_B$ , where  $V_A$  and  $V_B$  denote the volumes of the dodecahedral A-site and the octahedral B-site, respectively [47, 50, 51]. It can be shown that the polyhedral volume ratio is equal to 5 for an undistorted  $a^0a^0a^0$  structure,<sup>2</sup> while any rotational distortions will lower this value. Avdeev et al. [47] showed that the critical value for phase transitions between  $Pnma \leftrightarrow I4/mcm$  and  $Pnma \leftrightarrow R\bar{3}c$  occurs at  $V_A/V_B \sim 4.85$ , while the  $Imma$  space group is only stable in the range  $V_A/V_B \simeq 4.8$  to 4.9.

As mentioned, the rotations of the octahedra reduces the B–O–B angles from the ideal value of  $180^\circ$ . In the  $Pbnm$  structure<sup>3</sup> with tilt pattern  $a^-a^-c^+$ , there are two different B–O–B angles,  $\theta_{xy}$  and  $\theta_z$ . Both angles can be approximated from the Glazer tilt rotations as [52]:

$$\theta_{xy} \approx 2 \cot^{-1} \left( \sqrt{\tan^2 \alpha^- + \tan^2 \gamma^+} \right), \quad (2.2)$$

$$\theta_z \approx 2 \cot^{-1} \left( \sqrt{\tan^2 \alpha^-} \right), \quad (2.3)$$

where  $\alpha^- = \beta^-$  is the degree of out-of-phase rotation around the  $x$  and  $y$  pseudocubic directions, respectively, and  $\gamma^+$  is the degree of in-phase rotation around the  $z$  pseudocubic direction.

### 2.1.2 Polar Distortions

Another important type of structural distortion in perovskite oxides is the polar distortions as illustrated in Figure 2.2 c). Taking the centre of mass as a reference, the B-cation has off-centred from the high symmetry position in the middle of the octahedron, breaking the inversion symmetry. These distortions are important as they give rise to non-cancelling dipole moments. If these dipole moments are switchable by an electric field, the material is known as a ferroelectric.

Off-centring occurs as a result of competition between long range coulombic forces favouring the polar structure, and short range repulsions which favour the cubic structure. Cohen and Krakauer [21, 22] established theoretically in 1992 that for the prototypical ferroelectric perovskites  $BaTiO_3$  and  $PbTiO_3$  the partial covalency between the empty  $Ti_{3d}$  states and the occupied  $O_{2p}$  states is the driving force for this off-centring. Off-centring of the B-cation is further favoured if the B-cation is small relative the octahedral site, hence the non-polar structure is preferred when  $t > 1$ . The partial covalent bonding is not limited to

<sup>2</sup>E.g.:  $Pm\bar{3}m$ ,  $P4mm$  and  $R3m$ .

<sup>3</sup>The  $Pbnm$  structure with tilt pattern  $a^-a^-c^+$  is the same space group (#62) as the  $Pnma$  structure with tilt pattern  $a^+b^-b^-$ . They are related by a rotational transform.

the interaction between empty  $Ti_{3d}$  states and  $O_{2p}$ . Other empty  $d$ -states also show this behaviour, e.g.  $Nb_{4d}$  in  $KNbO_3$  [53].

Furthermore, Cohen and Krakauer investigated the different phase transitions of  $BaTiO_3$  and  $PbTiO_3$ .  $BaTiO_3$  has multiple phase transitions, going from high to low temperature they are: cubic, tetragonal, orthorhombic and rhombohedral [54]. The three latter phases are polar, with polarization along the pseudocubic  $\langle 100 \rangle$ ,  $\langle 110 \rangle$  and  $\langle 111 \rangle$ , respectively.  $PbTiO_3$  on the other hand has only one phase transition from non-polar cubic to tetragonal with a large polarization along  $\langle 100 \rangle$  [55]. This difference between  $BaTiO_3$  and  $PbTiO_3$  was found to be because the bonding between the barium and oxygen is almost completely ionic, while in  $PbTiO_3$  the lone pair  $Pb_{6s}$  states at the A-site hybridize with  $O_{2p}$ , stabilizing the tetragonal state and increasing the polarization [21, 22].

Some materials, such as  $SrTiO_3$  [56],  $CaTiO_3$  [57, 58] and  $KTaO_3$  [59, 60], are very close to being ferroelectric, and a ferroelectric phase transition is expected at low temperatures. However, it has been demonstrated that these transitions never occur, due to quantum fluctuations. For this reason, these materials are called incipient-ferroelectrics or quantum ferroelectrics [56].

While it is in general understood that octahedral rotations and ferroelectricity are competing modes [61–63], there are some materials that exhibit both types of distortions, such as  $BiFeO_3$  [49]. It has also been shown that it is possible to induce ferroelectricity by octahedral rotations in cation ordered perovskites [64]. Furthermore, Bousquet et al. [23] showed that the octahedral rotations could induce improper ferroelectricity in (001) oriented superlattices of  $SrTiO_3$  and  $PbTiO_3$ . The difference between proper and improper ferroelectricity is that for improper ferroelectricity the polarization is no longer the main order parameter of the system. The order parameter in improper ferroelectrics is instead another physical quantity whose transformation properties are different from those of the polarization [65]. Hence, in the (001)-oriented  $SrTiO_3/PbTiO_3$  superlattices the improper ferroelectricity gives rise to a large almost temperature independent dielectric constant [23].

## 2.2 Orbital Structure

Orbitals are important for the strong-structure property coupling in perovskite oxides, as they determine the shape of the electron wave functions and hence provide a strong link between the electron- and the crystal-structure. The orbitals that are most important for the functional properties of many perovskites oxides are the oxygen  $2p$  and the  $d$  orbitals on the B-site [66].

The three different  $O_{2p}$  states are labelled  $p_x$ ,  $p_y$  and  $p_z$ , and are all pointing

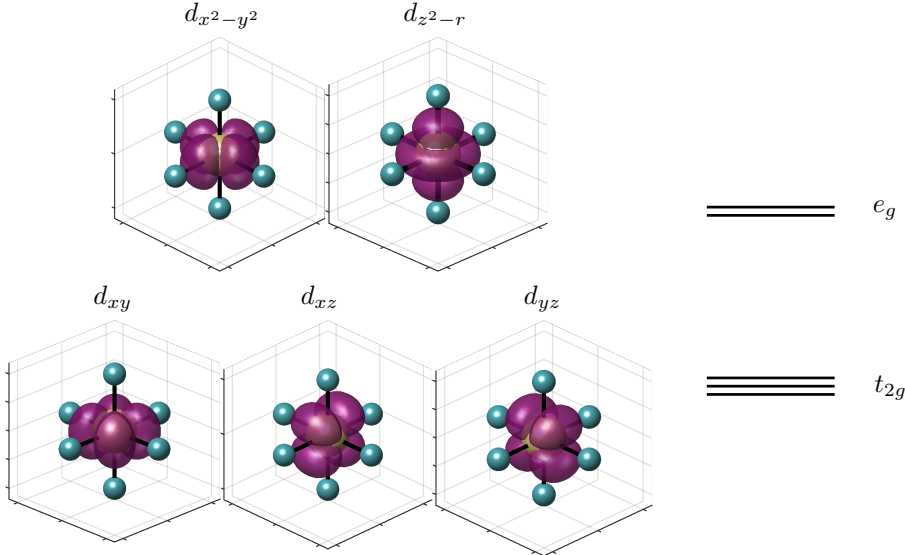


**Figure 2.4:** Isosurface plots of the five  $d$  orbitals shown in purple. Each of the  $d$  orbitals are centred on a B-cation (yellow) which are coordinated by the oxygen atoms (teal). To the right the effect of the crystal field splitting from the octahedra is shown. The crystal field splits the five  $d$  orbitals into  $e_g$  and  $t_{2g}$  orbitals.

towards B-sites in the  $x$ -,  $y$ - and  $z$ -directions, respectively. While there are five different  $d$  orbitals which are labelled of  $d_{xy}$ ,  $d_{xz}$ ,  $d_{yz}$ ,  $d_{x^2-y^2}$  and  $d_{z^2-r}$ . In a single atom, these different  $d$ -orbitals are degenerate. However, in a perovskite, the crystal field arising from the octahedral coordination of the B-site splits the  $d$ -states into  $t_{2g}$  and  $e_g$  states. As seen in Figure, 2.4, the  $e_g$  orbitals consisting of  $d_{x^2-y^2}$  and  $d_{z^2-r}$ , are raised in energy as their main lobes point directly towards the negatively charged oxygen ions. On the other hand, the  $t_{2g}$  states consisting of  $d_{xy}$ ,  $d_{xz}$ ,  $d_{yz}$  have their lobes in between the oxygen ions, and thus are lowered in energy. The  $t_{2g}$  and  $e_g$  states can be further split by e.g. applying strain to the structure; this is discussed in section 2.5.1.

### 2.3 Magnetic Structure

Magnetism typically arises from ordered unpaired  $d$  or  $f$  electrons, and in perovskites unpaired  $d$  electrons at the B-site is the most common reason for some sort of magnetic ordering. Hund's rules dictate that the *intra*-atomic alignment of the spins should be parallel. However if the crystal field splitting is large, a low spin state can arise. Furthermore, the *inter*-atomic spin alignment can be

ferromagnetically, i.e. all spins are in the same direction, giving a net magnetic moment, or antiferromagnetically, i.e. every second spin align oppositely giving zero net moment. If the alternating spins are unequal, the moments do not cancel out. This yields a small switchable moment, and is known as ferrimagnetism.

Ferromagnetic alignment of  $d$  states at different B-sites in perovskites oxides typically occurs due to a mechanism known as double-exchange [67]. Double-exchange arises if the electrons can hop from one  $d$  orbital to another mediated, through an  $O_{2p}$  orbital. This is favourable since the ability to hop (delocalize) reduces the kinetic energy. Furthermore, due to the Hund's coupling the energy is lowered if all the  $d$  orbitals on one site have the same spin. As the double-exchange requires hopping from an occupied state to an unoccupied state, it is strongest in systems with a mixed valence. An example is the hopping from a  $Mn^{3+}$  ion to a  $Mn^{4+}$  ion mediated by an  $O_{2p}$  state as illustrated in Figure 2.5 a). As shown, the electron in the  $e_g$  state at the  $Mn^{3+}$  can hop to the neighbouring  $O_{2p}$  orbital, but since this orbital is already filled, an electron with the same spin has to hop from the  $O_{2p}$  state to the empty  $e_g$  state at the  $Mn^{4+}$ . Due to the strong Hund's coupling, this hopping is only favourable if the other spins at the  $Mn^{4+}$  are parallel to the spins at the  $Mn^{3+}$ . Since the double-exchange occurs due to the hopping of electrons, it is closely related to electric conduction and gives itinerant electrons [67]. For this reason, when double-exchange is dominant, there is only one spin channel with available states at the Fermi level. Hence, strong double-exchange makes appropriately doped manganites into half-metals.

On the other hand, antiferromagnetic alignment of the  $d$  states at different B-sites in perovskites oxides are governed by a mechanism known as superexchange [68]. Superexchange occurs due to a virtual electron transfer between the  $d$ -states mediated by the oxygen  $O_{2p}$  state. An example showing the interaction between two  $Fe^{3+}$  ions mediated by an  $O_{2p}$  state is visualized in Figure 2.5 b). As shown, the superexchange occurs in accordance to the Pauli exclusion principle, because the electrons can spread out further if the spin at a  $d$ -orbital is orthogonal to the spin of the oxygen  $p$ -orbital pointing towards it. This is what is known a virtual exchange, since no electrons are actually moving. Furthermore, as shown in Figure 2.5 b), the other lobe of the  $O_{2p}$  orbital has to be antiparallel to the first, and this one again has to be antiparallel with the  $d$ -state at the next  $Fe^{3+}$ . Hence, the superexchange favours anti parallel alignment of the  $d$ -orbitals, and localized electrons. As shown, the virtual electron transfer is both between  $t_{2g}$  and  $e_g$  orbitals, but as the  $e_g$  orbitals overlap more with the  $O_{2p}$  states, the superexchange between  $e_g$  orbitals are generally stronger.

Perovskites can have superexchange in one direction and double-exchange in another, a typical example of this being  $LaMnO_3$  [69]. This can cause different types of magnetic orderings e.g.:

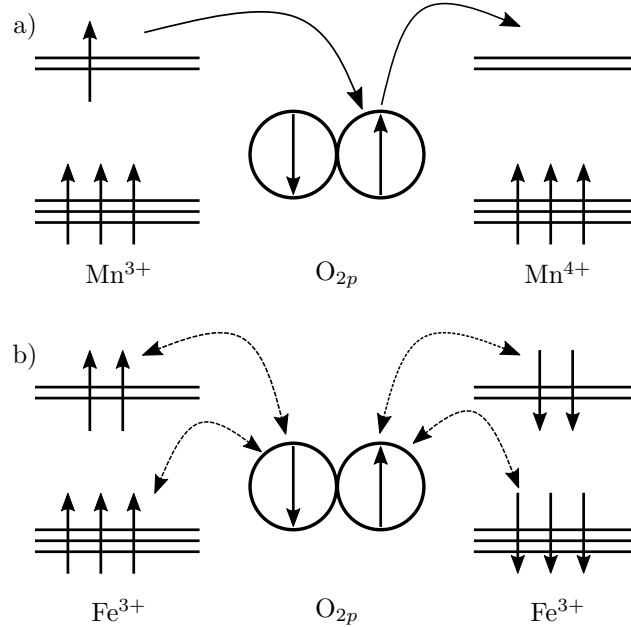


**Figure 2.5:** Examples of a) double-exchange and b) superexchange. a) shows the  $180^\circ$  double-exchange that occurs between  $\text{Mn}^{3+}$  and  $\text{Mn}^{4+}$  mediated by the  $\text{O}_{2p}$  orbitals. The result is strong ferromagnetism and itinerant electrons. b) shows the  $180^\circ$  superexchange that occurs between two  $\text{Fe}^{3+}$  ions, mediated by the  $\text{O}_{2p}$  orbitals. The result is strong antiferromagnetism and localized electrons. The solid arrows denote actual hopping, while the dashed lines denote virtual hopping.

- Superexchange in all three directions, known as G-type antiferromagnetism.
- Superexchange in two directions and double-exchange in one direction, known as C-type antiferromagnetism.
- Superexchange in one direction and double-exchange in two directions, known as A-type antiferromagnetism.
- Double-exchange in all three directions. This is the typical requirement for ferromagnetism.

As discussed in section 2.1.1, rotations of the oxygen octahedra is common if the tolerance factor is lower than unity. If the  $\text{BO}_6$  octahedra rotate, the B–O–B angles is reduced from its ideal value of  $180^\circ$ , e.g. as given by equations (2.2) and (2.3), hence the overlap between the  $e_g$  and  $\text{O}_{2p}$  orbitals is reduced. This reduced



overlap weakens the double- and superexchange interactions between the  $e_g$  and  $O_{2p}$  orbitals. This has for instance been shown in the orthoferrites, where the spin ordering transition temperature<sup>4</sup> is highest in  $\text{LaFeO}_3$ , and is reduced when La is replaced with other trivalent elements with lower radii. The replacement gives a lower  $t$ , and hence lower B–O–B angles [70].

Since both double- and superexchange interactions are present in perovskites, the dominating interaction depends on which one has the largest energy gain. This can in many cases be determined by the Goodenough-Kanamori rules [69, 71–73]. To apply these rules, one needs to know how many  $d$  electrons interact and in which directions. According to the rules, one typically needs interactions between different cations with different number of  $d$  electrons to get double-exchange in all directions, i.e. ferromagnetism, in perovskite oxides. For this reason, most stoichiometric perovskite oxides are antiferromagnetic, and double-exchange requires some form of chemical doping. An example is the doped manganites,  $\text{A}_{1-x}\text{A}'_x\text{MnO}_3$  ( $\text{A}=\text{La}$ ,  $\text{Pd}$  and  $\text{A}'=\text{Ca}$ ,  $\text{Sr}$  and  $\text{Ba}$ ), where the doping gives double-exchange interactions between  $\text{Mn}^{3+}$  and  $\text{Mn}^{4+}$ . In these materials, the strongest double-exchange interactions typically occur for  $x = 1/3$  [74].

## 2.4 Point Defects and Ordered Defect Structures

Point defects in perovskite oxides can in principle arise from cation excess or deficiency (A or B site), as well as oxygen deficiency and excess. However, interstitials of either constituent is not as common, as there is limited extra space available, making them energetically unfavoured [35]. We will here focus mainly on oxygen vacancies, as they are the most common defects in perovskites [35, 36]. When the concentration of point defects becomes large, the point defects start to interact and ordered superstructures can occur. Such effects will be discussed in the second part of this section.

### 2.4.1 Oxygen Vacancies

Oxygen vacancies change the stoichiometry in perovskites to  $\text{ABO}_{3-\delta}$  and have been shown to have a large coupling to the functional properties of oxides. E.g., they are known to be essential for the high temperature superconductivity of the cuprates [19, 31, 32, 75]. Point defects, such as oxygen vacancies, may be described using the Kröger-Vink notation [76], where all charges are given with respect to the perfect lattice. Kröger-Vink notation is written as  $X_S^C$ , where  $X$  is the species e.g. B for a B-cation or  $V$  for a vacancy.  $S$  is the site, e.g. O for an oxygen site or  $i$  for an interstitial, and  $C$  is the effective charge, where  $\bullet$ ,

<sup>4</sup>Known as the Néel temperature.

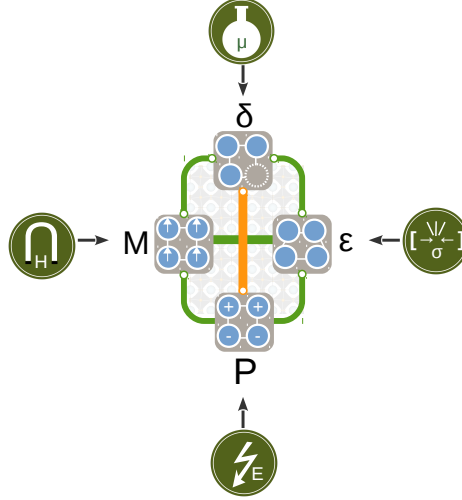
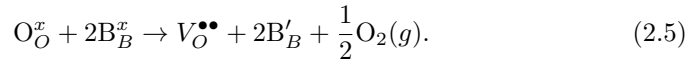
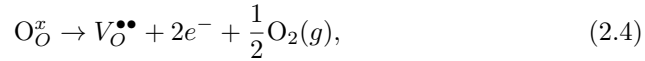


**Figure 2.6:** Illustration of the cooperative (green) and competing (orange) behaviour between oxygen vacancies  $\delta$ , magnetization  $M$ , stress  $\epsilon$  and polarization  $P$ . These properties can again be controlled by chemical potential  $\mu$ , magnetic field  $H$ , strain or pressure  $\sigma$  and electric field  $E$ , respectively. Figure from [75].

$+$  and  $x$  denote positive, negative and no effective charge, respectively. In this framework, an oxygen vacancy is effectively charged with a charge of +2. This charge has to be compensated in order to assure electroneutrality [77]. Using the Kröger-Vink notation, two limiting scenarios for charge compensating electrons can be identified:



Equation (2.4) represents the delocalized limit where the charge compensating electrons occupy well-dispersed states in the conduction band. Equation (2.5) on the other hand, represents the localized limit where the charge compensating electrons localize on two B-cations and reduce them. It should be noted that charge compensating electrons may not be physically localized close to the oxygen vacancy, e.g. they can reside on the surface or within adjacent electrode materials.

In figure 2.6, it is illustrated that the oxygen vacancies can couple to magnetization, stress and polarization of perovskite oxides. Each of these coupling mechanisms will be discussed in the following paragraphs.

Large concentrations of oxygen vacancies can in general be accommodated if the B-cation is a transition metal, as transition metals typically have multiple stable oxidation states. In these materials, the introduction of oxygen vacancies typically expands the lattice locally, which is known as chemical expansion. This occurs because the extra electrons that are generated during oxygen vacancy formation reduce the transition metals at the B-site, equation (2.5), which again increase their size [78–80]. If the electrons are delocalized, as in equation (2.4), a weaker global expansion is typically observed instead. Chemical expansion has been used to e.g. stabilize the perovskite phase of  $\text{SrMnO}_3$ , which in stoichiometric bulk is stable in a hexagonal state [38]. Chemical expansion is also detrimental when perovskites are used as solid oxide fuel cells, as it can lead to large stress gradients across oxide membranes [81]. Hence, there is a strong link between the oxygen vacancies and stress in Figure 2.6.

The coupling of oxygen vacancies to magnetism in Figure 2.6 can also be understood by the fact that changing the oxygen stoichiometry in magnetic perovskites typically changes the valence of the transition metal at the B-site, equation (2.5). Hence, as discussed in section 2.3, different valence on the B-cations change the balance between super- and double-exchange interactions. Oxygen vacancies have e.g. been used to change multiferroic  $\text{Eu}_{0.5}\text{Ba}_{0.5}\text{TiO}_{3-\delta}$  from a G-type antiferromagnet to a ferromagnet, because the oxygen vacancies lead to spin polarized  $\text{Ti}^{3+}$  ions on the B-site [82].

Furthermore, ferroelectricity is dampened by oxygen vacancies, as shown by the orange line in Figure 2.6. As was discussed in section 2.1.2, the polar distortions required for ferroelectricity occur due to a partial covalent bond between empty  $d$  orbitals and the  $\text{O}_{2p}$  states. Since the charge compensating electrons tend to fill up the  $d$  orbitals, as shown in equation (2.5), oxygen vacancies inhibit the polarization. This was shown for  $\text{AMnO}_3$  ( $A = \text{Ca}, \text{Sr}, \text{Ba}$ ) by Marthinsen et al. [75], where the ferroelectric instabilities were dampened by oxygen vacancies. Oxygen vacancies have furthermore been suggested as the reason for ferroelectric fatigue in  $(\text{Pb},\text{Zr})\text{TiO}_3$  thin films, especially if they cluster locally [83, 84].

### 2.4.2 Ordered Defect Structures

When the concentration of point defects increases, the defects start to interact. The defects can then form ordered layered structures, where  $n$  perovskite blocks are separated between a layer with a different crystal structure and/or chemistry. Thus, in the limit  $n \rightarrow \infty$ , the perovskite structure is regained. The layering typically decouples the octahedral building blocks which enforces anisotropic properties [85], and can induce hybrid-improper ferroelectricity in these materials [86, 87].

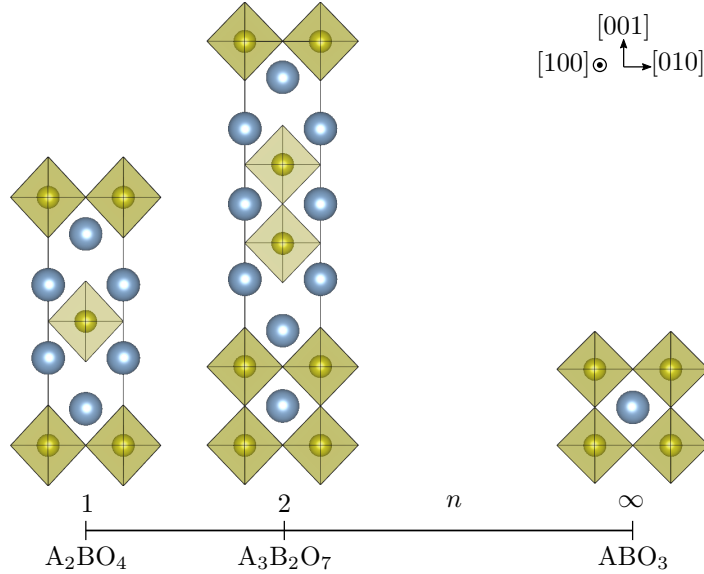


**Figure 2.7:** The relationship between the Ruddlesden-Popper phases and the perovskite structure,  $n$  denotes the number of octahedral layers between each rock salt AO layer.

For A and B non-stoichiometry, the layered structures can e.g. result in Ruddlesden-Popper  $A_{n+1}B_nO_{3n+1}$  [88], Aurivillius  $(Bi_2O_2)(A_{n-1}B_nO_{3n+1})$  [89] or Dion-Jacobson  $A'(A_{n-1}B_nO_{3n+1})$  [90, 91] phases. These phases all have layered stoichiometric perovskite slabs stacked along the [001]-direction, while their difference is the separating layers, and whether or not the layers are offset from each other. In the Ruddlesden-Popper phases, as illustrated in Figure 2.7, the separating layer is an AO rock salt layer, causing a shift of the different perovskite blocks by half a unit cell in the [100] and [010] directions. For the Aurivillius phases, the separating layer consists  $Bi_2O_2$ , while again there is a shift of the different perovskite blocks by half a unit cell in the [100] and [010] directions. The Dion-Jacobson phases have an alkali metal,  $A'$ , separating the layers, and whether or not any offset occurs depends on the specific alkali metal.

If there is a large concentration of oxygen vacancies, but an equal amount of A and B cations a brownmillerite phase can be formed [92]. The brownmillerite structure has general formula  $A_2B_2O_5$ ,<sup>5</sup> and is a good oxygen conductor which has been widely studied for use in solid oxide fuel cells [93–95]. As shown to the left of Figure 2.8, the oxygen vacancies are ordered in every second (001)

<sup>5</sup>Equivalent to  $ABO_{2.5}$ .

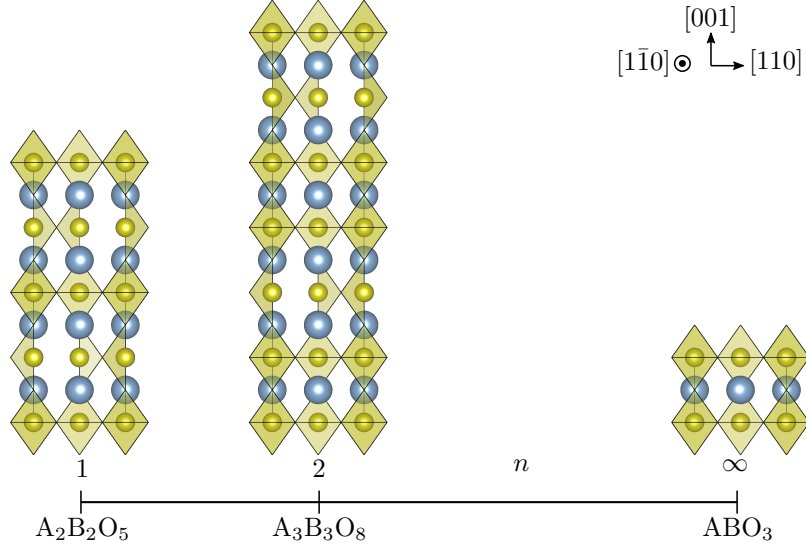


**Figure 2.8:** The relationship between the brownmillerite-like phases and the perovskite structure,  $n$  denotes the number of octahedral layers between each tetragonal layer. Note that the perovskite  $ABO_3$  structure is here rotated by  $45^\circ$  about the  $[001]$ -axis to be shown from the same angle as the brownmillerite phases.

$BO_2$  layer of the cubic perovskite structure, such that alternate  $[1\bar{1}0]$  rows of oxygen are missing [35]. Relying on a block by block approach, similar to the structures with A and B cation non-stoichiometry, like the Ruddlesden-Popper phases, one can write a general formula  $A_{n+1}B_{n+1}O_{3n+2}$  which is a series of brownmillerite-like structures as shown in Figure 2.8 [92, 96, 97]. It has e.g. been shown that a brownmillerite phase can occur in  $La_{2/3}Sr_{1/3}MnO_3$  grown on  $SrTiO_3$ , if oxygen deficient  $SrTiO_3$  is grown on top and used as a getter [98]. Furthermore, Yao et al. [99], showed that it is possible to apply an electric pulse to induce a brownmillerite structure in the perovskite phase of  $La_{2/3}Sr_{1/3}MnO_3$ . By reversing the voltage, the perovskite structure could be re-obtained. They also showed that the brownmillerite and perovskite phases had significantly different electrical conductance, making these effects interesting for resistive switching applications [99]. In addition, in  $SrCoO_{3-\delta}$ , electric field control of ions was obtained, resulting in three stable phases: perovskite  $SrCoO_{3-\delta}$ , brownmillerite  $SrCoO_{2.5}$  and a novel  $HSrCoO_{2.5}$  structure [100]. These three phases had different band gaps and different optical transparencies that could be used in smart windows applications [101].

In summary, point defects such as oxygen vacancies present an interesting direction to look for new avenues to control, enhance and tailor emergent properties at perovskite oxides. Especially if the point defects order in layered structures, enforcing anisotropic effects.

## 2.5 Effects of a Thin Film Geometry

By growing a perovskite oxide epitaxially as a thin film on a substrate, one can tune, control, and even induce new properties of perovskite oxides. In this section, some of the ways of exploiting these effects are discussed. The effects are divided into two main ways to control the properties:

1. Utilizing the epitaxial strain from the substrate, known as *strain engineering*.
2. Utilizing the interfaces either between epitaxially grown superstructures or, the thin film and substrate, known as *interface engineering*.

### 2.5.1 Strain Engineering

When a thin film is grown epitaxially on a substrate, the in-plane lattice vectors are clamped to those of the substrate while the out-of-plane lattice vector is allowed to relax according to the Poisson's ratio of the film [102]. This is true as long as the thickness of the film is thinner than the critical thickness where strain relaxation occurs, e.g. by introducing dislocations. By choosing a substrate with either smaller or larger lattice constant than the thin film, the film will be put under compression or tension, respectively. Strain engineering in the (001)-plane has been thoroughly studied over the last decades [20], and multiple strain accommodation mechanisms have been revealed. As illustrated in Figure 2.9, for perovskites there is not only elongation of bond lengths that occurs, which typically is the dominating accommodation for semiconductors [8]. As shown, multiple other types of accommodations may also occur, and the increasing quantity under each respective type of strain is shown in Figure 2.9 by a proceeding  $\uparrow$ . For this reason, strain engineering is a powerful tool to control the properties of a thin film. The different strain accommodations will be discussed in the following paragraphs.

#### Polar Distortions

Strain from an (001)-oriented substrate enhance or induce polar distortions in perovskites, this was first predicted theoretically by Pertsev et al. [103, 104]. They showed that, because of the extra space in the out-of-plane direction, compressive strain favours out-of-plane polarization. The opposite effect was seen under tensile

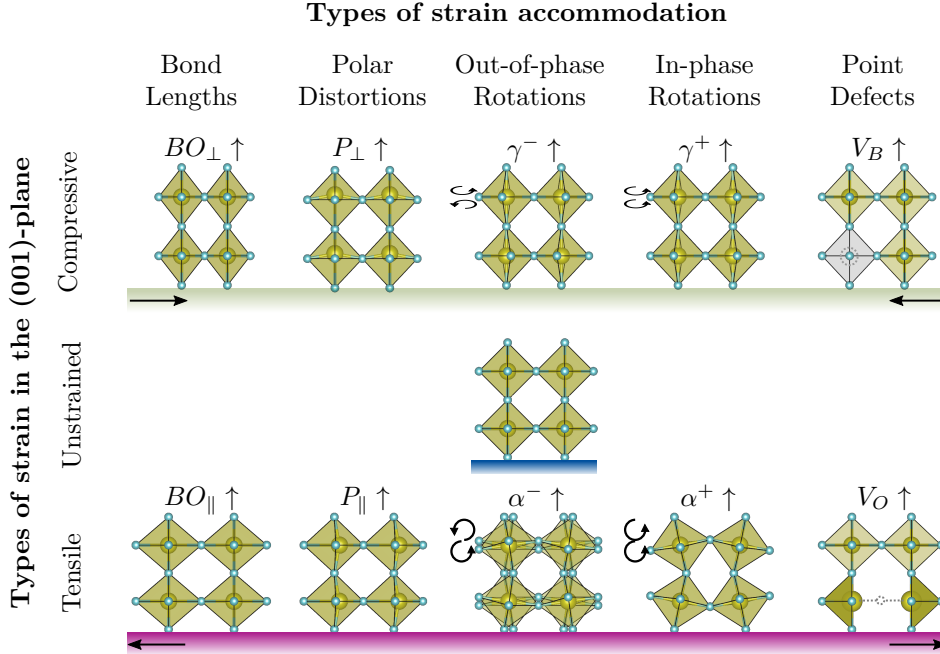


**Figure 2.9:** Possible strain accommodations under (001)-strain for perovskite oxides, A-cations omitted for clarity. The following notation is used:  $\uparrow$  denotes that the preceding quantity is increased under that type of strain,  $BO$  denotes bond lengths,  $P$  denotes polar distortion amplitude, subscript  $\perp$  or  $\parallel$  denotes out-of-plane and in-plane, respectively,  $\gamma$  and  $\alpha$  denotes out-of-phase and in-plane rotation amplitude, respectively, superscript  $-$  and  $+$  denotes out-of-phase and in-phase rotations, respectively,  $V_B$  and  $V_O$  denotes B-site or Oxygen vacancies, respectively.

strain, where the extra space in the in-plane direction cause the B-cation to displace off-centre in-plane. This is illustrated in Figure 2.9 by increasing out-of-plane polarization,  $P_{\perp}$ , for compressive (001)-strain, and increasing in-plane polarization,  $P_{\parallel}$ , for (001)-tensile strain. Similarly, the extra-space in the in-plane direction under tensile strain favours in-plane polarization. The predictions of Pertsev et al. have later been confirmed experimentally. It has e.g. been shown for  $\text{BaTiO}_3$  that (001)-strain enhances the Curie temperature by up to  $500^{\circ}\text{C}$  and polarization by up to 200 % [105]. Furthermore it was shown that  $\text{SrTiO}_3$ , which is a paraelectric material in bulk, could be made a ferroelectric with either out-of-plane or in-plane polarization, depending on whether the strain was compressive or tensile [106].

### Octahedral Rotations

It is expected the strain also affects octahedral rotations, as the different rotation patterns depend strongly on the size mismatch between the A- and B-cations as discussed in section 2.1.1. It has been shown that the out-of-phase octahedral rotations in rhombohedral  $\text{LaAlO}_3$  and  $\text{LaNiO}_3$  are increased (reduced) around the out-of-plane axis,  $\gamma^-$ , under (001)-compression (tension). While the in-plane rotations,  $\alpha^-$  and  $\beta^-$ , are increased (reduced) under (001)-tension (compression) [107–109]. This is shown in Figure 2.9, by increasing  $\gamma^-$  under compressive strain, and increasing  $\alpha^-$  under tensile strain. These effects can be understood by the fact that the increase (reduction) of certain lattice vectors effectively unwinds (twists) the oxygen octahedra with rotation axis in that direction, as illustrated in Figure 2.9. The same effects occur for in-phase rotations, as was shown for orthorhombic  $\text{SrRuO}_3$  and  $\text{CaTiO}_3$  [110, 111]. However, for these materials an extra level of complexity occurs. As they have tilt patterns  $a^- a^- c^+$  in bulk, there are two inequivalent ways to orient the sample with respect to a quadratic strain plane. These two different orientations can then be stabilized at different strain values [111].

### Point Defects

Due to the chemical expansion that follows oxygen vacancies, as discussed in section 2.4.1, the number of oxygen vacancies is expected to increase under tensile strain, as shown in Figure 2.9. On the other hand, compressive strain is expected to favour cation vacancies, as they reduce the lattice size. This was indeed showed Aschauer et al. [112, 113]. By DFT calculations they found that the formation energy of oxygen vacancies was reduced under tensile strain, while cation vacancies were favoured under compressive strain. The results for oxygen vacancies have later been confirmed experimentally [114]. Aschauer et al. also showed that the formation energy of oxygen vacancies is significantly lower for in-plane than for out-of-plane oxygen vacancies under compressive strain, which should favour oxygen vacancy ordering for tensile strained perovskites [112]. These effects are illustrated in Figure 2.9 as increasing concentration of B-site vacancies,  $V_B$ , under compressive strain and increasing concentration of oxygen vacancies,  $V_O$ , under tensile strain. Furthermore, oxygen vacancies in tensilely strained  $(\text{La,Sr})\text{MnO}_{3-\delta}$  has also been shown to order in a brownmillerite structure [98, 99, 115]. Furthermore, Young and Rondinelli [116] showed that in such layered structures, also the polyhedral rotations in the tetrahedral layers can contribute to accommodate the strain.



### Accommodation of Strain in the (111)-Plane

Despite the large success of using strain in the (001)-plane to control properties in perovskite oxides, strain in higher index planes such as the (111)-plane is far less explored. The studies that do exist have mainly focused on ferroelectric properties. It has been shown experimentally that nickelates strained in the (111)-plane can become polar metals [24]. Furthermore, it has been shown that BiFeO<sub>3</sub> strained in (111)-plane gives a monodomain polar phase, while (001)- and (110)-strain give multidomain monoclinic phases [117]. PbTiO<sub>3</sub> grown on LaAlO<sub>3</sub> was shown to have complex dislocations, different to what is expected for lower index strain planes [118]. Oja et al. [119] and Raeliarijaona and Fu [120] showed theoretically that out-of-plane polarization in BaTiO<sub>3</sub> is damped for compressive (111)-strain, while tensile (111)-strain can give both an in-plane and out-of-plane polarization component, substantially different than what is expected for (001)-strain. Even though the focus in this field has been on polar distortions, it is expected that (111)-strain can influence octahedral rotations and point defect formation energies as well.

### Crystal Field Splitting

Since the strain affects the relative bond lengths in different directions, it also changes the crystal field of the  $d$ -orbitals. These changes in the crystal field will consequently lift the degeneracies of the  $t_{2g}$  and  $e_g$  orbitals. As shown in Figure 2.10, the compressive (001)-strain increases the energy of the  $d$  orbitals with lobes in the  $xy$ -plane, while these orbitals are reduced in energy for tensile (001)-strain. The opposite trend occurs for the orbital with lobes in the  $z$  direction. As the electronic levels of  $d$ -states are tightly coupled to magnetism, these effects has been e.g. used to change the magnetic ordering in La<sub>1-x</sub>Sr<sub>x</sub>MnO<sub>3</sub> [121] and LaMnO<sub>3</sub>/SrMnO<sub>3</sub> multilayers [122, 123] from ferromagnetic to different types of antiferromagnetic orderings.

For the trigonal distortions occurring under (111)-strain, a different type of crystal field splitting occurs. The (111)-strain does not split the  $e_g$  orbitals, as shown in Figure 2.10, however it splits the  $t_{2g}$  states into the singlet  $a_{1g}$  orbital and the doublet  $e'_g$  states [66]. The  $a_{1g}$  and  $e'_g$  orbitals are related to the standard  $d$  orbitals by the following super-positions:

$$|a_{1g}\rangle = \frac{|d_{xy}\rangle + |d_{xz}\rangle + |d_{yz}\rangle}{\sqrt{3}}, \quad (2.6)$$

$$|e'_g\rangle = \frac{\zeta_m^0 |d_{xy}\rangle + \zeta_m^1 |d_{xz}\rangle + \zeta_m^2 |d_{yz}\rangle}{\sqrt{3}}, \quad (2.7)$$

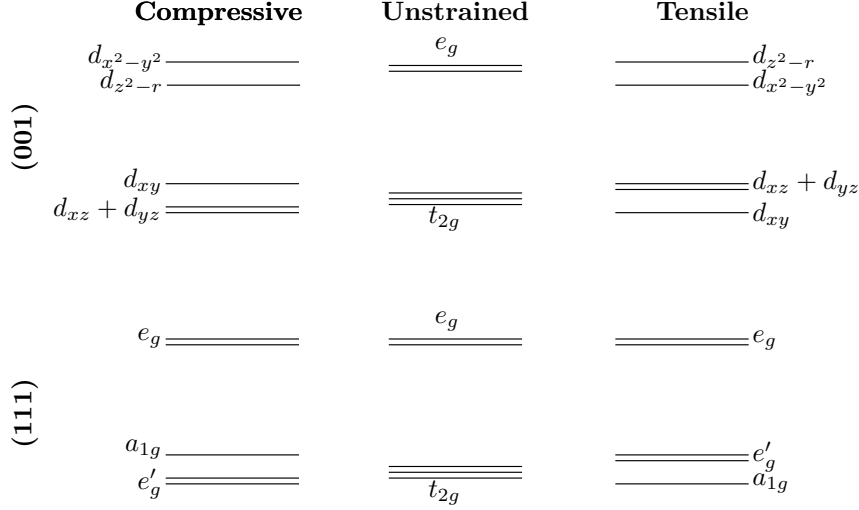


**Figure 2.10:** Crystal field splitting for octahedral sites under (001)-strain (top) and (111)-strain (bottom).

where  $\zeta_m = e^{2\pi im/3}$  and  $m = \pm 1$ . The  $a_{1g}$  and  $e'_g$  orbitals are illustrated in Figure 2.11. The (111)-strain splitting of these orbitals can be understood by considering in which directions the lobes and nodes  $a_{1g}$  and  $e'_g$  orbitals are pointing. When compressive (tensile) (111)-strain is applied, the oxygen atoms are pushed towards (away from) the main lobe of the  $a_{1g}$  orbital; hence, it is raised (lowered) in energy as shown in Figure 2.10. While the  $a_{1g}$  orbital has its main lobe pointing in the [111] direction, the  $e'_g$  orbital has nodes here. Hence, the splitting of the  $e'_g$  orbitals is opposite of that of the  $a_{1g}$  (Figure 2.10). It has been shown that this orbital splitting is essential for the symmetry breaking that occurs in [111]-oriented  $ABO_3$  superlattices and can lead to a graphene-like dirac point [124, 125].

### 2.5.2 Interface Engineering

Interface engineering of perovskite oxides had a revitalization in the 2000s after the discovery of a superconducting interface between the two band insulators  $LaAlO_3$  and  $SrTiO_3$  [17, 18]. As discussed in the preceding sections, a plethora of different properties occur in bulk perovskite oxides, and by introducing interfaces, the number of possible interactions that can occur becomes exceedingly large. Hence, in this section we limit ourselves to focus on charge transfer effects and coupling of octahedral rotations from one material to another. Finally we will review some of the possibilities by changing the interface from (001) to the (111)-interface

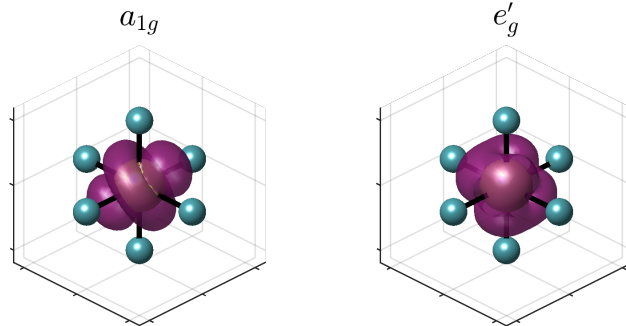


**Figure 2.11:** Isosurface plots of the  $d$  orbitals split by (111)-strain are shown in purple. Each of the  $d$  orbitals are centred on a B-cation (yellow) which are coordinated by the oxygen atoms (teal).

which has been enabled by recent advances in thin film synthesis [126, 127].

### Charge Transfer

Charge transfer can occur when two materials are brought together with different work functions, and in order to align the energy levels, electrons are transferred from one material to another. In semiconductors, it is usually the Fermi level that aligns, while as oxides share oxygen atoms at the interface, it is usually the oxygen  $O_{2p}$ -states that align [128, 129]. In both cases, this effectively donor dopes the unit cells closest to the interface on one side, and acceptor dopes the other side. In oxides, these interactions have been found to occur at a length scale analogous to the Thomas-Fermi screening length, equal to  $\sim 1 - 3$  unit cells using typical oxide material parameters [130, 131]. In transition metals oxides, these extra electrons/holes are likely to change the oxidation state of the transition metal, and as mentioned in section 2.3, the magnetic interactions are sensitive to changes in oxidation state. For instance, charge transfer has been utilized to induce magnetism at the interfaces of e.g.  $\text{CaMnO}_3/\text{CaRuO}_3$  [132] and  $\text{LaMnO}_3/\text{SrMnO}_3$  [133]. DFT calculations have shown that at the interface between the antiferromagnetic insulator  $\text{CaMnO}_3$  and paramagnetic  $\text{CaRuO}_3$ , the induced ferromagnetic moment is localized only in the Mn layer closest to the interface [134]. On the other hand, in the  $\text{LaMnO}_3/\text{SrMnO}_3$  superlattices, where both constituents are insulating antiferromagnets, calculations show that double-exchange at the interface leads to a spin polarized two dimensional electron gas at here [135].

A more complex form of charge transfer was shown to occur at the interface between the ferromagnet  $\text{La}_{2/3}\text{Ca}_{1/3}\text{MnO}_3$  and the high temperature superconductor

$\text{YBa}_2\text{Cu}_3\text{O}_7$ . In this system, a ferromagnetic moment is found on the copper ions which is antiparallel to the manganese moment. According to the Goodenough-Kanamori rules and using the bulk orbital occupancies, the exchange interactions should lead to a parallel alignment. However, a charge transfer occurs at the interface, changing the valence state of Mn and Cu. This furthermore leads to an orbital ordering at the interface, allowing for the antiparallel alignment [136].

### Oxygen Octahedral Coupling

Where two materials with different octahedral rotational patterns meet at an interface, a structural reconstruction has to occur, and the rotation pattern of one material can template into the other. As the physical properties of perovskite oxides depend heavily on the octahedral rotations, it is expected that this symmetry breaking has a large impact on physical properties [16, 20].

Using annular bright-field imaging in aberration-corrected scanning transmission electron microscopy, Aso et al. [137, 138] directly measured the coupling from a  $\text{GdScO}_3$  (001)-substrate into  $\text{SrRuO}_3$  and  $\text{ATiO}_3$  ( $A = \text{Ba}, \text{Sr}, \text{Sr}_{0.7}\text{Ca}_{0.3}$  and  $\text{Sr}_{0.5}\text{Ca}_{0.5}$ ), as shown in Figure 2.12. Their results show that size mismatch between the A and B cations is important for how long the rotations from the substrate propagate into the films. The shortest coupling was only one unit cell for  $\text{BaTiO}_3$  while the longest was around seven unit cells for  $\text{Sr}_{0.5}\text{Ca}_{0.5}\text{TiO}_3$ . This is expected, since as discussed in section 2.1.1, materials with lower tolerance factors are more prone to octahedral rotations.

DFT-calculations of the (001)-interface between  $\text{SrFeO}_3$  and  $\text{SrTiO}_3$  showed that the octahedral rotations of the low temperature phase of  $\text{SrTiO}_3$  only propagates into the first two layers of the cubic  $\text{SrFeO}_3$  [139]. He et al. [140] used DFT-calculations to impose zero octahedral rotations in one (001)-plane of  $\text{SrRuO}_3$  or  $(\text{La},\text{Sr})\text{MnO}_3$  while letting the rest of the cell relax, mimicking the effect of an infinitely rigid cubic substrate with no chemical discrepancies to the film. Using this approach, they isolated the effect of the different octahedral tilt patterns from that of different chemistry at the interface. They found that  $\text{SrRuO}_3$  regains its bulk structure over three unit cells, while  $(\text{La},\text{Sr})\text{MnO}_3$  never regains its bulk structure. Furthermore, they found that the magnetic moment of the Ru ions closest to the interface are significantly reduced, while the magnetic moments of the Mn ions are relatively unchanged with respect to their bulk value [140]. Qiao et al. [141], showed experimentally that the octahedral coupling between  $\text{LaCoO}_3/\text{SrTiO}_3$  leads to a transition between high spin and low spin at the Co. They explain this transition by different correlations on the cobalt  $d$ -states at the interface and in bulk, which they modelled with DFT by changing the Hubbard-U correction on Co [141].

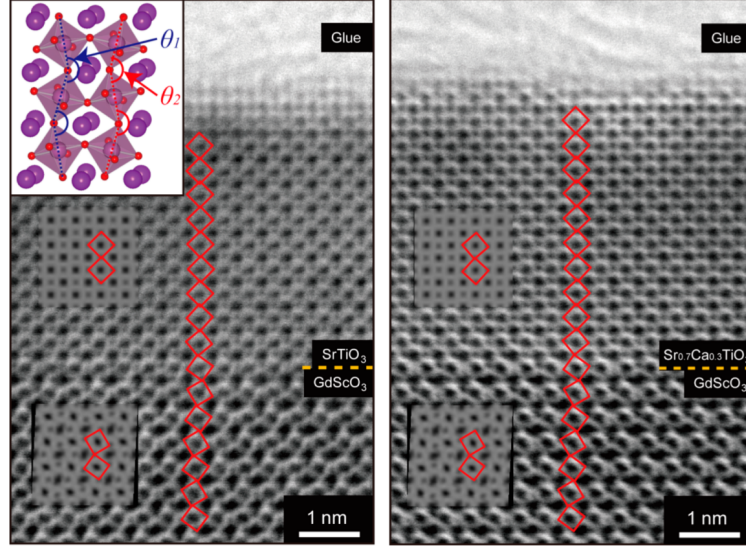


**Figure 2.12:** Annular bright field scanning transmission electron microscopy image of oxygen octahedra in  $\text{SrTiO}_3/\text{GdScO}_3$  (left) and  $\text{Sr}_{0.7}\text{Ca}_{0.3}\text{TiO}_3/\text{GdScO}_3$ . The insets show simulated ABF images of the bulk constituents. The projected oxygen octahedra are indicated with red squares. Figure from [138].

An extra-large octahedral rotation response is expected if a material with out-of-phase ( $-$ ) rotations meet an in-phase ( $+$ ) rotation at the interface, as this causes a completely mismatched state for half of the octahedras. This is possible e.g. if the two materials have  $a^-a^-a^-$  ( $R\bar{3}c$  symmetry) and  $a^-a^-c^+$  ( $Pnma$  symmetry) tilt patterns. However, for the (001)-interface it is also required that the  $a^-a^-c^+$  material is oriented such that the in-phase rotation is around one of the in-plane axes ([100] or [010], not [001]). To make sure this condition was met, Liao et al. [142] grew rhombohedral  $\text{La}_{2/3}\text{Sr}_{1/3}\text{MnO}_3$ , with tilt pattern  $a^-a^-a^-$  on the orthorhombic  $\text{NdGaO}_3$  substrates with tilt pattern  $a^-a^-c^+$ . Hence, by carefully selecting which of the pseudocubic  $\langle 001 \rangle$  directions the orthorhombic substrate was cleaved, they could make sure that the in-phase ( $+$ ) rotations were around [100], as shown in Figure 2.13 a). Furthermore, they showed that the mismatch is removed by inserting a  $\text{SrTiO}_3$  buffer layer, tilt pattern  $a^0a^0a^0$  in bulk at room temperature, between the  $\text{La}_{2/3}\text{Sr}_{1/3}\text{MnO}_3$  and  $\text{NdGaO}_3$ . The buffer layer dampened the mismatch even when the  $\text{SrTiO}_3$  was as thin as one unit cell, as shown in Figure 2.13 b-e). Finally, Liao et al. [142] showed that this mismatch between in-phase and out-of-phase rotations had a dramatic effect on the magnetic and electronic anisotropy in these heterostructures. Grutter

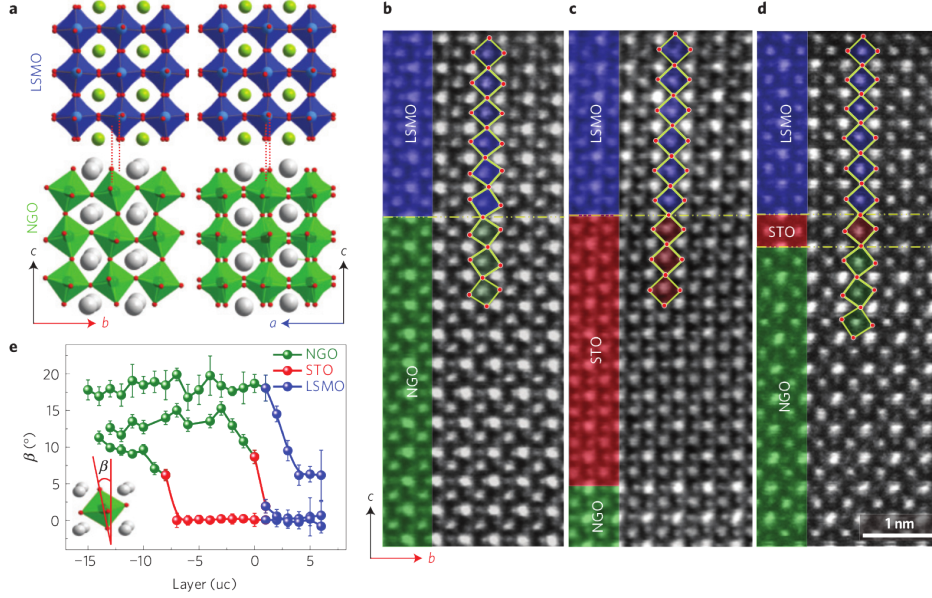


**Figure 2.13:** Oxygen octahedral coupling at the  $\text{La}_{2/3}\text{Sr}_{1/3}\text{MnO}_3$  (LSMO)/ $\text{NdGaO}_3$  (NGO) interface. a) schematic model of the LSMO and NGO crystal structures, showing the mismatch in-octahedral rotations around the *a* lattice vector. b-d) shows the inversed annular bright-field images of the LSMO/NGO interface, with an inserted  $\text{SrTiO}_3$  (STO) buffer of zero, nine and one unit cells (uc), respectively. e) mean octahedral in-phase rotation angle  $\beta$  as function of layer position, the data for the non-buffered sample is shifted upwards by  $6^\circ$  for clarity. Figure from [142].

et al. [143] explored the octahedral mismatch at the interface between the two orthorhombic materials  $\text{CaRuO}_3$  and  $\text{CaMnO}_3$ .  $\text{CaRuO}_3$  and  $\text{CaMnO}_3$  both have  $a^-a^-c^+$  tilt patterns, and earlier studies had shown that charge transfer in this system gives a ferromagnetic state at the interface [132, 134]. What Grutter et al. found, was that growth of odd and even number of layers had different preferred domain orientations in this system. Hence, by controlling exactly how many unit cells they grew, they could either match or mismatch the octahedral rotations at the interface. Furthermore, they found that the mismatched octahedral layers inhibited the charge transfer between the Ru and Mn, and hence suppressed the interfacial magnetism [143].

### (111)-Oriented Interfaces

The interface effects discussed so far have been mostly focused on the traditional (001)-interface, however higher index interfaces, such as the (111) change many of the structural aspects associated with the interface. Some of these aspects are illustrated in Figure 2.14, and (111)-oriented oxide interfaces are considered an important avenue to further develop oxide thin film technology [19, 33].

As seen in Figure 2.14 a) the stacking sequence in the [111]-direction is different from [001]. The (001)-interface has an  $\text{AO} + \text{BO}_2 + \text{AO} + \text{BO}_2 + \dots$  stacking with a spacing between similar layers of  $a$ , while along the [111]-direction the stacking is  $\text{AO}_3 + \text{BO} + \text{AO}_3 + \text{B} + \dots$  with a spacing of  $a/\sqrt{3}$ . Indeed, the interest for (111)-oriented perovskite interfaces started with the desire to create artificial magnetic materials based on 1-1 superlattices with  $\text{Fe}^{3+}$  and  $\text{Co}^{3+}/\text{Mn}^{3+}$  on the B-sites [144–146]. The motivation for this was that interaction between  $d^5$  and  $d^3$  ions is expected from the Goodenough-Kanamori rules to be ferromagnetic [73]. Hence, by relying on the different stacking along the [111]-direction, one could make sure that all neighbouring B-cations have different number of  $d$ -electrons. Indeed, initial experimental results showed signs of ferromagnetic coupling [144–146], however theoretical results indicated that ferrimagnetic ordering was more energetically favourable [147]. The ferrimagnetism has later been verified in more recent experiments [148–150]. Other exchange interactions have also been shown to be modified at interfaces between (111)-oriented antiferromagnets and ferromagnets, which has not been observed in (001)-oriented interfaces [151–153]. The different stacking along the [111]-direction also influences the nominal charge of the layers. This has been shown to be important for growth properties [126], and may cause polar catastrophe effects which can explain many of the properties of the conductive state at the  $\text{LaAlO}_3/\text{SrTiO}_3$  interface [154].

The (111)-interface has a hexagonal symmetry, while the (001) is quadratic, as shown in Figure 2.14 b). Haldane [155] showed that hopping on a 2D hexagonal lattice can result in a quantum Hall effect in the absence of a magnetic field, and can lead to topological insulating phases. In traditional topological insulators, large spin orbit coupling can break time reversal symmetry, allowing for gapless edge states [156]. However, it has been shown local symmetry breaking elements can be enough to create a topological insulator in (111)-oriented transition metal oxides [157–159]. Several interesting properties such as massive symmetry breaking and many topological non-trivial phases have been theoretically predicted in [111]-oriented superlattices of  $\text{AMO}_3/\text{LaAlO}_3$  ( $A = \text{Sr}, \text{La}$ ,  $M = \text{transition metal}$ ) [125, 160, 161]. Theoretical calculations have furthermore shown that these properties can be switched on and off electronically by using a ferroelectric spacer layer [162, 163]. However, experimentally, it has been difficult to grow the appropriate crystalline phases of e.g. the irridates [164]. In other (111)-oriented

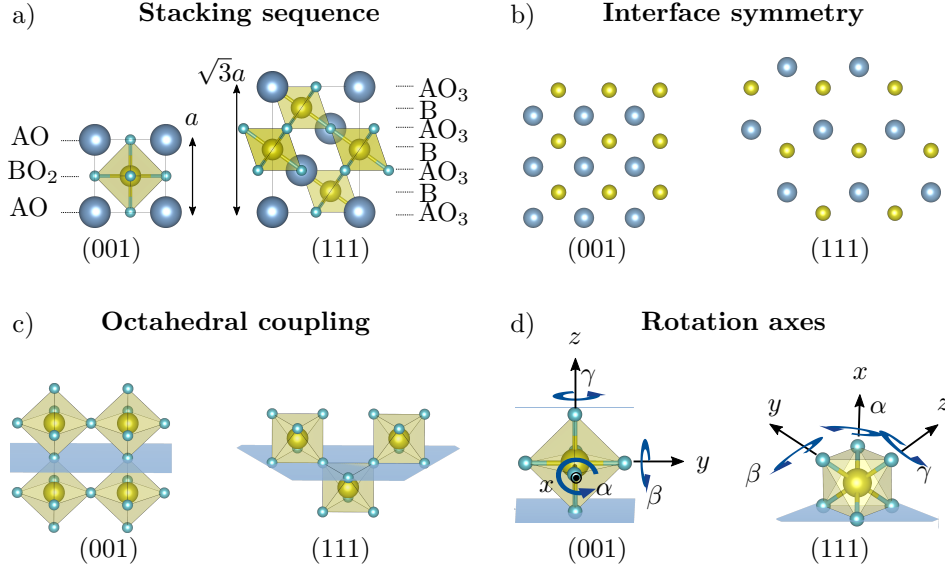


**Figure 2.14:** Structural differences between the (001)- and (111)-interface. a) Side-view of the (001)- and (111)-interfaces. The stacking sequence along the [001]-direction is  $\text{AO}+\text{BO}_2+\text{AO}+\text{BO}_2+\dots$ , while along the [111]-direction it is  $\text{AO}_3+\text{BO}+\text{AO}_3+\text{B}+\dots$ . b) Top-view of the (001)- and (111)-interfaces. The (001)-interface symmetry is quadratic, while the (111)-interface is hexagonal. c) The octahedral coupling at an (001)-interface is through an apex oxygen, while at (111)-interface it is through 3 face sharing oxygen atoms. d) The principal octahedral rotation axes are in (001) either perpendicular or parallel to the plane, while for (111) they are all pointing at angle of  $\cos^{-1}(1/\sqrt{3}) \approx 54.7^\circ$  with the interface.

structures, Mott insulating orbital ordered phases are found experimentally [165–167], interesting in itself, but not as exciting as topological insulators.

An additional opportunity opened by the hexagonal (111)-interface, is that (111)-oriented perovskites may behave similar to the hexagonal manganites,  $\text{RMnO}_3$  ( $\text{R} = \text{Sc}, \text{Y}, \text{Ho-Lu}$ ). These materials are known for their exotic multiferroic phenomena with coupled magnetic and ferroelectric domains at low temperature [168, 169].

As shown in Figure 2.14 c) the octahedral coupling across a (111)-oriented interface is significantly different from an (001)-oriented interface. At an (001)-interface, the oxygen octahedra couple through one apex oxygen atom, while at the (111)-interface they couple through three oxygen atoms at the octahedral face. Hence, it is expected that the octahedral coupling will be significantly different at the two



interfaces. E.g. as discussed on page 29, special engineering of the (001)-interface needs to be done, in order to make sure that the in-phase and out-of-phase rotations of an  $a^-a^-c^+$  and an  $a^-a^-a^-$  meet at the interface. For the [111]-direction however, this coupling will occur for all possible orientations of the film. Furthermore, for (001)-interfaces there is a possibility for different coupling between in-plane and out-of-plane pseudocubic rotations, as shown in Figure 2.14 d). However, this is not expected for the (111)-interface, as none of pseudocubic rotations axes are perpendicular nor parallel to the interface.

In summary, the [111]-direction provides an interesting field to look for new avenues to control, enhance and tailor emergent properties at oxide interfaces.

## 2.6 Open Challenges and Opportunities

As discussed in the preceding sections there have been large improvements in the scientific understanding of functional oxide thin films over the last decades. However, there are still many remaining challenges and opportunities. In this thesis we focus on the possibilities of using oxygen vacancies and (111)-oriented interfaces to control the structure, and hence the functional properties in these materials.

When it comes to oxygen vacancies, not much is known about their dynamics and how they can be stabilized and order over time. In addition, oxygen ordered structures are known for being good oxygen conductors, important solid oxide fuel cells applications [93–95]. However, how the ordering of oxygen vacancies can be used to control and enhance other functional properties, is less explored. Hence, we first explore the possibilities of having large concentrations of oxygen vacancies in (001)-oriented (La,Sr)MnO<sub>3</sub>, and if the oxygen vacancies are likely to interact and form ordered structures such as the brownmillerite. Furthermore, we investigate the opportunity, now opened by ordered vacancies, to control the magnetic properties in such systems.

(111)-oriented films are still in their infancy compared to their (001)-counterpart, although some topics have been studied the last decade. E.g., considering strain in the (111)-plane the few studies that exist have only looked at polar modes in a few model systems [24, 119, 120]. Hence, little is known about how the octahedral rotations are affected by (111)-strain, while it is clear from Figure 2.14 d) that the response cannot be the same as under (001)-strain. Hence, in this thesis we aim to give a general understanding of how (111)-strain affects both rotational and polar modes, and how they can be influenced by factors such as the tolerance factor  $t$  and the nominal charges of the A and B cations. We also aim to understand how the different structural responses affect electronic, magnetic and ferroelectric properties. Furthermore, whether the octahedral coupling is different between

(111)- and (001)-oriented interface remains an open question. In the final papers, we investigate this coupling and some of the opportunities it brings when it comes to tuning and inducing functional properties.



---

## Methods

*“First you guess. Don’t laugh, this is the most important step. Then you compute the consequences. Compare the consequences to experience. If it disagrees with experience, the guess is wrong. In that simple statement is the key to science. It doesn’t matter how beautiful your guess is or how smart you are or what your name is. If it disagrees with experience, it’s wrong. That’s all there is to it.”*

– Richard Feynman

This chapter first gives a brief introduction to the theory behind density functional theory (DFT). Then, some approaches on how to use DFT to model thin films are presented. Next, we will discuss how to use lattice dynamics to study plausible distortions in a material system. Finally the computational details used in this work are presented.

### 3.1 First-Principles Background

This section will discuss the basics of DFT. Mathematical details are kept at a minimum, and only general approximations are described, as there are numerous textbooks and review articles on this subject [170–175]. The same is to say for reviews of how the field has developed and future possibilities of DFT [28, 176–178].

#### 3.1.1 Many-Body Problem

A fundamental property of quantum mechanics is that all the information of a set of particles is given in its wave function. Hence, if one knows the full wave function of a system, it is possible to calculate all probabilities for any results of any measurement on the system. For a many-body problem with  $N$  electrons

and  $M$  nuclei, the wave function depends on  $3(N + M)$  variables. The time independent wave function can then be found by solving the Schrödinger equation for this set of  $N + M$  particles

$$H\Psi(\mathbf{r}_1, \dots, \mathbf{r}_N, \mathbf{R}_1, \dots, \mathbf{R}_M) = E\Psi(\mathbf{r}_1, \dots, \mathbf{r}_N, \mathbf{R}_1, \dots, \mathbf{R}_M), \quad (3.1)$$

where  $H$  is known as the Hamiltonian operator,  $\Psi$  is the many-body wave function,  $E$  is the corresponding energy,  $\mathbf{r}_i$  is the position of the electron  $i$ , and  $\mathbf{R}_i$  is the position of the nuclei  $i$ . For a set of atoms with surrounding electrons, the electrons are much lighter than the core. Hence, we can split the problem in two; first, we can solve the problem for the electrons for fixed positions of the atomic nuclei. Next, we can vary the positions of the nuclei until we find the lowest energy of the system, also known as the ground state energy. This approximation is known as the Born-Oppenheimer approximation. Thus, for a system of multiple interacting nuclei and electrons, we get the following Hamiltonian:

$$H = -\frac{\hbar^2}{2m} \sum_{i=1}^N \nabla_i^2 + \sum_{i=1}^N V(\mathbf{r}_i) + \sum_{i=1}^N \sum_{j<i}^N U(\mathbf{r}_i, \mathbf{r}_j), \quad (3.2)$$

where  $m$  is the electron mass. The summations represent each electron's kinetic energy, the interaction between each electron, and the nuclei and the interaction between electrons, respectively. Solving this eigenvalue problem is tedious, and exact solutions can only be found for simplistic illustrative examples such as the hydrogen atom. Although the wave function is the fundamental entity in quantum mechanics, the only thing that can be observed is the probability of the  $N$  electrons being at a particular set of coordinates given by  $\Psi^*(\mathbf{r}_1, \dots, \mathbf{r}_N, ) \Psi(\mathbf{r}_1, \dots, \mathbf{r}_N, )$ . Furthermore, it is physically impossible to determine which electron is labelled 1, and 2 etc., thus the interesting physical quantity can be reduced to the density of electrons at a certain position in space  $n(\mathbf{r})$ , which, if we assume spin degeneracy, can be expressed as:

$$n(\mathbf{r}) = 2 \sum_i \psi_i^*(\mathbf{r})\psi_i(\mathbf{r}), \quad (3.3)$$

here  $\psi_i$  is the individual electron wave function of electron  $i$  and the summation goes over all occupied wave functions. This simplifies the problem significantly, as the electron density has only 3 variables, while the full electron wave function has  $3N$  variables.

### 3.1.2 Density Functional Theory

So far, we have seen that the electron density is related to the observable probabilities of finding a number of electrons within a certain volume. However, can

the electron density give other valuable information as well, and is there a 'simple' way of finding the correct electron density? Hohenberg and Kohn [179] answered these questions, in what is now known as Hohenberg-Kohn theorems, which state:

**Theorem 1** *The ground-state energy from Schrödinger's equation is a unique functional of the electron density.*

**Theorem 2** *The electron density that minimizes the energy of the overall functional is the true electron density corresponding to the full solution of the Schrödinger equation.*

A *functional* is a mathematical expression, which takes a function as an input and assigns a certain number corresponding to the input. From the first theorem we learn that the ground state electron density uniquely defines all properties of the ground state, including its energy through the functional  $E = F[n(\mathbf{r})]$ . This means that instead of solving the full wave function of  $3N$  variables, it is sufficient to find the electron density, a function of three variables. This reduces the problem significantly, and as an example we can look at the simple case of a single unit cell of SrTiO<sub>3</sub>; the full wave function then has 204 variables, while the electron density requires only three.

The second theorem states that if we know what this functional is, then we can vary the electron density until we have found the one that minimizes the energy. This is important, as it gives us a way to find the correct electron density. There is, however, one problem; we do not know what this functional is. Thus, some approximations have to be done in practice.

The second important contribution to the field of density functional theory were made by Kohn and Sham [180], who described a way to efficiently solve these problems and is used in all practical implementations of DFT. Their approach was to replace the many-body problem through fictitious non-interacting wave functions or orbitals,  $\psi_i$ , that only interact with each other through a mean field. Thus, one can get rid of summations in equation (3.2). Through their reformulation, we get the Kohn-Sham equations:

$$\left[ -\frac{\hbar}{2m} \nabla^2 + V(\mathbf{r}) + V_H(\mathbf{r}) + V_{XC}(\mathbf{r}) \right] \psi_i(\mathbf{r}) = \varepsilon_i \psi_i(\mathbf{r}), \quad (3.4)$$

where on the left hand side we have three potentials,  $V$ ,  $V_H$  and  $V_{XC}$ . Here  $V$  is the potential the electron sees from the nuclei,  $V_H$  is known as the Hartree potential and is defined as:

$$V_H(\mathbf{r}) = e^2 \int \frac{n(\mathbf{r}')}{|\mathbf{r} - \mathbf{r}'|} d^3r'. \quad (3.5)$$

$V_H$  describes the Coulomb repulsions between the electron in one of the Kohn-Sham orbitals and the rest of the total electron density. As each electron is also part of the full electron density, the Hartree potential contains an unphysical self-interaction term. The correction to this self-interaction problem, and the difficult to treat quantum mechanical exchange and correlation contributions are lumped together in the exchange-correlation potential  $V_{XC}$ . This potential can be defined by the functional derivative of the exchange-correlation energy

$$V_{XC}(\mathbf{r}) = \frac{\delta E_{XC}[n(\mathbf{r})]}{\delta n(\mathbf{r})}. \quad (3.6)$$

Thus, the only unknown parameter in the Kohn-Sham equations is the exchange-correlation functional  $E_{XC}[n(\mathbf{r})]$ , and if it was known, the solutions to the equations would be exact. Still, multiple approximations exist, and they will be discussed in the following subsection.

However, there is another problem. One needs to know the electron density  $n(\mathbf{r})$  in order to calculate the one-electron wave functions  $\psi_i(\mathbf{r})$ , and to calculate the one-electron wave functions one needs to know the electron density. To break out of this loop, an iterative approach is suitable, outlined as:

1. Assume a trial electron density  $n(\mathbf{r})$ .
2. Use  $n(\mathbf{r})$  to solve the Kohn-Sham equations given in equation (3.4) to find the single electron wave functions,  $\psi_i(\mathbf{r})$ .
3. Calculate the electron density with equation (3.3), using the  $\psi_i(\mathbf{r})$  from the previous step. This gives a new electron density called  $n_{KS}(\mathbf{r})$ .
4. Compare the calculated electron density,  $n_{KS}(\mathbf{r})$  with the electron density used as an input in step 2,  $n(\mathbf{r})$ . If the difference between the two electron densities is small enough, the ground state electron density is found, and we can use this to calculate the total energy. If the difference between the two electron densities is too large, update the trial electron density  $n(\mathbf{r})$  in some way, and go back to step 2.

This algorithm makes sure that the solutions to the Kohn-Sham equations are self-consistent. How each of these steps are implemented in practice depends on the specific DFT-code.

### 3.1.3 Approximate Exchange-Correlation Functionals

As discussed in the previous section, the exchange-correlation functional needed to determine the ground state from the Kohn-Sham equations is not known. Hence,

some approximations need to be done, even though its existence is guaranteed through Hohenberg and Kohn first theorem.

The first approximation suggested to define the exchange-correlation functional is known as the local density approximation (LDA). In the LDA formalism the  $E_{XC}(\mathbf{r})$  depends only on electron density,  $n(\mathbf{r})$ , at the same point  $\mathbf{r}$ . This exchange-correlation energy is then equal to the exchange-correlation energy of a homogeneous electron gas with the same density

$$E_{XC}^{\text{LDA}}[n(\mathbf{r})] = \int \epsilon_{XC}^{\text{hom}}[n(\mathbf{r})]n(\mathbf{r}) \, d\mathbf{r}. \quad (3.7)$$

A Hartree-Fock technique can be used to get the analytical solution for exchange part of the homogeneous electron gas:

$$\epsilon_X^{\text{hom}}[n(\mathbf{r})] = -\frac{3}{4\pi} (3\pi^2 n(\mathbf{r}))^{1/3}. \quad (3.8)$$

While the correlation part of the homogeneous electron gas,  $\epsilon_C^{\text{hom}}[n(\mathbf{r})]$ , has been calculated using a Monte-Carlo simulation [181]. Hence, by combining these results, the exact form of the LDA-functional can be found.

Although the LDA approximation is quite crude, it can still calculate lattice constants with an accuracy of about 1 %. A more sophisticated approach is to not only include information about the electron density when calculating the exchange-correlation contribution, but also include information about the gradient of the electron density, i.e.  $E_{XC}^{\text{GGA}}(\mathbf{r}) = F[n(\mathbf{r}), \nabla n(\mathbf{r})]$ . This leads to the generalized gradient approximation (GGA), and a popular implementation of GGA is the PBE functional, named after its creators Perdew, Burke and Ernzerhof [27].

One of the major shortcomings of both GGA and LDA, is their inability to accurately predict the band gaps of a solid [174]. To improve this, and other properties of interest even more information can be included when constructing the functional. This is illustrated as Jacob's ladder in Figure 3.1 [182, 183]. However, as each step up the ladder significantly increases the amount of computational power needed, another approach that has been gaining popularity in recent years is the DFT+U solution.<sup>1</sup> This approach adds an energy cost  $U$  for multiple occupations of the same orbital, mimicking the Coulomb repulsion between electrons. This approach has accurately described many of the properties of heavily correlated materials, such as those with partially filled  $d$ -bands. Even though the  $U$ -value can be calculated self consistently [184, 185], it is more common to be added as an empirical parameter which is fitted to match a certain experimental electronic, atomic or magnetic structure. When there is no

<sup>1</sup>Also known as LDA+U, GGA+U, PBE+U ... depending on which functional being used.



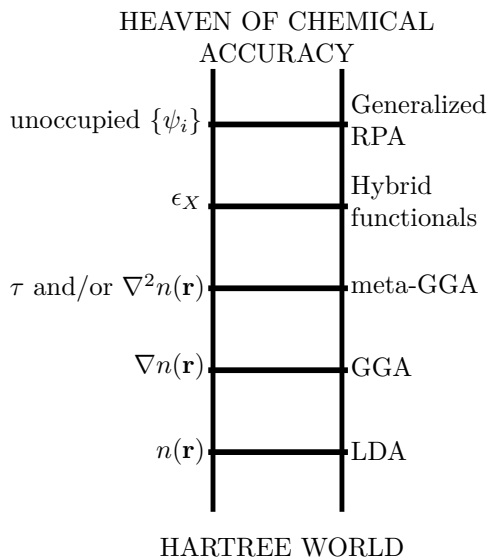


**Figure 3.1:** Jacob’s ladder of density functional approximations to the exchange energy. Each step up the ladder includes the components of the lower one, in addition to increased complexity. This should in principle increase the accuracy at the cost of heavier calculations. RPA stands for random phase approximation,  $\epsilon_X$  is the exact exchange from Hartree-Fock calculations, while  $\tau$  is the kinetic energy density. Adapted from [182].

experimental data available, an approach can be to first do some heavy hybrid calculations (the second highest step on Jacob’s ladder in Figure 3.1), and then later fit the  $U$ -value in order to match with a given parameter. This allows doing subsequent calculations in the cheaper DFT+ $U$  formalism, which would not be feasible for the heavy hybrid calculations [186, 187].

### 3.1.4 Other Approximations

Although the Born-Oppenheimer approximation, the mean field approach of DFT, and different approaches to estimate the exchange-correlation energy are important to solve many-body interactions in solids, some other simplifications are done in practical implementations of DFT. This section will discuss some of the most common approximations.

### Brillouin Zone Grid

Many of the mathematical problems one faces when solving the Kohn-Sham equations, such as calculating the electron density, reduces to some sort of integral of the form:

$$\bar{g} = \frac{\Omega}{(2\pi)^3} \int_{\text{BZ}} g(\mathbf{k}) \, d\mathbf{k}, \quad (3.9)$$

where  $\Omega$  is the volume of the cell. As seen, these integrals are in  $\mathbf{k}$ -space and one integrates over the Brillouin zone (BZ). Analytical solutions are often infeasible; hence, numerical integration is done instead. Then, one has to select a certain set of  $\mathbf{k}$ -points in the BZ where the function  $g(\mathbf{k})$  is sampled. The most common way to select these  $\mathbf{k}$ -points was developed by Monkhorst and Pack [188]. In their approach, one only specifies how many  $\mathbf{k}$ -points are used along each direction of the reciprocal lattice vectors. To decide how many  $\mathbf{k}$ -points are necessary, rigorous test calculations must be carried out to ensure convergence. However, as the size of the BZ is inversely proportional to the size in real space, larger cells in real space require less  $\mathbf{k}$ -points to yield the same  $\mathbf{k}$ -point density.

### Plane Wave Cutoff

A solid is a periodic structure where its size is typically much larger than its period. Hence, periodic boundary conditions<sup>2</sup> are often most practical. According to Bloch's theorem, the wave function can be written as a product between a plane wave and a function with the same period as the lattice,  $u_n(\mathbf{k}, \mathbf{r})$ :

$$\psi_{n,\mathbf{k}}(\mathbf{r}) = \frac{1}{\sqrt{\Omega}} u_n(\mathbf{k}, \mathbf{r}) e^{i\mathbf{k}\cdot\mathbf{r}}, \quad (3.10)$$

where  $n$  is a band index and  $\mathbf{k}$  is a wave vector. A periodic function can be decomposed in a Fourier series:

$$\psi_{n,\mathbf{k}}(\mathbf{r}) = \frac{1}{\sqrt{\Omega}} \sum_{\mathbf{G}} C_{n,\mathbf{k}}(\mathbf{G}) e^{i(\mathbf{k}+\mathbf{G})\cdot\mathbf{r}}, \quad (3.11)$$

where  $C_{n,\mathbf{k}}$  are the Fourier coefficients, and  $\mathbf{G}$  is a reciprocal lattice vector. As this summation is over an infinite number of plane waves, a truncation has to be done in numerical implementations. A common way to express this truncation criterion is only to consider plane waves with energy lower than a certain cutoff energy

$$\frac{\hbar^2}{2m} |\mathbf{k} + \mathbf{G}|^2 \leq E_{\text{cut}}. \quad (3.12)$$

Similar to what is described for the  $\mathbf{k}$ -points, the appropriate value for  $E_{\text{cut}}$  must be found through convergence testing.

<sup>2</sup>Also known as Born-Von Karman boundary conditions.

### Pseudopotentials

As higher plane wave energy corresponds to lower wavelength, large energy cutoffs are required for oscillations on short length scales, such as for the tightly bound core electrons [174]. However, the core electrons do not contribute significantly to chemical bonding or other physical properties of a material; here the valence electrons dominate.

Based on this rationale, it is common to use a pseudopotential approach [189], where one only treats the valence electrons, while the core electrons are considered frozen. This is known as the frozen-core approximation. A popular choice of generating pseudopotentials is known as the ultrasoft pseudopotentials (USPPs), as these require considerable lower cutoff energies than alternative approaches [190]. However, a disadvantage with the USPP is that they rely on several empirical parameters. Some of the disadvantages were overcome by another frozen core approach known as the projector augmented-wave (PAW) method, introduced by Blöchl [191]. Kresse and Joubert compared the USPP and PAW approach with all-electron calculations. They found that, as long as the USPPs and the PAW method are well constructed, they give similar results as the all-electron approach. Furthermore, in materials with large differences in electron negativity, or with large magnetic moments, the PAW method is superior to the USPPs [192]. Kresse and Joubert also discussed the need for treating the electrons in the second outermost shell as valence electrons for some elements in the periodic table, such as Ca [192].

## 3.2 DFT for Thin Films

In this section, the two main approaches for treating thin films with DFT are discussed: the homoepitaxial strain approach and the heteroepitaxial strain approach [20]. These techniques are based on strain and interface engineering that is made possible by the thin film geometry, as discussed in section 2.5, while most standard DFT-codes are focused on finding the properties of bulk materials.

### 3.2.1 Homoepitaxial Strain Approach

When a thin film is grown epitaxially on a substrate, the in-plane lattice vectors of the film are forced to be equal to those of the substrate. To accommodate this strain from the substrate, the thin film can change its out-of-plane lattice parameter and the atomic positions in the cell. To treat this phenomenon with DFT, we follow the approach described by Zayak et al. [110], where the in-plane lattice vector,  $\mathbf{a}$  and  $\mathbf{b}$ , are locked to that of the substrate, while the out-of-plane lattice vector,  $\mathbf{c}$ , and the atomic coordinates are allowed to relax, as illustrated

for a [001]-oriented film in Figure 3.2 a). Thus, the effect of the substrate are only implicitly included in the calculations through the changes in the in-plane lattice constants, and can be regarded as an approximation to how the thin film behaves far away from any interfaces. The strain from the substrate is defined as:

$$\epsilon = \frac{a - a_0}{a_0}, \quad (3.13)$$

where  $a$  is the in plane lattice parameter imposed by the substrate as shown in Figure 3.2 a), and  $a_0$  is the calculated lattice parameter for the bulk material. When doing relaxations of strained cells it is important to select an appropriate calculation cell that allows for all likely distortions and orbital and magnetic ordering patterns that may be induced. To include these effects supercells, such as those illustrated in Figure 3.2 b), are required. However, larger cells come at a higher computational cost. Still, the complexity of the calculation is usually considerably lower than calculations that include the substrate explicitly, as discussed in the following section. A further strength of this approach is that the in-plane strain can be varied continuously in the calculations, while if one was to do this experimentally only discrete strain values would be available due to a limited number of substrates being available [102]. Finally, this approach allows for isolating the effects of strain from other chemical and physical effects occurring close to an interface.

### 3.2.2 Heteroepitaxial Strain Approach

In the heteroepitaxial strain approach, two (or more) materials are included in the calculation, as illustrated for an (001)-interface in Figure 3.2 c). This can either be done to include the effects of the substrate or some kind of superstructure. When multiple components are present in the calculation, it is possible to identify how the physical properties differ as a function of distance from the interface. By comparing these results with results from the heteroepitaxial approach, one can isolate the effect of the interface.

When utilizing the heteroepitaxial strain approach, it is also important to select an appropriate unit cell, and one possible choice is shown in Figure 3.2 d). However, as periodic boundary conditions are utilized, there are always at least two interfaces inside a heteroepitaxial calculation cell, and the calculations are actually periodic superlattices. If the experimental situation one wants to model is a superlattice, then the repeating unit should be selected to closely mimic the periodicity of the experimental situation within available computational resources. If the experimental situation one wants to model is a single interface, the out-of-plane lattice parameter needs to be selected such that two interfaces in the cell are as decoupled from each other as possible, again limited by the computational

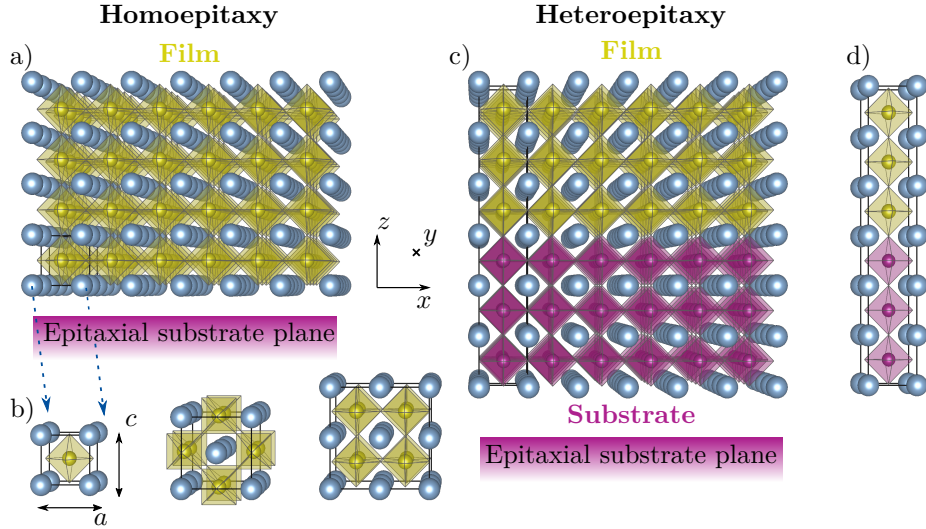


**Figure 3.2:** Illustration of the homo- and heteroepitaxial strain approaches for modelling thin films. a) Illustrates the homoepitaxial strain approach where the substrate is only included implicitly through the change in in-plane lattice parameters. b) The primitive five atom unit cell along with the  $\sqrt{2} \times \sqrt{2} \times 2$  and  $2 \times 2 \times 2$  supercells are shown from right to left. c) Shows heteroepitaxial strain approach where e.g. the substrate is explicitly included in the calculation. d) Shows a primitive heterostructure cell. Figure adapted from [20].

resources available. Depending on the physical problem one wants to model, it is also possible to apply epitaxial constraints to these kind of calculations by locking the in-plane lattice parameters. Furthermore, it can also be appropriate to lock some of the atomic positions far away from the interface to its bulk value. This last step is often done to be able to reduce the size of the supercell, and hence the computational cost.

In addition, care has to be taken when designing calculation cells for heteroepitaxial strain calculations to make sure that the cell is large enough in-plane to accommodate for all structural distortions such as octahedral rotations. Hence, the cell shown in in Figure 3.2 d), may not be appropriate. It is also important to make sure to have an even number of unit cells out-of-plane when having distortions that require a cell doubling such as for out-of-phase rotations of oxygen octahedra. Another point where the primitive cell suggested in Figure 3.2 d) is suboptimal, is that the cell is not symmetric along the  $z$ -axis. A mirror plane can be added at  $z = 1/2$  in fractional coordinates by shifting the origin by  $1/4$  along the  $z$ -axis. However, if the two materials in the cell are two perovskites where both

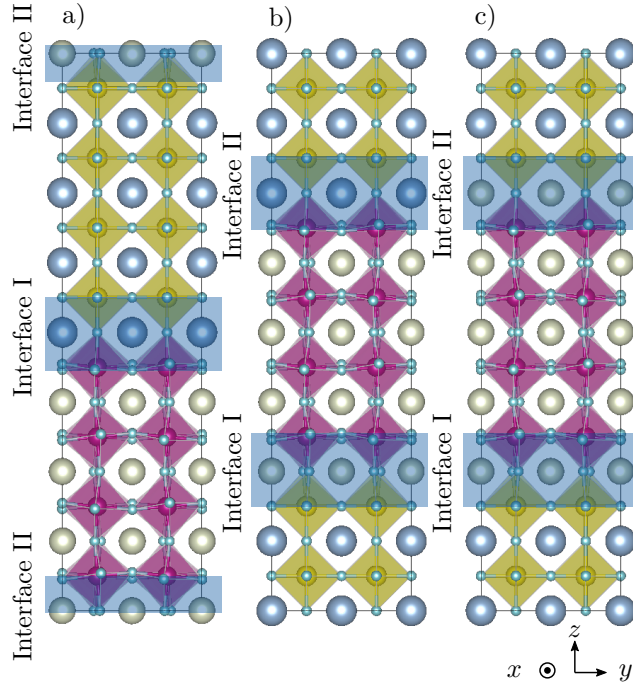


**Figure 3.3:** Generating symmetric calculation cells for heteroepitaxial strain calculations for perovskites with different A and B cations. a) Naive non-symmetric stoichiometric cell. b) shifted non-symmetric stoichiometric cell. c) shifted symmetric non-stoichiometric cell. The blue shaded areas shows the two interfaces in each cell. Due to periodic boundary conditions, the interface II in a) is split into two, where one half is on the bottom of the cell and the other half is on top of the cell. In a) and b) the interface I and II are not equivalent. To fix this problem the cell is made non-stoichiometric in c) this also ensures the that there is a mirror plane at  $z = 1/2$ .

the A and B cation differ, the cell has to also be made non-stoichiometric in order for the cell to achieve this mirror plane [193]. This is illustrated in Figure 3.3. In Figure 3.3 a), the naive solution based on placing two stoichiometric perovskites with different A and B cations on top of each other is shown. In Figure 3.3 b), we see that shifting this cell by  $z = 1/4$  does not make the cell symmetric, as interface I and II have different terminations. Thus, in order to make the interfaces symmetric and achieving a mirror plane at  $z = 1/2$  the calculation cell has to be made non-stoichiometric, as shown in Figure 3.3 c).

Another possibility, is that one of the components in the heteroepitaxial strain approach can be a vacuum region. This allows studying the effect of surfaces and

creates an infinite array of slabs. Similar to the situation for heterostructures, the vacuum region should be large enough out-of-plane to decouple the slabs from each other, and having a mirror plane at  $z = 1/2$  also reduces the computational power needed.

### 3.3 Lattice Dynamics

Many of the distortions that occur in perovskite oxides can be understood in the framework of soft modes. This was first done by Cochran [194] to explain the origin of ferroelectricity. Cochran explained that the ferroelectric phase transition occurs due to a transverse optical phonon mode that freezes-in below the transition temperature.

To calculate the phonon properties, a harmonic approximation is used. In this approximation the phonon frequencies and modes can be calculated as eigenvalues and eigenvectors from the dynamical equation

$$\sum_{\kappa'\beta} \tilde{D}_{\kappa\alpha,\kappa'\beta}(\mathbf{q}) \gamma_{m\mathbf{q}}(\kappa'\beta) = \omega_{m\mathbf{q}}^2 \gamma(\kappa\alpha), \quad (3.14)$$

where  $\alpha$  and  $\beta$  label the directions the atoms are displaced,  $\kappa$  and  $\kappa'$  are the labels of the different atoms,  $\omega_{m\mathbf{q}}$  is the phonon angular frequency of mode  $m$  at wave vector  $\mathbf{q}$ ,  $\gamma_{m\mathbf{q}}$  is the eigenvector corresponding to the given mode which describes the displacements of this mode, and  $\tilde{D}_{\kappa\alpha,\kappa'\beta}$  is known as the dynamical matrix. The dynamical matrix is defined as [195]:

$$\tilde{D}_{\kappa\alpha,\kappa'\beta}(\mathbf{q}) = \frac{\tilde{C}_{\kappa\alpha,\kappa'\beta}(\mathbf{q})}{\sqrt{M_\kappa M_{\kappa'}}}, \quad (3.15)$$

where  $M_\kappa$  and  $M_{\kappa'}$  is the masses of the atoms  $\kappa$  and  $\kappa'$ .  $\tilde{C}_{\kappa\alpha,\kappa'\beta}(\mathbf{q})$  is defined as the Fourier transform of the interatomic force constants in real space [196]:

$$C_{\kappa\alpha,\kappa'\beta}(l, l') = \frac{\partial^2 E}{\partial \tau_{\kappa\alpha}(l) \partial \tau_{\kappa'\beta}(l')}, \quad (3.16)$$

where  $l$  and  $l'$  label the unit cells, and  $\kappa$  and  $\kappa'$  are the atoms which are displaced  $\tau$  in the direction  $\alpha$  and  $\beta$ .

Combining equations (3.14), (3.15) and (3.16), we see that the square of the phonon frequencies,  $f_m^2 = \omega_m^2/4\pi^2$ , is proportional to the curvature in energy for the mode  $m$ . For a material in its equilibrium state all displacements of atoms will increase the energy, and thus  $f_m^2$  is positive for all  $m$ , hence, all  $f_m$  are real. If the material is not in its ground state, displacements along one or more modes

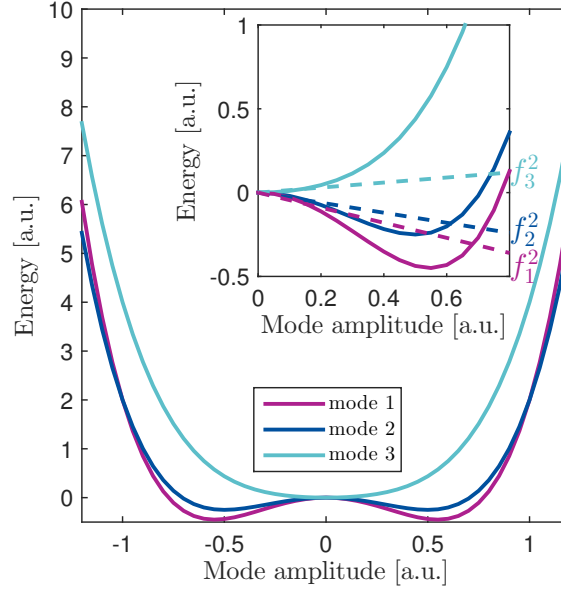


**Figure 3.4:** Plot of the energy versus mode amplitude for three different modes, labelled 1, 2 and 3 with mode frequencies  $f_1$ ,  $f_2$  and  $f_3$ , respectively. The inset shows the a zoom in at the situation around zero mode amplitude, where the square of the phonon frequencies are proportional to the curvature in energy.

will lower the energy of the system. For these modes, the curvature, proportional to  $f_m^2$ , is negative, thus the phonon frequencies are imaginary. An example of this latter situation is illustrated in Figure 3.4, here the modes 1 and 2 have a negative curvature at zero amplitude, thus  $f_1$  and  $f_2$  are imaginary. Mode 3 on the other hand have a positive curvature, and thus  $f_3$  is real. From this we learn that we can calculate the phonon spectra for the high symmetry aristotype of a material system and look for modes that have imaginary frequencies. This is a powerful tool to determine what kind of distortions are plausible to occur in the system [195].

### 3.4 Calculation Details

In this section, the computational details for the DFT-calculations performed in this work are presented.



### 3.4.1 General

All calculations in this work were performed with the PAW method [191, 192] as implemented in the Vienna Ab-initio Simulation Package (VASP) [197–200]. The integrals in reciprocal space were carried out on  $\Gamma$ -centred k-point meshes, convergence tests were done with respect to the number of k-points and in general  $8 \times 8 \times 8$  k-points were found to be sufficient for the cubic  $1 \times 1 \times 1$ , 5-atom cells, and corresponding densities in reciprocal space were used when different supercells were utilized. An energy cutoff of 550 eV was found to give well converged results for volume relaxations. This was mainly dictated by the oxygen potential, which requires a energy cutoff of at least 400 eV. However, cutoff energies as high as 800 eV were applied to confirm the degeneracy of the rotation axis of  $\text{LaAlO}_3$  under (111)-strain (Paper C), and in the calculations involving Li, a cutoff of 650 eV was used as lithium requires a higher cutoff than oxygen (499 eV, Paper D).

### 3.4.2 Potentials

The potentials used in this work are listed in table 3.1. Here, there are multiple potentials listed for Mn and Fe, and this is because less expensive potentials were used for the  $(\text{La,Sr})\text{MnO}_3/\text{SrTiO}_3$  and  $(\text{La,Sr})\text{MnO}_3/\text{LaFeO}_3$  supercells containing around 200 atoms (Paper F and G). For the heavy relaxations of supercells, initial relaxations were often performed where only the spherical terms were evaluated on the radial support grid. This approach gives efficient and fast calculations similar to the USPPs with PAW datasets. The outputs of these initial calculations were then used as a more proper starting point for standard relaxations [201]. The underscore 3 potentials for the *f*-block elements indicates that these elements have included the *f*-electrons as semi core states. This approximation was used to speed up convergence.

The Sr doping in  $(\text{La,Sr})\text{MnO}_3$  was mainly treated in a supercell approach, where the Sr atoms were evenly spread out on the different A-sites in the calculation cell. However, the virtual crystal approximation (VCA) [202], where an effective potential was created by a linear combination of the La and Sr potentials, was used in Paper F. The VCA approach has been widely used to model Sr doping in  $(\text{La,Sr})\text{MnO}_3$  [203], but is not a documented feature of VASP. The disadvantage of the supercell approach is that the discrete doping breaks the intended space group symmetry, and instead creates an artificial ordering of the dopant atoms. This is not the case with the VCA approach. Here one maintains the intended symmetry, but in doing this, one neglects local variations around the dopants.

**Table 3.1:** Minimal cutoff energy and  $E_{\text{cut}}$ , valence electron configurations of the PAW potentials used in the calculations. The names refer to the respective names in the VASP potential library [201].

Name	$E_{\text{cut}}$ [eV]	Electron configuration
Li_sv	499	$1s^2 2s^1$
Na_pv	260	$2p^6 3s^1$
K_sv	259	$3s^2 3p^6 4s^1$
Mg	200	$3s^2$
Ca_sv	267	$3s^2 3p^6 4s^2$
Sr_sv	229	$4s^2 4p^6 5s^2$
Ba_sv	187	$5s^2 5p^6 6s^2$
Sc_sv	223	$3s^2 3p^6 3d^1 4s^2$
Y_sv	203	$4s^2 4p^6 4d^1 5s^2$
La	219	$5s^2 5p^6 5d^1 6s^2$
Nd_3	183	$5s^2 5p^6 5d^1 6s^2$
Gd_3	154	$5p^6 5d^1 6s^2$
Dy_3	156	$5p^6 5d^1 6s^2$
Ti_sv	275	$3s^2 3p^6 3d^2 4s^2$
Zr_sv	230	$4s^2 4p^6 4d^2 5s^2$
Nb_sv	293	$4s^2 4p^6 4d^3 5s^2$
Ta_pv	224	$5p^6 5d^3 6s^2$
Mn	270	$3d^3 4s^2$
Mn_pv	270	$3p^6 3d^3 4s^2$
Mn_sv	387	$3s^2 3p^6 3d^3 4s^2$
Fe	268	$3d^4 4s^2$
Fe_pv	293	$3p^6 3d^4 4s^2$
Ag	250	$4d^9 5s^2$
Al	240	$3s^2 3p^1$
Ga_d	283	$3d^{10} 4s^2 4p^1$
O	400	$2s^2 2p^4$

### 3.4.3 Functional

The Perdew-Burke-Ernzerhof optimized for solids (PBE-sol) was the most used functional in this work, and was used for all relaxations. The PBE-sol functional has been found to give a more accurate description of the structure of solids compared to the standard PBE [27, 204].

The introduction of a Hubbard U-parameter was used to overcome some of the limitations with strongly correlated electrons that are typical for partially filled *d*-bands. The implementation of the Hubbard U correction introduced by Dudarev et al. [205] was used for the PBE-sol+U calculations. Different U-values were tested and for Fe and Mn values of  $U_{\text{Fe}} = 3$  eV and  $U_{\text{Mn}} = 3$  eV were found to give a satisfactory accuracy for both atomic and electronic structure of bulk LaFeO<sub>3</sub> and bulk (La,Sr)MnO<sub>3</sub>, respectively. A Hubbard U correction to the *f*-states of La was also found to be necessary in order to remove the *f*-states away from the bottom of the conduction band [109], and an  $U_{\text{La}} = 10$  eV was found to be appropriate, which was later confirmed by hybrid functional calculations. For the (111)-interface between (La,Sr)MnO<sub>3</sub>/LaFeO<sub>3</sub>, using different  $U_{\text{Fe}}$  and  $U_{\text{Mn}}$  values at the layers closest to the interface was found to be necessary to explain the magnetic reconstructions occurring, and different values were tested (Paper G). This is similar to the approach used by Qiao et al. to explain the experimental spin transitions in LaCoO<sub>3</sub>/SrTiO<sub>3</sub> heterostructures [141]. The hybrid functional calculations in Paper C were done with the HSE-sol functional, which is based on the PBE-sol functional, and uses 25 % Hartree-Fock exchange and a range separation of  $0.207 \text{ \AA}^{-1}$  [206].

### 3.4.4 Structural Relaxations and Strain

The relaxations were mainly done with the conjugate gradient method, which has been proved to give robust and efficient results, even when the starting guess is crude [201, 207]. The quasi-newton method was used in instances where the starting guess was close to the minimum [208]. The atoms and lattice vectors were relaxed until the Hellman-Feynman forces [209, 210] were below a certain value.  $1 \text{ meV/\AA}$  was found as a good criteria for relaxations of bulk and strained cells, while a less strict criteria of  $\sim 10 \text{ meV/\AA}$  was often used for the supercell calculations. For the relaxations of the highly symmetric cells for phonon calculations, the calculations were instead stopped when the energy difference between two subsequent ionic steps was less than  $10^{-8}$  eV, as the highly symmetric configuration causes most of the forces to be zero. When doing volume relaxations, the calculations were restarted after initial convergence was achieved. This restart was repeated until the calculations converged in a single ionic step, in order to reduce the effects of the Pulay stress [211].

To emulate the clamping effect of the substrate on a thin film, the in-plane lattice parameters were locked, while the out-of-plane lattice parameters and the atomic positions were relaxed, as described in section 3.2.1. In practice, locking the in-plane lattice parameters was achieved by modifying the source code of VASP to set the forces on two of the lattice vectors to zero before updating them. In-line with the work of Zayak et al. [110], quadratic strain is assumed, i.e. the two in-plane lattice vectors are assumed to have the same lengths when strained. The in-plane strain can then be applied to a certain crystallographic plane by setting up the calculation cell such that e.g. the  $\mathbf{a}$  and  $\mathbf{b}$  lattice vectors span this plane, while  $\mathbf{c}$  is a normal vector to this plane. As an example, (001)-strain can then be applied by rotating the calculation cell such that  $\mathbf{a} \parallel [100]$ ,  $\mathbf{b} \parallel [010]$  and  $\mathbf{c} \parallel [001]$ , while (111)-strain can be applied by rotating the cell such that  $\mathbf{a} \parallel [1\bar{1}0]$ ,  $\mathbf{b} \parallel [01\bar{1}]$  and  $\mathbf{c} \parallel [111]$ . This is illustrated in Figure 3.5. Going from an (001)-oriented cell to an (111)-oriented cell can be done by multiplying with the following rotation matrix:

$$T_{(001) \rightarrow (111)} = \begin{bmatrix} 1 & 0 & 1 \\ -1 & 1 & 1 \\ 0 & -1 & 1 \end{bmatrix}. \quad (3.17)$$

On the other hand, going from an (111)-oriented cell to an (001)-oriented cell can be done by multiplying with the corresponding inverse matrix:

$$T_{(111) \rightarrow (001)} = T_{(001) \rightarrow (111)}^{-1} = \frac{1}{3} \begin{bmatrix} 2 & -1 & -1 \\ 1 & 1 & -2 \\ 1 & 1 & 1 \end{bmatrix}. \quad (3.18)$$

The minimal calculation cell is then an  $1 \times 1 \times 1$  cell for (001)-strain and a  $\sqrt{2} \times \sqrt{2} \times \sqrt{3}$  cell for (111)-strain. These cells contain five and fifteen atoms, respectively. However, in order to contain all kinds of octahedral rotations and to support the most common antiferromagnetic orderings, a cell doubling along one or more of the lattice vectors was done when necessary.

### 3.4.5 Lattice Dynamics

The phonon spectra were calculated using the frozen phonon approximation as implemented in the PHONOPY code [212, 213]. Displacements of 0.01 Å were used to calculate the force constants in  $2 \times 2 \times 2$  supercells [214, 215]. The calculations were done in highly symmetric cells. In this way, unstable modes manifest as modes with imaginary frequencies, as discussed in section 3.3. For unstrained cells, the calculation cell has a  $Pm\bar{3}m$  symmetry, under (001)-strain the calculation cell has  $P4/mmm$  symmetry, while for the (111)-strained cell the symmetry is  $R\bar{3}m$ . Thus, in order to get a 40-atom cell for the (111)-strained cells, equation (3.18)

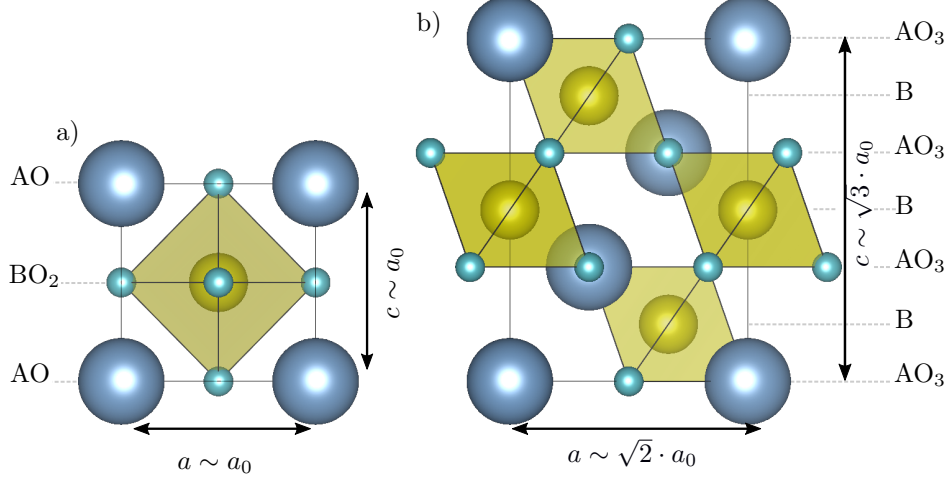


**Figure 3.5:** Minimal calculation cells for strain calculations of  $\text{ABO}_3$  perovskites, a)  $1 \times 1 \times 1$  cell for (001)-strain, b)  $\sqrt{2} \times \sqrt{2} \times \sqrt{3}$  cell for (111)-strain. Also shown is the relations between the lattice vectors, and the stacking sequence. Note that these cells will need to be doubled in all directions in order to support all kinds of octahedral rotations and common antiferromagnetic spin patterns.

was used to rotate the cells back to be [001]-oriented. In the unstrained case, all modes are triply degenerate due to the cubic symmetry. However, if quadratic strain is applied, these three modes are then split into one out-of-plane mode and two in-plane modes, with frequencies  $f_{\perp}$  and  $f_{\parallel}$ , respectively. To quantify this splitting, we define the frequency difference in Paper D as:

$$\Delta f = \begin{cases} f_{\parallel} - f_{\perp} & \text{if } \epsilon < 0, \\ f_{\perp} - f_{\parallel} & \text{if } \epsilon > 0. \end{cases} \quad (3.19)$$

This definition ensures that  $\Delta f$  is positive for modes corresponding to octahedral rotations and polar displacements under (001)-strain, as discussed in section 2.5.1. Furthermore, we also investigate how the frequencies of these modes are altered by applying strain in the (001)- and (111)-plane by analysing  $df/d\epsilon$  for the different in-plane and out-of-plane modes.

In order to get to the ground state from the high symmetry phase, unstable modes were displaced along their eigenvector and then the structure was relaxed.<sup>3</sup> This was then repeated until no more instabilities were found [24, 195]. Taking the situation illustrated in Figure 3.4 as an example, this corresponds to increasing

<sup>3</sup>Often referred to as freezing in the mode.

the amplitude of mode 1 and 2 until the minimum point is found. This procedure was repeated, looking for new unstable modes and then displace them along their eigenvector, until all phonon modes are real.

### 3.4.6 Electronic Structure

The electron density of states (DOS) and bands were projected onto site centred spherical harmonics by the use of VASP's internal routines [201]. The results were then summed over atoms in certain layers to get layer-projected DOS and band structures. Maximally localized Wannier functions (MLWF) were calculated from the DFT-Bloch functions with the WANNIER90 code [216–218], and then visualized with VESTA [34]. Atomic charges were found by Bader analysis, where charges are determined by the electron density that are contained inside a zero flux surface [219–221].



**Part II**  
**Papers**





---

## Author's contribution

*"Science is a field which grows continuously with ever expanding frontiers. Further, it is truly international in scope. . . . Science is a collaborative effort. The combined results of several people working together is often much more effective than could be that of an individual scientist working alone."*

– John Bardeen

In this thesis, DFT is used to study functional oxides for thin film applications with a focus on oxygen vacancy ordering and the effects of having a (111)-oriented substrate. The results of this work are presented in seven papers, numbered from A–G, and they are presented in the following chapters. Three main research questions have been answered, and the papers are numbered accordingly. Papers A and B present the results of ordered oxygen vacancies in  $(\text{La,Sr})\text{MnO}_{3-\delta}$  and how they affect the electronic and magnetic properties. Papers C, D and E discuss the effect of strain in the (111)-plane and how it is different from strain in the (001)-plane. The final papers, F and G, discuss the effect of (111)-interfaces and compare oxygen octahedral coupling and induced magnetic properties to corresponding effects at (001)-interfaces. The author's contribution to the publications is outlined in this chapter.

### Paper A

In *Structural phases driven by oxygen vacancies at the  $\text{La}_{0.7}\text{Sr}_{0.3}\text{MnO}_3/\text{SrTiO}_3$  hetero-interface*, the interface between  $\text{La}_{0.7}\text{Sr}_{0.3}\text{MnO}_3$  and  $\text{SrTiO}_3$  is investigated. Using scanning transmission electron microscopy, electron energy loss spectroscopy, and DFT, it is revealed that there is a large quantity of oxygen vacancies close to the interface that are initially disordered, but order over time in a brownmillerite structure. The author performed the DFT-calculations. The author took part

in the analysis and wrote the DFT-sections of the paper and supplementary information, in close collaboration with the other co-authors.

M. Nord, P-E. Vullum, M. Moreau, J-E. Boschker, S. M. Selbach, R. Holmestad and T. Tybell.

Applied Physics Letters **106**, 041604 (2015).

### Paper B

In *Spatially Confined Spin Polarization and Magnetic Sublattice Control in (La,Sr)MnO<sub>3-δ</sub> Thin Films by Oxygen Vacancy Ordering*, the electronic and magnetic properties of ordered oxygen vacancies in (La,Sr)MnO<sub>3-δ</sub> are assessed by DFT-calculations. The calculations reveal that the ordering of oxygen vacancies can control the magnetic sublattice and lead to spatially confined spin polarized conduction in the fully oxidized layers. The author performed the DFT-calculations. The author analysed the data and wrote the manuscript in close collaboration with both co-authors.

M. Moreau, S. M. Selbach and T. Tybell.

Scientific Reports **7**, 4386 (2017).

### Paper C

In *First-principles study of the effect of (111) strain on octahedral rotations and structural phases of LaAlO<sub>3</sub>*, how octahedral rotations of LaAlO<sub>3</sub> are affected by strain in the (111)-plane is investigated by DFT. It is revealed that there is an opposite splitting of in-plane and out-of-plane rotations, compared to (001)-strain, and that the in-plane rotations give rise to a Goldstone-like mode under compressive (111)-strain. The author performed the DFT-calculations. The author analysed the data and wrote the manuscript in close collaboration with all co-authors.

M. Moreau, A. Marthinsen, S. M. Selbach and T. Tybell.

Physical Review B **95**, 064109 (2017).

### Paper D

In *Strain-phonon coupling in (111)-oriented perovskite oxides*, DFT is used to study the coupling between (111)-strain and changes in the phonon frequencies of twenty different perovskite oxides. The work compares the results to strain in the (001)-plane and gives general guidelines for strain-phonon coupling in (111)-oriented perovskite oxides. The author performed the DFT-calculations. The author analysed the data and wrote the manuscript in close collaboration with all co-authors.

---

M. Moreau, A. Marthinsen, S. M. Selbach and T. Tybell.  
Physical Review B **96**, 094109 (2017).

### Paper E

In *Magnetic domain configuration of (111)-oriented LaFeO<sub>3</sub> epitaxial thin films*, the magnetic domains in (111)-oriented LaFeO<sub>3</sub> are investigated by x-ray magnetic dichroism spectroscopy and microscopy, revealing a coupling between antiferromagnetic domains and structural twin domains. Using phonon calculations, based on DFT, the twin domains are found to be a result of the strain in the (111)-plane. The author performed the DFT-calculations. The author took part in the analysis and reviewed the paper, in close collaboration with all co-authors.

I. Hallsteinsen, M. Moreau, R.V. Chopdekar, E. Christiansen, M. Nord, P-E. Vullum, J. K. Grepstad, R. Holmestad, S. M. Selbach, A. Scholl, E. Arenholz, E. Folven and T. Tybell.  
APL Materials **5**, 086107 (2017)

### Paper F

In *Octahedral coupling in (111)- and (001)-oriented La<sub>2/3</sub>Sr<sub>1/3</sub>MnO<sub>3</sub>/SrTiO<sub>3</sub> heterostructures*, the coupling of oxygen octahedra from a SrTiO<sub>3</sub> substrate into a La<sub>2/3</sub>Sr<sub>1/3</sub>MnO<sub>3</sub> thin film is investigated by DFT. The focus in this manuscript is on how the substrate orientation affects this coupling. The author performed the DFT-calculations. The author wrote the manuscript in close collaboration with both co-authors.

M. Moreau, S. M. Selbach and T. Tybell.  
Paper to be submitted.

### Paper G

In *Concurrent magnetic and structural reconstructions at the interface of (111)-oriented La<sub>0.7</sub>Sr<sub>0.3</sub>MnO<sub>3</sub>/LaFeO<sub>3</sub>*, an induced ferromagnetic moment in LaFeO<sub>3</sub> is revealed by x-ray magnetic dichroism spectroscopy and spin-polarized neutron reflectometry. The induced moment is correlated by an atomic reconstruction at the interface, studied by scanning transmission electron microscopy and DFT. The author performed the DFT-calculation and helped with the x-ray magnetic dichroism spectroscopy. The author took part in the analysis and wrote the DFT sections of the paper and supplementary information, in close collaboration with all co-authors.

I. Hallsteinsen, M. Moreau, A. Grutter, M. Nord, P.E. Vullum, D. A. Gilbert, T. Bolstad, J. K. Grepstad, R. Holmestad, S. M. Selbach, A. T. N'Diaye, B. J. Kirby,

E. Arenholz and T. Tybell.  
Physical Review B **94**. 201115(R) (2016).

**Paper not included as a part of the thesis**

In *Goldstone-like phonon modes in a (111)-strained perovskite*, DFT is used to reveal both rotational and polar Goldstone-like modes in SrMnO<sub>3</sub>. The results are discussed in terms of spontaneous symmetry breaking and possible emulation of Higgs modes in this system. The author performed supplementary DFT calculations. The author took part in the analysis and reviewed the paper, in close collaboration with all co-authors.

A. Marthinsen, S. M. Griffin, M. Moreau, T. Grande, T. Tybell and S. M. Selbach.  
Paper submitted.

---

# Structural phases driven by oxygen vacancies at the $\text{La}_{0.7}\text{Sr}_{0.3}\text{MnO}_3$ / $\text{SrTiO}_3$ hetero-interface

M. Nord, P-E. Vullum, M. Moreau, J.E. Boschker, S. M. Selbach, R. Holmestad and T. Tybell.

Published in Applied Physics Letters **106**, 041604 (2015)

DOI: <http://dx.doi.org/10.1063/1.4906920>





## Structural phases driven by oxygen vacancies at the $\text{La}_{0.7}\text{Sr}_{0.3}\text{MnO}_3/\text{SrTiO}_3$ hetero-interface

M. Nord,<sup>1</sup> P. E. Vullum,<sup>1,2</sup> M. Moreau,<sup>3</sup> J. E. Boschker,<sup>3</sup> S. M. Selbach,<sup>4</sup> R. Holmestad,<sup>1</sup> and T. Tybell<sup>3,a)</sup>

<sup>1</sup>Department of Physics, NTNU, 7491 Trondheim, Norway

<sup>2</sup>Materials and Chemistry, SINTEF, 7465 Trondheim, Norway

<sup>3</sup>Department of Electronics and Telecommunications, NTNU, 7491 Trondheim, Norway

<sup>4</sup>Department of Materials Science and Engineering, NTNU, 7491 Trondheim, Norway

(Received 12 October 2014; accepted 17 January 2015; published online 29 January 2015)

An oxygen vacancy driven structural response at the epitaxial interface between  $\text{La}_{0.7}\text{Sr}_{0.3}\text{MnO}_3$  films and  $\text{SrTiO}_3$  substrates is reported. A combined scanning transmission electron microscopy and electron energy loss spectroscopy study reveal the presence of an elongated out-of-plane lattice parameter, coupled to oxygen vacancies and reduced manganese oxidation state at the  $\text{La}_{0.7}\text{Sr}_{0.3}\text{MnO}_3$  side of the interface. Density functional theory calculations support that the measured interface structure is a disordered oxygen deficient brownmillerite structure. The effect of oxygen vacancy mobility is assessed, revealing an ordering of the vacancies with time. © 2015 AIP Publishing LLC. [<http://dx.doi.org/10.1063/1.4906920>]

Perovskite oxide materials exhibit interesting magnetic, electric, dielectric, and piezoelectric properties, which make them a promising and important class of functional materials. For example,  $\text{La}_{0.7}\text{Sr}_{0.3}\text{MnO}_3$  (LSMO) is a mixed-valence system where the interplay between  $\text{Mn}^{+3}$  and  $\text{Mn}^{+4}$  gives properties such as colossal magnetoresistance through double-exchange.<sup>1</sup> In particular, the LSMO/ $\text{SrTiO}_3$  (STO) heterostructure has been considered a promising system for devices such as magneto-tunneling junctions, metal-based spintronics, and magnetic memory. A recent development is the fabrication of oxygen-poor modulations of the perovskite structure as thin films. Ferguson *et al.*<sup>2</sup> induced oxygen vacancies in LSMO grown on STO, using a top layer of oxygen deficient STO as an oxygen getter. This resulted in a brownmillerite phase, where the oxygen vacancies ordered into a superstructure. Similar structures have also been reported in  $\text{La}_{0.5}\text{Sr}_{0.5}\text{CoO}_{3-\delta}$  (LSCO) heterostructures. Growing the LSCO on substrates with different lattice mismatch led to different kinds of oxygen vacancy ordering, driven by strain relief accommodation.<sup>3</sup> These structures are not only interesting for the ionic transport<sup>4</sup> properties but also for their effect on other functional properties. *Ab-initio* calculations predict oxygen vacancies close to the interface of tensile strained films.<sup>5</sup> There have also been several observations of changes in cation oxidation state<sup>6-8</sup> and lattice parameter<sup>9</sup> close to interfaces in similar systems. Understanding the correlation between oxygen vacancies and B-site cation oxidation state, and how the oxygen vacancies behave and order over time is important for implementation in devices.

In this letter, we report on a combined Scanning Transmission Electron Microscopy-Electron Energy Loss Spectroscopy (STEM-EELS) and Density Functional Theory (DFT) study of a LSMO/STO heterostructure, where a

coupling between oxygen vacancies, the manganese oxidation state, and an elongated out-of-plane lattice parameter in the LSMO film close to the interface is observed. We attribute these observations to a brownmillerite structure with disordered oxygen vacancies, which order over time.

35 nm thick epitaxial LSMO films were grown on (001)-oriented STO substrates using pulsed laser deposition and *in-situ* RHEED analysis.<sup>10</sup> The substrates were annealed for 1 h at 950 °C in oxygen ambient before the deposition. A KrF excimer laser ( $\lambda = 248$  nm) with a fluency of  $\sim 2$  J  $\text{cm}^{-2}$  and a repetition rate of 1 Hz was employed on a stoichiometric  $\text{La}_{0.7}\text{Sr}_{0.3}\text{MnO}_3$  target.<sup>10</sup> Cross sectional TEM foils were prepared using mechanical tripod wedge polishing followed by low-energy Ar-ion milling. A combined STEM-EELS and STEM-high angle angular dark field (HAADF) study was performed to probe the electronic and lattice structure at the interface using a probe corrected FEI Titan 80-300, with a beam energy of 300 keV. The energy resolution of EELS was found to be 1.0 eV from the full width at half maximum (FWHM) of the zero loss peak. The STEM and EELS study on the ordered brownmillerite after 1.5 years was performed on a probe- and image-corrected cold-FEG Jeol ARM 200F. For the EELS analysis, principal component analysis (PCA)<sup>11</sup> was used to reduce noise and standard power law background subtraction was done using HyperSpy.<sup>12</sup> To increase the electron count statistics, the EELS data were not collected at atomic resolution, but with a larger probe. To rule out the effect of the electron beam inducing changes in the material, the same EELS experiments were performed in similar regions with shorter exposure and at a beam energy of 120 keV, showing the same results as the 300 keV data at 3 s exposure time. In addition, electron beam exposure tests were performed, where the same area was exposed to the electron beam for 30 s under the same experimental conditions as the data in this work. No significant changes in the EELS data were observed. The DFT calculations were done with the Projector Augmented Wave (PAW) method<sup>13</sup> as

<sup>a)</sup>Author to whom correspondence should be addressed. Electronic mail: [thomas.tybell@iet.ntnu.no](mailto:thomas.tybell@iet.ntnu.no)



041604-2 Nord *et al.*

Appl. Phys. Lett. 106, 041604 (2015)

implemented in the Vienna *Ab-initio* Simulation Package (VASP),<sup>14,15</sup> using the PBEsol functional<sup>16</sup> with a GGA + U approximation.<sup>17</sup> The La, Sr\_sv, Mn\_sv, and standard O PBE PAW potentials supplied with VASP were used, and a Hubbard U correction of 3 eV and 10 eV was applied to the Mn 3d electrons and La 4f orbitals, respectively, in concordance with previous related investigations.<sup>5,18</sup> A 36 atom  $\text{La}_6\text{Sr}_2\text{Mn}_8\text{O}_{20}$  unit cell with a  $6 \times 6 \times 2$  gamma centered k-point mesh and a plane wave cutoff energy of 550 eV was used for the calculations of the oxygen deficient LSMO unit cells. The in-plane lattice constants were fixed at the equilibrium calculated value for cubic STO, while the ionic coordinated and out-of-plane lattice constant were allowed to relax until the Hellmann-Feynman forces on the ions were smaller than 0.01 eV/Å.

The structural quality of the thin film and substrate was investigated by STEM-HAADF. Fig. 1(a) shows typical data, revealing a coherent interface, and X-ray analysis confirms that the films are epitaxial.<sup>10</sup>

Possible strain around the epitaxial interface was analyzed relying on geometrical phase analysis (GPA)<sup>19</sup> of the STEM-HAADF data. Fig. 1(a) shows a STEM-HAADF image of the LSMO/STO heterostructure, and the corresponding out-of-plane strain data from GPA is displayed in Fig. 1(b). Using the lattice parameter of bulk STO, 3.905 Å, as a reference, the substrate averages as expected to 0% out-of-plane strain, with a standard deviation of 0.17%. For the film, an elongated out-of-plane lattice parameter is observed in the first 3 nm. This corresponds to a relative out-of-plane strain of 2.5% compared to the LSMO bulk pseudo cubic lattice parameter of 3.876 Å. Similar strain has been reported in BFO grown on LSMO/STO,<sup>9</sup> where the first few unit cells closest to the interface are elongated in the out-of-plane direction.

To further investigate the region with enlarged out-of-plane LSMO lattice parameter, we probe the electronic structure by EELS, providing information on both the manganese and oxygen electronic state through the Mn-L<sub>2,3</sub> and O-K core loss edges. EELS line scans were acquired in a line orthogonal to the film/substrate interface, as schematically shown in Fig. 2(a), with STEM-EELS data representative for (i) the bulk LSMO film (red), (ii) the interface on the film side (green), and (iii) the bulk STO (blue), presented in Fig. 2(b). The manganese edge consists of two peaks: L<sub>3</sub> (Mn

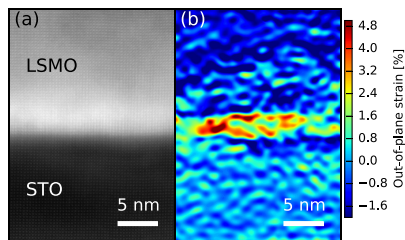


FIG. 1. (a) Cross-sectional STEM-HAADF image of the LSMO/STO heterostructure, showing a coherent interface. (b) Map of the out-of-plane strain in (a), using the STO-substrate (3.905 Å) as a reference.

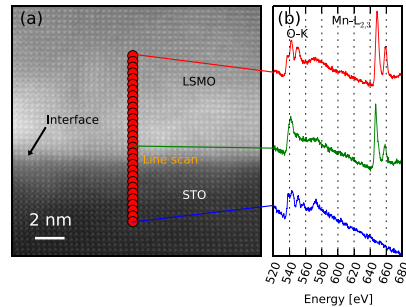


FIG. 2. (a) Cross-sectional STEM-HAADF image of the LSMO/STO heterostructure. (b) Results of an EELS line scan across the LSMO/STO interface.

$2P_{3/2} \rightarrow 3d$ ) and L<sub>2</sub> (Mn  $2P_{1/2} \rightarrow 3d$ ),<sup>11</sup> see Fig. 3(a). There is a clear difference between the Mn-L<sub>2,3</sub> spectra acquired at the interface and those acquired away from the interface. The intensity ratio between the L<sub>3</sub> and L<sub>2</sub> peaks (L<sub>3</sub>/L<sub>2</sub>-ratio)

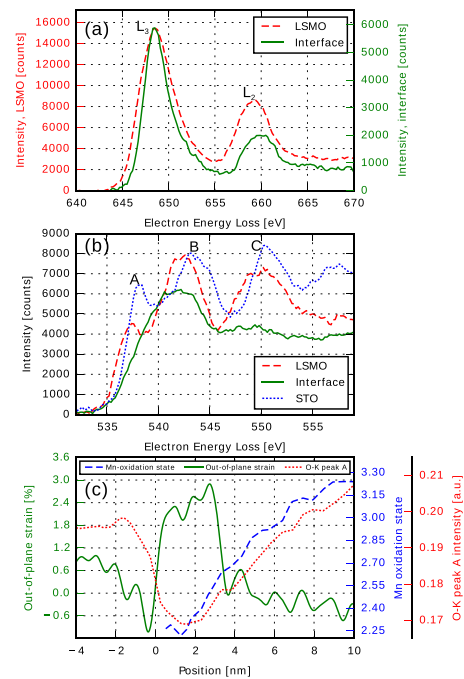


FIG. 3. (a) Manganese L<sub>2</sub>- and L<sub>3</sub>-edges from the middle of the LSMO film, and LSMO film side of the interface. (b) Oxygen K-edge from the LSMO film side of the interface, in the middle of the LSMO film, and STO substrate. (c) Integrated out-of-plane strain from Fig. 1(b), manganese oxidation state and integrated oxygen K-edge peak A intensity normalized to the total O-K edge intensity (shown in Fig. 3(b)).

is larger at the interface. This is indicative of a lower Mn oxidation state at the interface as compared to bulk LSMO, as the intensity of the  $L_3$  peak increases relative to the  $L_2$  peak when the Mn oxidation state is lowered.<sup>11,20</sup> We note that the FWHM line width of the Mn- $L_3$  peak is smaller at the interface as compared to the rest of the film, supporting a lower Mn oxidation state at the interface.<sup>20</sup> The Mn-oxidation state was estimated as in Varela *et al.*<sup>11</sup> and plotted in Fig. 3(c) (blue dashed line). As can be seen in Fig. 3(c), a clear trend for the Mn oxidation state was observed: starting at 3.2 far from the interface and monotonically decreasing towards 2.3 close to the interface. This trend of a reduction in Mn oxidation state has also been observed in (La,Ca)MnO<sub>3</sub>/STO<sup>6</sup> and TbMnO<sub>3</sub>/STO,<sup>7</sup> and has been proposed to explain the observed magnetic “dead layer” in similar systems.<sup>21</sup>

In order to investigate the possible presence of oxygen vacancies, known to be present in similar thin film systems,<sup>2</sup> the oxygen electronic structure was investigated. As seen in Fig. 2(b), large spectral differences are observed between the oxygen K-edges across the interface. The oxygen K-edges from the (i) middle of the film, (ii) film side of the interface, and (iii) STO bulk are shown in detail in Fig. 3(b). The main fine structure peaks are labeled as A, B, and C. The O-K edges from the bulk of the film, and the STO substrate, are consistent with LSMO<sup>8</sup> and STO bulk<sup>22</sup> data previously reported. However, the O-K edge at the LSMO side of the interface is not consistent with LSMO bulk. We observe that peak A is weak or not present in the LSMO interface region. Peak A is attributed to the covalent interaction between O 2p and Mn 3d states in the LSMO perovskite structures,<sup>11</sup> and is known to be sensitive to the Mn oxidation state. In addition, a weakening of peaks A and C in conjunction with a broadening of peak B has been correlated with oxygen vacancies.<sup>23</sup> The bond between Mn and O becomes more ionic as the Mn oxidation state decreases, reducing the interaction between the orbitals. A low Mn oxidation state then corresponds to a less intense peak,<sup>11</sup> consistent with the Mn L-edge data. We take the integrated intensity of peak A normalized over the total O-K intensity as a measure of oxygen content, the results of this shown in Fig. 3(c) (red dotted line). As can be seen, the amount of oxygen vacancies increases towards the interface, and subsequently decreases to a constant value in the substrate.

The strain, shift in Mn oxidation state and the changes in oxygen signal imply a deviation from the perovskite structure at the film side of the interface. The formal valence for Mn in La<sub>0.7</sub><sup>+3</sup>Sr<sub>0.3</sub><sup>+2</sup>Mn<sup>+3.3</sup>O<sub>3</sub><sup>-2</sup> (valence shown in superscript) is 3.3. Removing oxygen lowers the Mn oxidation state as the charge compensating electrons localize on Mn,

consistent with the data. We note that oxygen vacancies can be expected close to the interface in thin films that are tensile strained by the substrate.<sup>5</sup> Assuming that the whole shift in Mn oxidation state is due to oxygen vacancies, an oxygen deficiency of  $\delta = 0.5$  (LSMO<sub>3- $\delta$</sub> ) is found (corresponding to La<sub>0.7</sub>Sr<sub>0.3</sub>MnO<sub>2.5</sub>). This amount of oxygen vacancies is also consistent with the oxygen fine structure, which is similar to the one reported by Yao *et al.*<sup>23</sup> This large number of oxygen vacancies breaks the MnO<sub>6</sub> octahedron, and hence, destroys the perovskite structure.<sup>24</sup> A known cation non-stoichiometric phase is the Ruddlesden-Popper structure.<sup>25</sup> However, our high-resolution STEM-HAADF data are not consistent with the clear signature of such a phase. Other cation non-stoichiometries, such as La- or Mn-deficient phases, correspond to an increase in the formal Mn valence, not consistent with our EELS data. A possible reduction in Sr-content would lower the Mn oxidation state, however, this is not consistent with the O-K edge.<sup>26</sup> Therefore, we do not attribute the observed changes to cation non-stoichiometry.

The oxygen deficient brownmillerite structure, ABO<sub>2.5</sub> is compatible with the experimental data. Recently, there have been several reports on thin film synthesis of brownmillerites in multiple material systems.<sup>2,27–29</sup> For example, a brownmillerite phase, where oxygen vacancies are ordered, was shown in a LSMO/STO heterostructure by Ferguson *et al.*<sup>2</sup> In that work, the vacancies were ordered in preferred layers resulting in an out-of-plane lattice parameter of 16.47 Å, corresponding to four pseudo-cubic LSMO unit cells with a 6.1% elongation of the out-of-plane lattice parameter compared to the stoichiometric perovskite. This is considerably larger than the 2.5% elongation we measure close to the interface in this work. However, one possibility is that disordered oxygen vacancies result in a lower out-of-plane strain state. In order to test this hypothesis, we have performed DFT calculations on brownmillerites with ordered and disordered oxygen vacancy structures. The calculations were performed on structures with different oxygen vacancy positions (see supplementary material<sup>30</sup>), the results shown in Table I. There is a clear trend that structures with oxygen vacancies ordered in layers are more stable than oxygen vacancies distributed in all the Mn layers. The most stable structure, corresponding to the one observed by Ferguson *et al.*,<sup>2</sup> is 0.223 eV/f.u. more stable than the most stable disordered structure. However, the DFT calculations also reveal that the disordered structures all show an elongated out-of-plane lattice parameter in the order of 1%–2%, in good agreement with our experimental strain data, while the ordered structures show an elongation in the order of 6%–7%.

TABLE I. DFT calculated energy differences between the different oxygen vacancy brownmillerite structures and the most stable ordered structure, given per ABO<sub>2.5</sub> formula unit, and the corresponding out-of-plane strain compared to stoichiometric bulk LSMO. The different structures (A, B, C, and D) referring to different positioning of the oxygen vacancies, see supplementary material<sup>30</sup> for details.

	Ordered structure A	Ordered structure B	Ordered structure C	Disordered structure A	Disordered structure B	Disordered structure C	Disordered structure D
$\Delta E/\text{f.u. (eV)}$	0.014	0	0.035	0.304	0.357	0.223	0.238
Strain (%)	6.72	6.52	7.00	2.38	2.39	1.55	2.11

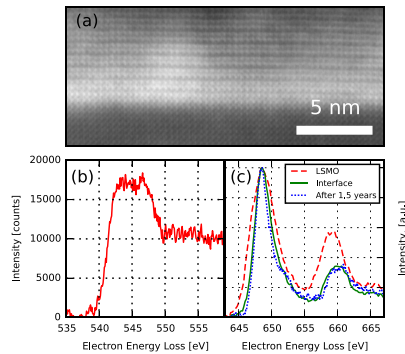
041604-4 Nord *et al.*Appl. Phys. Lett. **106**, 041604 (2015)

FIG. 4. (a) Cross sectional STEM-HAADF image from the same TEM lamella as Figs. 1(a) and 2(a), after approximately 1.5 years showing an ordered brownmillerite superstructure at the film side of the interface. (b) Representative STEM-EELS data from the superstructure in (a), showing an oxygen K-edge consistent with oxygen vacancies. (c) The same as (b) but for the Mn-L<sub>2,3</sub> edge, with the spectra from Fig. 3(a) as comparison.

Based on the above discussion, a brownmillerite phase with disordered oxygen vacancies at the LSMO side of the interface towards STO is the only interpretation that agrees with both STEM and EELS data and DFT calculations. Fig. 4(a) shows STEM-HAADF data taken on the same TEM lamellas after approximately 1.5 years. Here, we find an ordered, layered structure at the interface, compatible with an ordered brownmillerite phase.<sup>2</sup> Figs. 4(b) and 4(c) display representative O-K and Mn-L<sub>2,3</sub> EELS edges from the ordered structure, confirming the presence of oxygen vacancies and manganese oxidation state corresponding to the one observed close to the interface in the disordered phase. GPA of the layered structure reveals an elongated lattice parameter of 5%–6% compared to LSMO bulk, consistent with the DFT-calculations. However, just at the interface a larger elongation is observed. This ordering of the oxygen vacancies with time is in agreement with the ~0.2 eV energy difference between the ordered and disordered structures found using DFT.

In conclusion, we have studied the strain and electronic structure of a LSMO/STO heterojunction using STEM-HAADF and STEM-EELS. The results reveal a region with an elongated out-of-plane lattice parameter, reduced oxygen content, and lowered manganese oxidation state extending from the interface to about 3 nm into the LSMO film. These properties are attributed to the presence of a brownmillerite phase with disordered oxygen vacancies, in agreement with DFT calculations, not previously reported in as-grown LSMO/STO thin films. After approximately 1.5 years, the same TEM lamella show a brownmillerite phase with ordered oxygen vacancies. These findings shed light on the effect of oxygen vacancies on the structure of complex perovskite oxide interfaces, and reveal that they can order over time possibly affecting functional properties.

This project was supported by the Norwegian Research Council under Project No. 10239707 and The Norwegian

PhD Network on Nanotechnology for Microsystems. Takeshi Kasama at Center for Electron Nanoscopy at the Technical University of Denmark (CEN-DTU) was thankfully acknowledged for support with the STEM-EELS investigations. The Norwegian Metacenter for Computational Science (Notur) was acknowledged for providing computational resources for DFT-calculations through the project NN9301K.

<sup>1</sup>Y. Tokura, *Rep. Prog. Phys.* **69**, 797 (2006).

<sup>2</sup>J. D. Ferguson, Y. Kim, L. F. Kourkoutis, A. Vodnick, A. R. Woll, D. A. Muller, and J. D. Brock, *Adv. Mater.* **23**, 1226 (2011).

<sup>3</sup>J. Gazquez, S. Bose, M. Sharma, M. A. Torija, S. J. Pennycook, C. Leighton, and M. Varela, *APL Mater.* **1**, 012105 (2013).

<sup>4</sup>S. V. Kalinin and N. A. Spaldin, *Science* **341**, 858 (2013).

<sup>5</sup>U. Aschauer, R. Pfenninger, S. M. Selbach, T. Grande, and N. A. Spaldin, *Phys. Rev. B* **88**, 054111 (2013).

<sup>6</sup>A. Kobrinskii, A. Goldman, M. Varela, and S. Pennycook, *Phys. Rev. B* **79**, 094405 (2009).

<sup>7</sup>S. Venkatesan, M. Döblinger, C. Daumont, B. Kooi, B. Noheda, J. T. M. De Hosson, and C. Scheu, *Appl. Phys. Lett.* **99**, 222902 (2011).

<sup>8</sup>L. Samet, D. Imhoff, J.-L. Maurice, J.-P. Contour, A. Gloter, T. Manoubi, A. Fert, and C. Colliex, *Eur. Phys. J. B: Condens. Matter* **34**, 179 (2003), available at <http://link.springer.com/article/10.1140%2Fepjb%2F2003-00210-8>.

<sup>9</sup>A. Y. Borisevich, H. J. Chang, M. Huijben, M. P. Oxley, S. Okamoto, M. K. Niranjani, J. D. Burton, E. Y. Tsymlal, Y. H. Chu, P. Yu *et al.*, *Phys. Rev. Lett.* **105**, 087204 (2010).

<sup>10</sup>J. E. Boschker, E. Folven, Å. F. Monsen, E. Wahlström, J. K. Grepstad, and T. Tybell, *Cryst. Growth Des.* **12**, 562 (2012).

<sup>11</sup>M. Varela, M. Oxley, W. Luo, J. Tao, M. Watanabe, A. Lupini, S. Pantelides, and S. Pennycook, *Phys. Rev. B* **79**, 085117 (2009).

<sup>12</sup>See <http://hyperspy.org/> for HyperSpy: Hyperspectral data analysis toolbox.

<sup>13</sup>P. E. Blochl, *Phys. Rev. B* **50**, 17953 (1994).

<sup>14</sup>G. Kresse and D. Joubert, *Phys. Rev. B* **59**, 1758 (1999).

<sup>15</sup>G. Kresse and J. Furthmüller, *Phys. Rev. B* **54**, 11169 (1996).

<sup>16</sup>J. P. Perdew, A. Ruzsinszky, G. I. Csonka, O. A. Vydrov, G. E. Scuseria, L. A. Constantin, X. Zhou, and K. Burke, *Phys. Rev. Lett.* **100**, 136406 (2008).

<sup>17</sup>V. I. Anisimov, J. Zaanen, and O. K. Andersen, *Phys. Rev. B* **44**, 943 (1991).

<sup>18</sup>R. L. Johnson-Wilke, D. Marincel, S. Zhu, M. P. Warusawithana, A. Hatt, J. Sayre, K. T. Delaney, R. Engel-Herbert, C. M. Schlepütz, J.-W. Kim *et al.*, *Phys. Rev. B* **88**, 174101 (2013).

<sup>19</sup>M. J. Hytch, E. Snoeck, and R. Kilaas, *Ultramicroscopy* **74**, 131 (1998).

<sup>20</sup>T. Riedl, T. Gemming, and K. Wetzig, *Ultramicroscopy* **106**, 284 (2006).

<sup>21</sup>R. P. Borges, W. Guichard, J. G. Lunney, J. M. D. Coey, and F. Ott, *J. Appl. Phys.* **89**, 3868 (2001).

<sup>22</sup>D. A. Muller, N. Nakagawa, A. Ohtomo, J. L. Grazul, and H. Y. Hwang, *Nature* **430**, 657 (2004).

<sup>23</sup>L. Yao, S. Majumdar, L. Åkäslopmo, S. Inkinen, Q. H. Qin, and S. V. Dijken, *Adv. Mater.* **26**, 2789 (2014).

<sup>24</sup>S. Stølen, E. Bakken, and C. E. Mohn, *Phys. Chem. Chem. Phys.* **8**, 429 (2006).

<sup>25</sup>R. G. Palgrave, P. Borisov, M. S. Dyer, S. R. C. McMitchell, G. R. Darling, J. B. Claridge, M. Batuk, H. Tan, J. Verbeeck, J. Hadermann *et al.*, *J. Am. Chem. Soc.* **134**, 7700 (2012).

<sup>26</sup>A. B. Shah, Q. M. Ramasse, S. J. May, J. Kavich, J. G. Wen, X. Zhai, J. N. Eckstein, J. Freeland, A. Bhattacharya, and J. M. Zuo, *Phys. Rev. B* **82**, 115112 (2010).

<sup>27</sup>K. Matsumoto, M. Haruta, M. Kawai, A. Sakaiguchi, N. Ichikawa, H. Kurata, and Y. Shimakawa, *Sci. Rep.* **1**, 27 (2011).

<sup>28</sup>Y. M. Kim, J. He, M. D. Biegalski, H. Ambaye, V. Lauter, H. M. Christen, S. T. Pantelides, S. J. Pennycook, S. V. Kalinin, and A. Y. Borisevich, *Nat. Mater.* **11**, 888 (2012).

<sup>29</sup>H. Jeon, W. S. Choi, J. W. Freeland, H. Ohta, C. U. Jung, and H. N. Lee, *Adv. Mater.* **25**, 3651 (2013).

<sup>30</sup>See supplementary material at <http://dx.doi.org/10.1063/1.4906920> for details on the different positioning of the oxygen vacancies in the simulated structures.

*Supplementary material for:***Structural phases driven by oxygen vacancies at the  
La<sub>0.7</sub>Sr<sub>0.3</sub>MnO<sub>3</sub>/SrTiO<sub>3</sub> hetero-interface**

M. Nord<sup>1</sup>, P.E. Vullum<sup>1,2</sup>, M. Moreau<sup>3</sup>, J.E. Boschker<sup>3</sup>, S.M. Selbach<sup>4</sup>, R. Holmestad<sup>1</sup> and T. Tybell<sup>3, a)</sup>

<sup>1</sup> Department of Physics, NTNU, Trondheim, Norway

<sup>2</sup> Materials and Chemistry, SINTEF, Trondheim, Norway,

<sup>3</sup> Department of Electronics and Telecommunications, NTNU, Trondheim, Norway

<sup>4</sup> Department of Materials Science and Engineering, NTNU, Trondheim, Norway

a) Corresponding author: (e-mail) thomas.tybell@iet.ntnu.no

The DFT (Density Functional Theory) calculations were done with the Projector Augmented Wave (PAW)<sup>1,2</sup> method as implemented in the Vienna Ab-initio Simulation Package (VASP),<sup>3-6</sup> with the PBEsol functional<sup>7</sup> with a GGA + U approximation.<sup>8,9</sup> PAW potentials treating 11 valence electrons for La ( $4s^2 4p^6 5d^1 6s^2$ ), 10 for Sr ( $4s^2 4p^6 5s^2$ ), 15 for Mn ( $3s^2 3p^6 3d^5 4s^2$ ) and 6 for O ( $2s^2 2p^4$ ) were used. A Hubbard U correction of 3 eV was applied to the Mn 3d electrons, as this approach has previously well described a ternary manganese oxide with oxygen vacancies,<sup>10</sup> while a Hubbard U of 10 eV was applied to the La 4f orbital to move these orbitals away from the Fermi level.<sup>11</sup> A cutoff energy of 550 eV was used for the plane wave basis set. A 36 atom La<sub>6</sub>Sr<sub>2</sub>Mn<sub>8</sub>O<sub>20</sub> unit cell with a 6x6x2 gamma-centered k-point mesh for Brillouin zone integration was used for the calculations of the oxygen deficient LSMO unit cells. An initial ferromagnetic spin ordering was assumed. The unit cells for the four disordered structures are shown in Figure S1, while the three unit cells of the ordered structures are shown in Figure S2. The different structures have different ordering of the oxygen vacancies, in the ordered structures there are double vacancies in every second Mn layer, while in the disordered structures there are a single vacancy in every Mn layer. In order to take into account the strain imposed by the 001 SrTiO<sub>3</sub> substrate the in plane lattice constants were fixed to the equilibrium lattice constant calculated for cubic SrTiO<sub>3</sub> with the PBEsol functional, 550 eV cutoff energy, a 6x6x6

gamma-centered k-mesh and Sr\_sv, Ti\_sv (12 valence electrons:  $3s^23p^64s^23d^2$ ) and O PAW-potentials supplied with VASP. The internal coordinates of the ions and the out of plane lattice constant was allowed to relax until the Hellmann-Feynman forces on the ions were below  $0.01 \text{ eV/\AA}$ . The calculated out-of-plane lattice parameter and all atom positions are shown in Table S1.

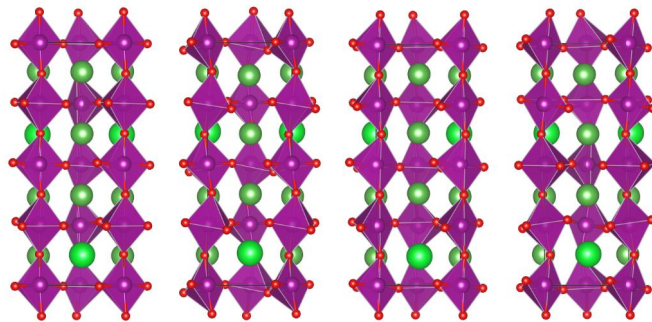


**Figure S1:** The 36 atom unit cells of the *disordered* structures investigated. The different structures have different oxygen vacancy ordering. Dark green: La, light green: Sr, purple: Mn, red: O.

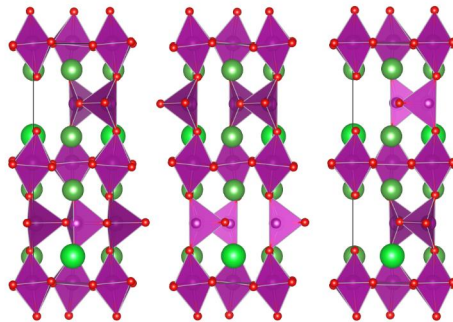


**Figure S2:** The 36 atom unit cells of the *ordered* structures investigated. The different structures have different oxygen vacancy ordering. Dark green: La, light green: Sr, purple: Mn, red: O.

**Table S1:** Calculated out-of-plane lattice parameter and atomic positions for the vacancy structures investigated. Empty cells correspond to the location of the vacancies.

	ORDER A	ORDER B	ORDER C	DISORDER A	DISORDER B	DISORDER C	DISORDER D
c	16,512	16,48	16,556	15,841	15,841	15,713	15,799
La (1)	(0.494,0.004,0.889)	(0.505,0.012,0.889)	(0.496,0.015,0.890)	(0.497,0.990,0.882)	(0.504,0.995,0.877)	(0.514,0.991,0.872)	(0.515,0.970,0.877)
La (2)	(0.508,0.982,0.111)	(0.490,0.987,0.112)	(0.513,0.020,0.111)	(0.510,0.991,0.122)	(0.503,0.997,0.127)	(0.520,0.997,0.116)	(0.521,0.988,0.128)
La (3)	(0.997,0.480,0.890)	(0.996,0.490,0.891)	(0.011,0.491,0.892)	(0.995,0.507,0.880)	(0.005,0.492,0.866)	(0.986,0.509,0.878)	(0.978,0.473,0.872)
La (4)	(0.502,0.982,0.392)	(0.504,0.990,0.391)	(0.494,0.008,0.392)	(0.505,0.990,0.363)	(0.488,0.008,0.366)	(0.518,0.996,0.369)	(0.485,0.999,0.366)
La (5)	(0.979,0.496,0.389)	(0.995,0.512,0.389)	(0.009,0.485,0.390)	(0.011,0.504,0.371)	(0.992,0.507,0.376)	(0.982,0.504,0.381)	(0.995,0.512,0.372)
La (6)	(0.001,0.477,0.611)	(0.010,0.487,0.612)	(0.991,0.481,0.611)	(0.986,0.509,0.625)	(0.992,0.509,0.625)	(0.980,0.503,0.634)	(0.986,0.514,0.625)
Sr (1)	(0.984,0.494,0.112)	(0.997,0.506,0.114)	(0.004,0.493,0.113)	(1.000,0.509,0.125)	(0.997,0.501,0.133)	(0.988,0.514,0.120)	(0.020,0.520,0.129)
Sr (2)	(0.495,0.999,0.613)	(0.503,0.006,0.614)	(0.499,0.008,0.613)	(0.500,0.980,0.622)	(0.496,0.002,0.634)	(0.512,0.986,0.630)	(0.498,0.025,0.630)
Mn (1)	(0.439,0.535,0.249)	(0.461,0.455,0.249)	(0.547,0.554,0.249)	(0.501,0.485,0.247)	(0.493,0.500,0.251)	(0.504,0.504,0.248)	(0.507,0.492,0.249)
Mn (2)	(0.493,0.490,0.003)	(0.498,0.499,0.003)	(0.505,0.506,0.003)	(0.502,0.481,0.000)	(0.508,0.510,0.002)	(0.483,0.485,0.999)	(0.501,0.495,0.001)
Mn (3)	(0.040,0.029,0.249)	(0.965,0.047,0.250)	(0.041,0.945,0.250)	(0.001,0.007,0.249)	(0.996,0.004,0.250)	(0.015,0.007,0.248)	(0.988,0.013,0.249)
Mn (4)	(0.993,0.989,0.001)	(0.999,0.998,0.003)	(0.004,0.004,0.002)	(0.006,0.005,0.002)	(0.990,0.992,0.002)	(0.017,0.013,0.999)	(0.006,0.996,0.002)
Mn (5)	(0.524,0.540,0.749)	(0.535,0.547,0.750)	(0.463,0.555,0.750)	(0.483,0.503,0.749)	(0.496,0.498,0.751)	(0.483,0.487,0.751)	(0.486,0.505,0.750)
Mn (6)	(0.491,0.487,0.503)	(0.501,0.498,0.503)	(0.501,0.496,0.502)	(0.511,0.498,0.499)	(0.505,0.511,0.501)	(0.485,0.493,0.502)	(0.494,0.500,0.500)
Mn (7)	(0.035,0.942,0.748)	(0.039,0.955,0.749)	(0.959,0.947,0.749)	(0.008,0.003,0.750)	(0.000,0.001,0.750)	(0.017,0.015,0.751)	(0.002,1.000,0.750)
Mn (8)	(0.992,0.989,0.502)	(0.002,0.999,0.503)	(0.999,0.994,0.503)	(0.991,0.995,0.499)	(0.987,0.994,0.501)	(0.996,0.996,0.502)	(0.003,0.010,0.500)
O (1)			(0.923,0.588,0.255)	(0.786,0.724,0.263)		(0.797,0.719,0.263)	(0.771,0.740,0.234)
O (2)	(0.405,0.924,0.250)		(0.427,0.917,0.250)	(0.306,0.797,0.243)	(0.236,0.735,0.258)	(0.310,0.815,0.239)	(0.278,0.784,0.246)
O (3)	(0.460,0.445,0.865)	(0.493,0.453,0.866)	(0.492,0.468,0.867)	(0.491,0.443,0.874)	(0.451,0.461,0.874)	(0.433,0.468,0.876)	(0.420,0.505,0.878)
O (4)	(0.742,0.751,0.986)	(0.752,0.758,0.990)	(0.763,0.758,0.991)	(0.710,0.785,0.992)	(0.782,0.716,0.969)	(0.730,0.770,0.992)	(0.783,0.716,0.990)
O (5)	(0.237,0.745,0.993)	(0.243,0.756,0.985)	(0.256,0.768,1.000)	(0.228,0.713,0.996)	(0.286,0.805,0.004)	(0.234,0.727,0.007)	(0.290,0.779,0.019)
O (6)	(0.519,0.510,0.132)	(0.508,0.552,0.133)	(0.502,0.465,0.133)	(0.517,0.463,0.122)	(0.535,0.545,0.130)	(0.476,0.437,0.122)	(0.490,0.427,0.123)
O (7)	(0.085,0.403,0.253)	(0.088,0.401,0.254)		(0.200,0.289,0.245)	(0.268,0.226,0.228)		(0.222,0.270,0.270)
O (8)		(0.583,0.094,0.250)			(0.759,0.273,0.257)	(0.735,0.221,0.259)	
O (9)	(0.974,0.044,0.862)	(0.966,0.058,0.862)	(0.040,0.047,0.862)	(0.006,0.027,0.873)	(0.047,0.052,0.882)	(0.067,0.032,0.874)	(0.077,0.017,0.876)
O (10)	(0.248,0.222,0.008)	(0.248,0.238,0.004)	(0.245,0.252,0.003)				
O (11)	(0.756,0.242,1.000)	(0.754,0.241,0.010)	(0.755,0.243,0.994)	(0.784,0.284,0.996)	(0.709,0.207,0.002)	(0.757,0.266,0.988)	(0.719,0.220,0.982)
O (12)	(0.944,0.960,0.135)	(0.037,0.955,0.136)	(0.961,0.024,0.135)	(0.967,0.002,0.127)	(0.958,0.965,0.122)	(0.011,0.050,0.124)	(0.987,0.065,0.125)
O (13)	(0.906,0.580,0.750)	(0.917,0.594,0.750)	(0.583,0.912,0.755)	(0.799,0.712,0.755)		(0.770,0.730,0.758)	(0.774,0.724,0.768)
O (14)	(0.411,0.895,0.754)	(0.412,0.901,0.754)	(0.076,0.583,0.749)	(0.317,0.821,0.752)	(0.275,0.769,0.756)	(0.266,0.773,0.743)	
O (15)	(0.532,0.502,0.366)	(0.534,0.558,0.362)	(0.467,0.453,0.362)	(0.471,0.448,0.377)	(0.453,0.454,0.374)	(0.424,0.457,0.374)	(0.542,0.543,0.377)
O (16)	(0.748,0.743,0.510)	(0.746,0.741,0.510)	(0.745,0.739,0.491)	(0.688,0.808,0.488)	(0.714,0.783,0.468)	(0.703,0.781,0.487)	
O (17)	(0.234,0.742,0.496)	(0.252,0.738,0.504)	(0.251,0.735,0.500)	(0.208,0.688,0.505)	(0.204,0.714,0.502)	(0.190,0.685,0.511)	(0.194,0.693,0.496)
O (18)	(0.450,0.457,0.633)	(0.463,0.455,0.636)	(0.541,0.476,0.635)	(0.517,0.456,0.623)	(0.541,0.537,0.629)	(0.489,0.450,0.626)	(0.522,0.556,0.623)
O (19)				(0.164,0.317,0.747)	(0.216,0.280,0.728)		(0.211,0.285,0.731)
O (20)					(0.725,0.235,0.758)	(0.743,0.234,0.762)	(0.715,0.223,0.766)
O (21)	(0.939,0.950,0.362)	(0.007,0.953,0.366)	(0.010,0.031,0.367)	(0.041,0.022,0.374)	(0.047,0.049,0.381)	(0.076,0.043,0.376)	(0.937,0.976,0.375)
O (22)	(0.235,0.232,0.484)	(0.257,0.256,0.485)	(0.258,0.250,0.503)				(0.317,0.186,0.493)
O (23)	(0.754,0.239,0.497)	(0.748,0.258,0.490)	(0.748,0.255,0.494)	(0.811,0.312,0.495)	(0.799,0.289,0.503)	(0.765,0.279,0.491)	(0.804,0.320,0.502)
O (24)	(0.992,0.041,0.634)	(0.992,0.052,0.633)	(0.001,0.036,0.633)	(0.979,0.013,0.627)	(0.961,0.962,0.622)	(0.024,0.063,0.628)	(0.962,0.962,0.625)

Geometrical phase analyses (GPA)<sup>13</sup> of STEM-HAADF data was used to map the strain state of the system, using a probe corrected FEI TITAN 80-300 on "year 0" (Fig. 1, 2 and 3 in

article) and a double corrected JEM-ARM 200F on "year 1.5" (Fig. 4 in article). The STEM data was acquired with the fast scan direction parallel to the direction we wanted to analyze the strain. For example, for the out-of-plane strain analyses the fast scan direction was parallel to the out-of-plane direction (001). This to avoid scan distortions in the slow scan direction introducing artifacts in the GPA. No drift correction was used, since the sample had little drift in the acquisition period. The GPA was done with the software "GPA for DigitalMicrograph"<sup>14</sup>, using the SrTiO<sub>3</sub> (STO) substrate as a reference. The average strain, as shown in Fig. 3c in the article, was found by taking the mean in the in-plane direction of the strain map. In the substrate, far away from the interface, we have standard STO bulk lattice parameter. To calculate the uncertainty of the average strain, the standard deviation of the average strain in this region is used. Which gives an uncertainty of 0.17%.

## References

- <sup>1</sup> P. E. Blochl, *Phys. Rev. B* **50** (24), 17953 (1994).
- <sup>2</sup> G. Kresse and D. Joubert, *Phys. Rev. B* **59** (3), 1758 (1999).
- <sup>3</sup> G. Kresse and J. Furthmuller, *Comput. Mater. Sci.* **6** (1), 15 (1996).
- <sup>4</sup> G. Kresse and J. Furthmuller, *Phys. Rev. B* **54** (16), 11169 (1996).
- <sup>5</sup> G. Kresse and J. Hafner, *Phys. Rev. B* **47** (1), 558 (1993).
- <sup>6</sup> G. Kresse and J. Hafner, *Phys. Rev. B* **49** (20), 14251 (1994).
- <sup>7</sup> J. P. Perdew, A. Ruzsinszky, G. I. Csonka, O. A. Vydrov, G. E. Scuseria, L. A. Constantin, X. L. Zhou, and K. Burke, *Physical Review Letters* **100** (13) (2008).
- <sup>8</sup> V. I. Anisimov, J. Zaanen, and O. K. Andersen, *Phys. Rev. B* **44** (3), 943 (1991).
- <sup>9</sup> S. L. Dudarev, G. A. Botton, S. Y. Savrasov, C. J. Humphreys, and A. P. Sutton, *Phys. Rev. B* **57** (3), 1505 (1998).
- <sup>10</sup> U. Aschauer, R. Pfenninger, S. M. Selbach, T. Grande, and N. A. Spaldin, *Phys. Rev. B* **88** (5) (2013).
- <sup>11</sup> R. L. Johnson-Wilke, D. Marincel, S. Zhu, M. P. Warusawithana, A. Hatt, J. Sayre, K. T. Delaney, R. Engel-Herbert, C. M. Schlepuetz, J. W. Kim, V. Gopalan, N. A. Spaldin, D. G. Schlom, P. J. Ryan, and S. Trolor-McKinstry, *Phys. Rev. B* **88** (17) (2013).
- <sup>12</sup> Koichi Momma and Fujio Izumi, *Journal of Applied Crystallography* **44**, 1272 (2011).
- <sup>13</sup> M.J. Hytch, E. Snoeck, and R. Kilaas, *Ultramicroscopy* **74**, 131 (1998)
- <sup>14</sup> <http://www.hremresearch.com/Eng/plugin/GPAEng.html>

---

# Spatially Confined Spin Polarization and Magnetic Sublattice Control in (La,Sr)MnO<sub>3-δ</sub> Thin Films by Oxygen Vacancy Ordering

M. Moreau, S. M. Selbach and T. Tybell.

Published in Scientific Reports **7**, 4386 (2017)

DOI: <http://dx.doi.org/10.1038/s41598-017-04103-y>






# SCIENTIFIC REPORTS

OPEN

## Spatially Confined Spin Polarization and magnetic sublattice control in (La,Sr)MnO<sub>3-δ</sub> Thin Films by Oxygen Vacancy Ordering

Magnus Moreau<sup>1</sup>, Sverre M. Selbach<sup>2</sup> & Thomas Tybell<sup>1</sup> 

Received: 8 July 2015  
Accepted: 10 May 2017  
Published online: 29 June 2017

Perovskite oxides are known for their strong structure property coupling and functional properties such as ferromagnetism, ferroelectricity and high temperature superconductivity. While the effect of ordered cation vacancies on functional properties have been much studied, the possibility of tuning the functionality through anion vacancy ordering has received much less attention. Oxygen vacancies in ferromagnetic La<sub>0.7</sub>Sr<sub>0.3</sub>MnO<sub>3-δ</sub> thin films have recently been shown to accumulate close to interfaces and form a brownmillerite structure (ABO<sub>2.5</sub>). This structure has alternating oxygen octahedral and tetrahedral layers along the stacking direction, making it a basis for a family of ordered anion defect controlled materials. We use density functional theory to study how structure and properties depend on oxygen stoichiometry, relying on a block-by-block approach by including additional octahedral layers in-between each tetrahedral layer. It is found that the magnetic and electronic structures follow the layers enforced by the ordered oxygen vacancies. This results in spatially confined electronic conduction in the octahedral layers, and decoupling of the magnetic sub-lattices in the octahedral and tetrahedral layers. These results demonstrate that anion defect engineering is a promising tool to tune the properties of functional oxides, adding a new avenue for developing functional oxide device technology.

The ABO<sub>3</sub> perovskite structure is prone to changes in stoichiometry, and recently there has been considerable interest in layered perovskite-derived structures like the Ruddlesden-Popper, Aurivillius and Dion-Jacobson families with cation ordering<sup>1–3</sup>. Layering enforces anisotropic properties in the materials by decoupling the octahedral building blocks, and enabling functional properties such as ferroelectricity<sup>4</sup>, ferromagnetism<sup>5</sup>, and superconductivity<sup>6</sup>, making them interesting for novel device applications such as tunable microwave filters and optoelectronic components<sup>7,8</sup>. Interfaces between, or superlattices of, perovskites has also been used to confine electrons into 2 dimensions resulting in a 2-dimensional electron gas, where the most studied system is the LaAlO<sub>3</sub>/SrTiO<sub>3</sub> (LAO/STO) interface<sup>7–9</sup>. Combining spin polarization with 2-dimensional conductivity is interesting both on a fundamental level as well as for spintronic applications<sup>10</sup>. Such realizations have been achieved in various superlattice configurations such as LaMnO<sub>3</sub>/SrMnO<sub>3</sub><sup>11–13</sup>, LaAlO<sub>3</sub>/SrMnO<sub>3</sub><sup>14</sup>, and SrTiO<sub>3</sub>/SrRuO<sub>3</sub><sup>15</sup>.

While most of these studies have been on the ordering of cations and cation vacancies, anion vacancy ordering has recently been demonstrated as a route for altering the properties of thin films<sup>16,17</sup>. Further it has been shown experimentally that it is possible to order anion vacancies in layers in thin films of ferromagnetic (La,Sr)MnO<sub>3-δ</sub> (LSMO), e.g. in a brownmillerite structure with ABO<sub>2.5</sub> stoichiometry<sup>18–20</sup>, making LSMO a model system for controlling functionality through anion ordering.

Inspired by the possibility to realize layered oxygen vacancy ordered thin films with different stoichiometry<sup>21</sup>, we investigate oxygen vacancy ordering as a tool for controlling the magnetic properties and electronic structure of oxygen deficient LSMO. The brownmillerite structure consists of alternating BO<sub>6</sub> octahedral layers and BO<sub>4</sub> tetrahedral layers along the stacking direction. An increasing number octahedral layers between the oxygen deficient tetrahedral layers is schematically shown in Fig. 1, where the oxygen stoichiometry can be controlled in a block-by-block approach, going from ABO<sub>2.5</sub> with one octahedral and one tetrahedral layer superlattice (1:1), *via*

<sup>1</sup>Department of Electronic Systems, NTNU - Norwegian University of Science and Technology, 7491, Trondheim, Norway. <sup>2</sup>Department of Materials Science and Engineering, NTNU - Norwegian University of Science and Technology, 7491, Trondheim, Norway. Correspondence and requests for materials should be addressed to T.T. (email: thomas.tybell@iet.ntnu.no)

www.nature.com/scientificreports/

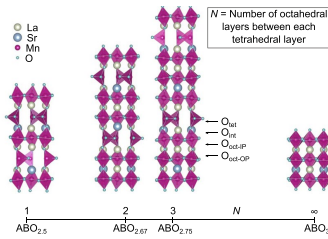


**Figure 1.** The evolution from brownmillerite,  $ABO_{2.5}$ , to perovskite,  $ABO_3$  for  $(La,Sr)MnO_{3-\delta}$  (LSMO). The labels  $O_{oct}$ ,  $O_{oct-IP}$  and  $O_{oct-OP}$  defines the different oxygen positions. Note that there is no  $O_{oct-OP}$  for  $ABO_{2.5}$  and no  $O_{tet}$  and no  $O_{int}$  for  $ABO_3$ .

Spin ordering:	G-type	FM	C-type	A-type
$\Delta E$ [meV/f.u.]	87.1	0	52.5	42.2

**Table 1.** Energy differences of different spin orderings for stoichiometric  $ABO_3$  system.

	$ABO_{2.5}$	$ABO_{2.67}$	$ABO_{2.75}$	$ABO_3$
$Mn_{oct} - O_{oct-IP}$ [Å]	1.958	1.955	1.962	1.962
$Mn_{oct} - O_{oct-OP}$ [Å]	N/A	1.998	1.985	1.957
$Mn_{oct} - O_{int}$ [Å]	2.247	2.159	2.191	N/A
$Mn_{tet} - O_{int}$ [Å]	2.073	2.069	2.065	N/A
$Mn_{int} - O_{int}$ [Å]	1.989	2.000	1.996	N/A
$\angle Mn_{int} - O_{int} - Mn_{int}$ [°]	153.13	157.18	154.95	N/A
$R$ [Å]	4.899	4.923	4.909	N/A
$\Delta$ [ $\times 10^4$ ]	50.639	15.231	13.820	0.9622

**Table 2.** Average Mn-O bond lengths and Mn-O-Mn angles as a function of oxygen stoichiometry, as well as  $R$  and  $\Delta$ . The subscripts are defined in Fig. 1.

$ABO_{2.67}$  and  $ABO_{2.75}$  for 2:1 and 3:1 superlattices, respectively, approaching  $ABO_{3.0}$  for a pure octahedral based thin film<sup>22</sup>. We find that the ordering of oxygen vacancies decouples the magnetic sublattices in the octahedral and tetrahedral layers. Furthermore, a large electronic band gap and low dispersion in the tetrahedral layers results in electron confinement in the octahedral layers.

## Results and Discussion

**Atomic structure.** Before relying on a block-by-block approach to investigate the magnetism, we start by defining the stoichiometric  $ABO_{3.0}$  system and the (1:1)  $ABO_{2.5}$  oxygen deficient system. We lock the in-plane lattice parameters to that of STO, in order to simulate the effect of the substrate on the thin film. For the  $La_{0.75}Sr_{0.25}MnO_3$  system we reproduce the experimentally known ferromagnetic ground state<sup>23</sup>, where the energy difference compared to the most stable antiferromagnetic ordering is 42.3 meV per formula unit (f.u.) as shown in Table 1. For the  $ABO_{2.5}$  system different oxygen vacancy positions within the unit cell were investigated, both oxygen vacancy ordered tetrahedral layers, as well as disordered vacancies throughout the unit cell<sup>16</sup>. The lowest energy is found for the experimentally reported<sup>18–20</sup> antiparallel alignment of the two tetrahedrons as shown in Fig. 1. The ordered oxygen vacancies make up tetrahedral chains that can have either left- of right-handed rotations. There are three symmetry equivalent combinations of these tetrahedral rotation modes, a left-left left-left (LL-LL) with a  $I2bm$ -like symmetry, right-left left-right RL-LR with  $Pbcm$ -like symmetry, or left-left right-right (LL-RR) with  $Pnma$ -like symmetry<sup>24</sup>. For the  $ABO_{2.5}$  system strained to STO we find that the LR-LR tetrahedral chain with  $Pbcm$ -like symmetry is always lowest in energy for any given magnetic ordering. Due to the discrete Sr doping the structural models used in the calculations have  $P1$  symmetry. When investigating the Mn-O bond lengths shown in Table 2, the  $Mn_{oct} - O_{int}$  bond is found to be considerably longer than the other bonds for all values of  $N$ , the number of octahedral layers in-between each tetrahedral layer. However, the  $Mn_{oct} - O_{int}$  bond does not follow a monotonic decreasing trend with increasing oxygen content. As shown in Table 2, it is longer for  $N = 1$  and  $N = 3$  ( $ABO_{2.5}$  and  $ABO_{2.75}$ ) than it is for  $N = 2$  ( $ABO_{2.67}$ ). This is a well-known phenomenon for other layered perovskite system<sup>25</sup>, and is related to the different symmetries exhibited by odd and even numbers of  $N$ , giving rise to different octahedral and tetrahedral rotations. To test this scenario the  $Mn_{oct} - O_{int} - Mn_{int}$  angle, the tetrahedral chain distance  $R$ , and octahedral bond length variation  $\Delta$  as defined by Young and Rondinelli<sup>24</sup> was

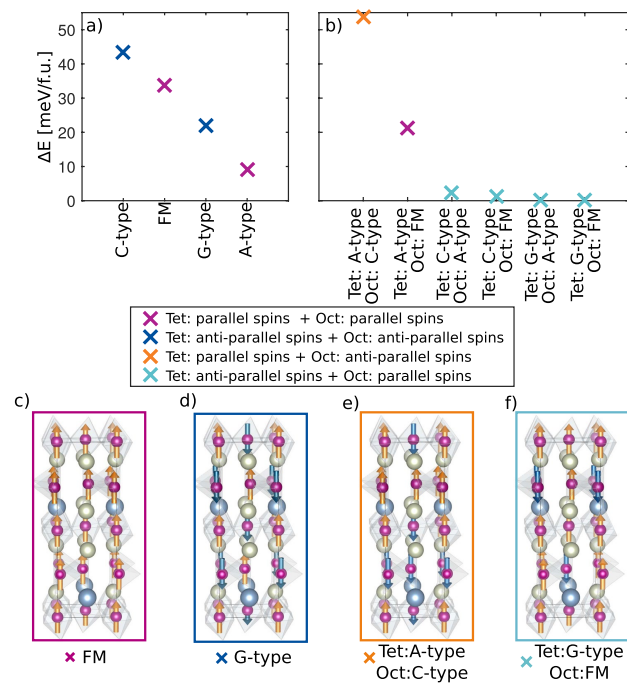


**Figure 2.** (a,b) Energy difference between different magnetic structures in the LSMO brownmillerite cell. (a) Same spin ordering in the entire structure. (b) Different magnetic sublattices in the tetrahedral (Tet) and octahedral (Oct) layers. It is possible to order the magnetic sublattices in four categories, in-plane parallel spins in both octahedral and tetrahedral layers, in-plane anti-parallel spins in both the octahedral and tetrahedral layers, and in-plane parallel spins in only the tetrahedral or only the octahedral layers. The lowest energy is observed when the octahedral layers have in-plane parallel spins and the tetrahedral layers have in-plane anti-parallel spins. (c–f) Depicts one example of spin ordering corresponding to each of the four categories.

also calculated. As shown in Table 2, the data with deviating  $\text{Mn}_{\text{Oct}}\text{-O}_{\text{int}}\text{-Mn}_{\text{Oct}}$  angle and  $R$  value for  $\text{ABO}_{2.5}$  points towards a symmetry induced rotation difference. Still, the longer  $\text{Mn}_{\text{Oct}}\text{-O}_{\text{int}}$  bond length can reduce the coupling between octahedral and tetrahedral layers<sup>1</sup>, and thus enable different magnetic sublattices in these layers.

**Magnetic structure.**  $\text{ABO}_{2.5}$  Next the magnetic ground state of the  $\text{ABO}_{2.5}$  system is established. First it is assumed that the unit cell has a given magnetic order throughout the unit cell, either, ferromagnetic (FM), A-, C- or G-type antiferromagnetic (AFM) order. The total energy for the different spin orderings are shown in (Fig. 2a), revealing that the  $\text{ABO}_{2.5}$  system is prone to A-type AFM ordering. This differs from other brownmillerite oxides, e.g.  $\text{SrCoO}_{2.5}$  which was found to have a G-type AFM ground state<sup>26</sup>.

A-type spin ordering in  $\text{ABO}_{2.5}$  implies anti-parallel spins in the octahedral and tetrahedral layers, in agreement with the possibility of different magnetic sublattices in the octahedral and tetrahedral layers. Motivated by this idea, and that the longer  $\text{Mn}_{\text{Oct}}\text{-O}_{\text{int}}$  can decouple the magnetic sublattices, we investigate the effect of different magnetic sublattices in the various layers. Different magnetic sublattices have also earlier been suggested to explain an anomaly in the magnetic susceptibility of brownmillerite  $\text{CaFeO}_{2.5}$ <sup>27,28</sup>. Parallel ordering of spins in the octahedral layers combined with anti-parallel ordering of spins in the tetrahedral layers are found to be more stable than other configurations with parallel spins in the tetrahedral layers and/or anti-parallel spins octahedral layers, as shown in (Fig. 2b). Hence, by enforcing a parallel spin ordering in the octahedral layers and anti-parallel spins in the tetrahedral layers we get four possible combinations of spin ordering in the investigated brownmillerite unit cell (Fig. 2). For the octahedral layers there are two possibilities; firstly, all octahedral layers can be

parallel, giving a net moment to the unit cell; or secondly, every second octahedral layer can be anti-parallel in an A-type like AFM ordering between the octahedral layers, resulting in no net moment. There are also two possibilities in the tetrahedral layers, C- and G-type AFM ordering. For C-type AFM ordering each tetrahedral layer has the same configuration, while for G-type AFM every second tetrahedral layer have opposite spin directions. Note that an A-type like order in the tetrahedral layers is not favored as A-type order has parallel spins within one tetrahedral layer. As shown in (Fig. 2b), the energy differences between these four spin orderings are small, less than 1 meV/f.u., and thus in the order of the resolution limit of density functional theory (DFT) calculations. However, the calculations clearly show that the layered magnetic structures are considerably lower in energy as compared to a homogeneous magnetic ground state, e.g. 9.3 meV/f.u. The ordering of the tetrahedral chains considered only weakly influences the magnetic ground state (See Supplementary Note 2 and Figure S1), with parallel spins in the octahedral layers and antiparallel spins in the tetrahedral layers being the most stable. For STO strained  $\text{ABO}_{2.5}$ , independent of the tetrahedral chain ordering, the most stable spin structure is ferromagnetic order in octahedral layers and G-type antiferromagnetic order in tetrahedral layers.

As shown by Mitra *et al.*<sup>26</sup>, the magnetic ground state can be explained by only including magnetic nearest neighbor interactions. For the system investigated, this means that the octahedrons will only interact with the other octahedrons within the same layer and the closest tetrahedral layers. Assuming that the coupling from one octahedral (tetrahedral) layer to another, through a tetrahedral (octahedral) layer, is low, the magnetic interaction between an octahedral layer and either G- or C-like AFM ordered tetrahedral layer is similar in energy, as shown in Fig. 2. This can be rationalized from the spin structure, as both G- and C-type AFM tetrahedral layers have the same ratio of aligned/non-aligned spins adjacent to the octahedral layers, independent of the spin polarization direction in the octahedral layers. The magnetic coupling can depend on the Mn oxidation state. With the Sr doping investigated here, the average Mn oxidation state is +2.25 for the  $\text{ABO}_{2.5}$  system. Analyzing the magnetic moment of each site, we find that all of the tetrahedral sites have an oxidation state of +2, while half of the octahedral sites have a +2 state and the other half a +3 state. Using this to calculate the magnetic interaction parameters,  $J$ , we find that the least squares solution to the over-determined equation set based on the energies shown in Fig. 2 gives ferromagnetic coupling between two octahedrally coordinated Mn ions with  $J_{\text{Oct-Oct}} = 6.20$  meV, and antiferromagnetic coupling between two tetrahedrally coordinated Mn ions with  $J_{\text{Tet-Tet}} = -3.49$  meV. This is in agreement with two different magnetic sublattices in the octahedral and tetrahedral layers having parallel spins in each octahedral layer and anti-parallel spins in each tetrahedral layer.

**$\text{ABO}_{2.67}$  and  $\text{ABO}_{2.75}$ .** Having established the magnetic ground state for the 1:1  $\text{ABO}_{2.5}$ , the effect of the oxygen stoichiometry is investigated by increasing  $N$ . Based on the results for  $N=1$  ( $\text{ABO}_{2.5}$ ) and  $N=\infty$  ( $\text{ABO}_3$ ), we focus on the case with different magnetic sublattices in the octahedral and tetrahedral layers, where each octahedral layer have parallel spins and each tetrahedral layer have an antiferromagnetic ordering. The octahedral layers can all be polarized in the same direction giving a net moment; or every second or third octahedral layer can be polarized oppositely, called double or triple A-type for  $\text{ABO}_{2.67}$  and  $\text{ABO}_{2.75}$ , respectively, resulting in no net moment. By the same arguments used for  $N=1$ , C-type and G-type AFM ordering are possible for the tetrahedral layers, resulting in four different combinations of in-plane parallel spin ordering in the octahedral layers and in-plane anti-parallel spin orderings in the tetrahedral layers. As shown in Fig. 3, the energy differences between these possible spin configurations are small, both for the case of  $N=2$  ( $\text{ABO}_{2.67}$ ) and  $N=3$  ( $\text{ABO}_{2.75}$ ). Similar to the  $N=1$  ( $\text{ABO}_{2.5}$ ), any combination of parallel ordering in the octahedral layers and anti-parallel in the tetrahedral layers are considerably lower in energy than a pure FM state. For  $N=2$ ,  $\text{ABO}_{2.67}$ , the lowest energy is found for the magnetic structure with double A-type octahedral layers and C-type tetrahedral layers, with an energy difference of 0.54 meV per formula unit compared to the next lowest energy spin ordering (Fig. 3). For  $N=3$ ,  $\text{ABO}_{2.75}$ , the lowest energy is found for triple A-type octahedral layers and G-type ordered tetrahedral layers. Also for the  $N=2$ ,  $\text{ABO}_{2.67}$  there is only a weak dependence of the spin ordering to the tetrahedral chain type, see Supplementary Note 2 and Figure S2.

**Electronic structure.** Next, the electronic properties are correlated with the orbital ordering to rationalize how the magnetic structure evolves with  $N$ , the number of octahedral layers between each tetrahedral layer. The spin up band structure and layer resolved electronic density of states (DOS) are shown in Fig. 4, only the band structure for the spin configurations with the lowest energy of  $\text{ABO}_{2.5}$  and  $\text{ABO}_{2.67}$  are shown, as the band structure of  $\text{ABO}_{2.75}$  is qualitatively similar to that of  $\text{ABO}_{2.67}$ . Further, the only notable difference between the different spin orderings is whether the two different octahedral layers are polarized parallel or anti-parallel. The band structures and DOSes for spin down and  $\text{ABO}_{2.75}$  are shown in Supplementary Note 3. When inspecting the layer resolved DOSes we see that the tetrahedral layers have a band gap of  $\sim 1.5$  eV for all magnetic structures. The octahedral layers display either an indirect band gap of  $\sim 0.5$  eV for  $\text{ABO}_{2.5}$ , or no band gap (metallic) for  $\text{ABO}_{2.67}$  and  $\text{ABO}_{2.75}$ . Furthermore, the band structure has low dispersion perpendicular to the layers compared to the in-plane band directions. Such flat bands perpendicular to the layers imply large effective mass and low electronic mobility out-of-plane compared to in-plane, resulting in strongly anisotropic electronic conductivity<sup>11,29</sup>. With a large band gap only in the tetrahedral layers as well as low dispersion perpendicular to the layers, spin polarized two-dimensional electronic conduction in the octahedral layers is possible: a quasi-2D spin polarized electron gas. We note that, as the top of the conduction band and the bottom of the valence band consists mainly of octahedral states, there are only minute differences in the electronic structure around the Fermi level for different tetrahedral chain orderings.

In order to illustrate the 2D localization of the charge carriers maximally localized Wannier functions<sup>30,31</sup> of the valence band and conduction band of the  $\text{ABO}_{2.5}$  structure are calculated. An iso-surface plot of the maximally localized Wannier function is showed in Fig. 5. The Wannier function has a  $d_{x^2-y^2}$  character and is confined to the octahedral layers. Based on the Wannier function and the projected DOS, the Goodenough-Kanamori

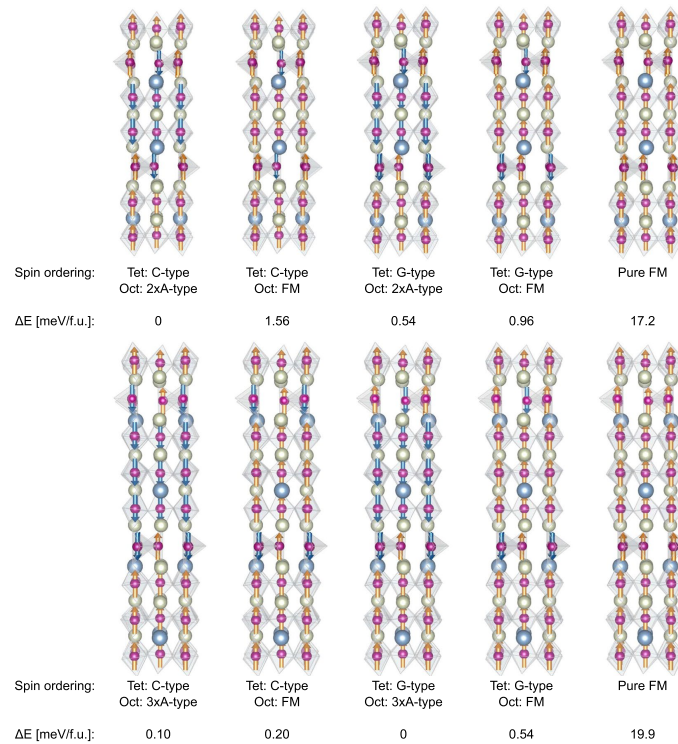


**Figure 3.** Energy difference of the low energy spin orderings, which all have an in-plane anti-parallel spins in the tetrahedral layers and in-plane parallel spins in the octahedral layers. Top: the ABO<sub>2.67</sub> system, bottom: the ABO<sub>2.75</sub> system. Pure ferromagnetic order is included as a reference.

rules<sup>32,33</sup> can explain the spin ordering within in-plane ferromagnetically coupled octahedral sites. With the current Sr doping, half of the octahedral sites have a  $d^5$  ( $Mn^{2+}$ ) state and the other half a  $d^4$  ( $Mn^{3+}$ ) state. Hence the direction of the  $e_g$  orbitals then determines if the interaction is AFM superexchange or FM double exchange. As seen in Figs 4 and 5, the  $d_{x^2-y^2}$  states from  $Mn^{2+}$  are at the top of the valence band, pointing towards the  $Mn^{3+}$  sites which are mainly occupied by  $d_{z^2-r}$  states. Hence, the magnetic coupling between the octahedral layers should be in-plane double exchange and ferromagnetic according to the Goodenough-Kanamori rules. When the number of octahedral layers between each tetrahedral layer increases, an increased mix of  $d_{x^2-y^2}$  and  $d_{z^2-r}$  states at the Fermi level give rise to strong double exchange in each octahedral layer and a metallic state. We note, however, that the Goodenough-Kanamori rules can not be used to determine the exchange type for tetrahedral sites<sup>35</sup>.

**Strain dependence.** Finally, we turn to the possibility to tune the magnetic ground state through epitaxial strain for the case of one octahedral layer between every tetrahedral layer (ABO<sub>2.5</sub>). The energy difference between FM and A-type octahedral layers has an almost linear dependence on in-plane strain, as shown in Fig. 6. The approximate 1% compressive strain resulting from preparing ABO<sub>2.5</sub> (LSMO) on a SrTiO<sub>3</sub> substrate is just on the side where a FM ordering of the octahedral layers is calculated to have slightly lower energy than an AFM ordering of the octahedral layers. However, the energy differences between the different spin states are small and within the uncertainty of the calculations. These small energy differences can also point towards high magnetic susceptibility due to multiple close lying transition temperatures<sup>34</sup>. For increased compressive strain, e.g. from a LaAlO<sub>3</sub> substrate, the FM ordering is more favored, with an energy difference of approximately 0.47 meV per

www.nature.com/scientificreports/

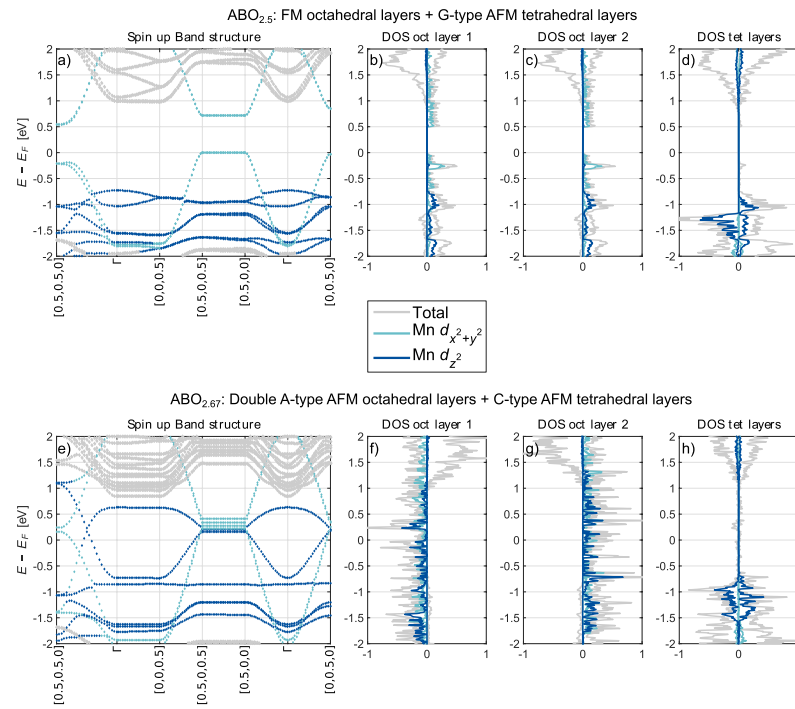


**Figure 4.** Band structure and layer resolved density of states (DOS) for the octahedral and tetrahedral layers of LSMO brownmillerite (a–d)  $ABO_{2.5}$  with ferromagnetic coupling in the octahedral layers and G-type antiferromagnetism in the tetrahedral layers, and (e–h)  $ABO_{2.67}$  with A-type antiferromagnetism in the octahedral layers and C-type antiferromagnetism in the tetrahedral layers. For the bands, the  $k_x$  and  $k_y$  are parallel to the layers, while the  $k_z$  is normal to the layers. The bands and DOS are further projected onto spherical harmonics. The bands where the projection on the Mn:  $d_{x^2-y^2}$  and Mn:  $d_{z^2}$  orbitals on each k-point exceeds 33% are coloured according to the legend; the rest of the points are coloured grey. (b,c), and (f,g) show the projection on the different octahedral layers for  $ABO_{2.5}$  and  $ABO_{2.67}$  respectively (DOS oct layer), while (d) and (h) shows the sum of both tetrahedral layers (DOS tet layer).

formula unit. If a tensile strain is applied, e.g. approximately 3%, AFM ordering of the octahedral layers is favored, with an energy difference of 0.23 meV per formula unit, compared to the lowest energy FM coupling between the octahedral layers. The energy difference between FM and AFM coupled octahedral layers shows a linear positive response to in-plane strain (Fig. 6b), indicating that antiferromagnetic coupling from one octahedral layer to another increases when the out-of-plane lattice parameter decreases. These results point to the possibility of using strain to engineer also the magnetic properties in materials with ordered oxygen vacancies<sup>35–37</sup>.

### Conclusion

Layered ordering of vacancies in anion deficient perovskite structures is a novel route to induce anisotropic properties similar to what can be achieved with cation vacancies in the Ruddlesden-Popper, Aurivillius and Dion-Jacobson families. For LSMO we show that these oxygen deficient systems are prone to show an in-plane spin coupling that is dominating the out-of-plane coupling. The in-plane coupling in the octahedral layers is shown to be ferromagnetic, while for the tetrahedral layers the in-plane coupling is antiferromagnetic. Different combinations of in-plane FM octahedral layers and AFM tetrahedral layers are close in energy and should thus be tunable through external means such as epitaxial strain, chemical doping or applied magnetic field. As the band

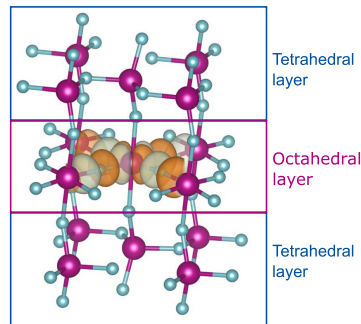


**Figure 5.** Iso-surface plot of the maximally localized Wannier functions for the valence band of the LSMO  $ABO_3$  structure centered on octahedrally coordinated Mn. Positive isosurfaces are coloured orange while negative isosurfaces are green. The iso-surface level is set to 1.

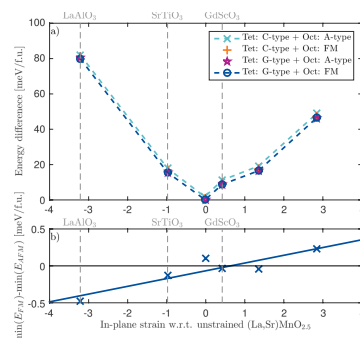


**Figure 6.** (a) Energy difference as a function of in-plane strain for the four low energy magnetic structures. Note that the evolution around the zero strain point deviates from the expected parabolic shape because here the in-plane lattice vectors are no longer equal. The dashed coloured lines are guides to the eye, while the grey vertical lines represent the strain from some commercially available substrates. (b) Energy difference between the lowest ferromagnetic structure and the lowest antiferromagnetic structure in (La, Sr)  $MnO_{2.5}$  brownmillerite as a function of in-plane strain. Positive values mean that the structures where the octahedrons are A-type antiferromagnetic (AFM) coupled have the lowest energy, while negative values means that ferromagnetic (FM) coupling of the octahedrons are favored, the solid line correspond to a linear fit to the data.

gap in the tetrahedral layers is 1.5 eV, and the system exhibit flat bands perpendicular to the layering direction, a confined spin polarized conduction can be foreseen in the octahedral layers, where the band gap is zero with significant band dispersion along in-plane directions. These results point to the possibility to rely on anion ordering to control functional properties for device applications.

#### Methods

The DFT calculations were performed with the Projector Augmented Wave (PAW)<sup>38,39</sup> method as implemented in the Vienna Ab-initio Simulation Package (VASP)<sup>39,40</sup>, with the Perdew-Burke-Ernzerhof generalized gradient approximation for solids (PBEsol)<sup>41</sup>. The plane wave cutoff energy was set to 550 eV and PAW-potentials with 11, 10, 15 and 6 valence electrons were used for La, Sr, Mn and O, respectively. GGA + U (Dudarev *et al.*<sup>42</sup>) was used with  $U = 3$  eV for Mn 3d and  $U = 10$  eV for La 4f states<sup>37,43,44</sup>. For stoichiometric LSMO we used a 40 atom  $La_6Sr_2Mn_6O_{24}$  cell with a  $4 \times 4 \times 4$   $\Gamma$ -centered k-point mesh to sample the Brillouin zone, with corresponding k-point densities for oxygen deficient cells. The Sr atoms were distributed evenly across the unit cell, and different



www.nature.com/scientificreports/

possible distributions were tested. Biaxial strain was simulated by fixing the in-plane lattice parameter to those calculated for the respective substrates, while the out of plane lattice parameter was allowed to relax. Atomic positions and lattice vectors were relaxed until the Hellmann-Feynman forces on the ions were below 0.01 eV/Å. Maximally localized Wannier functions were calculated from the DFT-Bloch functions with the wannier90 code<sup>30,31,45</sup>. For a more detailed description of the calculation details, please see Supplementary Note 1.

## References

- Balachandran, P. V. & Rondinelli, J. M. Massive Band Gap Variation in Layered Oxides through Cation Ordering. *Nat. Commun.* **6**, 6191 (2015).
- Rijnders, G. Oxide Heterostructures: Atoms on the Move. *Nat. Mater.* **13**, 844–845 (2014).
- Mulder, A. T., Benedek, N. A., Rondinelli, J. M. & Fennie, C. J. Turning ABO<sub>3</sub> Antiferroelectrics into Ferroelectrics: Design Rules for Practical Rotation-Driven Ferroelectricity in Double Perovskites and A<sub>2</sub>B<sub>2</sub>O<sub>7</sub> Ruddlesden-Popper Compounds. *Adv. Funct. Mater.* **23**, 4810–4820 (2013).
- Battle, P. D. *et al.* Layered Ruddlesden–Popper Manganese Oxides: Synthesis and Cation Ordering. *Chem. Mater.* **9**, 552–559 (1997).
- Ishida, K. *et al.* Spin-Triplet Superconductivity in Sr<sub>2</sub>RuO<sub>4</sub> Identified by 17O Knight Shift. *Nature* **396**, 658–660 (1998).
- Lee, C.-H. *et al.* Exploiting Dimensionality and Defect Mitigation to create Tunable Microwave Dielectrics. *Nature* **502**, 532–536 (2013).
- Ohno, A. & Hwang, H. Y. A High-Mobility Electron Gas at the LaAlO<sub>3</sub>/SrTiO<sub>3</sub> Heterointerface. *Nature* **427**, 423–426 (2004).
- Thiel, S., Hammerl, G., Schmehl, A., Schneider, C. W. & Mannhart, J. Tunable Quasi-Two-Dimensional Electron Gases in Oxide Heterostructures. *Science* **313**, 1942–1945 (2006).
- Xie, Y., Bell, C., Yajima, T., Hikita, Y. & Hwang, H. Y. Charge Writing at the LaAlO<sub>3</sub>/SrTiO<sub>3</sub> Surface. *Nano Lett.* **10**, 2588–2591 (2010).
- Zutić, L., Fabian, J. & Das Sarma, S. Spintronics: Fundamentals and Applications. *Rev. Mod. Phys.* **76**, 323–410 (2004).
- Nanda, B. R. K. & Satpathy, S. Spin-Polarized Two-Dimensional Electron Gas at Oxide Interfaces. *Phys. Rev. Lett.* **101**, 127201 (2008).
- Nanda, B. R. K. & Satpathy, S. Electronic and Magnetic Structure of the (LaMnO<sub>3</sub>)<sub>2n</sub>/(SrMnO<sub>3</sub>)<sub>n</sub> Superlattices. *Phys. Rev. B* **79**, 054428 (2009).
- Nanda, B. R. K. & Satpathy, S. Polar Catastrophe, Electron Leakage, and Magnetic Ordering at the LaMnO<sub>3</sub>/SrMnO<sub>3</sub> Interface. *Phys. Rev. B* **81**, 224408 (2010).
- Hou, F., Cai, T.-Y., Ju, S. & Shen, M.-R. Half-Metallic Ferromagnetism via the Interface Electronic Reconstruction in LaAlO<sub>3</sub>/SrMnO<sub>3</sub> Nanosheet Superlattices. *ACS Nano* **6**, 8552–8562 (2012).
- Verissimo-Alves, M., Garcia-Fernandez, P., Bilc, D. I., Ghosez, P. & Junquera, J. Highly Confined Spin-Polarized Two-Dimensional Electron Gas in SrTiO<sub>3</sub>/SrRuO<sub>3</sub> Superlattices. *Phys. Rev. Lett.* **108**, 107003 (2012).
- Kalinin, S. V., Borisevich, A. & Fong, D. Beyond Condensed Matter Physics on the Nanoscale: The Role of Ionic and Electrochemical Phenomena in the Physical Functionalities of Oxide Materials. *ACS Nano* **6**, 10423–10437 (2012).
- Aschauer, U., Pfenninger, R., Selbach, S. M., Grande, T. & Spaldin, N. A. Strain-Controlled Oxygen Vacancy Formation and Ordering in CaMnO<sub>3</sub>. *Phys. Rev. B* **88**, 054111 (2013).
- Nord, M. *et al.* Structural Phases Driven by Oxygen Vacancies at the La<sub>0.7</sub>Sr<sub>0.3</sub>MnO<sub>3</sub>/SrTiO<sub>3</sub> Hetero-Interface. *Appl. Phys. Lett.* **106**, 041604 (2015).
- Ferguson, J. D. *et al.* Epitaxial Oxygen Getter for a Brownmillerite Phase Transformation in Manganite Films. *Adv. Mat.* **23**, 1226–1230 (2011).
- Yao, L. *et al.* Electron-Beam-Induced Perovskite–Brownmillerite–Perovskite Structural Phase Transitions in Epitaxial La<sub>0.7</sub>Sr<sub>0.3</sub>MnO<sub>3</sub> Films. *Adv. Mat.* **26**, 2789–2793 (2014).
- Mehta, V. *et al.* Long-Range Ferromagnetic Order in LaCoO<sub>3</sub> Epitaxial Films due to the Interplay of Epitaxial Strain and Oxygen Vacancy Ordering. *Phys. Rev. B* **91**, 144418 (2015).
- Zhang, G. & Smyth, D. Defects and Transport of the Brownmillerite Oxides with High Oxygen Ion Conductivity—Ba<sub>2</sub>In<sub>2</sub>O<sub>7</sub>. *Solid State Ionics* **82**, 161–172 (1995).
- Hemberger, J. *et al.* Structural, Magnetic, and Electrical Properties of Single-Crystalline La<sub>1-x</sub>Sr<sub>x</sub>MnO<sub>3</sub> (0.4 < x < 0.85). *Phys. Rev. B* **66**, 094410 (2002).
- Young, J. & Rondinelli, J. M. Crystal structure and electronic properties of bulk and thin film brownmillerite oxides. *Phys. Rev. B* **92**, 174111 (2015).
- Aleksandrov, K. S. & Bartolome, J. Octahedral tilt phases in perovskite-like crystals with slabs containing an even number of octahedral layers. *J. Phys.: Condens. Matter* **6**, 8219 (1994).
- Chandrima, M., Randy, S. E., Satoshi, O., Ho Nyung, L. & Fernando, A. R. Ground-State and Spin-Wave Dynamics in Brownmillerite SrCoO<sub>2.5</sub>—a Combined Hybrid Functional and LSDA + U Study. *J. Phys.: Condens. Matter* **26**, 036004 (2014).
- Auckett, J. E. *et al.* Neutron Laue Diffraction Study of the Complex Low-Temperature Magnetic Behaviour of Brownmillerite-Type Ca<sub>2</sub>Fe<sub>2</sub>O<sub>7</sub>. *J. Appl. Crystallogr.* **48**, 273–279 (2015).
- Marchukov, P. *et al.* Static Magnetic Properties of the Many-Sublattice Antiferromagnet Ca<sub>2</sub>Fe<sub>2</sub>O<sub>7</sub>. *Phys. Rev. B* **48**, 13538–13546 (1993).
- Pickett, W., Cohen, R. & Krakauer, H. Precise Band Structure and Fermi-Surface Calculation for YBa<sub>2</sub>Cu<sub>3</sub>O<sub>7</sub>: Importance of Three-Dimensional Dispersion. *Phys. Rev. B* **42**, 8764–8767 (1990).
- Marzari, N. & Vanderbilt, D. Maximally Localized Generalized Wannier Functions for Composite Energy Bands. *Phys. Rev. B* **56**, 12847–12865 (1997).
- Souza, I., Marzari, N. & Vanderbilt, D. Maximally Localized Wannier Functions for Entangled Energy Bands. *Phys. Rev. B* **65**, 035109 (2001).
- Goodenough, J. B. *Magnetism and the chemical bond*. (Interscience Publishers, 1963).
- Kanamori, J. Superexchange Interaction and Symmetry Properties of Electron Orbitals. *J. Phys. Chem. Solids* **10**, 87–98 (1959).
- Moriya, T. Nuclear Magnetic Relaxation near the Curie Temperature. *Prog. Theor. Phys.* **28**, 371–400 (1962).
- Rondinelli, J. M. & Spaldin, N. A. Structure and Properties of Functional Oxide Thin Films: Insights From Electronic-Structure Calculations. *Adv. Mat.* **23**, 3363–3381 (2011).
- Lee, J. H. & Rabe, K. M. Epitaxial-Strain-Induced Multiferroicity in SrMnO<sub>3</sub> from First Principles. *Phys. Rev. Lett.* **104**, 207204 (2010).
- Bhattacharjee, S., Bousquet, E. & Ghosez, P. Engineering Multiferroism in CaMnO<sub>3</sub>. *Phys. Rev. Lett.* **102**, 117602 (2009).
- Bloch, P. E. Projector Augmented-Wave Method. *Phys. Rev. B* **50**, 17953–17979 (1994).
- Kresse, G. & Joubert, D. From ultrasoft pseudopotentials to the projector augmented-wave method. *Phys. Rev. B* **59**, 1758–1775 (1999).
- Kresse, G. & Furthmüller, J. Efficient Iterative Schemes for Ab Initio Total-Energy Calculations Using a Plane-Wave Basis Set. *Phys. Rev. B* **54**, 11169–11186 (1996).
- Perdew, J. P. *et al.* Restoring the Density-Gradient Expansion for Exchange in Solids and Surfaces. *Phys. Rev. Lett.* **100**, 134606 (2008).

42. Dudarev, S. L., Botton, G. A., Savrasov, S. Y., Humphreys, C. J. & Sutton, A. P. Electron-Energy-Loss Spectra and the Structural Stability of Nickel Oxide: An LSDA + U Study. *Phys. Rev. B* **57**, 1505–1509 (1998).
43. Pavone, M., Muñoz-García, A. B., Ritzmann, A. M. & Carter, E. A. First-Principles Study of Lanthanum Strontium Manganite: Insights into Electronic Structure and Oxygen Vacancy Formation. *J. Phys. Chem. C* **118**, 13346–13356 (2014).
44. Johnson-Wilke, R. L. *et al.* Quantification of Octahedral Rotations in Strained LaAlO<sub>3</sub> Films via Synchrotron X-ray Diffraction. *Phys. Rev. B* **88**, 174101 (2013).
45. Mostofi, A. A. *et al.* wannier90: A Tool for Obtaining Maximally-Localised Wannier Functions. *Comput. Phys. Commun.* **178**, 685–699 (2008).

#### Acknowledgements

The Norwegian Metacentre for Computational Science (NOTUR) is acknowledged for providing computational resources for DFT-calculations through the project NN9301K.

#### Author Contributions

M.M. performed the D.F.T. calculations. M.M. wrote the main manuscript and all authors reviewed the manuscript. S.M.S. and T.T. initiated and supervised the research.

#### Additional Information

**Supplementary information** accompanies this paper at doi:10.1038/s41598-017-04103-y

**Competing Interests:** The authors declare that they have no competing interests.

**Publisher's note:** Springer Nature remains neutral with regard to jurisdictional claims in published maps and institutional affiliations.



**Open Access** This article is licensed under a Creative Commons Attribution 4.0 International License, which permits use, sharing, adaptation, distribution and reproduction in any medium or format, as long as you give appropriate credit to the original author(s) and the source, provide a link to the Creative Commons license, and indicate if changes were made. The images or other third party material in this article are included in the article's Creative Commons license, unless indicated otherwise in a credit line to the material. If material is not included in the article's Creative Commons license and your intended use is not permitted by statutory regulation or exceeds the permitted use, you will need to obtain permission directly from the copyright holder. To view a copy of this license, visit <http://creativecommons.org/licenses/by/4.0/>.

© The Author(s) 2017

## Spatially Confined Spin Polarization and magnetic sublattice control in (La,Sr)MnO<sub>3-δ</sub> Thin Films by Oxygen Vacancy Ordering

Magnus Moreau,<sup>1</sup> Sverre M. Selbach,<sup>2</sup> and Thomas Tybell<sup>1</sup>, \*

1 Department of Electronics and Telecommunications, NTNU, 7491 Trondheim, Norway

2 Department of Materials Science and Engineering, NTNU, 7491 Trondheim, Norway

\*) Corresponding Author

### Supplementary Note 1: Computational details

The DFT calculations were performed with the Projector Augmented Wave (PAW)<sup>1,2</sup> method as implemented in the Vienna Ab-initio Simulation Package (VASP),<sup>3-6</sup> with the Perdew-Burke-Ernzerhof generalized gradient approximation for solids (PBEsol).<sup>7</sup> The PAW-potentials treating 11 valence electrons for La ( $4s^2 4p^6 5d^1 6s^2$ ), 10 for Sr ( $4s^2 4p^6 5s^2$ ), 15 for Mn ( $3s^2 3p^6 3d^5 4s^2$ ) and 6 for O ( $2s^2 2p^4$ ) supplied with VASP were used. We use the rotational invariant GGA+U approach introduced by Dudarev et al.<sup>8</sup> Tests for different U values were done in the range of 0-5 eV for the Mn 3d electrons, and a value of 3 eV was chosen as this well reproduces the density of states of stoichiometric bulk LSMO, this value has also previously well described manganese oxides with oxygen vacancies<sup>9,10</sup>. Tests for a Hubbard U values in the range 0-12 eV were performed for the La 4f orbitals, and a value of 10 eV was chosen in order to move the 4f states away from the Fermi level<sup>11</sup>. A cutoff energy of 550 eV was used for the plane wave basis set. For stoichiometric LSMO a 40 atoms La<sub>6</sub>Sr<sub>2</sub>Mn<sub>8</sub>O<sub>24</sub> was used with a 4x4x4  $\Gamma$ -centered k-point mesh to sample the Brillouin zone. A 36 atom La<sub>6</sub>Sr<sub>2</sub>Mn<sub>8</sub>O<sub>20</sub> unit cell with a 6x6x2  $\Gamma$ -centered k-point mesh for Brillouin zone was used for calculation of the oxygen deficient structures with general formula ABO<sub>2.5</sub>. For the structures with general formula ABO<sub>2.67</sub> and ABO<sub>2.75</sub> a k-point mesh of 6x6x1 points centered on the  $\Gamma$  point was used, while the unit cell consisted of La<sub>9</sub>Sr<sub>3</sub>Mn<sub>12</sub>O<sub>32</sub> and La<sub>12</sub>Sr<sub>4</sub>Mn<sub>16</sub>O<sub>44</sub> respectively. Different distributions of the Sr atoms were tested, however it did not influence the relative energies of the magnetic orderings, unless all the Sr atoms were clustered in one

corner of the unit cell. To accommodate for the  $Pbcm$ -like symmetry with Left-Right Right-Left (LR-RL) tetrahedral chain order, the cell was doubled along the in-plane b-axis and the number of K-points along this direction was halved. To simulate the epitaxial strain of a substrate, the in plane lattice parameter was fixed in accordance with the equilibrium lattice parameter calculated for the respective substrate, while the out of plane lattice parameter was allowed to relax. The atomic positions and lattice vectors were relaxed until the Hellmann-Feynman forces on the ions were below  $0.01 \text{ eV/\AA}$ . Collinear spins on the Mn ions were assumed for all calculations. These parameters reproduced the experimentally known ferromagnetic ground state of LSMO when strained to a STO substrate (calculated lattice parameter for cubic STO:  $3.896 \text{ \AA}$ ) with a energy difference of  $42 \text{ meV}$  compared to the lowest antiferromagnetic ordering (see supplementary info). The maximally localized Wannier functions were calculated from the DFT-Bloch functions with the wannier90 code.<sup>12-14</sup>

#### Supplementary Note 2: Tetrahedral chain order

As discussed in detail by Young and Rondinelli,<sup>15</sup> the tetrahedral chains can be ordered in three symmetry inequivalent patterns depending on the chirality of the tetrahedral chain rotations. These rotation patterns are left-left left-left (LL-LL) with a  $I2bm$ -like symmetry, right-left left-right RL-LR with  $Pbcm$ -like symmetry or left-left right-right (LL-RR) with  $Pnma$ -like symmetry. As shown in Figure S1, for the  $\text{SrTiO}_3$  strained  $\text{ABO}_{2.5}$  system the RL-LR  $Pbcm$ -like symmetry has the lowest energy,  $\Delta E \approx 5 \text{ meV}$  with respect to the LL-LL  $I2bm$ -like symmetry. However, different tetrahedral chains give an energy cost that is almost independent of the spin ordering. For a given magnetic ordering, the RL-LR tetrahedral chain is always lowest in energy followed by LL-LL ordering and finally the LL-RR, the only exception to this is seen for the C-type ordering, which is high in energy and thus not important for the physical properties. For the  $N = 2 \text{ ABO}_{2.67}$  a similar development of the

tetrahedral chain ordering is found, the lowest energy is for the LL-LL tetrahedral chain pattern. Here we also see that the four different layering magnetic orderings with parallel spins in octahedral layers and anti-parallel spins in the tetrahedral layers, are similar in energy for a given tetrahedral chain pattern.

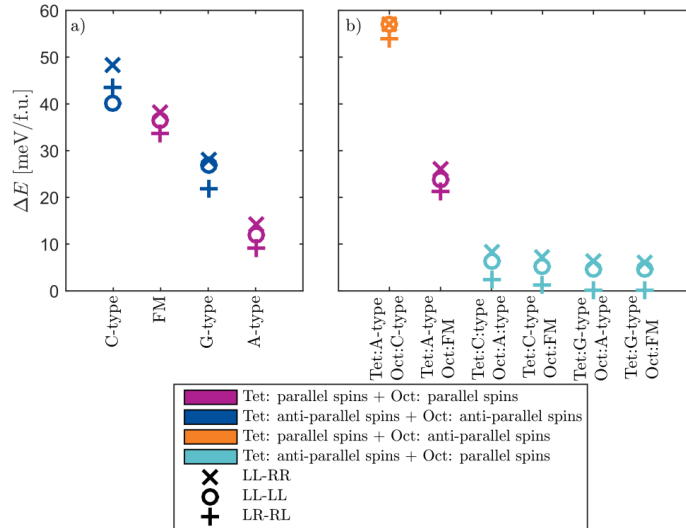


**Figure S1**, Energy difference between the different spin orderings and tetrahedral chains for the SrTiO<sub>3</sub>-strained ABO<sub>2.5</sub> system.

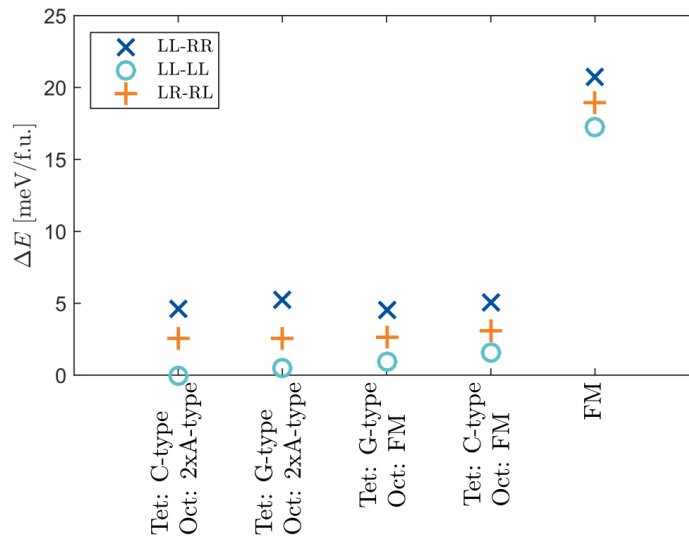
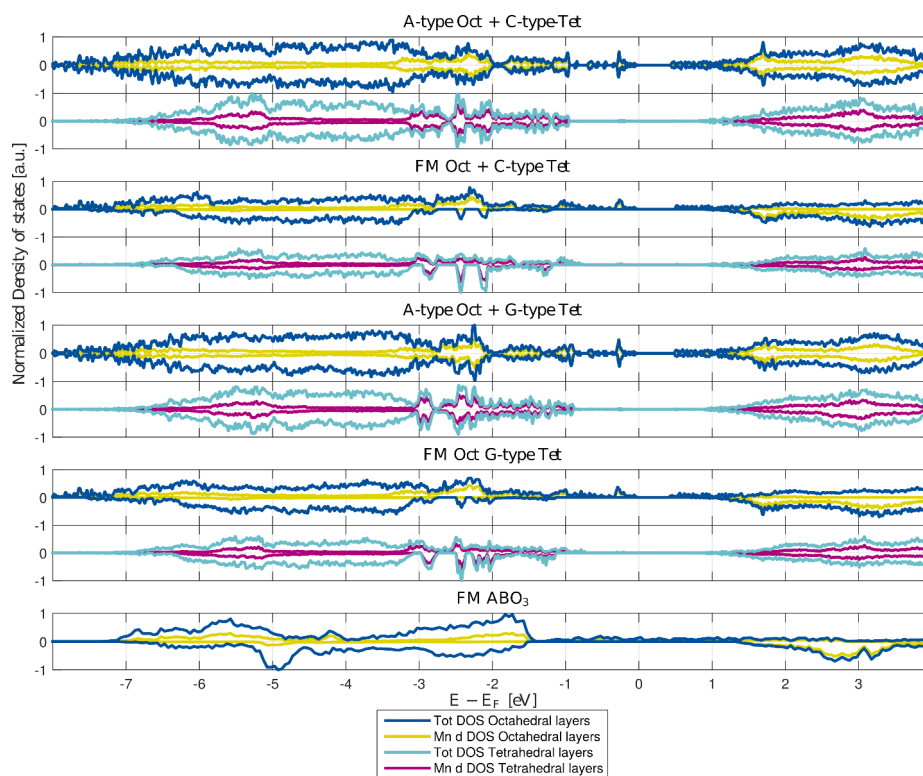


**Figure S2**, energy difference between the four different low lying magnetic orderings with parallel spins in octahedral layers and anti-parallel spins in the tetrahedral layers, and compared to the pure ferromagnetic structure.

**Supplementary Note 3: Electronic structure**

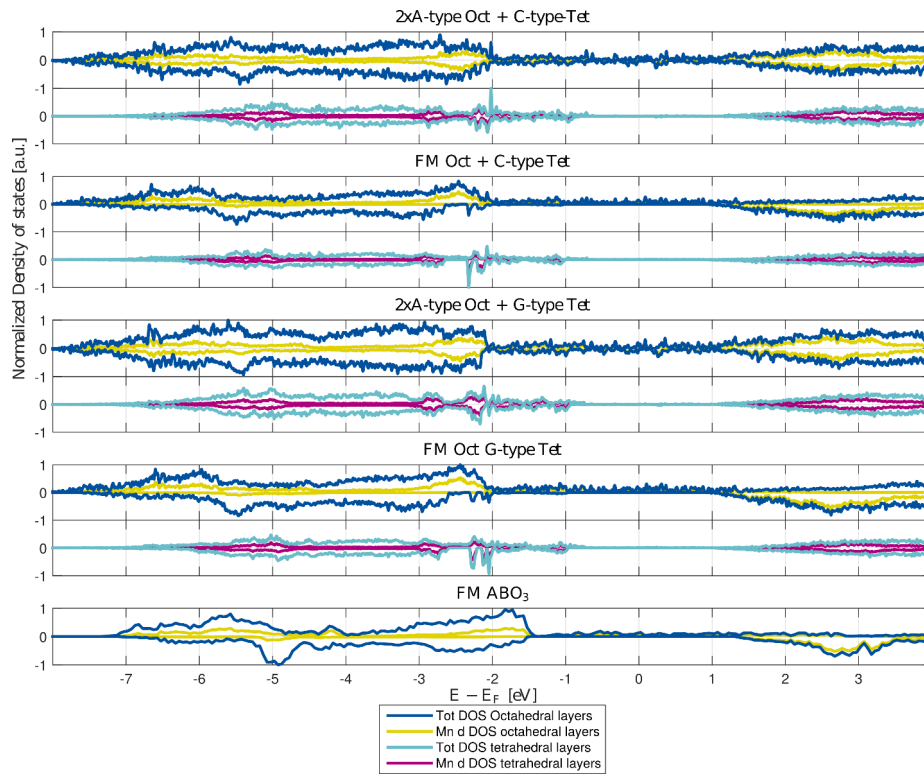
Figure S3 – S5 show the density of states for the four different low energy spin orderings as a function of oxygen stoichiometry. No qualitative change is observed when going from  $\text{ABO}_{2.67}$  to  $\text{ABO}_{2.75}$  as seen in Figure S4 and S5. Further, as shown in figure S5, there are also only small differences between the ferromagnetically coupled octahedral layers in the  $\text{ABO}_{2.75}$  and  $\text{ABO}_3$  system, indicating that 2-3 layers is enough to get bulk like properties between the tetrahedral layers.

Figure S6 and S7 show the band structure for the spin up and spin down bands respectively for the four different low energy spin orderings as a function of oxygen stoichiometry. The figures show that the in-plane confinement of carriers are present for all spin orderings with in-plane parallel spins in the octahedral layers and in-plane antiparallel spins in the tetrahedral layers.



**Figure S3**, DOS for the different low energy spin orderings for  $\text{ABO}_{2.5}$ ,  $\text{ABO}_3$  included as a reference. Note that the two octahedral layers are summed up to one, unlike what is shown in Figure 4 in the main paper.





**Figure S4**, DOS for the different low energy spin orderings for  $ABO_{2.67}$ ,  $ABO_3$  included as a reference. Note that the two octahedral layers are summed up to one, unlike what is shown in Figure 4 in the main paper.

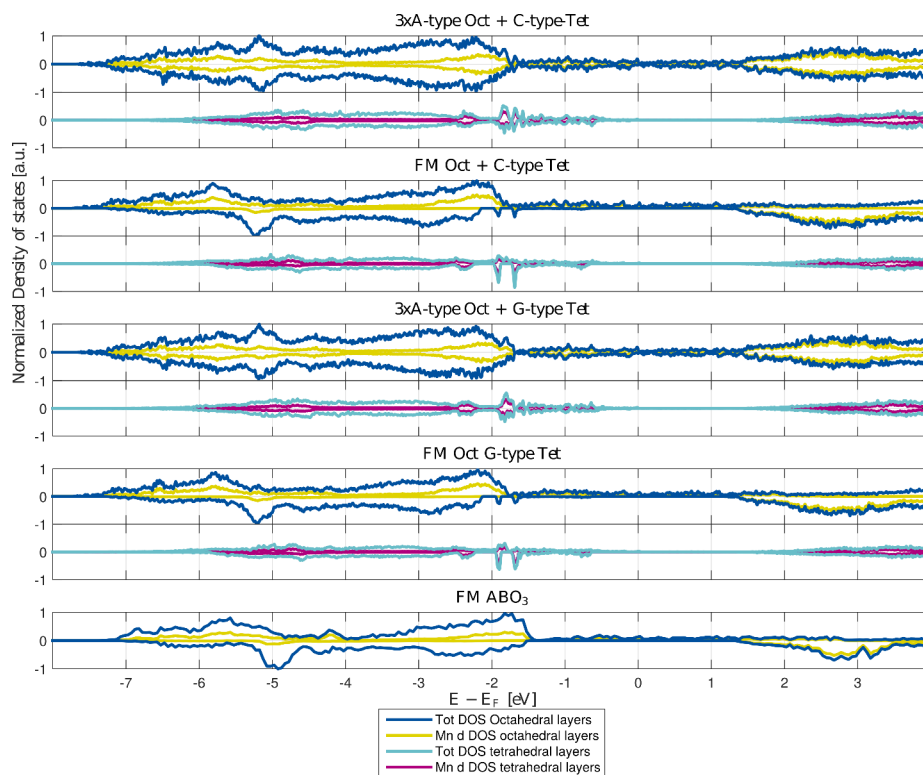


**Figure S5**, DOS for the different low energy spin orderings for  $ABO_{2.75}$ ,  $ABO_3$  included as a reference. Note that the two octahedral layers are summed up to one, unlike what is shown in Figure 4 in the main paper.

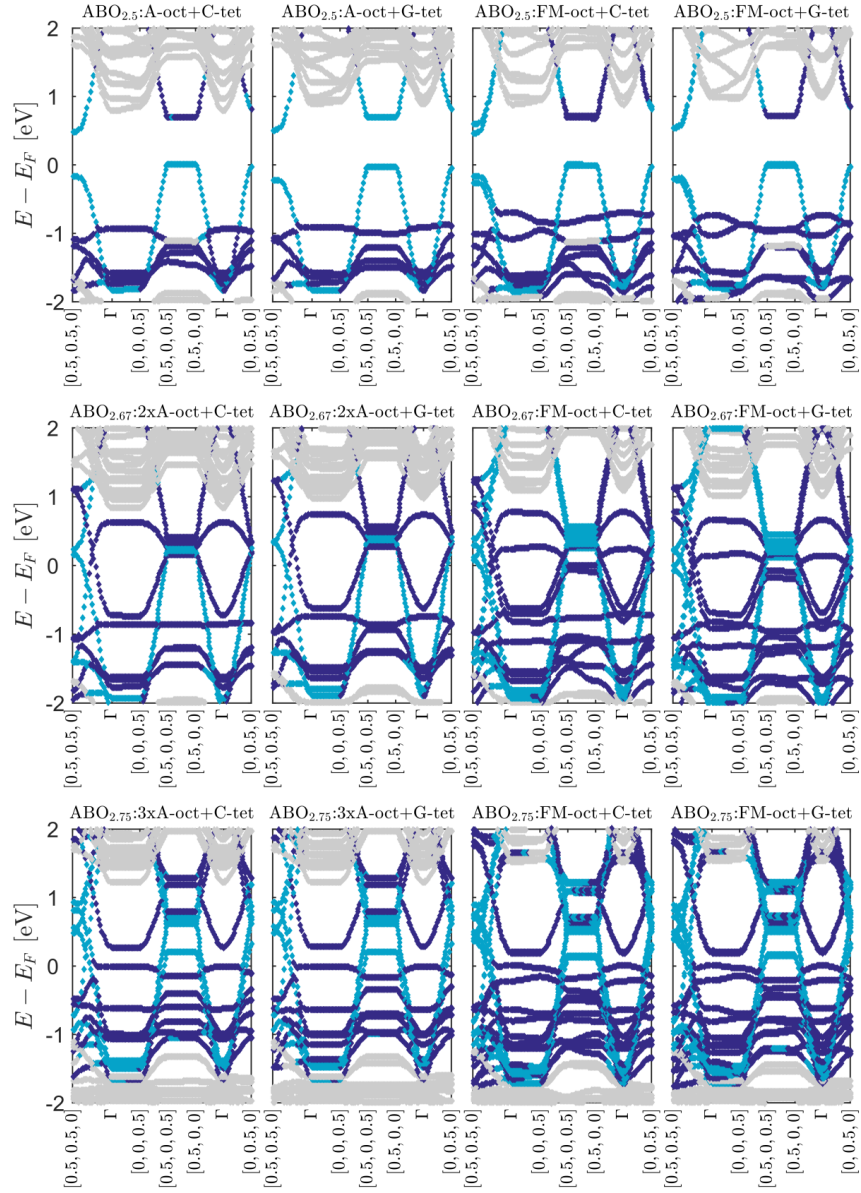


**Figure S6**, Spin up band structure for the different low energy spin orderings as a function of oxygen stoichiometry.

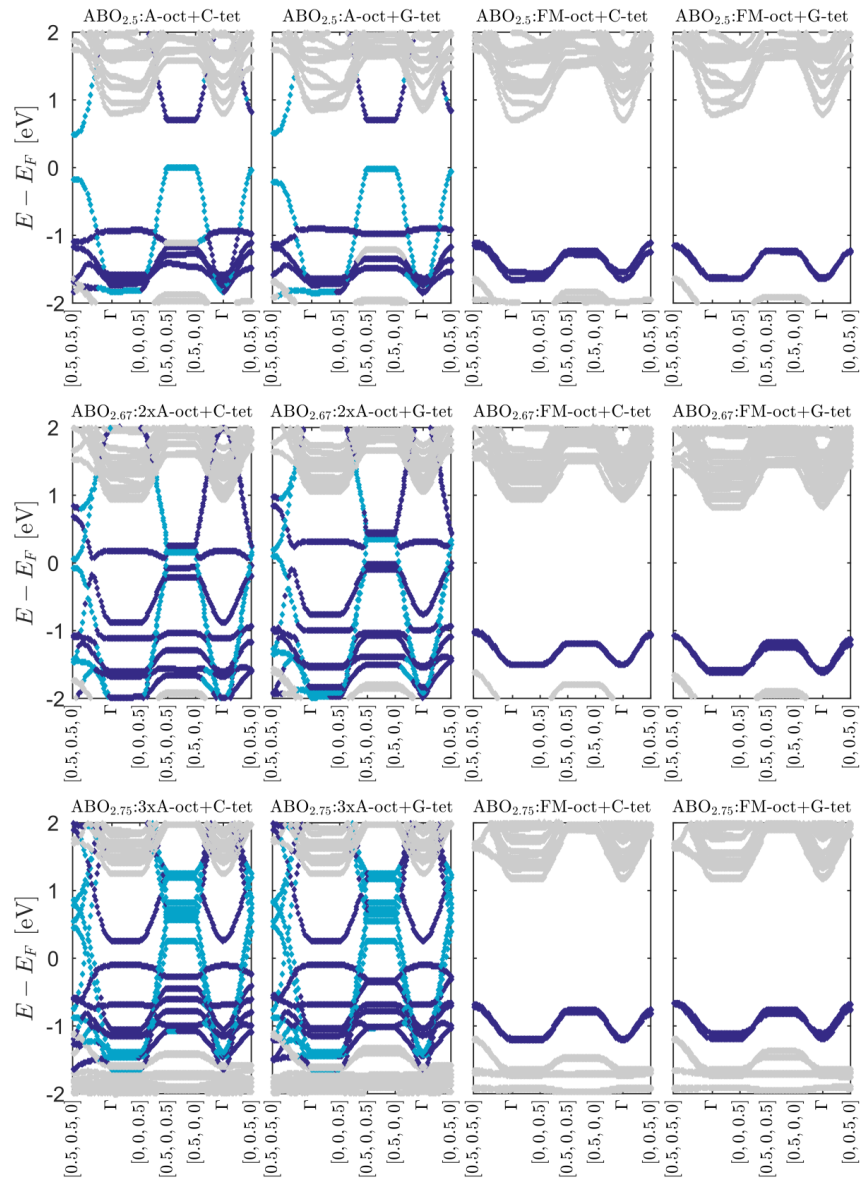


**Figure S7**, Spin down band structure for the different low energy spin orderings as a function of oxygen stoichiometry

**References**

- 1 Bloch, P. E. Projector Augmented-Wave Method. *Phys. Rev. B* **50**, 17953-17979, (1994).
- 2 Kresse, G. & Joubert, D. From Ultrasoft Pseudopotentials to the Projector Augmented-Wave Method. *Phys. Rev. B* **59**, 1758-1775, (1999).
- 3 Kresse, G. & Furthmuller, J. Efficiency of ab-initio total energy calculations for metals and semiconductors using a plane-wave basis set. *Comput. Mater. Sci.* **6**, 15-50, (1996).
- 4 Kresse, G. & Furthmuller, J. Efficient Iterative Schemes for Ab Initio Total-Energy Calculations Using a Plane-Wave Basis Set. *Phys. Rev. B* **54**, 11169-11186, (1996).
- 5 Kresse, G. & Hafner, J. Abinitio molecular-dynamics for liquid-metals *Phys. Rev. B* **47**, 558-561, (1993).
- 6 Kresse, G. & Hafner, J. Ab-initio molecular-dynamics simulation of the liquid-metal amorphous-semiconductor transition in germanium *Phys. Rev. B* **49**, 14251-14269, (1994).
- 7 Perdew, J. P. *et al.* Restoring the Density-Gradient Expansion for Exchange in Solids and Surfaces. *Phys. Rev. Lett.* **100**, 136406, (2008).
- 8 Dudarev, S. L., Botton, G. A., Savrasov, S. Y., Humphreys, C. J. & Sutton, A. P. Electron-Energy-Loss Spectra and the Structural Stability of Nickel Oxide: An LSDA+U Study. *Phys. Rev. B* **57**, 1505-1509, (1998).
- 9 Aschauer, U., Pfenninger, R., Selbach, S. M., Grande, T. & Spaldin, N. A. Strain-Controlled Oxygen Vacancy Formation and Ordering in  $\text{CaMnO}_3$ . *Phys. Rev. B* **88**, 054111, (2013).
- 10 Pavone, M., Muñoz-García, A. B., Ritzmann, A. M. & Carter, E. A. First-Principles Study of Lanthanum Strontium Manganite: Insights into Electronic Structure and Oxygen Vacancy Formation. *J. Phys. Chem. C* **118**, 13346-13356, (2014).
- 11 Johnson-Wilke, R. L. *et al.* Quantification of Octahedral Rotations in Strained  $\text{LaAlO}_3$  Films via Synchrotron X-ray Diffraction. *Phys. Rev. B* **88**, 174101, (2013).
- 12 Souza, I., Marzari, N. & Vanderbilt, D. Maximally Localized Wannier Functions for Entangled Energy Bands. *Phys. Rev. B* **65**, 035109, (2001).
- 13 Mostofi, A. A. *et al.* wannier90: A Tool for Obtaining Maximally-Localised Wannier Functions. *Comput. Phys. Commun.* **178**, 685-699, (2008).
- 14 Marzari, N. & Vanderbilt, D. Maximally Localized Generalized Wannier Functions for Composite Energy Bands. *Phys. Rev. B* **56**, 12847-12865, (1997).
- 15 Young, J. & Rondinelli, J. M. Crystal structure and electronic properties of bulk and thin film brownmillerite oxides. *Phys. Rev. B* **92**, 174111, (2015).
- 16 Momma, K. & Izumi, F. VESTA 3 for Three-Dimensional Visualization of Crystal, Volumetric and Morphology Data. *J. Appl. Crystallogr.* **44**, 1272-1276, (2011).

# **First-principles study of the effect of (111) strain on octahedral rotations and structural phases of $\text{LaAlO}_3$**

M. Moreau, A. Marthinsen, S. M. Selbach and T. Tybell

Published in Physical Review B **95**, 064109 (2017)

DOI: <http://dx.doi.org/10.1103/PhysRevB.95.064109>



## First-principles study of the effect of (111) strain on octahedral rotations and structural phases of $\text{LaAlO}_3$

Magnus Moreau,<sup>1</sup> Astrid Marthinsen,<sup>2</sup> Sverre M. Selbach,<sup>2</sup> and Thomas Tybell<sup>1,\*</sup>

<sup>1</sup>Department of Electronic Systems, NTNU – Norwegian University of Science and Technology, 7491 Trondheim, Norway

<sup>2</sup>Department of Materials Science and Engineering, NTNU – Norwegian University of Science and Technology, 7491 Trondheim, Norway

(Received 11 August 2016; revised manuscript received 19 December 2016; published 21 February 2017)

The structural and electronic response of  $\text{LaAlO}_3$  to biaxial strain in the (111) plane is studied by density functional theory (DFT) and compared with strain in the (001) plane and isostatic strain. For (111) strain, in-plane rotations are stabilized by compressive strain and out-of-plane rotations by tensile strain. This is an opposite splitting of the modes compared with (001) strain. Furthermore, for compressive (111) strain, in-plane rotations are degenerate with respect to the rotation axis, giving rise to Goldstone-like modes. We rationalize these changes in octahedral rotations by analyzing the  $V_A/V_B$  polyhedral volume ratios. Finally, we investigate how strain affects the calculated band gap, and find a 28% difference between the strain planes under 4% tension. This effect is attributed to different A-site dodecahedral crystal field splitting for (001) and (111) strains.

DOI: 10.1103/PhysRevB.95.064109

### I. INTRODUCTION

A central trait of the perovskite oxides is their strong structure property coupling. From a thin film point of view, this opens the possibility to tune and modify the properties by epitaxial strain. Examples include induced room temperature ferroelectricity in  $\text{SrTiO}_3$ , which is nonpolar in bulk [1]; induced metal insulator transitions in manganites [2]; enhanced Curie temperature and polarization in  $\text{BaTiO}_3$  [3]; increased superconducting critical temperature in  $\text{La}_{2-x}\text{Sr}_x\text{CuO}_4$  [4]; and induced multiferroicity in  $\text{SrMnO}_3$  [5]. This makes strain a valuable tool not only for applications, but also for understanding the physics of perovskite oxides.

Particularly interesting is the strain response of the corner-sharing  $\text{BO}_6$  octahedra, which is essential to the physical properties of perovskite materials. In general, strain in perovskites can be accommodated by either changes in B-O bond lengths, rotations of the oxygen octahedra, or the formation of dislocations or point defects [6]. In bulk materials, octahedral rotations reduce the size of the A-site dodecahedron, thereby mitigating the size mismatch between A and B cations when the Goldschmidt tolerance factor is below unity [7]. Generally it has been shown that compressive strain in the (001) plane increases the rotations around the out-of-plane axis and reduces rotations around in-plane directions, while for tensile strain in the (001) plane, the rotations around in-plane directions increases [7–10]. It has further been shown that these effects can be tuned by changing the out-of-plane lattice parameter through strain doping by light noble elements such as He [11].

Recent advances in thin-film technology have opened up for high-quality epitaxial growth along other crystallographic facets, such as [111] [12]. The (111) interface is interesting because its buckled honeycomb lattice can result in exotic topological states [13], strong magnetic reconstructions due to a reduced interlayer distance [14], and strong octahedral coupling compared with the (001) interface [15]. The pseudocubic rotation axes of the oxygen octahedra are neither

parallel nor perpendicular to the strain plane for (111)-oriented strain, which is the case for (001)-oriented strain [Figs. 1(a) and 1(b)], expected to affect the strain relaxation mechanism. Strain engineering based on the (111) plane is however less studied compared with strain applied in the (001) plane. The studies that do exist have shown experimentally, for example, that (111) strain preserves the bulk rhombohedral symmetry of  $\text{BiFeO}_3$ , where (111) strain gave a single domain polar phase, while (001) and (110) strains resulted in monoclinic phases [16]. Density functional theory (DFT) studies of  $\text{BaTiO}_3$  and  $\text{PbTiO}_3$  have shown that the effect on electric polarization depends strongly on whether the strain is in the (001) or the (111) plane [17]. The (111) strain in  $\text{SrTiO}_3$  was further found to be a viable route to tailor the electronic band gap for optoelectronic devices [18], while recently it was shown experimentally that strained  $\text{LaNiO}_3$  (111) can result in a polar metal [19]. Still, as the octahedral rotations are essential for the properties of many perovskites, there is, to the best of our knowledge, no systematic study of how octahedral rotations behave when strained in the (111) plane compared with the (001) plane.

In this paper, DFT is used to study how the octahedral rotations are affected by biaxial strain in the (111) plane and compared with (001) strain. To this extent,  $\text{LaAlO}_3$  (LAO) is chosen as the model system, as bulk LAO only exhibit rotational distortions with no Jahn-Teller or ferroelectric instabilities. The choice is further motivated by the findings of a quasi two-dimensional electron gas at the (001) interface between LAO and  $\text{SrTiO}_3$  [20], which has later been extended to also include the (111) interface [21]. The octahedral response of LAO to (001) strain is well established [9,10]. For strain in the (001) plane, even small values of strain changes symmetry away from bulk  $R\bar{3}c$ , which has octahedral rotations around the [111] axis. Compressive strain results in  $I4/mcm$  symmetry with rotations around the [001] out-of-plane axis, and tensile strain in  $Imma$  with rotations around the [110] in-plane axis [9,10]. We show that strain along the (111) facet results in different crystallographic phases with different octahedral rotation patterns compared with (001) strain, where the in-plane rotations are stabilized by compressive strain, while out-of-plane rotations are stabilized by tensile strain.

\*thomas.tybell@iet.ntnu.no



MOREAU, MARTHINSEN, SELBACH, AND TYBELL

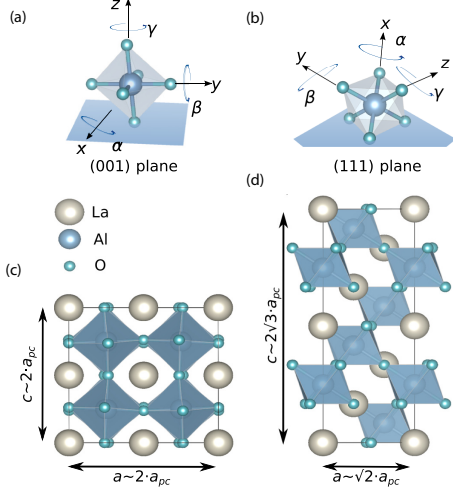
PHYSICAL REVIEW B **95**, 064109 (2017)

FIG. 1. (a), (b) The definition of the rotation axes for (001) and (111) strains, respectively. For (001) strain, the  $x$  and  $y$  axes are parallel to the strain plane, while the  $z$  axis is perpendicular to the strain plane. For (111) strain, neither the  $x$ ,  $y$ , or  $z$  axes are parallel or perpendicular to the strain plane. Note that under the assumption of quadratic strain, the assignment of  $x$ ,  $y$ , and  $z$  for (111) strain is arbitrary. (c) The 40-atom cell used for (001) strain calculations. (d) The 30-atom unit cell used for (111) strain calculations. For the cells in (c) and (d), the  $a$ - $b$  plane spans the (001) and (111) pseudocubic planes, respectively. For quadratic strain, we have  $a = b$ , which are the locked in-plane lattice parameters, while  $c$  is the free to relax out-of-plane lattice parameter, and  $a_{pc}$  denotes the pseudocubic lattice parameter. Atomic structure figures made with VESTA [47].

Furthermore, any combination of the two stabilized orthogonal in-plane rotations for (111) strain are degenerate, giving rise to Goldstone-like modes. The choice of strain plane also affects orbital splitting, and in LAO this manifests as significant changes to the band gap. This paper is structured as follows: In Sec. II, the calculation details are given. Section III discusses the different crystalline phases that are stable for different values of strain, followed by Sec. IV, where we discuss how the octahedral rotations depend on strain and compare it with the calculated polyhedral volume ratio. Finally, in Sec. V, the effect of the strain plane on crystal field splitting of the orbital energies and the electronic band gap is discussed.

## II. COMPUTATIONAL DETAILS

The calculations were performed with the projected augmented wave (PAW) method [22,23] as implemented in the Vienna *Ab initio* Simulation Package (VASP) [23,24]. All relaxations were done with the Perdew-Burke-Ernzerhof generalized gradient approximation for solids (PBE-sol) functional, which has been shown to give better results than the standard PBE for structural relaxations [25]. The PAW potentials with

electron configurations  $4s^2 4p^6 5d^1 6s^2$ ,  $3s^2 3p^1$ , and  $2s^2 2p^4$  were used for La, Al, and O, respectively, while the plane wave cutoff was set to 550 and 800 eV for (001) and (111) strains, respectively. The generalized gradient approximation (GGA)+ $U$  (Dudarev *et al.* [26]), with  $U = 10$  eV, was applied to the La  $f$  states in order to move them away from the bottom of the conduction band [10,27]. This assumption was later confirmed by the hybrid functional calculations, which were done with the Heyd-Scuseria-Ernzerhof (HSE)-sol functional [28].

To simulate the effect of epitaxial strain, the in-plane lattice parameters were locked, while the out-of-plane lattice parameter was allowed to relax. We define (001) strain and (111) strain as strain in the (001) plane and (111) plane, respectively. Strain is calculated as  $\epsilon_{\parallel} = (a - a_0)/a_0$ , where  $a$  is the enforced in-plane lattice parameter, and  $a_0$  is the equilibrium PBE-sol lattice parameter along the [100] and [010], or  $[1\bar{1}0]$  and  $[10\bar{1}]$  pseudocubic directions, depending on strain plane [see Figs. 1(c) and 1(d)]. Quadratic strain was assumed for all calculations. Constant volume calculations were used to calculate the effects of hydrostatic pressure. The internal coordinates of the ions and the out-of-plane lattice parameter were relaxed until the forces on the ions were below 10 and 1 meV/formula unit (f.u.) for (001) and (111) strains, respectively. We allowed less strict convergence for (001) strain, as our calculations were in excellent agreement with the results from Hatt and Spaldin [9]. The calculations for strain in the (001) plane were done with a 40-atom  $2 \times 2 \times 2$  supercell [Fig. 1(c)] to allow for all types of octahedral rotations. In this structure, lattice vectors  $a$ ,  $b$ , and  $c$  are along the [100], [010], and [001] pseudocubic directions, respectively, while the calculations for strain in the (111) plane and the calculations with constant volume were done with a 30-atom  $\sqrt{2} \times \sqrt{2} \times 2\sqrt{3}$  supercell [Fig. 1(d)], where  $a$ ,  $b$ , and  $c$  lattice vectors are along the  $[1\bar{1}0]$ ,  $[10\bar{1}]$ , and  $[111]$  pseudocubic directions, respectively. For the 40-atom  $2 \times 2 \times 2$  supercell a  $4 \times 4 \times 4$   $\Gamma$ -centered  $k$ -point mesh was used to sample the Brillouin zone, while for the 30-atom  $\sqrt{2} \times \sqrt{2} \times 2\sqrt{3}$  supercell, a  $6 \times 6 \times 3$   $\Gamma$ -centered  $k$ -point mesh was used. Phonon calculations were performed utilizing the frozen phonon approach [29] and analyzed with the phonopy software [30]. The phonon calculations were performed with  $2 \times 2 \times 2$  supercells of the ideal five-atom perovskite structure:  $Pm\bar{3}m$  symmetry for the unstrained cells and  $P4/mmm$  and  $R\bar{3}m$  for (001) and (111) strains, respectively. These cells were relaxed until the energy difference between subsequent ionic steps were lower than  $10^{-8}$  eV. The determination of space groups were done with the FINDSYM software with a tolerance of  $0.005 \text{ \AA}$  [31].

Rotation angles  $\alpha$ ,  $\beta$ , and  $\gamma$  about the pseudocubic axes  $x$ ,  $y$ , and  $z$ , respectively, are defined as shown in Figs. 1(a) and 1(b). For (001) strain, the  $x$  and  $y$  directions are in the strain plane and  $z$  is out of plane, while for (111) strain, none of the directions are perpendicular or parallel to the strain plane. All crystallographic directions are given in the pseudocubic setting unless otherwise stated.

## III. STRUCTURAL PHASES

LAO has  $R\bar{3}c$  symmetry, which deviates from the aristotype cubic  $Pm\bar{3}m$  perovskite with anti-phase rotations around one

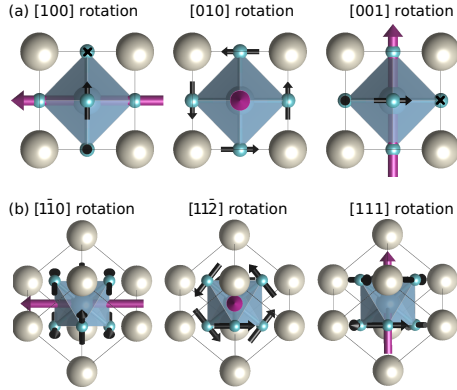


FIG. 2. Illustration of the in-plane and out-of-plane rotational modes under (a) (001) strain and (b) (111) strain. For (001) strain, [100] and [010] are in-plane, while [001] is out-of-plane. For (111) strain, [110] and [112] are in-plane, while [111] is out-of-plane.

of the pseudocubic (111) axes ([111], [11 $\bar{1}$ ], [1 $\bar{1}$ 1], or [ $\bar{1}$ 11]), which can be described in the Glazer tilt system as  $a^-a^-a^-$  [32]. The equilibrium structure based on our calculations has lattice parameters of  $a = 5.384$  Å (pseudocubic 3.807 Å) and  $c = 13.146$  Å (pseudocubic 3.795 Å) in the hexagonal setting and has rotations of the oxygen octahedra around the [111] axis of  $4.75^\circ$ , all in good agreement with the literature [33]. Hydrostatic pressure results in a decrease of the rotation angle, and for compressive isotropic strain of more than 2%, the cubic  $Pm\bar{3}m$  phase is lower in energy than  $R\bar{3}c$ . This is also in good agreement with experiments on bulk LAO, where the rotation angles decrease with increasing hydrostatic pressure until a phase transition to cubic  $Pm\bar{3}m$  occurs at 14 GPa [34]. This hydrostatic pressure corresponds to a compression of all lattice parameters of about 2%, in good agreement with our calculated isotropic strain at the phase transition.

To investigate the effect of strain on lattice distortions, the phonon frequencies were calculated for cubic LAO under both (001) and (111) strains, focusing on the unstable modes with imaginary frequencies. For 0% strain, three degenerate lattice instabilities were found at the  $R$  point of the five-atom  $Pm\bar{3}m$  cell. These instabilities correspond to anti-phase rotations, as expected, since LAO bulk displays an  $a^-a^-a^-$  tilt pattern. As illustrated in Fig. 2, when the structure is strained either in the (001) or the (111) plane, these rotational modes are split into orthogonal in-plane and out-of-plane modes. Figure 3 shows how the strain affects the phonon frequencies. As expected, compressive (001) strain favors rotations around the [001] out-of-plane axis, while tensile strain favors rotations around the in-plane [100] and [010] axes, as seen in Fig. 3(a). Further, as shown in Fig. 3(b), (111) strain splits the three degenerate modes at 0% strain into out-of-plane [111] rotations and in-plane [110] and [112] rotations. However, we note that the splitting of in-plane and out-of-plane rotations is opposite with respect to (001) strain. Under compressive (111) strain, in-

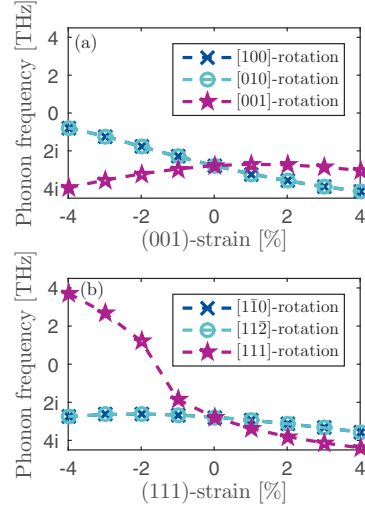


FIG. 3. Phonon frequencies for the different rotational modes as a function (a) (001) strain and (b) (111) strain. Illustrations of the different rotational modes are shown in Fig. 2. The dashed lines are guides to the eye.

plane rotations are favored, while for tensile (111) strain, out-of-plane rotations are favored.

To identify which possible space groups are stable under applied strain, the effect of freezing in different rotational modes is investigated. For (001) strain, this results in a tetragonal  $I4/mcm$  symmetry for the out-of-plane mode with rotations around [001]; the in-plane [100] and [010] rotations stabilized by tensile (001) strain both result in an orthorhombic  $Fmmm$  symmetry, while a superposition with equal amount of [100] and [010] rotations gives an  $Imma$  symmetry. For the out-of-plane [111] rotations stabilized by tensile (111) strain, we find a rhombohedral  $R\bar{3}c$  symmetry, similar to bulk LAO. While the rotations around the in-plane [110] and [112] axes yield monoclinic  $C2/m$  and  $C2/c$  symmetry, respectively, an arbitrary combination of rotations about the [110] and [112] axes results in  $P\bar{1}$  symmetry.

From this we calculate the phase diagram as a function of (001) and (111) strains. The results are shown in Fig. 4. For (001) strain, the results reported by Hatt and Spaldin are reproduced [9]. For compressive (001) strain, the tetragonal  $I4/mcm$ , with rotations around the [001] axis, Glazer tilt pattern  $a^0a^0c^-$ , has the lowest energy, while for tensile strain, the tetragonal  $Imma$  structure, with tilt pattern  $a^-a^-c^0$ , has the lowest energy. For small levels of (001) strain ( $\pm 0.25\%$ ) LAO accommodates a monoclinic  $C2/c$  structure. This  $C2/c$  structure is similar to the  $R\bar{3}c$  space group but has tilt pattern  $a^-a^-c^-$  instead of  $a^-a^-a^-$ , as the out-of-plane lattice parameter is no longer equal to the in-plane lattice parameter, and any perturbation from the unstrained system has to change the symmetry. However, as the deviation from the  $R\bar{3}c$  space

MOREAU, MARTHINSEN, SELBACH, AND TYBELL

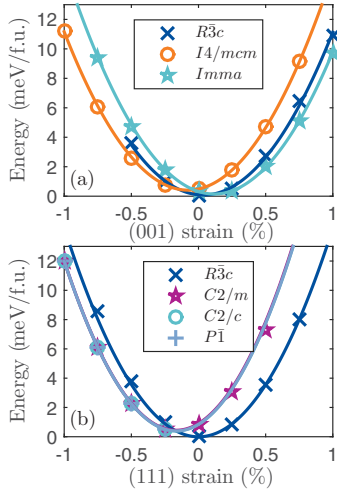
PHYSICAL REVIEW B **95**, 064109 (2017)

FIG. 4. Energy vs strain for the different phases. (a) (001) strain, (b) (111) strain. The solid lines correspond to fits to parabolic functions, as described in the text. The data points correspond to the strain values where the respective phases were stable under geometry optimization.

group is small within the limited strain window where this  $C2/c$  structure is stable, we will label it  $R\bar{3}c$  for the rest of this paper. For (111) strain, as shown in Fig. 4(b), tensile strain preserves the bulk  $R\bar{3}c$  symmetry. In this case, the rotation axes of the octahedra are now always perpendicular to the strain plane (i.e., the four (111)-axes are no longer degenerate). Also in accordance with the phonon calculations, for compressive (111) strain, the three different monoclinic phases ( $C2/m$ ,  $C2/c$ , and  $P\bar{1}$ ) are degenerate. The energy differences between these three phases are calculated to be less than 0.1 meV/f.u. Also, these three monoclinic phases are lower in energy than the bulk  $R\bar{3}c$  phase for all compressive strain values considered. The structural parameters from the different phases for representative values of strain are shown in Table I.

Another difference between (001)- and (111)-strained LAO is the difference in out-of-plane lattice parameter response as shown in Fig. 5. Epitaxial thin films generally compensate for tensile (compressive) strain by reducing (increasing) the out-of-plane lattice parameter. We quantify this by estimating the Poisson's ratio, and LAO strained in the (001) plane have a significantly larger Poisson's ratio, 0.265–0.305, compared with LAO strained in the (111) plane, 0.178–0.195. This value for (001) strain is closer to the experimental bulk value of 0.26 [35]. Hence, strain in the (001) plane is more prone to preserve the volume.

As shown in Fig. 3, the two in-plane modes have degenerate phonon frequencies, indicating that the second-order terms in a harmonic approximation are equal [36]. However, the

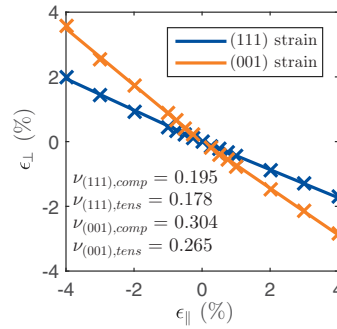


FIG. 5. Out-of-plane vs in-plane strain for the (001) and (111) planes. The different Poisson's ratios  $\nu$  are calculated from the linear fits to the data. For (001) strain, the 0% strain point is from another space group and, hence, is not included in any of the fitted lines. For tensile (111) strain, the different degenerate phases relax to the same out-of-plane lattice parameter; thus, they have the same  $\nu$ .

fourth-order terms do not need to be equal, which in turn could make certain in-plane rotation axes favored. Hence, to investigate if there are favored in-plane directions for the rotations, the two in-plane modes are simultaneously frozen to identify possible combinations giving an energy lowering. Figure 6 depicts the energy landscape from such calculations of the degenerate modes for 1% tensile (001) strain and 1% compressive (111) strain. For tensile (001) strain, it is found that the global minimum is for an equal amount of [100] and [010] rotations, resulting in a tetragonal  $Imma$  structure with rotations around [110] [Fig. 6(c)]. In contrast, no single global minimum for combinations of  $[1\bar{1}0]$  and  $[1\bar{1}\bar{2}]$  rotations is found under compressive (111) strain. Instead, a circle of continuous minima is obtained, resulting in a Mexican hat-shaped energy surface. Any arbitrary point along the circle corresponds to the space group  $P\bar{1}$ , which is a subgroup of both  $C2/c$  and  $C2/m$ . We note such a circular energy landscape as under (111) compression is compatible with Goldstone-like modes [37]. While such modes are common in *isotropic* materials, few experimental observations are available for *anisotropic* crystals, with one exception being superconducting  $Cd_2Re_2O_7$  [38]. Goldstone-like modes have been proposed to occur in carefully engineered ferroelectric Ruddlesden-Popper phases from DFT calculations [39]. Further, we note that under quadratic (111) strain there is only  $30^\circ$  between symmetry-equivalent axes of the orthogonal rotations ( $(1\bar{1}0)$  and  $(1\bar{1}\bar{2})$ ), while for (001) strain, these axes ( $(100)$  and  $(010)$ ) are separated by  $90^\circ$ . Hence, it is possible that the underlying energy landscape is not a perfect circle but, instead, a regular dodecagon where the energy differences between possible local minima and maxima are less than 0.1 meV/f.u., lower than the resolution of the DFT calculations.

From a thin film perspective, by relying on compressive (111) strain, there is no apparent driving force for domain formation; e.g., it should be possible to synthesize compressively (111) strained structurally monodomain

TABLE I. Summary of the calculated structural parameters of different phases at representative values of strain. The rotations are given in Glazer tilt notation [32]. Note that the labels  $a$ ,  $b$ , and  $c$  are the conventional lattice parameters of the given space groups, not the pseudocubic lattice parameters. Furthermore,  $\alpha$ ,  $\beta$ , and  $\gamma$  are the conventional cell angles, not the rotations of the oxygen octahedral around the different pseudocubic axes.

Rotations	Strain	$a$ [Å]	$b$ [Å]	$c$ [Å]	$\alpha$ [°]	$\beta$ [°]	$\gamma$ [°]	Wyckoff Position	$x$	$y$	$z$	
$R\bar{3}c$	$a^-a^-a^-$	Unstrained	5.385	5.385	13.146	90	90	120	La (6a)	0	0	0.25
									Al (6b)	0	0	0
									O (18e)	0.4760	0	0.25
$I4/mcm$	$a^0a^0c^-$	-1% (001)	5.325	5.325	7.677	90	90	90	La (4b)	0	0.5	0.25
									Al (4c)	0	0	0
									O (8h)	0.2709	0.7709	0
									O (4a)	0	0	0.25
$Imma$	$a^-a^-c^0$	+1% (001)	7.544	5.433	5.433	90	90	90	La (4b)	0	0.25	0.74996
									Al (4c)	0.25	0.25	0.25
									O (8f)	0.2333	0	0
									O (4e)	0	0.25	0.2829
$C2/m$	$a^-a^-c^0$	-1% (111)	9.235	5.332	5.380	90	124.905	90	La (4i)	0.7496	0	0.7494
									Al (2b)	0	0.5	0
									Al (2c)	0	0	0.5
									O (8j)	-0.0138	0.2502	0.7361
$C2/c$	$a^-a^-c^-$	-1% (111)	9.235	5.332	7.574	90	144.375	90	O (4i)	0.2500	0	0.7774
									La (4e)	0	0.0003	0.25
									Al (4b)	0	0.5	0
									O (8f)	0.7651	0.2349	0.7736
$P\bar{1}$	$a^-b^-c^-$	-1% (111)	5.332	5.332	5.380	90	119.707	120	O (4e)	0	0.5166	0.25
									La (2i)	-0.0005	0.2496	0.2498
									Al (1f)	0.5	0	0.5
									Al (1e)	0.5	0.5	0
$R\bar{3}c$	$a^-a^-a^-$	+1% (111)	5.439	5.439	13.086	90	90	120	O (2i)	0.4697	0.2285	0.2284
									O (2i)	-0.0001	0.2549	0.7247
									O (2i)	0.4798	0.7338	0.2460
									La (6a)	0	0	0.25
$Pm\bar{3}m$	$a^0a^0a^0$	-2% isostatic	3.7272	3.7272	3.7272	90	90	90	Al (6b)	0	0	0
									O (18e)	0.5299	0	0.25
									La (1b)	0.5	0.5	0.5
									Al (1a)	0	0	0
									O (3d)	0.5	0	0

LAO thin films. However, the choice of substrate could lift this degeneracy, either through imprinting the rotation pattern of the substrate or through nonquadratic strain from, e.g., an orthorhombic substrate.

#### IV. OCTAHEDRAL ROTATIONS AND POLYHEDRAL VOLUME RATIO

We now turn to how the strain is mitigated through octahedral rotations in the different phases by comparing the rotations projected on the pseudocubic axes. Figure 7 shows how the strain affects the rotations for the different symmetries as a function of (001) and (111) strains. For (001) strain in Fig. 7(a), the tilt pattern switches from the bulk  $a^-a^-a^-$  tilt pattern to  $a^0a^0c^-$  for compressive strain and to  $a^-a^-c^0$  outside the small window ( $\pm 0.25\%$ ) where the  $a^-a^-a^-$  tilt is stable. We further confirm that the rotation amplitudes of the respective phase behaves approximately linear for increasing absolute value of strain, as reported by Hatt and Spaldin [9]. However, for (111) strain in Figs. 7(b)–7(d), a different trend is

observed. For tensile strain in the (111) plane, which preserves the  $R\bar{3}c$  symmetry, the rotations around the pseudocubic axes are almost constant at  $2.65^\circ$  each, corresponding closely to the bulk rotation value around the [111] axis of  $4.75^\circ$ . The small changes in the rotation angles can be attributed to the fact that none of the pseudocubic directions are perpendicular or parallel to the strain plane, effectively locking the rotations with (111) strain. For compressive strain in the (111) plane, we find that as the rhombohedral symmetry is lifted, the crystal has larger possibilities to accommodate the strain through octahedral rotations. As seen in Figs. 7(b) and 7(c), the  $C2/m$  and  $C2/c$  structures have rotation patterns  $a^-a^-c^0$  and  $a^-a^-c^-$ , corresponding to rotations around the in-plane  $[1\bar{1}0]$  and  $[11\bar{2}]$  axes, respectively. (Note that for the rotations around  $[11\bar{2}]$  in Fig. 7(c), the  $\alpha$  and  $\beta$  rotations are about half the  $\gamma$  rotations.) The evolution of the pseudocubic rotation angles for one of the arbitrary combinations of in-plane  $[1\bar{1}0]$  and  $[11\bar{2}]$  rotation with  $P\bar{1}$  symmetry is depicted in Fig. 7(d), where this illustrated specific combination of rotations has an  $a^-b^-c^-$  tilt pattern. Even though the rotation patterns are

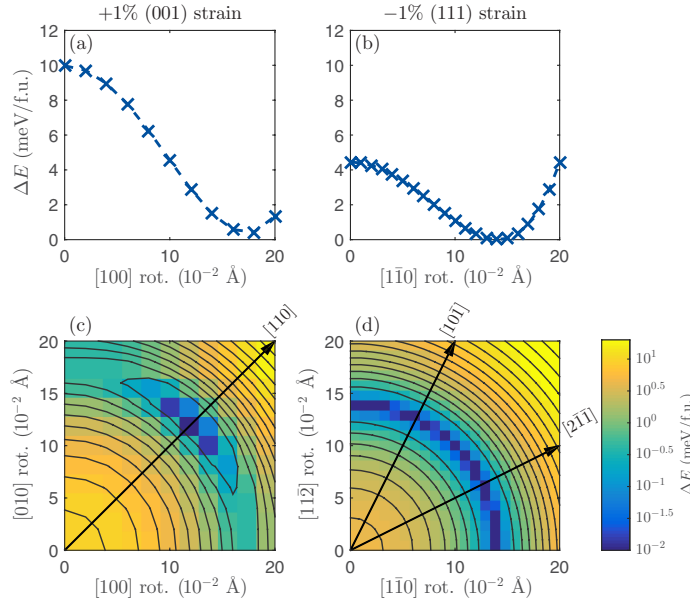


FIG. 6. Energy difference with respect to the global minimum as a function of mode amplitude for the in-plane rotational (rot.) modes. (a) One percent tensile (001) strain where the [100] in-plane rotation mode with  $Fmmm$  symmetry is frozen in. (The [010] mode is degenerate for all amplitudes.) (b) One percent compressive (111) strain, where the  $[1\bar{1}0]$  phonon mode with symmetry  $C2/m$  is frozen in. (The  $[11\bar{2}]$  mode with  $C2/c$  symmetry is degenerate for all amplitudes.) (c) Logarithmic energy difference for 1% tensile (001) strain when both the degenerate in-plane rotational modes [100] and [010] are frozen in simultaneously. A global energy minimum is observed for a single point with equal amplitude of [100] and [010] rotations, giving  $Imma$  symmetry. (d) Logarithmic energy difference for 1% compressive (111) strain when both the degenerate in-plane rotational modes  $[1\bar{1}0]$  and  $[11\bar{2}]$  are frozen in simultaneously. The global energy minimum is no longer a single point but a circle with constant mode amplitude resembling a Mexican hat potential. For (c) and (d), each pixel represents the energy from one calculation; the black lines are contour plots of the energy landscape, and the arrows show the relationship to other high-symmetry directions.

different, their response to strain is similar, in the sense that the largest rotation for all three tilt patterns is about  $3^\circ$  for  $-0.25\%$  (111) strain and decreases to about  $2^\circ$  for  $-4\%$  strain.

To better understand the anisotropic effects of strain, a comparison with calculations with isostatic strain emulating hydrostatic pressure is performed. The results are shown in Fig. 7(e). For the degenerate LAO phases, the rotation amplitude decreases monotonically with increasing compressive strain [Figs. 7(b)–7(d)]. This is qualitatively similar to the response to hydrostatic pressure [34] and is attributed to the higher compressibility of the  $Al^{3+}$  octahedra than the  $La^{3+}$  dodecahedra, as is commonly found for III-III perovskites [40]. We note that even though the rotation amplitudes are reduced for (111) compression, a possible phase without any rotations such as  $R\bar{3}m$  or  $Pm\bar{3}m$  is never obtained for the range of strains considered here. This is in contrast with the response of hydrostatic pressure [Fig. 7(e)], resulting in a  $Pm\bar{3}m$  phase for compressive strain larger than 2%.

In order to better quantify how strain distorts the crystal, we have calculated the polyhedral volume ratio  $V_A/V_B$ , the

volume of the A-site dodecahedron divided by the volume of the B-site octahedron. The ratio  $V_A/V_B$  is equal to 5.0 for the cubic structure without octahedral tilt, and the deviation from 5.0 is proportional to the degree of structural distortion [41,42]. The polyhedral volume ratio as a function of strain in the (001) and (111) planes is shown in Fig. 8, as well as how it changes for isostatic strain. For (001) and (111) strains [Figs. 8(a) and 8(b)], a clear trend is seen that the phase with the most distorted crystal structure, the lowest  $V_A/V_B$ , also has the lowest energy. This trend is different from what is observed when the polyhedral volume ratio is studied experimentally as a function of temperature or pressure, for which the different space groups have different ranges of  $V_A/V_B$ , where the different distortions are stable, giving rise to steps in the  $V_A/V_B$  ratio [41,43]. The reason why (001) strain favors out-of-plane rotations under compression and in-plane rotations under tension, while it is opposite for (111) strain, can now be explained as the structure minimizing the  $V_A/V_B$  ratio. Considering that while the stacking sequence in the perovskite structure along the [001] direction is  $AO \rightarrow BO_2 \rightarrow AO \rightarrow$

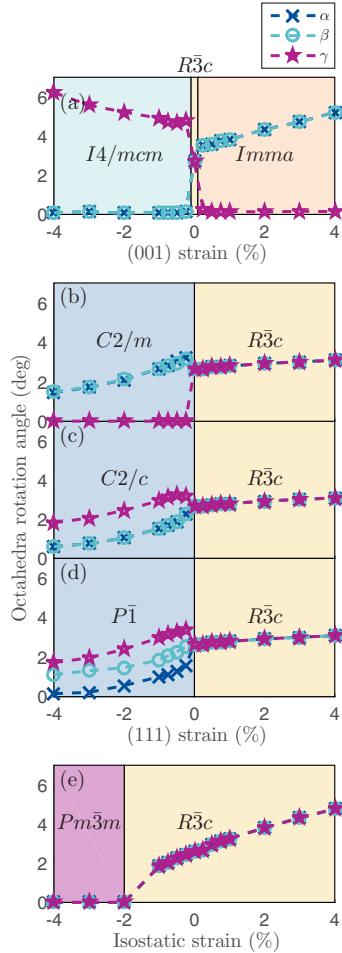


FIG. 7. (a) Pseudocubic octahedral rotation angles (degrees) vs (001) strain. (b)–(d) (111) strain. (e) Isostatic strain.  $\alpha$ ,  $\beta$ , and  $\gamma$  are defined in Fig. 1. The colors and labels represent which space group has the lowest energy in this strain range. (b)–(d) The response for the three different space groups, which are degenerate under compressive strain in the (111) direction. Note that the response is equal for tensile strain. For the  $P\bar{1}$  symmetry in (d), one arbitrary combination of  $[1\bar{1}0]$  and  $[11\bar{2}]$  rotation is shown. The dashed lines are guides to the eye.

$BO_2 \rightarrow \dots$ , along the  $[111]$  direction it is  $AO_3 \rightarrow B \rightarrow AO_3 \rightarrow B \rightarrow \dots$ . Hence, to optimize the coordination of the small A cation under (111) strain without increasing the  $V_A/V_B$  ratio, the oxygen atoms are pushed up and down by the in-plane octahedral rotations under compressive strain. Under

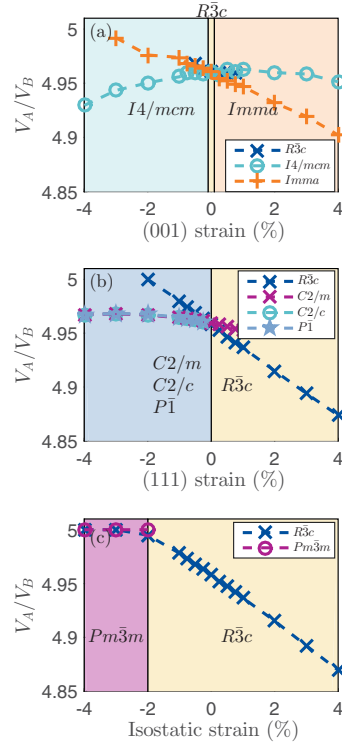


FIG. 8. Polyhedral volume ratio as a function of strain: (a) (001) strain, (b) (111) strain, (c) isostatic strain. The colors and labels represent which space groups have the lowest energy in this strain range.  $V_A/V_B = 5$  for the unrotated cubic phase and then decreases from this value as the distortions are increased. The dashed lines are guides to the eye.

(111) tensile strain, there is a possibility to move in the strain plane, as illustrated by the black arrows in Fig. 2(b). This differs from the situation under (001) strain, where the oxygen movements are in the same directions as compression when the  $V_A/V_B$  ratio is minimized. Finally, we note that the  $R\bar{3}c$  structure has a similar response to (111) strain and hydrostatic pressure [see Figs. 8(b) and 8(c)]; i.e., tensile strain in the (111) plane of perovskites gives the same distortions as under negative isostatic pressure, which is not easily accessible by experiments.

It is now possible to rationalize the increased energy cost for straining in the (111) plane compared with (001) strain. The total energy as a function of strain (see Fig. 4) can be fitted to the equation  $E = A\epsilon_{\parallel}^2 + B\epsilon_{\parallel} + C$ , where  $\epsilon_{\parallel}$  is the in-plane strain, and  $A$ ,  $B$ , and  $C$  are the fitting parameters. For (111) strain, we find that  $A_{111} \approx 16 \text{ meV}/\%^2\text{-f.u.}$ , while for (001),

MOREAU, MARTHINSEN, SELBACH, AND TYBELL

$A_{001} \approx 12 \text{ meV}/\%^2$  -f.u. is obtained. This can be understood by considering that when strain is applied in the (001) plane, the structure can more easily compensate for changes in strain by rotating the oxygen octahedra, compared with strain in the (111) plane, as the oxygen movements are in the same directions as the structure is compressed. This effect is also observed when taking into account the larger Poisson's ratio for (001) strain, meaning that (001) strain has smaller changes in volume for increasing compressive or tensile strain.

### V. ORBITAL SPLITTING AND BAND GAP

Having established how (001) and (111) strains affects the symmetry and octahedral rotations of LAO, we turn to how strain affects the electronic properties. The band gap in LAO is between the occupied  $O_{2p}$  states in the valence band and empty  $La_{5d}$  states in the conduction band [27] (see Supplemental Material [44] for the projected density of states (DOS) of the hybrid functional calculations). It is known that the different strain planes affects the crystal field splitting of  $d$  states. As shown for dodecahedral sites in Fig. 9, the cubic distortion from (001) strain splits both the top  $t_{2g}$  and the bottom  $e_g$  levels, while the trigonal distortion from (111) strain only splits the top  $t_{2g}$  states [45]. (For illustration of the dodecahedrally coordinated  $d$  states, see Supplemental Material [44]). This change in crystal field splitting does indeed affect the electronic properties. In Fig. 10, the PBE-sol band gap is plotted vs strain in the (001) and (111) planes and compared with the results for isotropic strain. As seen, the band gap for (001) strain is decreasing for both tensile and compressive strain, while for (111) strain the band gap is decreasing for compressive strain and increasing for tensile strain, similar to the effect of hydrostatic pressure. Since the trend is opposite for tensile (001) and (111) strains, LAO has a significantly different band gap for different strain planes,  $\sim 0.8 \text{ eV}$  at 4% tensile strain, corresponding to a change of 28%. There is also a slight

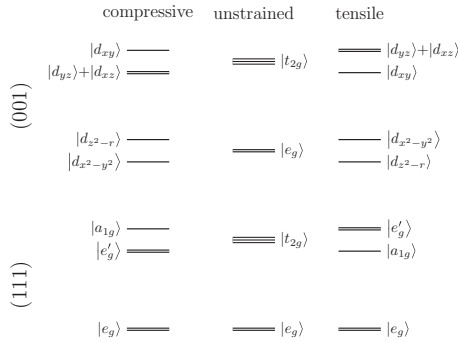


FIG. 9. Splitting of  $d$  states of dodecahedral coordinated sites for (001) and (111) strain. Note that  $e_g$  and  $t_{2g}$  levels are reversed for dodecahedral sites compared with octahedral sites. The trigonal distortion from (111) strain splits the  $t_{2g}$  levels into  $a_{1g}$  and  $e'_g$ , which are superpositions of the  $d_{xy}$ ,  $d_{yz}$ , and  $d_{zx}$  states [45].

PHYSICAL REVIEW B 95, 064109 (2017)

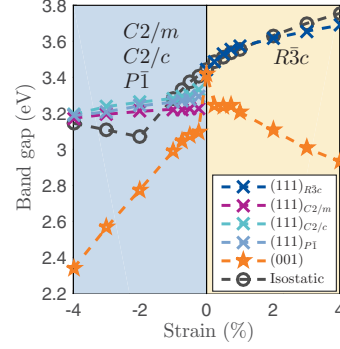


FIG. 10. PBE-sol band gap of the different structures as a function of different strains. The colors and labels corresponds to which space groups are stable for (111) strain in the given strain range. For (001) strain, there is a change in symmetry at 0% strain, while for isotropic strain, there is a change in symmetry at  $-2\%$  strain. For the  $P\bar{1}$  symmetry, we have selected the same arbitrary combination of  $[1\bar{1}0]$  and  $[11\bar{2}]$  rotations, as in Fig. 7(d). The dashed lines are guides to the eye.

difference in band gap between the degenerate monoclinic phases, where  $C2/c$  has the highest band gap followed by  $P\bar{1}$  and  $C2/m$ . However, these differences are below 0.1 eV for 0.25% compressive strain and are further reduced for increasing compressive strain, due to all the rotation angles being reduced; thus, the structures become more and more similar.

The difference between (001) and (111) strains, as well as the reason why (111) strain behaves as if under hydrostatic pressure, can be understood by considering the orbital splitting differences between (001) and (111) strains. Under strain in the (001) and (111) planes, the  $5d$  states of the 12 coordinated La are split as shown in Fig. 9. As (111) strain only splits the top orbitals in the top of the conduction band, the changes observed in the band gap are dominated by changes in interatomic distances, similar to what is seen for hydrostatic pressure. For (001) strain, the effect of change in interatomic distances is also present, but it is superimposed on the stronger effect of splitting of the  $e_g$  orbitals; thus, the band gap is reduced also for tensile (001) strain, however less compared with compressive (001) strain. This is all summarized in schematic DOS shown in Fig. 11. A difference in calculated band gap between (001) and (111) strains were also reported for  $SrTiO_3$ . However, for  $SrTiO_3$ , the effects were attributed to suppression of ferroic distortions [18] instead of different orbital splitting, as we show here.

### VI. CONCLUSIONS

Epitaxial strain in the (001) and (111) planes is nonequivalent. The (001) strain is known to favor tetragonal phases with out-of-plane rotations for compressive strain and in-plane rotations for tensile strain. As we have shown, this trend is opposite for LAO under (111) strain, where compressive strain

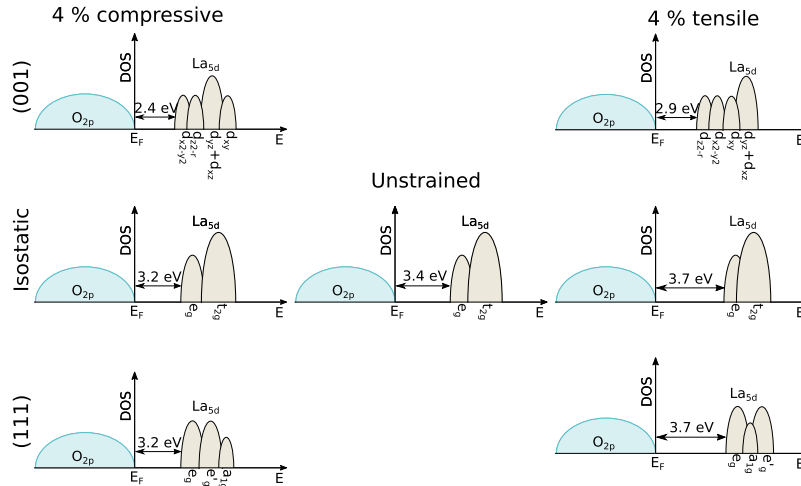


FIG. 11. Schematic density of states showing the splitting of the  $La_{5d}$  states under (001), isostatic, and (111) strains. It is further shown how the splittings are related to the changes in band gap when LAO is strained.

favors in-plane rotations and tensile strain favors out-of-plane rotations. Further, we have shown that the in-plane rotation directions for (111) strain are degenerate, giving rise to Goldstone-like modes. The fact that strain in the (111) plane can result in degenerate LAO phases having different octahedral tilt patterns has implications for other rhombohedral materials systems where the functional properties are strongly coupled to the octahedral rotations, such as  $(La,Sr)MnO_3$  [46]. Due to the different orbital splitting from (001) and (111) strain, the band gap of LAO depends on the strain plane, giving a change in PBE-sol band gap of 28% for 4% tensile strain depending on the strain plane. This significant difference in band gap needs to be taken into account when designing functional [111]-oriented superlattices based on effects such as charge transfer. Hence, epitaxial (111)-oriented thin films

are an exciting avenue for tailoring systems with different octahedral responses and opens up ways to tailor band gaps, e.g., for optoelectronic devices.

#### ACKNOWLEDGMENTS

The Norwegian Metacenter for Computational Science is acknowledged for providing computational resources Uninet Sigma 2, Project No. NN9301K. T.T. acknowledges the Research Council of Norway Grant No. 231290. We thank Gerhard Henning Olsen for valuable discussions about phonon calculations and Ulrich Aschauer for providing the fropo script. We also thank Nicola Spaldin for valuable discussions about the Goldstone-like modes.

- [1] J. H. Haeni, P. Irvin, W. Chang, R. Uecker, P. Reiche, Y. L. Li, S. Choudhury, W. Tian, M. E. Hawley, B. Craigo *et al.*, *Nature* **430**, 758 (2004).
- [2] K. H. Ahn, T. Lookman, and A. R. Bishop, *Nature* **428**, 401 (2004).
- [3] K. J. Choi, M. Biegalski, Y. L. Li, A. Sharan, J. Schubert, R. Uecker, P. Reiche, Y. B. Chen, X. Q. Pan, V. Gopalan *et al.*, *Science* **306**, 1005 (2004).
- [4] I. Bozovic, G. Logvenov, I. Belca, B. Narimbetov, and I. Sveklo, *Phys. Rev. Lett.* **89**, 107001 (2002).
- [5] J. H. Lee and K. M. Rabe, *Phys. Rev. Lett.* **104**, 207204 (2010).
- [6] U. Aschauer, R. Pfenninger, S. M. Selbach, T. Grande, and N. A. Spaldin, *Phys. Rev. B* **88**, 054111 (2013).
- [7] J. M. Rondinelli and N. A. Spaldin, *Adv. Mater.* **23**, 3363 (2011).
- [8] A. T. Zayak, X. Huang, J. B. Neaton, and K. M. Rabe, *Phys. Rev. B* **74**, 094104 (2006).
- [9] A. J. Hatt and N. A. Spaldin, *Phys. Rev. B* **82**, 195402 (2010).
- [10] R. L. Johnson-Wilke, D. Marincel, S. Zhu, M. P. Warusawithana, A. Hatt, J. Sayre, K. T. Delaney, R. Engel-Herbert, C. M. Schlepuetz, J. W. Kim *et al.*, *Phys. Rev. B* **88**, 174101 (2013).
- [11] A. Herklotz, A. T. Wong, T. Meyer, M. D. Biegalski, H. N. Lee, and T. Z. Ward, *Sci. Rep.* **6**, 26491 (2016).
- [12] I. Hallsteinsen, J. E. Boschker, M. Nord, S. Lee, M. Rzchowski, P. E. Vullum, J. K. Grepstad, R. Holmestad, C. B. Eom, and T. Tybell, *J. Appl. Phys.* **113**, 183512 (2013).



MOREAU, MARTHINSEN, SELBACH, AND TYBELL

PHYSICAL REVIEW B **95**, 064109 (2017)

- [13] D. Doennig, W. E. Pickett, and R. Pentcheva, *Phys. Rev. Lett.* **111**, 126804 (2013); Y. Weng, X. Huang, Y. Yao, and S. Dong, *Phys. Rev. B* **92**, 195114 (2015).
- [14] M. Gibert, P. Zubko, R. Scherwitzl, J. Íñiguez, and J.-M. Triscone, *Nat. Mater.* **11**, 195 (2012); C. Piamonteze, M. Gibert, J. Heidler, J. Dreiser, S. Rusponi, H. Brune, J. M. Triscone, F. Nolting, and U. Staub, *Phys. Rev. B* **92**, 014426 (2015).
- [15] I. Hallstensen, M. Moreau, A. Grutter, M. Nord, P. E. Vullum, D. A. Gilbert, T. Bolstad, J. K. Grepstad, R. Holmestad, S. M. Selbach *et al.*, *Phys. Rev. B* **94**, 201115 (2016).
- [16] J. F. Li, J. L. Wang, M. Wuttig, R. Ramesh, N. Wang, B. Ruetter, A. P. Pyatakov, A. K. Zvezdin, and D. Viehland, *Appl. Phys. Lett.* **84**, 5261 (2004).
- [17] A. Raelarijaona and H. Fu, *J. Appl. Phys.* **115**, 054105 (2014); R. Oja, K. Johnston, J. Frantti, and R. M. Nieminen, *Phys. Rev. B* **78**, 094102 (2008).
- [18] R. F. Berger, C. J. Fennie, and J. B. Neaton, *Phys. Rev. Lett.* **107**, 146804 (2011).
- [19] T. H. Kim, D. Puggioni, Y. Yuan, L. Xie, H. Zhou, N. Campbell, P. J. Ryan, Y. Choi, J. W. Kim, J. R. Patzner *et al.*, *Nature* **533**, 68 (2016).
- [20] A. Ohtomo and H. Y. Hwang, *Nature* **427**, 423 (2004).
- [21] G. Herranz, F. Sánchez, N. Dix, M. Scigaj, and J. Fontcuberta, *Sci. Rep.* **2**, 758 (2012).
- [22] P. E. Blochl, *Phys. Rev. B* **50**, 17953 (1994).
- [23] G. Kresse and D. Joubert, *Phys. Rev. B* **59**, 1758 (1999).
- [24] G. Kresse and J. Furthmuller, *Phys. Rev. B* **54**, 11169 (1996).
- [25] J. P. Perdew, A. Ruzsinszky, G. I. Csonka, O. A. Vydrov, G. E. Scuseria, L. A. Constantin, X. L. Zhou, and K. Burke, *Phys. Rev. Lett.* **100**, 136406 (2008).
- [26] S. L. Dudarev, G. A. Botton, S. Y. Savrasov, C. J. Humphreys, and A. P. Sutton, *Phys. Rev. B* **57**, 1505 (1998).
- [27] S.-G. Lim, S. Kriventsov, T. N. Jackson, J. H. Haeni, D. G. Schlom, A. M. Balbashov, R. Uecker, P. Reiche, J. L. Freeouf, and G. Lucovsky, *J. Appl. Phys.* **91**, 4500 (2002).
- [28] L. Schimka, J. Harl, and G. Kresse, *J. Chem. Phys.* **134**, 024116 (2011).
- [29] K. Kunc and R. M. Martin, *Phys. Rev. Lett.* **48**, 406 (1982).
- [30] A. Togo and I. Tanaka, *Scripta Materialia* **108**, 1 (2015).
- [31] H. T. Stokes and D. M. Hatch, *J. Appl. Crystallogr.* **38**, 237 (2005).
- [32] A. Glazer, *Acta Crystallogr. Sect. B* **28**, 3384 (1972); A. Glazer, *Acta Crystallogr. Sect. A* **31**, 756 (1975).
- [33] K. A. Müller, W. Berlinger, and F. Waldner, *Phys. Rev. Lett.* **21**, 814 (1968).
- [34] P. Bouvier and J. Kreisel, *J. Phys.: Condens. Matter* **14**, 3981 (2002); M. Guennou, P. Bouvier, G. Garbarino, and J. Kreisel, *ibid.* **23**, 395401 (2011).
- [35] X. Luo and B. Wang, *J. Appl. Phys.* **104**, 073518 (2008).
- [36] W. Cochran, *Phys. Rev. Lett.* **3**, 412 (1959).
- [37] J. Goldstone, A. Salam, and S. Weinberg, *Phys. Rev.* **127**, 965 (1962).
- [38] C. A. Kendziora, I. A. Sergienko, R. Jin, J. He, V. Keppens, B. C. Sales, and D. Mandrus, *Phys. Rev. Lett.* **95**, 125503 (2005); J. C. Petersen, M. D. Caswell, J. S. Dodge, I. A. Sergienko, J. He, R. Jin, and D. Mandrus, *Nat. Phys.* **2**, 605 (2006).
- [39] S. M. Nakhmanson and I. Naumov, *Phys. Rev. Lett.* **104**, 097601 (2010).
- [40] R. J. Angel, J. Zhao, and N. L. Ross, *Phys. Rev. Lett.* **95**, 025503 (2005); J. Zhao, N. L. Ross, and R. J. Angel, *J. Phys.: Condens. Matter* **16**, 8763 (2004); T. Tohei, A. Kuwabara, T. Yamamoto, F. Oba, and I. Tanaka, *Phys. Rev. Lett.* **94**, 035502 (2005).
- [41] M. Avdeev, E. N. Caspi, and S. Yakovlev, *Acta Crystallogr. Sect. B* **63**, 363 (2007).
- [42] N. Thomas, *Acta Crystallogr. Sect. B* **52**, 16 (1996); **52**, 954 (1996).
- [43] S. M. Selbach, J. R. Tolchard, A. Fossdal, and T. Grande, *J. Solid State Chem.* **196**, 249 (2012).
- [44] See Supplemental Material at <http://link.aps.org/supplemental/10.1103/PhysRevB.95.064109> for the projected density of states of the hybrid functional calculations and for illustration of the dodecahedrally coordinated *d* states.
- [45] D. I. Khomskii, *Transition Metal Compounds* (Cambridge University Press, Cambridge, UK, 2014).
- [46] Z. Liao, M. Huijben, Z. Zhong, N. Gauquelin, S. Macke, R. J. Green, S. Van Aert, J. Verbeeck, G. Van Tendeloo, K. Held *et al.*, *Nat. Mater.* **15**, 425 (2016).
- [47] K. Momma and F. Izumi, *J. Appl. Crystallogr.* **44**, 1272 (2011).

## SUPPLEMENTARY INFORMATION

**A first principles study of the effect of (111)-strain on octahedral rotations and structural phases of LaAlO<sub>3</sub>**

Magnus Moreau,<sup>1</sup> Astrid Marthinsen,<sup>2</sup> Sverre M. Selbach,<sup>2</sup> and Thomas Tybell<sup>1,\*</sup>

1) Department of Electronics and Telecommunications, NTNU Norwegian University of Science and Technology, 7491 Trondheim, Norway

2) Department of Materials Science and Engineering, NTNU Norwegian University of Science and Technology, 7491 Trondheim, Norway

\*E-mail: [thomas.tybell@ict.ntnu.no](mailto:thomas.tybell@ict.ntnu.no)

## ORBITAL SPLITTING

As stated in the main manuscript the bottom of the conduction band consists of  $e_g$  orbitals of the La 5d states. In FIG S1, we show that these orbitals are lower in energy as compared to the  $t_{2g}$  orbitals due to the dodecahedral coordination of the 5d states where the  $t_{2g}$  orbitals have their lobes pointing towards the oxygen anions, while the lobes of the  $e_g$  orbitals are in between the oxygen. For compressive (001)-strain we see that the  $e_g$  orbitals are split with the  $d_{x^2-y^2}$  orbital reduced in energy as the top and bottom oxygens are pushed towards the nodes, while the  $d_{z^2-r}$  orbital is increased in energy as the oxygens are pushed towards the lobes of the  $d_{z^2-r}$  orbital. For tensile (001)-strain the situation is reversed and the  $d_{x^2-y^2}$  state is increased in energy and the  $d_{z^2-r}$  is reduced in energy. However, for the trigonal distortion from (111)-strain none of the oxygens are being pushed explicitly towards the nodes or the lobes of the different  $e_g$  orbitals, thus the  $e_g$  states are degenerate under (111)-strain.<sup>1</sup> (111)-strain does however affect the crystal field splitting of the  $t_{2g}$  orbitals, as they can be decomposed into the trigonal  $a_{1g}$  and  $e'_g$  orbitals,<sup>1</sup> however these orbitals are not at the bottom of the conduction band for LaAlO<sub>3</sub>, and thus does not affect the band gap.

## DENSITY OF STATES FROM THE HYBRID FUNCTIONAL CALCULATIONS

Figure S2 shows the density of states for representative values of strain as calculated with the HSE-sol hybrid functional.<sup>2</sup> As shown, the band gap of the unstrained system increases from 3.4 eV calculated with PBE-sol to 5.0 eV, significantly closer to the experimental bulk value of 5.6 eV.<sup>3</sup> Still, we observe here that the bottom of the conduction band consist of La 5d states, with the La 4f states is centered at the same energy window as the 5d  $t_{2g}$  orbitals, and thus do not affect the band gap. The Al s and p states are even higher in energy, which is not surprising given that the band gaps of the binary oxides La<sub>2</sub>O<sub>3</sub> and Al<sub>2</sub>O<sub>3</sub> (corundum) are in the order of 6 and 8.8 eV, respectively.<sup>4</sup> We further confirm the main findings from the PBE-sol calculations, the changes in band gap observed for (001)-strain is dominated by different splitting of the  $e_g$  states. While as the  $e_g$  states are degenerate for (111)-strain, the changes in the band gap here are dominated by the weaker effect of changes in the interatomic distances.

## REFERENCES

<sup>1</sup> D. I. Khomskii, *Transition Metal Compounds* (Cambridge University Press, 2014).

<sup>2</sup> L. Schimka, J. Harl, and G. Kresse, *J. Chem. Phys.* **134**, 024116 (2011).

<sup>3</sup> S.-G. Lim, S. Kriventsov, T. N. Jackson, J. H. Haeni, D. G. Schlom, A. M. Balbashov, R. Uecker, P. Reiche, J. L. Freeouf, and G. Lucovsky, *J. Appl. Phys.* **91**, 4500 (2002).

<sup>4</sup> G. Shang, P. W. Peacock, and J. Robertson, Appl. Phys. Lett. **84**, 106 (2004); E. O. Filatova and A. S. Konashuk, The Journal of Physical Chemistry C **119**, 20755 (2015).

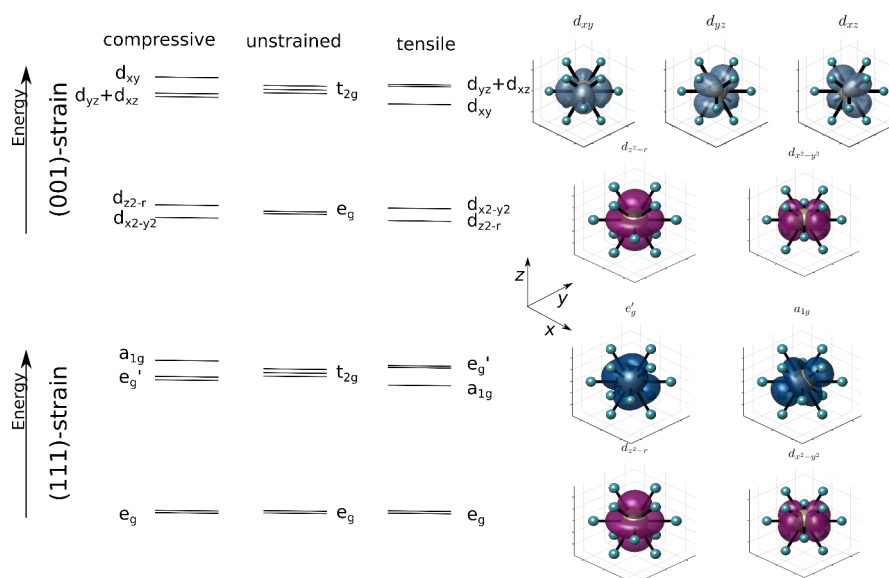


Figure S1, visualization of the different dodecahedrally coordinated  $La_{3d}$  orbitals and how they are affected by the crystal field splitting. The orbitals plotted is the 3d orbitals, while it is the 5d orbitals which are at the bottom of the conduction band, however going from 3d to 5d only adds additional radial nodes, and thus do not affect the character of the orbital splitting.

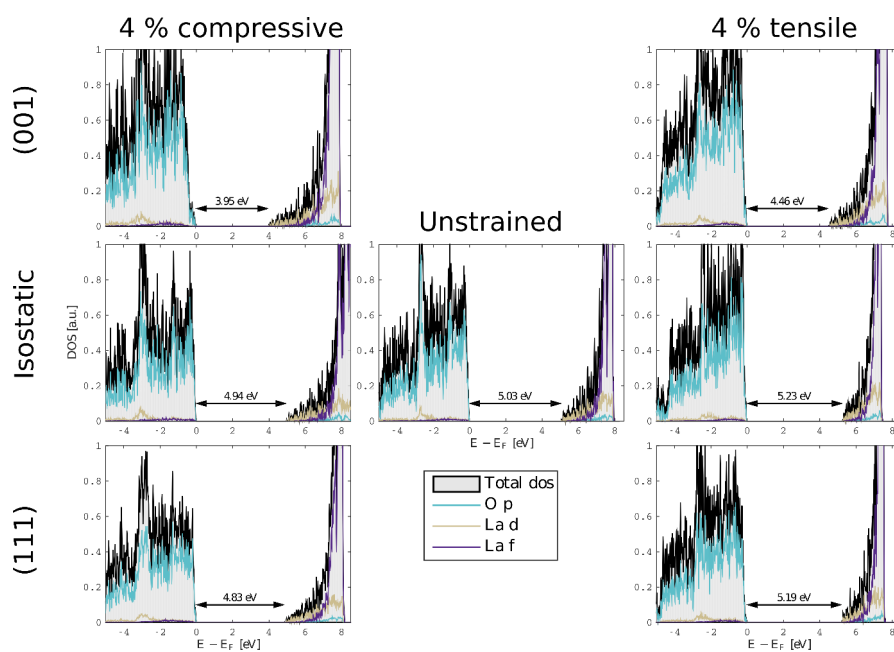


FIG S2, the density of states (DOS) calculated with the HSE-sol hybrid functional for different strain cases. For 4% compressive (111)-strain the three degenerate phases have similar DOS and band gap, thus only the results for the  $C2/c$  phase is shown.



# Strain-phonon coupling in (111)-oriented perovskite oxides

M. Moreau, A. Marthinsen, S. M. Selbach and T. Tybell

Published in Physical Review B **96**, 094109 (2017)

DOI: <http://dx.doi.org/10.1103/PhysRevB.96.094109>



## Strain-phonon coupling in (111)-oriented perovskite oxides

Magnus Moreau,<sup>1</sup> Astrid Marthinsen,<sup>2</sup> Sverre M. Selbach,<sup>2</sup> and Thomas Tybell<sup>1,\*</sup>

<sup>1</sup>*Department of Electronic Systems, NTNU Norwegian University of Science and Technology, 7491 Trondheim, Norway*

<sup>2</sup>*Department of Materials Science and Engineering, NTNU Norwegian University of Science and Technology, 7491 Trondheim, Norway*

(Received 22 June 2017; revised manuscript received 15 August 2017; published 20 September 2017)

Strain-phonon coupling, in terms of the shift in phonon frequencies under biaxial strain, is studied by density functional theory calculations for 20 perovskite oxides strained in their (111) and (001) planes. While the strain-phonon coupling under (001) strain follows the established, intuitive trends, the response to (111) strain is more complex. Here we show that strain-phonon coupling under (111) strain can be rationalized in terms of the Goldschmidt tolerance factor and the formal cation oxidation states. The established trends for coupling between (111) strain and in-phase and out-of-phase octahedral rotational modes as well as polar modes provide guidelines for rational design of (111)-oriented perovskite thin films.

DOI: 10.1103/PhysRevB.96.094109

### I. INTRODUCTION

Perovskite oxides, with general formula  $ABO_3$ , are known for their strong structure property coupling, making them susceptible to external stimuli. Hence, synthesis of epitaxial thin films on substrates with different lattice parameters open for strain engineering of physical properties. Strain engineering in the (001) plane has, e.g., been utilized to induce ferroelectricity in  $SrTiO_3$  (STO), effectively transforming the system from a paraelectric state with out-of-phase octahedral rotations in  $I4/mcm$  symmetry, represented by Glazer tilt system  $a^0a^0c^-$  [1], to a ferroelectric state with  $P4mm$  symmetry [2,3]. (001) strain has further enhanced the Curie temperature and polarization in  $BaTiO_3$  (BTO) [4] or induced multiferroicity in  $SrMnO_3$  (SMO) [5]. These strain-induced changes of functional properties are often linked to certain phonon modes, which either condense or have their amplitudes altered by the imposed strain. Important phonon modes for functional properties of perovskite oxides include rotations/tilts of the oxygen octahedra and polar cation displacements. Strain-phonon coupling, the effect of strain on the phonon modes, has been much studied for (001) strain over the last decades [3,6–12]. As shown in Fig. 1, it has been established for octahedral rotations that compressive (001) strain softens rotations around the out-of-plane axis, while tensile (001) strain softens rotations around the in-plane axes [6–8,10,11]. Similarly, out-of-plane polar modes are softened under (001) compression, while in-plane polar phonon modes are softened under tensile (001) strain [2–4,9,10,12].

An interesting proposition is to rely on higher index surfaces such as (111) [13], because its structure resembles a buckled honeycomb lattice similar to two-dimensional (2D) materials, giving prospect for novel topological properties [14]. It has been shown experimentally that (111) compression in rare earth nickelates ( $RNiO_3$ ) can result in a polar metal [15], (111) strain of  $PbTiO_3$  grown on  $LaAlO_3$  (LAO) (111) substrates displayed complex dislocations different to what is expected for low index interfaces [16], and compressive (111) strain in  $BiFeO_3$  results in a monodomain polar phase [17]. In addition, theoretical studies of strain in the (111) plane has revealed

different responses of the octahedral rotations in LAO [18] and the polar modes of BTO [19] and  $PbTiO_3$  [20], as compared to (001) strain. Furthermore, in-plane octahedral rotations in LAO under compressive (111) strain has been shown to exhibit a Goldstone-like behavior [18]. Finally, we note that a mismatch between out-of-phase and in-phase octahedral rotations across an interface can induce novel magnetic states [21], which can induce a magnetic moment without charge transfer in (111)-oriented thin films [22]. Thus understanding general trends for how (111) strain affects phonon frequencies, and developing routes to tailor soft and hard phonon modes in a material, is essential for rational design of new functional materials for electronic and spintronic applications.

In order to advance the overall understanding of the interplay between epitaxial strain, applied to (111)-oriented thin films, and octahedral rotations and polar modes, we present a density functional theory (DFT) study of the (111)-strain response of phonon frequencies for a large number of perovskite oxides. Results for (001) strain are also presented for comparison. Data are presented for III-III, II-IV, and I-V perovskite systems, focusing mainly on  $d^0$  or  $d^{10}$  materials to minimize effects from magnetism and strongly correlated electrons. However, the general trends presented should still be valid for other numbers of  $d$  electrons [23,24], as demonstrated here for the  $d^5$  material  $LaFeO_3$  (LFO). It is shown that the result of phonon-strain coupling for (111) strain can be related to the Goldschmidt tolerance factor [25]  $t$  describing the size mismatch between the A and B cation. Furthermore, while (001) strain typically affects in-phase and out-of-phase rotations similarly, this is not the case for (111) strain.

The article is structured as follows: first, the methodology including the calculation details is presented, before two examples are given to highlight the difference in phonon response for (001) and (111) strain. Finally, the general results for (111) strain on relevant phonon modes are presented, emphasizing the effect on octahedral rotations and polar displacements of the B cations.

### II. METHODOLOGY

This work focuses on three different types of modes, at different locations in the Brillouin zone, which have all been shown to be important for different functional properties of

\*thomas.tybell@iet.ntnu.no



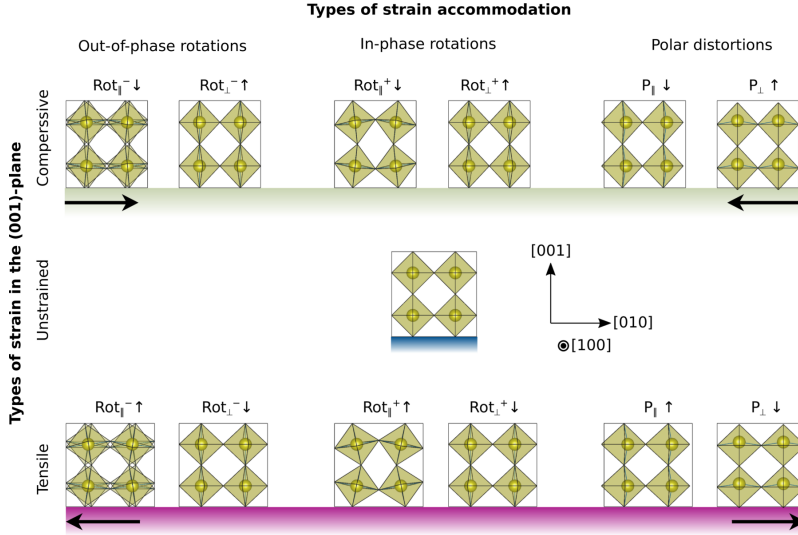


FIG. 1. Strain-phonon coupling for (001) strain. The sketches show the different phonon modes in  $2 \times 2 \times 2$  supercells, A cations and oxygen atoms omitted for clarity. The modes discussed in this paper are out-of-phase rotations denoted  $\text{Rot}^-$ , in-phase rotations denoted  $\text{Rot}^+$ , and polar distortions of the B cation denoted  $P$ . Subscript  $\parallel$  and  $\perp$  denotes in-plane and out-of-plane modes, respectively. Arrow up (down) denotes that the preceding mode type is softer (harder) for that type of strain.

perovskite oxides [6]. These modes are: out-of-phase octahedral rotations, where every second layer along the rotation rotates in the opposite direction, centered at the  $R = (\frac{1}{2}, \frac{1}{2}, \frac{1}{2})$  point [Fig. 2(a)], in-phase rotations, where every second layer along the rotation axis rotates in the same direction, centered at the  $M = (\frac{1}{2}, \frac{1}{2}, 0)$  point [Fig. 2(b)], and polar displacements of the B cation at the  $\Gamma = (0, 0, 0)$  point [Fig. 2(c)]. For a cubic perovskite, each mode is triply degenerate. However, under quadratic in-plane strain they are typically split into two degenerate in-plane modes and one out-of-plane mode [18]. For (001) strain the out-of-plane modes have rotation or polar axis along [001], while it has in-plane axes along [100] and [010], as shown in Fig. 1. On the other hand, for (111) strain the out-of-plane axis is along [111], while the in-plane axes are along the  $[1\bar{1}0]$  and  $[11\bar{2}]$  directions. Hence, while the in-plane modes for (001) strain has the same symmetry, this is not the case for (111) strain [18]. All crystallographic directions are given in the pseudocubic setting, unless otherwise stated.

To understand the general trends of these modes under strain, the phonon frequencies have been calculated for systems with different tolerance factors and oxidation states of the A and B cations. Since the compressibility of the cations are significantly different for III-III, II-IV, and I-V perovskites, the effect of the oxidation state is also considered [26]. The calculations were performed for both (001) and (111) strain, in order to elucidate possible differences between these two strain planes. The III-III perovskites studied in this work are (ground state space group in parentheses): LAO ( $R\bar{3}c$  [27])  $\text{NdAlO}_3$  (NAO,  $R\bar{3}c$  [28]),  $\text{LaGaO}_3$  (LGO,  $Pnma$  [29,30])

LFO ( $Pnma$  [31]),  $\text{YAlO}_3$  (YAO,  $Pnma$  [32])  $\text{GdScO}_3$  (GSO,  $Pnma$  [30]), and  $\text{DyScO}_3$  (DSO,  $Pnma$  [33]). The II-IV perovskites include BTO ( $R3m$  [34]) STO ( $I4/mcm$  [35])  $\text{BaZrO}_3$  (BZO,  $Pm\bar{3}m$  [36]),  $\text{CaTiO}_3$  (CTO,  $Pnma$  [37]), and  $\text{SrZrO}_3$  (SZO,  $Pnma$  [38]). While the I-V perovskites studied in this work are  $\text{KNbO}_3$  (KNO,  $R3m$  [39]),  $\text{KTaO}_3$  (KTO,  $Pm\bar{3}m$  [40]),  $\text{NaTaO}_3$  (NTO,  $Pnma$  [41]),  $\text{NaNbO}_3$  (NNO, coexisting  $R3m$  and  $Pbcm$  phases [42]), and  $\text{AgNbO}_3$  (ANO,  $Pmc2_1$  [43]). In addition, the materials  $\text{MgTiO}_3$  (MTO,  $R\bar{3}$  [44]) and  $\text{LiNbO}_3$  (LNO,  $R3c$  [45]), which are only metastable in a perovskite phase, were also analyzed as perovskites in order to extend trends for II-IV and I-V materials to  $t$  below 0.9. In order to take into account that these 20 different perovskites crystallize in different space groups with different levels of distortions, the methodology by Hong *et al.* [24] was employed. This method consists of analyzing changes in phonon frequencies in a highly symmetric phase. This phase has cubic  $Pm\bar{3}m$  symmetry when the material is unstrained, while under (001) strain it becomes tetragonal with  $P4/mmm$  symmetry and under (111) strain it becomes rhombohedral with  $R\bar{3}m$  symmetry.

The DFT calculations were done with the Vienna *ab initio* simulation package (VASP, version 5.3.3) [46,47] employing the projector augmented wave method (PAW) [47,48]. The Perdew-Burke-Ernzerhof generalized gradient approximation for solids (PBEsol) was chosen as it has been shown to accurately reproduce the crystal structure and lattice parameters of solids [49]. The different material systems were first relaxed in the high symmetry, cubic  $Pm\bar{3}m$  phase using  $1 \times 1 \times 1$

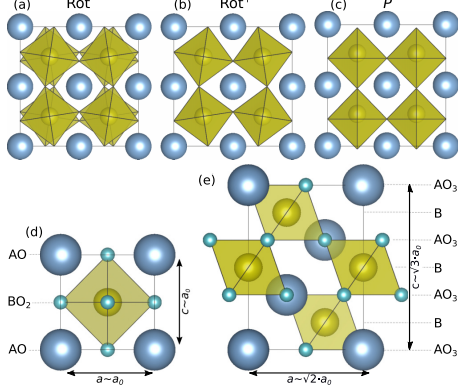


FIG. 2. (a)–(c) Three important phonon modes for perovskite oxides, here depicted in  $2 \times 2 \times 2$  supercells which were used for the phonon calculations. (a) Visualization of the out-of-phase rotations at the  $R$  point of the Brillouin zone, denoted  $\text{Rot}^-$ . (b) Visualization of the in-phase rotations at the  $M$  point of the Brillouin zone, denoted  $\text{Rot}^+$ . (c) Visualization of the polar distortions of the B cation at  $\Gamma$  point of the Brillouin zone, denoted  $P$ . In (a)–(c) the oxygen atoms are omitted for clarity. (d) and (e) Calculation cells used for (001) and (111) strain, respectively, along with the relations between the lattice vectors and the stacking sequence.

cells. The only exception to this is LFO, where a  $2 \times 2 \times 2$  supercell was used in order to properly account for  $G$ -type antiferromagnetism [50]. As shown in Fig. 2(d), for (001) strain the unit cells was arranged such that the  $a$  and  $b$  lattice vectors, pointing along the in-plane [100] and [010] direction, respectively, were fixed, while the  $c$  lattice vector, which is along the out-of-plane [001] direction, was allowed to relax [8]. As shown in Fig. 2(e), for (111) strain the calculation cells were rotated with the following rotation matrix:

$$R = \begin{bmatrix} 1 & 0 & 1 \\ \bar{1} & 1 & 1 \\ 0 & \bar{1} & 1 \end{bmatrix}, \quad (1)$$

such that the  $a$  and  $b$  lattice vectors were along  $[1\bar{1}0]$ - and the  $[01\bar{1}]$ -pseudocubic directions, respectively, while the  $c$  lattice vector was along the  $[111]$  direction. With this configuration, the (111) strain could be introduced by fixing in the effective  $a$  and  $b$  lattice vectors while the cell was allowed to relax along the  $c$  lattice vector. The minimal unit cell for the (111)-strain calculations is a  $\sqrt{2} \times \sqrt{2} \times \sqrt{3}$  supercell containing 15 atoms, while a  $\sqrt{2} \times \sqrt{2} \times 2\sqrt{3}$  cell containing 30 atoms is needed to include the  $G$ -type antiferromagnetism of LFO.

The plane-wave energy cutoff was set to 550 eV for all calculations, except the ones including Li, where it was increased to 650 eV. For the  $1 \times 1 \times 1$  cells an  $8 \times 8 \times 8$   $\Gamma$ -centered  $k$ -point mesh was used, while a  $6 \times 6 \times 5$  mesh was used for the  $\sqrt{2} \times \sqrt{2} \times \sqrt{3}$  cells used for (111)-strain calculations. Corresponding  $k$ -point densities were used for the supercells. The electronic structure was minimized until

the energy difference between two steps were smaller than  $10^{-9}$  eV, while the ionic optimization was minimized until the energy difference between two subsequent steps was smaller than  $10^{-8}$  eV. The recommended PAW potentials supplied with the VASP package [51] were used for Li, Na, K, Mg, Ca, Sr, Ba, Sc, Y, La, Nd, Gd, Dy, Ti, Zr, Nb, Ta, Fe, Ag, Al, Ga, and O. These have electronic configurations  $1s^2 2s^1$ ,  $2p^6 3s^1$ ,  $3s^2 3p^6 4s^1$ ,  $3s^2$ ,  $3s^2 3p^6 4s^2$ ,  $4s^2 4p^6 5s^2$ ,  $5s^2 5p^6 6s^2$ ,  $3s^2 3p^6 3d^1 4s^2$ ,  $4s^2 4p^6 4d^1 5s^2$ ,  $4s^2 4p^6 4d^1 5s^2$ ,  $4p^6 5d^1 6s^2$ ,  $4p^6 5d^1 6s^2$ ,  $3s^2 3p^6 3d^2 4s^2$ ,  $4s^2 4p^6 4d^2 5d^2$ ,  $4s^2 4p^6 4d^3 5s^2$ ,  $5p^6 5d^3 6s^2$ ,  $3p^6 3d^6 4s^2$ ,  $4d^9 5s^2$ ,  $3s^2 3p^1$ ,  $3d^{10} 4s^2 4p^1$ , and  $2s^2 2p^4$ , respectively. Hence, the  $f$  electrons were treated as core electrons for Nd, Gd, and Dy. The GGA +  $U$  approach as introduced by Dudarev *et al.* [52] was used for La  $f$  states and the Fe  $d$  states with a  $U$  value of 10 and 3 eV, respectively [11]. Phonon calculations were performed utilizing the frozen phonon approach [53] and analyzed with the phonopy software [54]. The phonon calculations were done in  $2 \times 2 \times 2$  supercells, and it was confirmed that all phonon calculations resulted in three degenerate acoustic modes at approximately zero frequency.

Two different measures are introduced to quantify the effect of strain on phonon structure,  $\Delta f$  the frequency difference between in-plane and out-of-plane modes, and  $df/d\epsilon$ , the derivative of the phonon frequency with respect to strain. The frequency difference between in-plane and out-of-plane modes is defined as

$$\Delta f = \begin{cases} f_{\parallel} - f_{\perp} & \text{if } \epsilon < 0 \\ f_{\perp} - f_{\parallel} & \text{if } \epsilon > 0 \end{cases}, \quad (2)$$

where  $f_{\parallel}$  and  $f_{\perp}$  are the frequencies of the in-plane and out-of-plane modes, respectively. Here  $\epsilon$  is the strain with respect to the high symmetric cubic phase defined as  $\epsilon = (a - a_0)/a_0$ , where  $a_0$  is the relaxed lattice parameter in the cubic  $Pm\bar{3}m$  phase. As illustrated in Fig. 1, this definition of  $\Delta f$  ensures that changing the sign of  $\epsilon$  does not change the sign of  $\Delta f$ , and that  $\Delta f$  is positive for (001) strain for the modes considered here. In this work  $\Delta f$  is evaluated at  $\pm 1\%$  strain, and the average value is presented; this value is chosen to minimize numerical errors that can take place close to zero strain in the calculations, and to ensure that nonlinear effects prominent at large levels of strain are minimized.  $df/d\epsilon$  is taken as a measure of how susceptible a phonon mode is to be destabilized by strain.  $df/d\epsilon$  is evaluated at  $\epsilon \approx 0$ , hence a positive (negative)  $df/d\epsilon$  corresponds to a mode being softened by compressive (tensile) strain. While  $\Delta f$  directly compares the in-plane and out-of-plane modes of the same type,  $df/d\epsilon$  is more suitable when comparing different types of modes. Illustration of the atomic structures were made with VESTA [55].

### III. RESULTS

#### A. Lattice parameters and Poisson's ratios

The effect of strain is closely coupled to the Poisson's ratio of a material. In Table I the relaxed lattice parameters of the aristotype cubic phase, as well as calculated Poisson's ratios  $\nu$  for (001) and (111) strain are presented. Under a given amount of strain, the  $\nu$  will determine the amount of distortion in the high-symmetry phases, for discussion about the effect see the Supplemental Material [56]. The overall

MOREAU, MARTHINSEN, SELBACH, AND TYBELL

PHYSICAL REVIEW B **96**, 094109 (2017)

TABLE I. Tolerance factor  $t$  [57], relaxed lattice constant  $a_0$  in the aristotype cubic phases, and Poisson's ratio  $\nu$  for (001) and (111) strain for the material systems studied. The table is sorted first with respect to the oxidation state of the A and B cations, then after declining tolerance factor.

Material system	Abbreviation	$t$	$a_0$ (Å)	$\nu_{(001)}$	$\nu_{(111)}$
III-III					
LaAlO <sub>3</sub>	LAO	0.995	3.800	0.272	0.184
NdAlO <sub>3</sub>	NAO	0.975	3.734	0.250	0.193
LaGaO <sub>3</sub>	LGO	0.956	3.890	0.275	0.245
LaFeO <sub>3</sub>	LFO	0.942	3.912	0.272	0.277
NdGaO <sub>3</sub>	NGO	0.936	3.835	0.258	0.261
YAlO <sub>3</sub>	YAO	0.867	3.676	0.231	0.214
GdScO <sub>3</sub>	GSO	0.866	3.976	0.160	0.333
DyScO <sub>3</sub>	DSO	0.856	3.967	0.157	0.340
II-IV					
BaTiO <sub>3</sub>	BTO	1.063	3.984	0.260	0.213
SrTiO <sub>3</sub>	STO	1.001	3.895	0.228	0.245
BaZrO <sub>3</sub>	BZO	1.000	4.190	0.206	0.273
CaTiO <sub>3</sub>	CTO	0.946	3.844	0.216	0.279
SrZrO <sub>3</sub>	SZO	0.942	4.133	0.180	0.303
MgTiO <sub>3</sub>	MGO	0.848	3.802	0.229	0.331
I-V					
KNbO <sub>3</sub>	KNO	1.090	3.986	0.155	0.286
KTaO <sub>3</sub>	KTO	1.085	3.989	0.146	0.290
AgNbO <sub>3</sub>	ANO	0.974	3.948	0.202	0.382
NaNbO <sub>3</sub>	NNO	0.972	3.942	0.144	0.326
NaNbO <sub>3</sub>	NTO	0.968	3.949	0.134	0.329
LiNbO <sub>3</sub>	LNO	0.853	3.922	0.143	0.349

trend for  $\nu$  is opposite for systems under (001) and (111) strain.  $\nu_{(001)}$  increases for increasing tolerance factor, while  $\nu_{(111)}$  is reduced for increasing tolerance factor. For materials with similar  $t$  but with different oxidation states,  $\nu_{(001)}$  goes from largest to smallest in the order of III-III, II-IV, and I-V, while for  $\nu_{(111)}$  it goes from largest to smallest in the opposite order, I-IV, II-IV, and III-III. This can be rationalized from the difference in compressibility of the A-O and B-O bonds for III-III, II-IV, and I-V perovskites, respectively [26]. In the case of (001) strain, the strain is parallel to the in-plane B-O bonds, while for (111) strain the strain is parallel to the in-plane A-O bonds [see Figs. 2(d) and 2(e)]. Hence, for (001) strain the compressibility of the B-O bonds are dominating and lowest for I-V perovskites, while for (111) strain it is the compressibility of the A-O bonds, largest for I-V perovskites, that is the most important [26]. Deviations from these trends are observed from materials with different electron configurations, such as LFO for III-III perovskites, the difference between Ti and Zr in II-IV perovskites, and ANO for I-V perovskites.

We now exemplify the introduced measures  $\Delta f$  and  $df/de$  through two materials either susceptible to polar instabilities, STO, or rotational instabilities, NTO. Corresponding data for the other material systems are given in the Supplemental Material, Figs. S2–S19 [56].

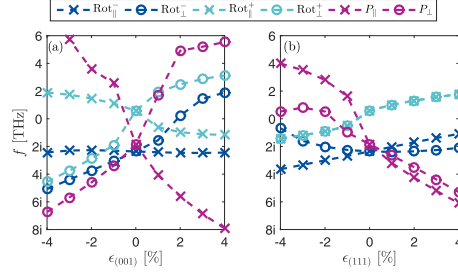


FIG. 3. The frequencies of the three different phonon modes considered as a function of in-plane strain in the (a) (001) plane and (b) (111) plane for SrTiO<sub>3</sub> (STO). Under strain the phonon frequencies are split into two degenerate perpendicular in-plane modes denoted with a subscript  $\parallel$ , and one out-of-plane mode denoted with a subscript  $\perp$ . The three different modes considered are out-of-phase rotations denoted by Rot<sup>-</sup>, in-phase rotations denoted by Rot<sup>+</sup>, and polar displacement of the B cation denoted by P. For (001) strain the in-plane directions are [100] and [010], while the out-of-plane direction is [001]. For (111) strain the in-plane directions are [110] and [112] while the out-of-plane direction is [111]. The dashed lines are guides to the eye.

#### B. Example 1: II-IV SrTiO<sub>3</sub>, $t = 1.001$

STO, having a tolerance factor close to unity [35,57], exhibit a large strain-phonon coupling [2,3], and could in principle condensate any of the three different types of phonon modes studied here. In order to calculate  $\Delta f$  and  $df/de$ , the phonon frequencies for the central modes are calculated as a function of both (001) and (111) strain. At 0% strain, STO have both imaginary out-of-phase rotations and polar modes, while the in-phase rotations are real, but relatively low in frequency (0.58 THz). For (001) type strain, compressive strain softens rotational modes around the out-of-plane axis and out-of-plane polar modes, while tensile strain softens rotational modes around the in-plane axis and in-plane polar modes, as shown in Fig. 3(a). Based on the data, a positive  $\Delta f$  is deduced for all three kinds of modes under (001) strain, as expected from the definition of  $\Delta f$  [2,7]. For (111) strain on the other hand, different trends are observed. It is shown in Fig. 3(b) for the out-of-phase rotations that STO follows the same trend as was found for LAO [18], in-plane rotations around the [110] and [112] are softened under compressive strain while out-of-plane rotations around [111] are softened for tensile strain, resulting in a negative  $\Delta f_{rot-}$ . In contrast to the case for (001) strain, (111) strain does not split the in-phase rotations into two in-plane components and one out-of-plane component. Instead, the three in-phase rotations are degenerate for all (111)-strain values, i.e.,  $\Delta f_{rot+} = 0$ . However, (111) strain changes the frequencies of the in-phase rotations, which for STO become imaginary at compressive strain. Thus depending on the competition between the other modes, the in-phase rotations could condensate, as has been shown experimentally for (001)-strained La<sub>1-x</sub>Sr<sub>x</sub>MnO<sub>3</sub> [58]. Finally, the polar modes follow the same trend as was earlier deduced for BTO under (111) strain [19,20], having both the

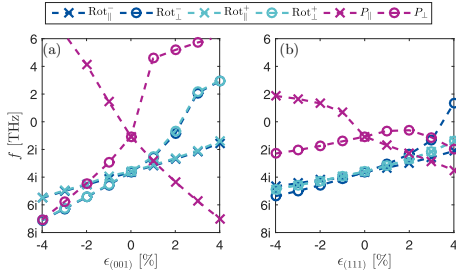


FIG. 4. The frequencies of the three different phonon modes considered as a function of in-plane strain in the (a) (001) plane and (b) (111) plane for NaTaO<sub>3</sub> (NTO). Under strain the phonon frequencies are split into two degenerate perpendicular in-plane modes denoted with a subscript  $\parallel$ , and one out-of-plane mode denoted with a subscript  $\perp$ . The three different modes considered are out-of-phase rotations denoted by Rot $^-$ , in-phase rotations denoted by Rot $^+$ , and polar displacement of the B cation denoted by P. For (001) strain the in-plane directions are [100] and [010], while the out-of-plane direction is [001]. For (111) strain the in-plane directions are [1 $\bar{1}$ 0] and [11 $\bar{2}$ ], while the out-of-plane direction is [111]. The dashed lines are guides to the eye.

in-plane and out-of-plane polar modes softened for tensile strain, i.e.,  $df_{\text{pol}}/d\epsilon_{(111)} < 0$  for both in-plane and out-of-plane modes. Thus, by compressively straining STO in the (111) plane, any ferroelectric instability will be suppressed; while by increasing (111) tension in STO one could condense both an in-plane and an out-of-plane polarization component.

#### C. Example 2: I-V NaTaO<sub>3</sub>, $t = 0.968$

NTO, having a bulk  $Pnma$  symmetry [41] with an  $a^-b^+a^-$  Glazer tilt pattern [1], has a tolerance factor  $t = 0.968$  [57] and is thus prone to octahedral rotations and tilts. The phonon frequencies are plotted as a function of (001) and (111) strain in Fig. 4. As seen, for 0% strain both the in-phase and out-of-phase rotations have a large imaginary frequency. Based on this, both modes are expected to condensate, consistent with the  $a^-b^+a^-$  bulk tilt pattern. For (001) strain, depicted in Fig. 4(a), NTO follows the same trends as STO, for compressive (001) strain out-of-plane rotational and polar modes are softer, while for tensile (001) strain the in-plane rotational and polar modes are softer. Hence, in line with the definition, all modes have a positive  $\Delta f$ . From the calculated phonon frequencies as a function of strain it is inferred that both the in-plane and out-of-plane rotations have a positive  $df_{\text{rot}\pm}/d\epsilon$  for both (001) and (111) strain. This can be understood by the low compressibility of the B-O bonds in I-V perovskites, and that the volume is reduced (increased) under compressive (tensile) strain making rotations softer (harder). Furthermore, we see that, similar to STO, the polar modes exhibit larger positive  $df/d\epsilon$  than the rotational modes under (001) strain, pointing towards a polar transition under sufficiently large strain. However, while NTO follows the same trends as STO for (001) strain, the response to (111) strain is

considerably different [Fig. 4(b)]. The splitting of out-of-phase modes are not reversed for (111) strain with respect to (001) strain. For NTO the out-of-plane out-of-phase rotations are preferred for compressive strain, while in-plane out-of-phase rotations are preferred for tensile strain, i.e.,  $\Delta f_{\text{rot}-}$  is positive, similar to (001) strain. For the polar modes,  $df/d\epsilon$  for the out-of-plane polarization is similar to what is observed for (001) strain, hence  $df_{\text{pol}\perp}/d\epsilon_{(111)} > 0$  at zero strain. However, for tensile strain values larger than 2% it saturates, and shifts sign. As  $df_{\text{rot}\pm}/d\epsilon_{(111)} > 0$  and  $df_{\text{pol}\perp}/d\epsilon_{(111)} < 0$  for  $\epsilon > 2\%$ , a ferroelectric transition is also expected at about 3%-4% tensile strain. The shift in sign of  $df_{\text{pol}\perp}/d\epsilon_{(111)}$  is consistent with the polar modes having fewer symmetry restrictions than the rotational modes, since both the A and B cations can contribute to the displacement. This contributes to a more nonlinear frequency-strain response of the polar modes as compared to the rotational modes. For compressive (111) strain the displacement is more dominated by A sites than B sites (see Fig. S20 in the Supplemental Material [56]), in agreement with BTO under hydrostatic pressure [59].

#### D. Overview of the strain-phonon coupling in the (111) orientation

As discussed in the previous sections, STO and NTO have significant different strain-phonon couplings, in disagreement with (001) strain for which there is a universal strain response [6]. In analogy to Fig. 1, which summarizes the strain-phonon coupling for (001) strain, we present an overview of the strain-phonon coupling for (111) strain in Fig. 5 clearly displaying a different strain response as compared to (001) strain. The tolerance factor  $t$ , a measure of stress on the A-O and B-O bonds in the unstrained  $Pm\bar{3}m$  phase, is taken as a control parameter [60]. As shown in Fig. 5, for low tolerance factors ( $\sim 0.9$ ), the strain-phonon coupling in the (111) plane for out-of-phase rotations and polar modes is similar to what is observed for (001) strain, i.e.,  $\Delta f_{\text{rot}-} > 0$ , and  $df_{\text{pol}\perp}/d\epsilon_{(111)}$  and  $df_{\text{pol}\parallel}/d\epsilon_{(111)}$  have the opposite sign. In contrast, for larger tolerance factors ( $\sim 1.0$ ), the out-of-phase rotations display opposite splitting compared to (001) strain. The in-plane and out-of-plane polar modes have the same sign, hence affected in the same manner for both compressive and tensile strain, i.e.,  $\Delta f_{\text{rot}-} < 0$ , and  $df_{\text{pol}\perp}/d\epsilon_{(111)}$  and  $df_{\text{pol}\parallel}/d\epsilon_{(111)}$  have the same sign. Finally, in-phase rotations are not split under (111) strain regardless of tolerance factor.

In the following sections, we confirm these trends by analyzing all 20 different oxides. Furthermore, we show that the exact tolerance factor where these changes in strain-phonon coupling occur is sensitive to the oxidation state of the A and B cations.

#### E. Out-of-phase rotations

The two measures introduced above ( $\Delta f$  and  $df/d\epsilon$ ) will now be used to analyze trends for rotational and polar modes in various perovskites under (111)-type strain. First the out-of-phase rotational modes [illustrated in Fig. 2(a)] are analyzed. Such modes were shown to have an inverse splitting between in-plane and out-of-plane modes between (001) and (111) strain for STO and LAO [18], but not for NTO. In

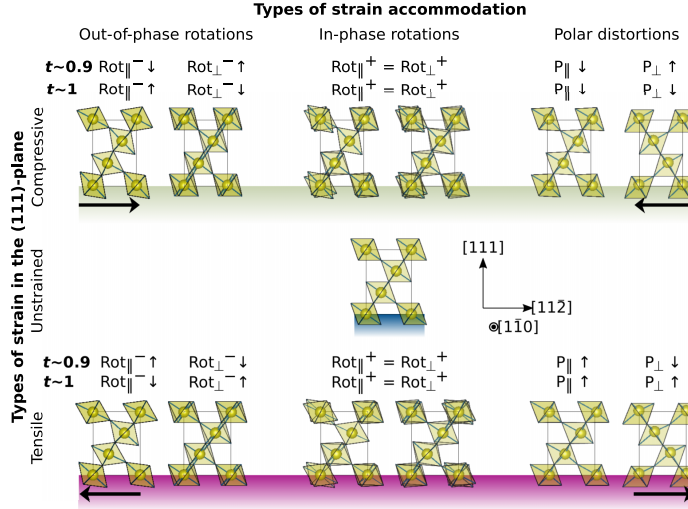


FIG. 5. Strain-phonon coupling for (111) strain. The schematic shows the different phonon modes in  $\sqrt{2} \times \sqrt{2} \times \sqrt{3}$  supercells, A cations and oxygen omitted for clarity. Arrow up (down) denotes that the preceding mode type is softer (harder) for that type of strain. The strain-phonon coupling for (111) strain is different for high ( $t \sim 1$ ) and low ( $t \sim 0.9$ ) tolerance factors, as discussed in the text. The exact crossover depends on the relative charge of the A and B cations. For low tolerance factors, the response is similar to what is known for (001) strain, except for in-plane rotations, which are not split for (111) strain, while for high tolerance factors, different responses are seen.

Fig. 6  $\Delta f_{\text{rot-}}$  vs tolerance factor is shown for the materials considered in this study. For (001) strain  $\Delta f_{\text{rot-}}$  is always positive [Fig. 6(a)], however  $\Delta f_{\text{rot-}}$  is reduced with reducing tolerance factor approaching zero for  $t$  less than 0.9. Thus, for

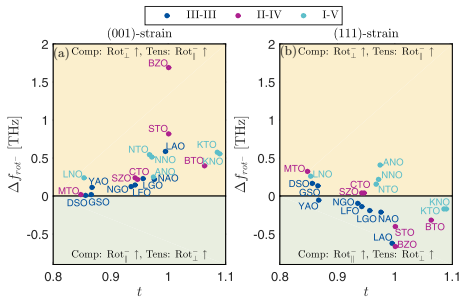


FIG. 6. The degree of splitting  $\Delta f_{\text{rot-}}$  between in-plane and out-of-plane out-of-phase rotations as a function for  $\pm 1\%$  (a) (001) strain and (b) (111) strain as a function of tolerance factor  $t$ . A positive  $\Delta f_{\text{rot-}}$ , yellow area, indicates (001)-like splitting where out-of-plane rotations are softer for compressive (comp) strain and out-of-plane rotations are softer for tensile (tens) strain. In the green area an opposite splitting is seen, where in-plane rotations are softer for comp strain, and out-of-plane rotations are softer for tens strain. See Table I for abbreviations.

all the materials studied here, out-of-plane rotations are softer for compressive (001) strain and in-plane rotations are softer for tensile strain as expected.

For (111) strain a different trend is observed [Fig. 6(b)]. When the tolerance factor is approximately unity  $\Delta f_{\text{rot-}}$  is negative, i.e., in-plane rotations are softer for compressive strain and out-of-plane rotations are softer for tensile strain. However, as the tolerance factor is reduced,  $\Delta f_{\text{rot-}}$  changes sign. The critical tolerance factor where this change occurs appears to be largest for I-V perovskites and lowest for III-III perovskites. However, no clear monotonic trend in the  $\Delta f_{\text{rot-}}$  as a function of tolerance factor can be inferred.

To better understand this tolerance factor dependence of  $\Delta f_{\text{rot-}}$  an analysis of how the derivative of phonon frequencies change as a function of strain at 0% strain is presented. The evolution of  $d f_{\text{rot-}}/d\epsilon$  with tolerance factor for in-plane modes for (001) strain and out-of-plane modes for (111) strain is depicted in Fig. 7. As can be seen, there is a clear trend with increased  $\Delta f_{\text{rot-}}$  values for lower tolerance factors and lower oxidation states of the A cation. The different oxidation states, represented by different colors, each have an almost linear dependence with tolerance factor. However, when analyzing the derivatives for the out-of-plane modes for (001) strain and the in-plane modes for (111) strain no such clear trend is found, as shown in Fig. 8.

Three materials, STO, BZO, and ANO, are deviating from the trends discussed above. Interestingly these same materials deviate from the trend for both (001) strain and (111) strain. For STO and BZO the deviations in the derivative of the

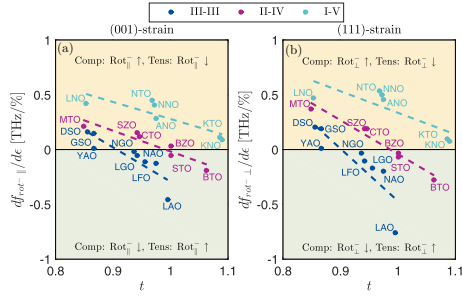


FIG. 7. Derivative of the in-plane out-of-phase rotational modes with respect to (a) (001) strain and (b) (111) strain. A positive  $df/de$ , yellow area, means that the respective mode is softened by compressive (comp) strain and hardened by tensile (tens) strain, while a negative  $df/de$ , green area, means that the respective mode is softened tens strain and hardened for comp strain and softened for tens strain. See Table I for abbreviations. The dashed lines are guides to the eye, based on linear fits to the data.

out-of-plane rotations for (001) strain and in-plane rotations for (111) strain is consistent by the fact that these two materials both have a tolerance factor very close to unity. When the tolerance factor is unity ( $1 \pm 0.005$ ) the cubic phase with degenerate phonon modes becomes stable, and a small amount of strain can then result in destabilization of different modes. This is consistent with the increase of the  $df/de$  values for STO and BZO. For ANO on the other hand, it is the fact that ANO has a significantly larger Poisson's ratio (Table I) than the other I-V perovskites. A larger Poisson's ratio increases the octahedral distortions (see the Supplemental Material, Fig. S1 [56]), and hence weakens the coupling between the strain and the phonon frequencies.

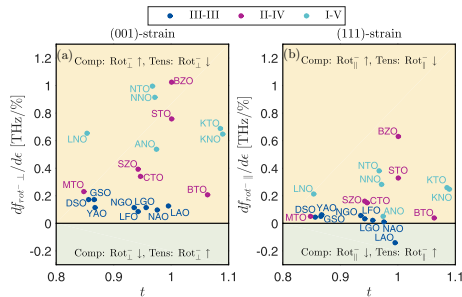


FIG. 8. Derivative of the out-of-plane out-of-phase rotational modes with respect to (a) (001) strain and (b) (111) strain. A positive  $df/de$ , yellow area, means that the respective mode is softened by compressive (comp) strain and hardened by tensile (tens) strain, while a negative  $df/de$ , green area, means that the respective mode is softened tens strain and hardened for comp strain and softened for tens strain. See Table I for abbreviations. No trend lines are added, as no given trend is seen.

Combining these results, the change in sign of the splitting  $\Delta f_{rot-}$  for (111) strain can be rationalized by the  $AO_3 + B + AO_3 + B + \dots$  stacking along the (111) direction, as shown in Fig. 2(e). For large tolerance factors the A cation and the oxygen atoms are in the same plane, hence a negative  $\Delta f_{rot-}$ . The exact crossover point from negative to positive  $\Delta f_{rot-}$  depends on the oxidation state as shown in Fig. 6(b). Under compressive (tensile) strain the oxygen atoms are closer to (further away from), the A cation, hence the A cation is forcing the oxygen atoms to rotate in-plane (out-of-plane) to optimize its coordination. However, when the A cation is smaller (i.e., reduced tolerance factor), the elastic forces it exerts on the oxygen atoms are reduced and  $\Delta f_{rot-}$  becomes positive in-line with what is expected for (001) strain. Similarly, when the oxidation state of the A cation is lowered, the force it exerts on the oxygen atoms is reduced. Hence, this geometric argument is consistent with  $\Delta f_{rot-}$  changing sign for largest  $t$  for I-V perovskites, intermediate  $t$  for the II-IV perovskites, and lowest  $t$  for III-III perovskites (Fig. 7). There is also a duality between in-plane modes for (001) strain and out-of-plane modes for (111) strain, which follow the trends, and a similar duality between out-of-plane modes for (001) strain and in-plane modes for (111) strain which does not follow a given trend.

#### F. In-phase rotations

The in-phase rotational modes [illustrated in Fig. 2(b)] were not split by (111) strain for STO [Fig. 3(b)] nor NTO [Fig. 4(b)], i.e.,  $\Delta f_{rot+} = 0$ . Under (111) strain  $\Delta f_{rot+}$  was in fact found to be zero for all materials considered in this study, hence no splitting of in-phase rotations is found. The observation that  $\Delta f_{rot+} = 0$  for all perovskites under quadratic (111) strain can be understood from a symmetry argument. Any in-phase or untilted system requires a mirror plane perpendicular to the rotations axis [1], and these mirror planes are removed as the pseudocubic cell angle  $\alpha_{pc}$  (see the Supplemental Material, Fig. S1 [56]) deviates from 90 deg.

Even though the splitting is still of importance, as that determines if the modes become more or less destabilized by the applied strain. In Fig. 9 the derivative of the in-phase rotations is presented, and  $df_{rot+}/de$  is reduced with an increasing tolerance factor. An A cation larger in size will be more sensitive to volumetric changes than a small A cation, and the octahedra will need to rotate more when the volume is reduced. Hence an increased tolerance factor reduces the slope of the strain-phonon frequency relationship. The trend in Fig. 9 is found for the III-III perovskites (blue), and most II-IV (pink) and I-V (cyan) perovskites studied. Once again, the results for STO, BZO, and ANO deviate from these trends. STO and BZO have a tolerance factor at approximately unity, making them sensitive to small changes in strain, while ANO has a significantly different Poisson's ratio than the other I-V perovskites; as discussed above. Furthermore, for LNO and MTO it seems that the trends have saturated, as these materials are not stable in the perovskite phase.

#### G. Polar modes

The final mode type that is discussed in this work is polar displacements of the B cations, illustrated in Fig. 2(c). As

MOREAU, MARTHINSEN, SELBACH, AND TYBELL

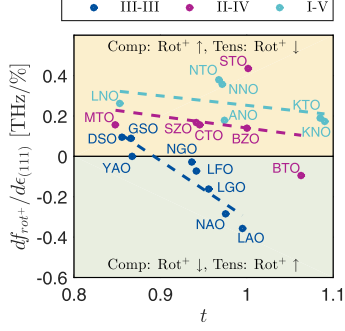
PHYSICAL REVIEW B **96**, 094109 (2017)

FIG. 9. Derivative of the in-phase rotational modes with respect to (111) strain as a function of tolerance factor  $t$ . Note that since the in-phase rotations are not split under (111) strain, this plot shows both in-plane and out-of-plane modes, as they are degenerate. A positive  $df/d\epsilon$ , yellow area, means that the respective mode is softened by compressive (comp) strain and hardened by tensile (tens) strain, while a negative  $df/d\epsilon$ , green area, means that the respective mode is softened by tens strain and hardened for comp strain and softened for tens strain. See Table I for abbreviations. The dashed lines are guides to the eye, based on linear fits to the data.

was shown for STO in Fig. 3(b), an out-of-plane polarization component is softened for tensile (111) strain, not for compressive (111) strain. This at first seems counterintuitive, as it means that the out-of-plane polarization is reduced when the structure is elongated out-of-plane [19]. However, we note that this trend was not observed in NTO for most strain values [Fig. 4(b)]. In Fig. 10 the derivative of the out-of-plane

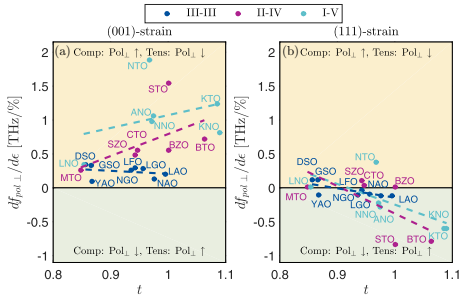


FIG. 10. Derivative of the out-of-plane polar modes as a function of tolerance factor  $t$  with respect to (a) (001) strain and (b) (111) strain as a function of tolerance factor  $t$ . A positive  $df/d\epsilon$ , yellow area, means that the respective mode is softened by compressive (comp) strain and hardened by tensile (tens) strain, while a negative  $df/d\epsilon$ , green area, means that the respective mode is softened by tens strain and hardened for comp strain and softened for tens strain. See Table I for abbreviations. The dashed lines are guides to the eye, based on linear fits to the data.

polarization frequency around 0% strain is shown for all the materials studied. As seen in Fig. 10(a) all materials follows the expected trend for (001) strain, [9] where  $\frac{df_{\text{pol}\pm}}{d\epsilon_{(001)}} > 0$ , i.e., out-of-plane polarization is softened by compressive strain. However for (111) strain [Fig. 10(b)] there is a shift in the sign of the derivative of the out-of-plane polarization, going from negative at large tolerance factors and turning positive for lower tolerance factors. The trends seen in Fig. 10 are not as clear as those observed for the rotational modes in, e.g., Fig. 7, with respect to oxidation state. As discussed for NTO, (111) strain allows for significant movement of both A and B cations, hence the lower symmetry requirements for polar modes compared to rotational modes weaken possible trends. In contrast to the out-of-plane modes, the in-plane polar modes follow similar trends for both (001) and (111) strain, data given in the Supplemental Material, Fig. S21 [56].

This phenomena of hardening of the out-of-plane polarization under (111) compression was first found for BTO by Oja *et al.* [20] and later elaborated on by Raelarijaona and Fu [19], who explained a negative  $\frac{df_{\text{pol}\pm}}{d\epsilon_{(111)}}$ , by considering the stacking sequence along the [111] direction [Fig. 2(e)]. They found that under (111) compression the oxygen atoms occupy the space the B cation should off-center to, thus suppressing the out-of-plane polarization. This can now be extended to other perovskites with lower tolerance factors. For a material with low tolerance factor, the A cation is typically small and there is hence more room in the plane for the oxygen atoms to shift position. Hence the reduced tendency for the oxygen atoms to inhibit movement of the B cation. At a critical value around  $t = 0.95$ , the elongation (compression) of the out-of-plane lattice parameter under compression (tension) becomes more important, and the  $\frac{df_{\text{pol}\pm}}{d\epsilon_{(111)}}$  becomes positive, similar to what is observed for (001) strain.

#### IV. DISCUSSION AND CONCLUSION

The strain-phonon coupling of (111)-oriented oxide perovskites depend on both the tolerance factor and the formal valence of the A and B cations. The fact that (111) strain has a symmetry induced difference between out-of-phase and in-phase rotations, which is not seen for (001) strain, opens up new avenues for tailoring the octahedral response. Such tuning can be of interest for epitaxial perovskite interfaces where two octahedral tilt patterns meet, as a mismatch between octahedral in-phase and out-of-phase rotations have been shown experimentally to have large influence on the magnetic properties [21,22]. Furthermore, the different behavior between in-phase and out-of-phase rotations opens interesting vistas for tuning of perovskite iodides and bromides, where in-phase rotations are more common than in their oxide counterpart [61]. On the other hand, for the polar modes for  $t \sim 1$ , both the in-plane and out-of-plane polarization is almost equally affected, and compressive (111) strain suppresses the overall ferroelectricity. Also for (111) strain, the piezoelectric coefficient  $e_{31} = \frac{\Delta P_3}{\epsilon_1} = \frac{\Delta P_{\pm}}{\Delta \epsilon_{(111)}} \sim \frac{df_{\text{pol}\pm}}{d\epsilon_{(111)}}$  is positive for high tolerance factors and becomes negative for lower tolerance factors, while it is always negative for (001) strain [19]. A positive  $e_{31}$  implies that an increasing out-of-plane polarization will actually increase the in-plane

strain, not decrease it as expected for (001)-oriented films. Especially interesting in this regard is (111)-strained  $\text{KNbO}_3$  (see the Supplemental Material, Fig. S15 [56]), which has  $\frac{df_{\text{pol}}}{d\epsilon_{(111)}} < \frac{df_{\text{pol}}}{d\epsilon_{(111)}}$  for all tensile strain values, indicating that the out-of-plane polarization will be the dominant polarization component. A positive  $e_{31}$  should in principle be possible for all materials with a positive  $\frac{df_{\text{pol}}}{d\epsilon_{(111)}}$  in Fig. 10(b), however in the III-III perovskites studied here,  $f_{\text{pol}}$  are in the order of 7 THz or larger, and the absolute value of  $\frac{df_{\text{pol}}}{d\epsilon_{(111)}}$  is too low for such modes to condensate under experimentally achievable strain values.

Taken together these results illustrates that the complexity of (111) strain can be taken as additional tuning parameters

both for octahedral rotations and polar distortions of perovskite oxides. This points towards that (111) strain is an interesting avenue for tailoring both magnetic and ferroelectric properties for functional devices.

#### ACKNOWLEDGMENTS

The Norwegian Metacenter for Computational Science is acknowledged for providing computational resources, Uninett Sigma 2, Project No. NN9301K. T. T. acknowledges funding through the Research Council of Norway Grant No. 231290. We thank Gerhard Henning Olsen for valuable discussions about phonon calculations and Ulrich Aschauer for providing the script for automating the phonopy calculations.

- [1] A. M. Glazer, *Acta Crystallogr. Sect. B* **28**, 3384 (1972).
- [2] J. H. Haeni, P. Irvin, W. Chang, R. Uecker, P. Reiche, Y. L. Li, S. Choudhury, W. Tian, M. E. Hawley, B. Craigo *et al.*, *Nature (London)* **430**, 758 (2004).
- [3] N. A. Pertsev, A. K. Tagantsev, and N. Setter, *Phys. Rev. B* **61**, R825 (2000).
- [4] K. J. Choi, M. Biegalski, Y. L. Li, A. Sharan, J. Schubert, R. Uecker, P. Reiche, Y. B. Chen, X. Q. Pan, V. Gopalan *et al.*, *Science* **306**, 1005 (2004).
- [5] J. H. Lee and K. M. Rabe, *Phys. Rev. Lett.* **104**, 207204 (2010).
- [6] J. M. Rondinelli and N. A. Spaldin, *Adv. Mater.* **23**, 3363 (2011).
- [7] A. J. Hatt and N. A. Spaldin, *Phys. Rev. B* **82**, 195402 (2010).
- [8] A. T. Zayak, X. Huang, J. B. Neaton, and K. M. Rabe, *Phys. Rev. B* **74**, 094104 (2006).
- [9] N. A. Pertsev, A. G. Zembilgotov, and A. K. Tagantsev, *Phys. Rev. Lett.* **80**, 1988 (1998).
- [10] A. Marthinsen, C. Faber, U. Aschauer, N. A. Spaldin, and S. M. Selbach, *MRS Commun.* **6**, 182 (2016).
- [11] R. L. Johnson-Wilke, D. Marincel, S. Zhu, M. P. Warusawithana, A. Hatt, J. Sayre, K. T. Delaney, R. Engel-Herbert, C. M. Schlepuetz, and J. W. Kim *et al.*, *Phys. Rev. B* **88**, 174101 (2013).
- [12] K. M. Rabe, *Curr. Opin. Solid State Mater. Sci.* **9**, 122 (2005).
- [13] J. Chakhalian, A. J. Millis, and J. Rondinelli, *Nat. Mater.* **11**, 92 (2012); I. Hallsteinsen, J. E. Boschker, M. Nord, S. Lee, M. Rzechowski, P. E. Vullum, J. K. Grepstad, R. Holmestad, C. B. Eom, and T. Tybell, *J. Appl. Phys.* **113**, 183512 (2013).
- [14] D. Doennig, W. E. Pickett, and R. Pentcheva, *Phys. Rev. Lett.* **111**, 126804 (2013); S. Middey, D. Meyers, D. Doennig, M. Kareev, X. Liu, Y. Cao, Z. Yang, J. Shi, L. Gu, P. J. Ryan *et al.*, *ibid.* **116**, 056801 (2016); S. Raghu, X. L. Qi, C. Honerkamp, and S. C. Zhang, *ibid.* **100**, 156401 (2008); D. Xiao, W. Zhu, Y. Ran, N. Nagaosa, and S. Okamoto, *Nat. Commun.* **2**, 596 (2011); K.-Y. Yang, W. Zhu, D. Xiao, S. Okamoto, Z. Wang, and Y. Ran, *Phys. Rev. B* **84**, 201104 (2011).
- [15] T. H. Kim, D. Puggioni, Y. Yuan, L. Xie, H. Zhou, N. Campbell, P. J. Ryan, Y. Choi, J. W. Kim, J. R. Patzner *et al.*, *Nature (London)* **533**, 68 (2016).
- [16] Y. B. Xu, Y. L. Tang, Y. L. Zhu, Y. Liu, S. Li, S. R. Zhang, and X. L. Ma, *Sci. Rep.* **6**, 35172 (2016).
- [17] J. F. Li, J. L. Wang, M. Wuttig, R. Ramesh, N. Wang, B. Ruetter, A. P. Pyatakov, A. K. Zvezdin, and D. Viehland, *Appl. Phys. Lett.* **84**, 5261 (2004).
- [18] M. Moreau, A. Marthinsen, S. M. Selbach, and T. Tybell, *Phys. Rev. B* **95**, 064109 (2017).
- [19] A. Raeliarijaona and H. X. Fu, *J. Appl. Phys.* **115**, 054105 (2014).
- [20] R. Oja, K. Johnston, J. Frantti, and R. M. Nieminen, *Phys. Rev. B* **78**, 094102 (2008).
- [21] A. J. Grutter, A. Vailionis, J. A. Borchers, B. J. Kirby, C. L. Flint, C. He, E. Arenholz, and Y. Suzuki, *Nano Lett.* **16**, 5647 (2016); Z. Liao, M. Huijben, Z. Zhong, N. Gauquelin, S. Macke, R. J. Green, S. Van Aert, J. Verbeeck, G. Van Tendeloo, K. Held *et al.*, *Nat. Mater.* **15**, 425 (2016).
- [22] I. Hallsteinsen, M. Moreau, A. Grutter, M. Nord, P. E. Vullum, D. A. Gilbert, T. Bolstad, J. K. Grepstad, R. Holmestad, S. M. Selbach *et al.*, *Phys. Rev. B* **94**, 201115 (2016).
- [23] J. M. Rondinelli and C. J. Fennie, *Adv. Mat.* **24**, 1961 (2012).
- [24] J. Hong, A. Stroppa, J. Íñiguez, S. Picozzi, and D. Vanderbilt, *Phys. Rev. B* **85**, 054417 (2012).
- [25] V. M. Goldschmidt, *Die Naturwissenschaften* **14**, 477 (1926).
- [26] R. J. Angel, J. Zhao, and N. L. Ross, *Phys. Rev. Lett.* **95**, 025503 (2005); J. Zhao, N. L. Ross, and R. J. Angel, *J. Phys.: Condens. Matter* **16**, 8763 (2004); T. Tohei, A. Kuwabara, T. Yamamoto, F. Oba, and I. Tanaka, *Phys. Rev. Lett.* **94**, 035502 (2005); J. Zhao, N. L. Ross, and R. J. Angel, *Acta Crystallogr. Sect. B* **62**, 431 (2006).
- [27] K. A. Muller, W. Berlinger, and F. Waldner, *Phys. Rev. Lett.* **21**, 814 (1968).
- [28] M. Marezio, P. D. Dernier, and J. P. Remeika, *J. Solid State Chem.* **4**, 11 (1972).
- [29] I. K. Bdikin, I. M. Shmyt'ko, A. M. Balbashov, and A. V. Kazansky, *J. Appl. Crystallogr.* **26**, 71 (1993).
- [30] S. Geller, *Acta Crystallogr.* **10**, 243 (1957).
- [31] M. Eibschütz, S. Shtrikman, and D. Treves, *Phys. Rev.* **156**, 562 (1967); S. Geller and P. M. Raccach, *Phys. Rev. B* **2**, 1167 (1970).
- [32] R. Diehl and G. Brandt, *Mater. Res. Bull.* **10**, 85 (1975).
- [33] R. P. Liferovich and R. H. Mitchell, *J. Solid State Chem.* **177**, 2188 (2004).
- [34] G. H. Kwei, A. C. Lawson, S. J. L. Billinge, and S. W. Cheong, *J. Phys. Chem.* **97**, 2368 (1993).
- [35] L. Rimai and G. A. deMars, *Phys. Rev.* **127**, 702 (1962).
- [36] D. M. Helen, *Proc. Phys. Soc.* **58**, 133 (1946).
- [37] H. F. Kay and P. C. Bailey, *Acta Crystallogr.* **10**, 219 (1957).
- [38] L. Carlsson, *Acta Crystallogr.* **23**, 901 (1967).
- [39] A. W. Hewat, *J. Phys. C: Solid State Phys.* **6**, 2559 (1973).



MOREAU, MARTHINSEN, SELBACH, AND TYBELL

PHYSICAL REVIEW B **96**, 094109 (2017)

- [40] G. A. Samara and B. Morosin, *Phys. Rev. B* **8**, 1256 (1973); C. H. Perry and T. F. McNelly, *Phys. Rev.* **154**, 456 (1967).
- [41] M. Ahtee and C. N. W. Darlington, *Acta Crystallogr. Sect. B* **36**, 1007 (1980).
- [42] S. K. Mishra, N. Choudhury, S. L. Chaplot, P. S. R. Krishna, and R. Mittal, *Phys. Rev. B* **76**, 024110 (2007).
- [43] M. Yashima, S. Matsuyama, R. Sano, M. Itoh, K. Tsuda, and D. Fu, *Chem. Mater.* **23**, 1643 (2011).
- [44] B. A. Wechsler and R. B. Von Dreele, *Acta Crystallogr. Sect. B* **45**, 542 (1989).
- [45] S. C. Abrahams, J. M. Reddy, and J. L. Bernstein, *J. Phys. Chem. Solids* **27**, 997 (1966).
- [46] G. Kresse and J. Furthmuller, *Phys. Rev. B* **54**, 11169 (1996).
- [47] G. Kresse and D. Joubert, *Phys. Rev. B* **59**, 1758 (1999).
- [48] P. E. Blochl, *Phys. Rev. B* **50**, 17953 (1994).
- [49] J. P. Perdew, A. Ruzsinszky, G. I. Csonka, O. A. Vydrov, G. E. Scuseria, L. A. Constantin, X. Zhou, and K. Burke, *Phys. Rev. Lett.* **100**, 136406 (2008).
- [50] W. C. Koehler and E. O. Wollan, *J. Phys. Chem. Solids* **2**, 100 (1957).
- [51] VASP manual, <https://cms.mpi.univie.ac.at/vasp/vasp/vasp.html> (2017).
- [52] S. L. Dudarev, G. A. Botton, S. Y. Savrasov, C. J. Humphreys, and A. P. Sutton, *Phys. Rev. B* **57**, 1505 (1998).
- [53] K. Kunc and R. M. Martin, *Phys. Rev. Lett.* **48**, 406 (1982).
- [54] A. Togo and I. Tanaka, *Scr. Mater.* **108**, 1 (2015).
- [55] K. Momma and F. Izumi, *J. Appl. Crystallogr.* **44**, 1272 (2011).
- [56] See Supplemental Material at <http://link.aps.org/supplemental/10.1103/PhysRevB.96.094109> for discussion about the octahedral distortions, data for the supplementing materials, relative eigenvalue amplitude of NaTaO<sub>3</sub>, and in-plane polar mode analysis.
- [57] Tolerance Factor Calculator, <http://www.me.utexas.edu/~benedekgroup/ToleranceFactorCalculator/> (Accessed 20.01.2017).
- [58] A. Vailionis, H. Boschker, W. Siemons, E. P. Houwman, D. H. A. Blank, G. Rijnders, and G. Koster, *Phys. Rev. B* **83**, 064101 (2011).
- [59] E. Bousquet and P. Ghosez, *Phys. Rev. B* **74**, 180101 (2006).
- [60] H. J. Xiang, M. Guennou, J. Íñiguez, J. Kreisel, and L. Bellaiche, *Phys. Rev. B* **96**, 054102 (2017).
- [61] J. Young and J. M. Rondinelli, *J. Phys. Chem. Lett.* **7**, 918 (2016).

Supplementary information for

## Strain-phonon coupling in (111)-oriented perovskite oxides

Magnus Moreau,<sup>1</sup> Astrid Marthinsen,<sup>2</sup> Sverre M. Selbach,<sup>2</sup> and Thomas Tybell<sup>1,\*</sup>

1) Department of Electronic Systems, NTNU Norwegian University of Science and Technology, 7491 Trondheim, Norway

2) Department of Materials Science and Engineering, NTNU Norwegian University of Science and Technology, 7491 Trondheim, Norway

\*E-mail: [thomas.tybell@iet.ntnu.no](mailto:thomas.tybell@iet.ntnu.no)

### OCTAHEDRAL DISTORTIONS

Imposing strain will result in a distorted unit cell, affecting the oxygen octahedra structure. In order to establish an overall non-material specific picture, the response of  $P4/mmm$  ((001)-strain) and  $R\bar{3}m$  ((111)-strain) to strain structures is presented. For the  $P4/mmm$  structure under (001)-strain the octahedra are tetragonally distorted, giving different BO bond lengths for the in- and out-of-plane directions. The tetragonality, defined  $c/a$ , depends on both in-plane strain  $\epsilon_{(001)}$  and the Poisson's ratio  $\nu_{(001)}$ . Relying on

$$a = a_0(1 + \epsilon_{(001)}), \quad (S1)$$

$$c = a_0(1 + \epsilon_{(001),\perp}), \quad (S2)$$

$$\frac{\epsilon_{\perp}}{\epsilon} = \frac{-2\nu}{1-\nu}, \quad (S3)$$

where  $\epsilon_{(001)}$ ,  $\epsilon_{(001),\perp}$  and  $\nu_{(001)}$  are the in-plane and out-of-plane strain in the (001)-plane respectively,  $a_0$  is the lattice parameter of the aristotype  $Pm\bar{3}m$  structure, and  $\nu$  is the Poisson's ratio corresponding to the strain plane, the following expression for the degree of tetragonality under (001)-strain is obtained:

$$\frac{c}{a} = \frac{2\epsilon_{(001)}\nu_{(001)} + \nu_{(001)} - 1}{(1 + \epsilon_{(001)})(\nu_{(001)} - 1)}. \quad (S4)$$

For the  $R\bar{3}m$  structure under (111)-strain all B-O bond lengths are equal. However, the rhombohedral has a pseudocubic cell angle  $\alpha_{pc}$  that will deviate from the aristotype value of  $90^\circ$  as shown in Figure S1 a). As a consequence, the oxygen octahedra are distorted with O-B-O angles equal to  $\alpha_{pc}$ . Based on this  $\alpha_{pc}$  is used as a measure of octahedral distortion under (111)-strain. Using the identities

$$a_H^2 = 2a_0^2(1 - \cos \alpha_{pc}), \quad (S5)$$

$$c_H^2 = 3a_0^2(1 + 2 \cos \alpha_{pc}), \quad (S6)$$

where  $a_H$  and  $c_H$  are the lattice parameters of the of the  $R\bar{3}m$  structure in the hexagonal setting given by

$$a_H = \sqrt{2}a_0(1 + \epsilon_{(111)}), \quad (S7)$$

$$c_H = \sqrt{3}a_0(1 + \epsilon_{(111),\perp}), \quad (S8)$$

where  $\epsilon_{(111)}$ , and  $\epsilon_{(111),\perp}$  are the in-plane and out-of-plane strain in the (111)-plane respectively, the following relationship between pseudocubic cell angle  $\alpha_{pc}$ , the in-plane strain,  $\epsilon_{(111)}$ , and the Poisson's ratio,  $\nu_{(111)}$  is obtained:

$$\cos \alpha_{pc} = \frac{\left(\frac{1 - \frac{2\nu_{(111)}}{1 - \nu_{(111)}}\epsilon_{(111)}}{1 + \epsilon_{(111)}}\right)^2 - 1}{\left(\frac{1 - \frac{2\nu_{(111)}}{1 - \nu_{(111)}}\epsilon_{(111)}}{1 + \epsilon_{(111)}}\right)^2 + 2}. \quad (S9)$$

The dependence of  $\alpha_{pc}$  on strain,  $\epsilon_{(111)}$ , and Poisson's ratio,  $\nu_{(111)}$ , is plotted as a contour plot in Figure S1 b). The amount of octahedral distortions increases non-linearly with both increasing strain and Poisson's ratio. As the angle is no longer, 90 degrees, it will remove the three mirror planes and affect the strain response.

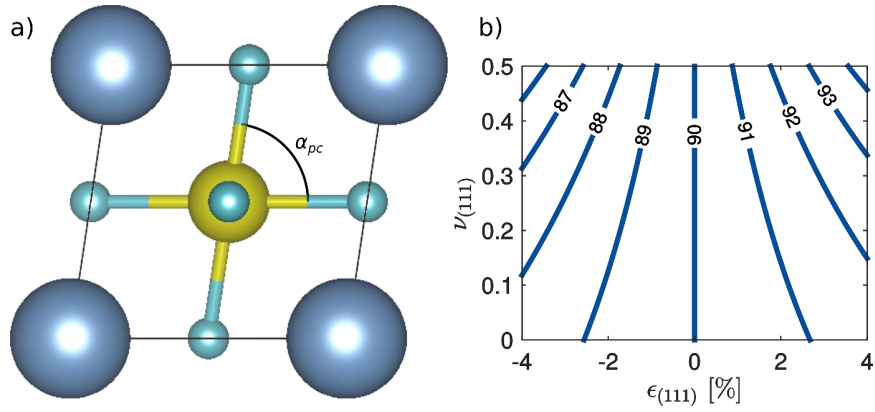


Figure S1: a) Illustration of the pseudocubic cell angle  $\alpha_{pc}$  in the  $R\bar{3}m$  structure. b) Contour plot of  $\alpha_{pc}$  given in degrees as a function of strain in the (111)-plane,  $\epsilon_{(111)}$ , and the Poisson's ratio for (111)-strain,  $\nu_{(111)}$ .

#### DATA FOR COMPLEMENTING MATERIALS

In the main text we showed how the different phonon modes depends on strain in SrTiO<sub>3</sub> and NaTaO<sub>3</sub>, here we show the same information for the 18 other materials studied in this work. First we present the results for III-III, then II-IV and finally I-V perovskites.

- Figures S2-S9 shows the strain phonon coupling for LaAlO<sub>3</sub>, NdAlO<sub>3</sub>, LaGaO<sub>3</sub>, LaFeO<sub>3</sub>, NdGaO<sub>3</sub>, YAlO<sub>3</sub>, GdScO<sub>3</sub> and DyScO<sub>3</sub> respectively.
- Figures S10-S14 shows the strain phonon coupling for BaTiO<sub>3</sub>, BaZrO<sub>3</sub>, CaTiO<sub>3</sub>, SrZrO<sub>3</sub> and MgTiO<sub>3</sub> respectively.
- Figures S15-S19 shows the strain phonon coupling for KNbO<sub>3</sub>, KTaO<sub>3</sub>, AgNbO<sub>3</sub>, NaNbO<sub>3</sub> and LiNbO<sub>3</sub> respectively.

## III-III Perovskites

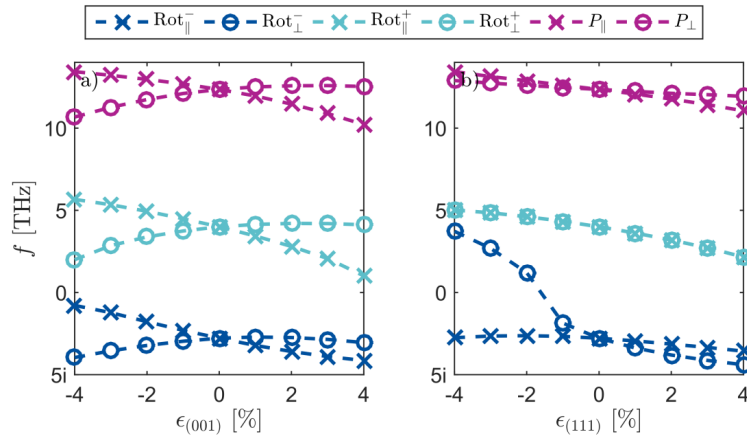


Figure S2: the frequencies of the three different phonon modes considered as a function of in-plane strain in the a) (001)-plane and b) (111)-plane for  $\text{LaAlO}_3$ .

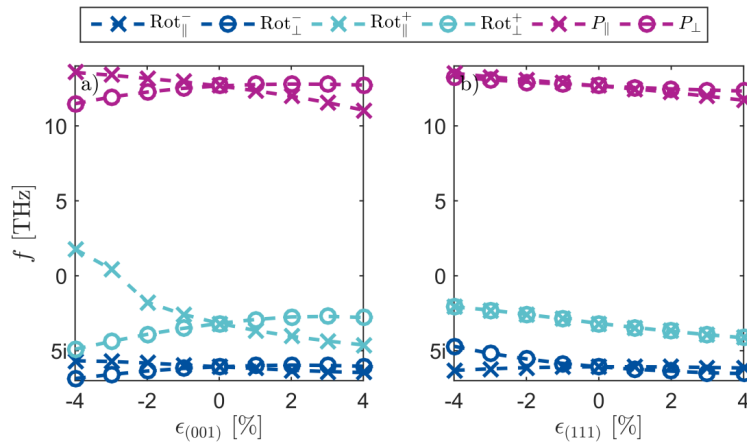


Figure S3: the frequencies of the three different phonon modes considered as a function of in-plane strain in the a) (001)-plane and b) (111)-plane for  $\text{NdAlO}_3$ .

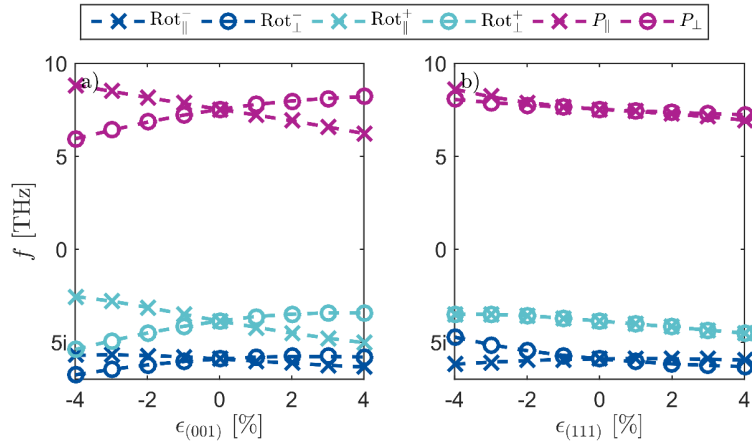


Figure S4: the frequencies of the three different phonon modes considered as a function of in-plane strain in the a) (001)-plane and b) (111)-plane for LaGaO<sub>3</sub>.

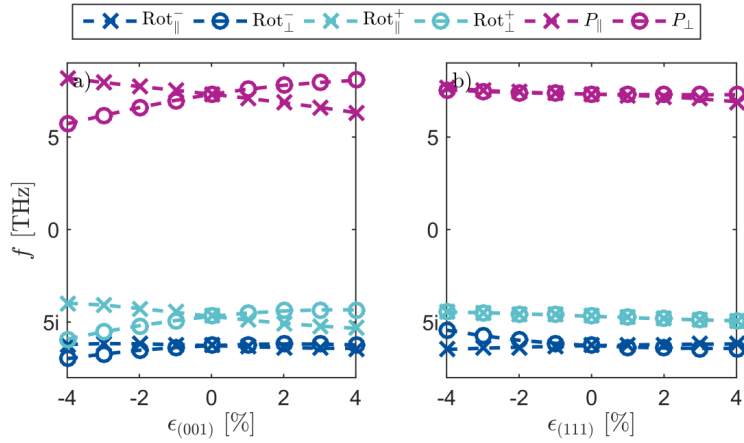


Figure S5: the frequencies of the three different phonon modes considered as a function of in-plane strain in the a) (001)-plane and b) (111)-plane for LaFeO<sub>3</sub>.

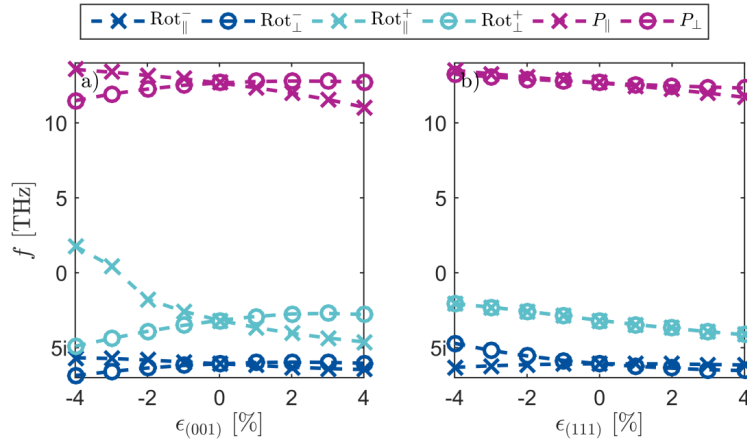


Figure S6: the frequencies of the three different phonon modes considered as a function of in-plane strain in the a) (001)-plane and b) (111)-plane for NdGaO<sub>3</sub>.

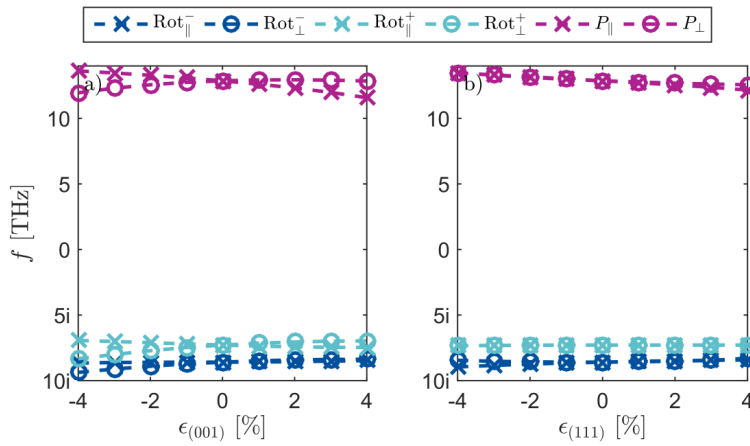


Figure S7: the frequencies of the three different phonon modes considered as a function of in-plane strain in the a) (001)-plane and b) (111)-plane for YAlO<sub>3</sub>.

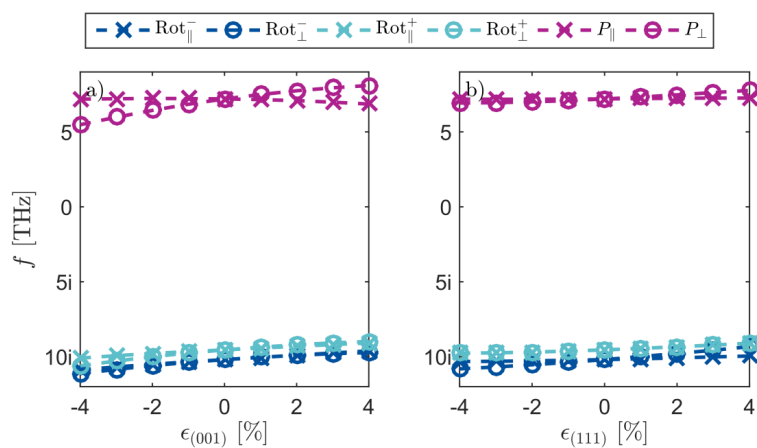


Figure S8: the frequencies of the three different phonon modes considered as a function of in-plane strain in the a) (001)-plane and b) (111)-plane for GdScO<sub>3</sub>.

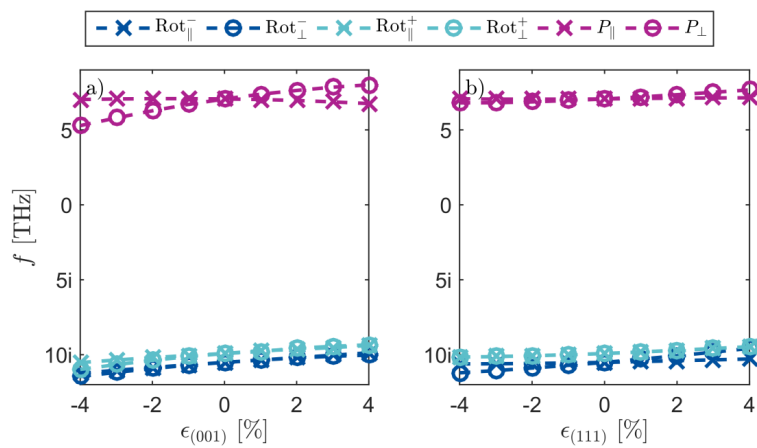


Figure S9: the frequencies of the three different phonon modes considered as a function of in-plane strain in the a) (001)-plane and b) (111)-plane for DyScO<sub>3</sub>.



## II-IV Perovskites

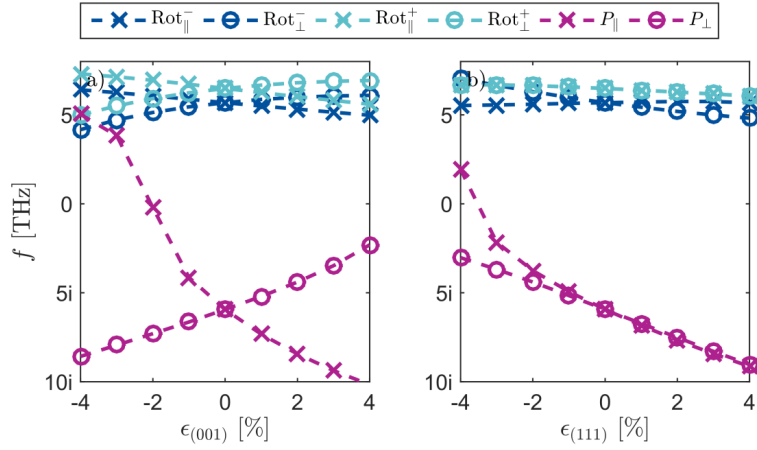


Figure S10: the frequencies of the three different phonon modes considered as a function of in-plane strain in the a) (001)-plane and b) (111)-plane for BaTiO<sub>3</sub>.

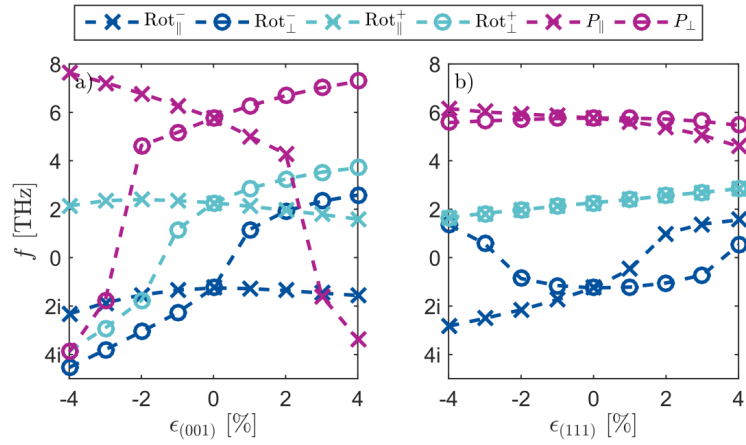


Figure S11: the frequencies of the three different phonon modes considered as a function of in-plane strain in the a) (001)-plane and b) (111)-plane for BaZrO<sub>3</sub>.

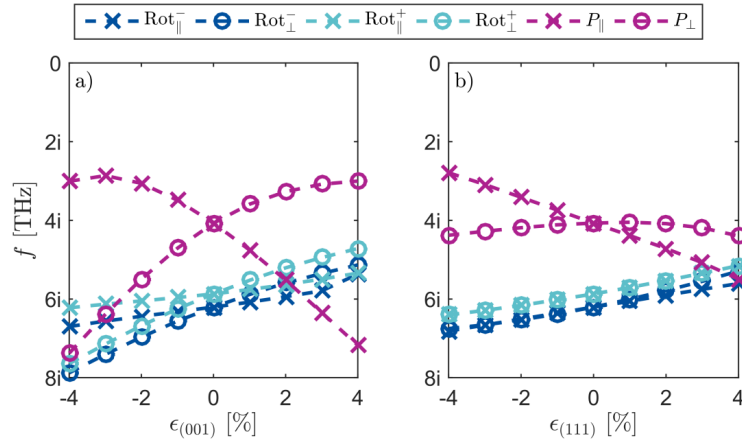


Figure S12: the frequencies of the three different phonon modes considered as a function of in-plane strain in the a) (001)-plane and b) (111)-plane for  $\text{CaTiO}_3$ .

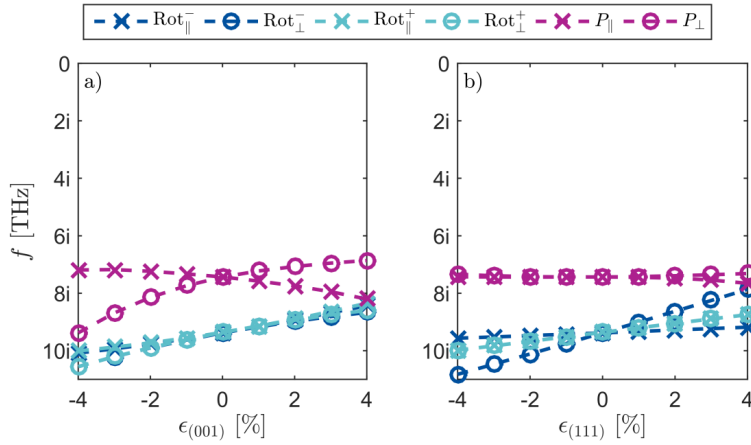


Figure S13: the frequencies of the three different phonon modes considered as a function of in-plane strain in the a) (001)-plane and b) (111)-plane for  $\text{SrZrO}_3$ .

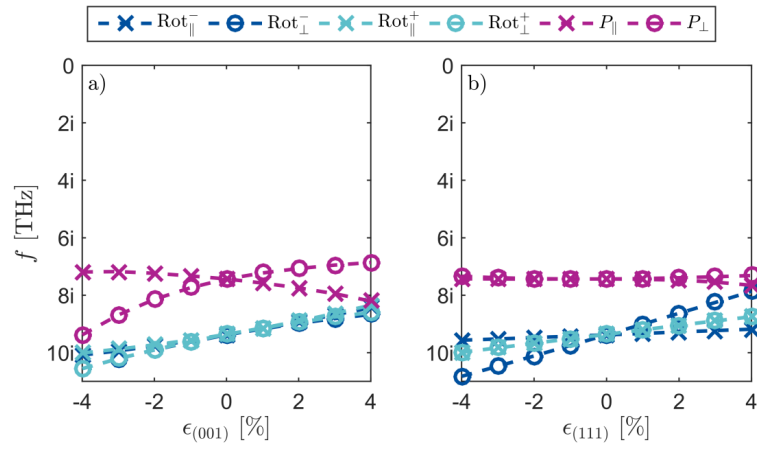


Figure S14: the frequencies of the three different phonon modes considered as a function of in-plane strain in the a) (001)-plane and b) (111)-plane for MgTiO<sub>3</sub>.

I-V Perovskites

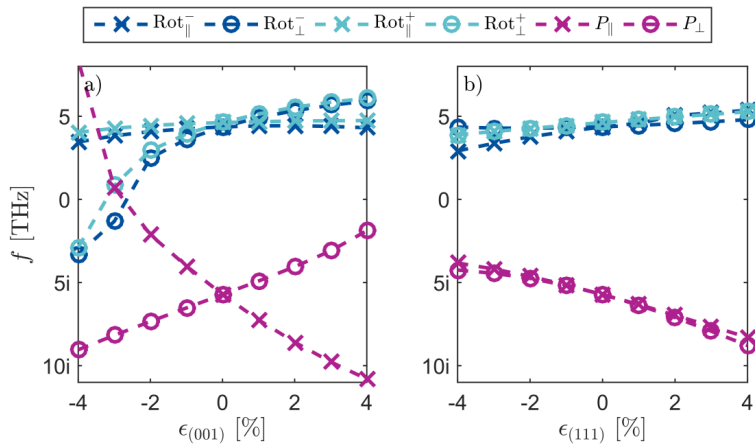


Figure S15: the frequencies of the three different phonon modes considered as a function of in-plane strain in the a) (001)-plane and b) (111)-plane for KNbO<sub>3</sub>.

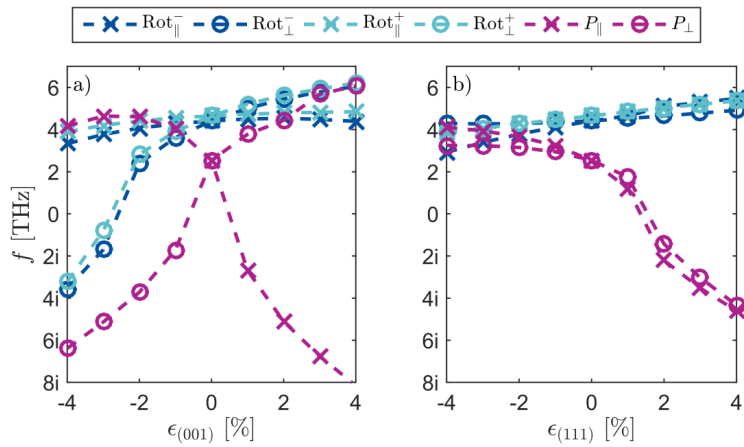


Figure S16: the frequencies of the three different phonon modes considered as a function of in-plane strain in the a) (001)-plane and b) (111)-plane for KTaO<sub>3</sub>.

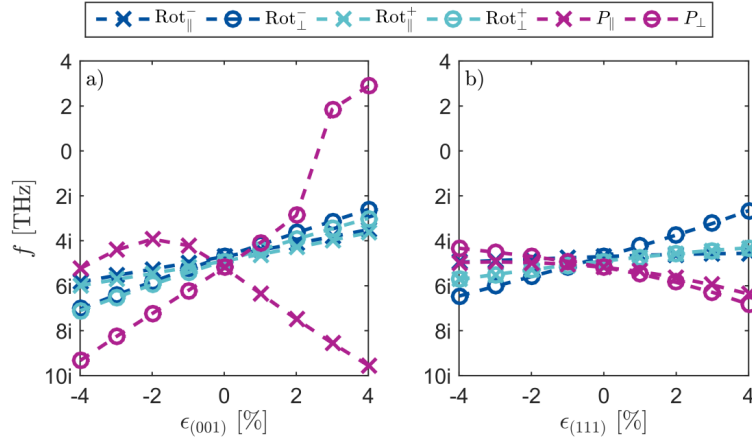


Figure S17: the frequencies of the three different phonon modes considered as a function of in-plane strain in the a) (001)-plane and b) (111)-plane for  $\text{AgNbO}_3$ .

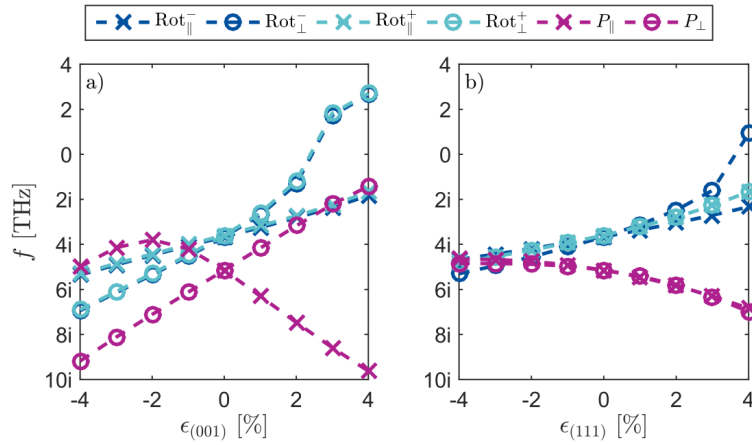


Figure S18: the frequencies of the three different phonon modes considered as a function of in-plane strain in the a) (001)-plane and b) (111)-plane for  $\text{NaNbO}_3$ .

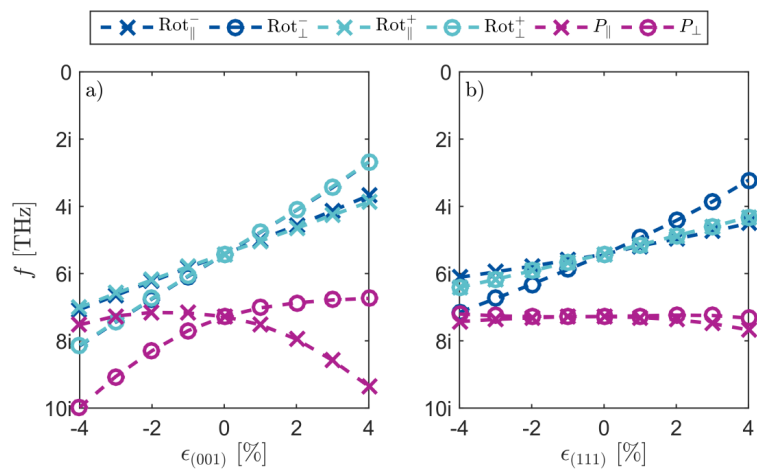


Figure S19: the frequencies of the three different phonon modes considered as a function of in-plane strain in the a) (001)-plane and b) (111)-plane for  $\text{LiNbO}_3$ .

## CONTRIBUTIONS OF A- AND B-CATIONS TO POLAR MODE

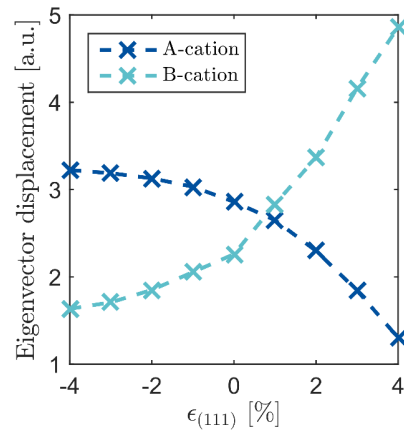


Figure S20: the displacement relative displacements of the A- and B-cation of  $\text{NaTaO}_3$  under (111)-strain for the out-of-plane polar mode, given by the relative eigenvector amplitude times the atomic mass. As seen, there is a crossover from A-cation dominated to B-cation dominated at 1 % compressive strain e.g. right before the point where the  $df_{pol,\perp}/d\epsilon_{(111)}$  changes sign as shown in Figure 4 b in the main manuscript.

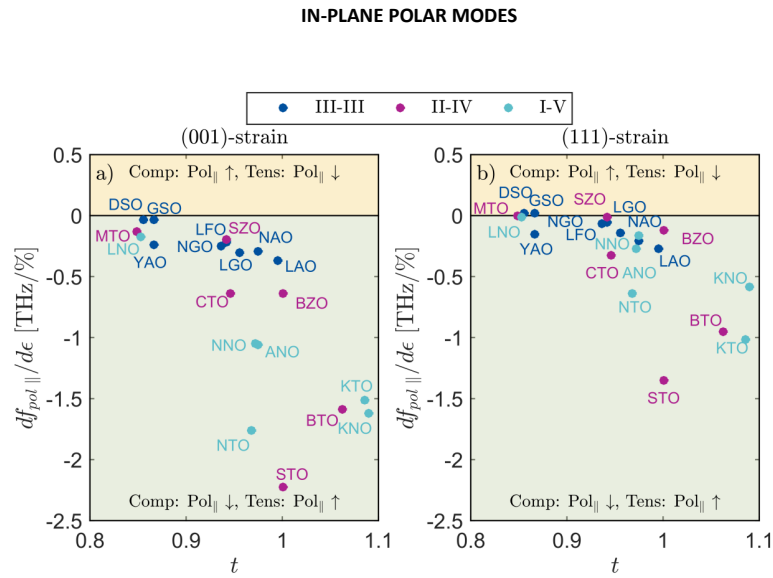


Figure S21: Derivative of the out-of-plane polar modes as a function of tolerance factor  $t$  with respect to a) (001)-strain and b) (111)-strain as a function of tolerance factor  $t$ . A positive  $df/d\epsilon$ , yellow area, means that the respective mode is softened by compressive (comp) strain and hardened by tensile (tens) strain, while a negative  $df/d\epsilon$ , green area, means that the respective mode is softened by tens strain and hardened for comp strain and favored for tens strain. See Table I in the main manuscript for abbreviations. The in-plane polar modes show similar behavior for both (001)- and (111)-strain.






---

# Magnetic domain configuration of (111)-oriented $\text{LaFeO}_3$ epitaxial thin films

I. Hallsteinsen, M. Moreau, R.V. Chopdekar, E. Christiansen, M. Nord, P-E. Vullum, J. K. Grepstad, R. Holmestad, S. Selbach, A. Scholl, E. Arenholz, E. Folven and T. Tybell

Published in APL Materials **5**, 086107 (2017)

DOI: <http://dx.doi.org/10.1063/1.4986555>







## Magnetic domain configuration of (111)-oriented LaFeO<sub>3</sub> epitaxial thin films

I. Hallsteinsen,<sup>1,2</sup> M. Moreau,<sup>1</sup> R. V. Chopdekar,<sup>3</sup> E. Christiansen,<sup>4</sup> M. Nord,<sup>4</sup> P.-E. Vullum,<sup>5</sup> J. K. Grepstad,<sup>1</sup> R. Holmestad,<sup>4</sup> S. M. Selbach,<sup>6</sup> A. Scholl,<sup>2</sup> E. Arenholz,<sup>2</sup> E. Folven,<sup>1</sup> and T. Tybell<sup>1,a</sup>

<sup>1</sup>Department of Electronic Systems, NTNU–Norwegian University of Science and Technology, Trondheim 7491, Norway

<sup>2</sup>Advanced Light Source, Lawrence Berkeley National Laboratory, Berkeley, California 94720, USA

<sup>3</sup>Department of Chemical Engineering and Materials Science, University of California, Davis, California 95616, USA

<sup>4</sup>Department of Physics, NTNU–Norwegian University of Science and Technology, Trondheim 7491, Norway

<sup>5</sup>SINTEF Materials and Chemistry, Trondheim 7491, Norway

<sup>6</sup>Department of Materials Science and Engineering, NTNU–Norwegian University of Science and Technology, Trondheim 7491, Norway

(Received 6 June 2017; accepted 9 August 2017; published online 22 August 2017)

In antiferromagnetic spintronics control of the domains and corresponding spin axis orientation is crucial for devices. Here we investigate the antiferromagnetic axis in (111)-oriented LaFeO<sub>3</sub>/SrTiO<sub>3</sub>, which is coupled to structural twin domains. The structural domains have either the orthorhombic *a*- or *b*-axis along the in-plane (1 $\bar{1}$ 0) cubic directions of the substrate, and the corresponding magnetic domains have the antiferromagnetic axis in the sample plane. Six degenerate antiferromagnetic axes are found corresponding to the  $\langle 1\bar{1}0 \rangle$  and  $\langle 11\bar{2} \rangle$  in-plane directions. This is in contrast to the biaxial anisotropy in (001)-oriented films and reflects how crystal orientation can be used to control magnetic anisotropy in antiferromagnets. © 2017 Author(s). All article content, except where otherwise noted, is licensed under a Creative Commons Attribution (CC BY) license (<http://creativecommons.org/licenses/by/4.0/>). [<http://dx.doi.org/10.1063/1.4986555>]

Antiferromagnetic (AF) spintronics technology has recently emerged as a promising avenue for future electronic device technology.<sup>1,2</sup> AF insulators incorporated in devices are robust against external magnetic fields, produce no stray field that could perturb neighboring devices, have ultra-fast magnetization dynamics, and as no moving charges are involved, their power reduction is significant as compared to charge based electronics used today.<sup>3</sup> In current magnetoelectronic device applications, AF layers play a passive but important role, where they typically serve to pin an adjacent ferromagnetic (FM) layer by force of the exchange-bias coupling.<sup>4</sup> However, the AF layer can also be an active component of electronic devices. Recently, Wadley *et al.*<sup>5</sup> demonstrated switching of the AF spin axis by electric current. Further it was shown that the magnetic domain orientation was correlated to the electrical resistance<sup>6</sup> and used in a multilevel memory device.<sup>7</sup> Both exchange-bias and AF dynamics depend on the AF domain structure, hence a detailed understanding of domain formation and possibly domain engineering are both essential for further device development.<sup>1,5,8</sup>

The mechanisms responsible for domain formation in AF materials are not as straightforward as in the case of FM materials, since there is no macroscopic demagnetizing field. Commonly multi domain configurations are observed in AF materials, which are explained in terms of lattice imperfections, such as crystalline twins or dislocations.<sup>9</sup> In magnetic perovskites oxides, there is a strong coupling between crystalline structure and magnetic properties.<sup>10</sup> Engineered distortions of the crystalline structure, e.g., in epitaxial thin films, couple to the magnetic order parameter through magnetoelastic

<sup>a</sup>Author to whom correspondence should be addressed: [thomas.tybell@iet.ntnu.no](mailto:thomas.tybell@iet.ntnu.no)



effects and play a key role in the AF domain formation.<sup>11</sup> Bulk LaFeO<sub>3</sub> (LFO) is orthorhombic (space group *Pnma* with  $a = 5.557 \text{ \AA}$ ,  $b = 5.5652 \text{ \AA}$ , and  $c = 7.8542 \text{ \AA}$ ) with the AF easy axis oriented along the crystallographic *a*-axis. The AF domains of LFO thin films epitaxially grown in the pseudocubic (001)-orientation are extensively studied and strongly coupled to structural changes.<sup>9,12</sup> The strong coupling to the lattice makes LFO an ideal model system to investigate manipulation of the AF domain structure. Seo *et al.*<sup>13</sup> showed that different strain states and miscut of the substrate produce different structural domains which are reflected in the AF domains. In addition, new sets of AF easy axes can be found when LFO is coupled to FM materials.<sup>14</sup>

Until recently, research on epitaxial perovskite thin films has been largely focused on pseudocubic (001)-oriented surfaces; however, different surface orientations can be used as a tool for domain engineering. Recently we have shown that the ferromagnetic anisotropy is biaxial for tensile strained La<sub>0.7</sub>Sr<sub>0.3</sub>MnO<sub>3</sub> films in the (001)-orientation, while it has a weak anisotropy following the trigonal crystal symmetry in (111)-oriented films.<sup>15</sup> The (111)-oriented perovskite lattice has a threefold in-plane rotational symmetry that forms a buckled honeycomb structure resembling that of topological insulators<sup>16</sup> and multiferroic hexagonal manganites,<sup>17</sup> opening up the possibility for emergent electronic and magnetic behavior. In this letter, we investigate the anisotropy of the AF domains of (111)-oriented LFO. It is shown that LFO strained to a (111)-oriented SrTiO<sub>3</sub> (STO) surface has six possible orientations of the orthorhombic unit cell and that the AF domains are similar in size and shape to the structural twins. The AF easy axis is shown to be in the plane of the films along six different crystallographic axes, reflecting the symmetry of the (111)-oriented surface.

Epitaxial 20 nm thick LFO films were fabricated on (111)-oriented Nb-doped (0.05%) STO substrates by pulsed laser deposition. The doped substrates were chosen to prevent charging during the local domain imaging with x-rays. Single terminated smooth substrates were prepared by ultrasonic agitation in deionized water at 70 °C, etching in buffered hydrofluoric acid for 45 s and annealing for 1 h at 1050 °C in an oxygen ambient.<sup>18</sup> A KrF excimer laser ( $\lambda = 248 \text{ nm}$ ) with a fluence of  $\sim 2 \text{ J cm}^{-2}$  and repetition rate 1 Hz was employed to ablate material from a stoichiometric LFO target. The deposition took place in 0.35 mbars of oxygen at 540 °C, with a substrate-to-target separation of 45 mm, consistent with growth conditions with minimal resputtering.<sup>19</sup> After deposition, the films were cooled to room temperature in 100 mbars of oxygen. The growth was monitored *in situ* with reflection high energy electron diffraction (RHEED), and the surface topography was characterized by atomic force microscopy (AFM, Veeco Nanoscope V) showing a smooth, step-and-terrace surface morphology. The crystalline structure was examined with a four-circle, high-resolution x-ray diffractometer (XRD, Bruker D8), showing fully epitaxial films.

In order to investigate the energetics of possible structural twin arrangements, calculations of the phonon spectrum based on density functional theory (DFT) were performed. The Vienna *Ab initio* Simulation Package (VASP)<sup>20</sup> with the Perdew-Burke-Ernzerhof generalized gradient approximation for solids (PBE-sol) functional and<sup>21</sup> a plane wave cutoff energy of 550 eV and the recommended projected augmented wave (PAW)-PBE potentials supplied with VASP for La, Fe, and O were used. Applying the Dudarev method,<sup>22</sup> a Hubbard U potential of 3 and 10 eV was applied to the Fe 3*d* and La 4*f* orbitals, respectively. Phonon calculations were performed with the frozen phonon approach<sup>23</sup> and analyzed with the Phonopy software.<sup>24</sup> To include the effect of strain, the  $[\bar{1}\bar{1}0]$  and  $[0\bar{1}\bar{1}]$  in-plane lattice parameters of LFO were fixed to those calculated for STO, while the out-of-plane lattice parameter along the  $[111]$ -direction was allowed to relax. We note that the PBEsol functional has a typical absolute error in lattice parameter of 0.019 Å for transition metals compounds compared to experimental values.<sup>21</sup> Our relaxed value for cubic STO is 3.895 Å, as compared to the experimental 3.905 Å, and for the out of-plane LFO parameter,  $d_{111}$ , when strained to STO, we obtain 2.289 Å by DFT as compared to the experimental value of 2.279 Å; that is, both are well within the typical error range.

The AF properties were measured by x-ray magnetic linear dichroism (XMLD) at BL 4.0.2 of the Advanced Light Source (ALS). XMLD provides information on the projection of the AF spin axis along the E-vector of linearly polarized x-rays. Thus, it is possible to obtain the components of the AF spin axis by rotating the sample relative to the incident beam of x-rays. The spectra shown here were measured in total-electron-yield mode by monitoring the sample drain current, across the Fe L<sub>2,3</sub> edges (700-730 eV), with the x-rays incident at 30° (grazing incidence) and at 90° to the sample surface (normal incidence). The polarization E-vector was varied between s- (in-plane at

grazing incidence) and p-polarization ( $60^\circ$  out-of-plane at grazing incidence), where the difference between them results in the XMLD spectra. In order to probe the microscopic response of individual domains, the films were imaged by x-ray photoemission electron microscopy (X-PEEM) combined with XMLD at the Surface/Interface: Microscopy (SIM) beam line at the Swiss Light Source (SLS) (Figs. 2 and 4) and BL 11.0.1 at ALS (Fig. 5). Due to different storage ring operating conditions, the incoming photon flux was a factor of  $\sim 14$  higher at SLS as compared to ALS. X-PEEM allows spatial mapping of x-ray absorption at the lateral length scale of single magnetic domains. Thus, when combined with XMLD, the AF spin axis of individual AF domains can be determined. The AF XMLD intensity has a  $\cos^2 \theta$  dependence, where  $\theta$  is the angle between the E-vector and the AF spin axis. Therefore, the image contrast is strongest between AF domains with the spin axis parallel and perpendicular to the E-vector. The XMLD-PEEM images presented are obtained by taking the signal ratio between images recorded at the Fe  $L_{2A}$  (722.15 eV) and Fe  $L_{2B}$  (724.0 eV) peaks, for a given polarization. This procedure removes contributions from the surface topography and enhances the AF contrast. The inclination with the film surface of the incident x-rays was  $16^\circ$  at SLS and  $30^\circ$  at ALS, and all measurements were done at room temperature. The spectra are shown without any attempt to correct for saturation effects, as it does not affect the qualitative interpretation.<sup>25,26</sup>

Figure 1(a) shows the x-ray absorption spectra obtained with s- and p-polarization and the resulting XMLD spectrum at grazing incidence. A clear dichroism signal is obtained, indicating AF order. Through comparison with modeled spectra,<sup>27</sup> the sign of the dichroism indicates an in-plane AF axis. We note that spectra taken at normal incidence with s- and p-polarization (not shown) corresponding to the  $[110]$  and  $[1\bar{1}2]$  in plane directions, respectively, give almost no dichroism. Hence, the magnetic AF response is similar for the two crystallographic axes, and the structural linear dichroism is negligible. In Fig. 1(b), the XMLD spectra recorded while rotating the sample relative to the incoming x-rays at grazing incidence are shown. The in-plane azimuthal rotation is defined to be  $\varphi = 0^\circ$  when the incoming x-ray projection on the film plane is parallel to  $[1\bar{1}0]$  and  $\varphi = 90^\circ$  when parallel to the  $[11\bar{2}]$  crystallographic direction. The magnitude of the dichroism is approximately the same for all angles. With an x-ray spot size of  $\sim 100 \mu\text{m} \times 100 \mu\text{m}$ , we are averaging over many domains with different spin axes. The clear dichroism in Fig. 1(b) points towards in-plane

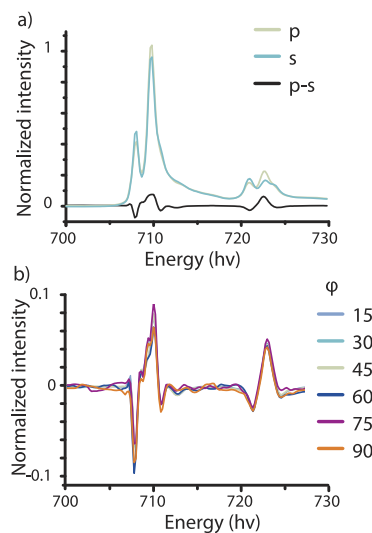


FIG. 1. (a) X-ray absorption spectra of the Fe  $L_{2,3}$ -edge (700-730 eV) in grazing incidence with polarization p (green) and s (turquoise) and their difference spectrum (black). (b) X-ray linear dichroism spectra of the Fe  $L_{2,3}$ -edge in grazing incidence upon sample rotation from  $\omega = 15^\circ$  to  $90^\circ$ , where  $\omega = 0^\circ$  refers to the in-plane projection of x-rays incident parallel to the  $[110]$  cubic substrate crystallographic direction.

AF spin axes; however, the lack of difference as a function of the azimuth angle indicates that we are averaging over domains with many different in-plane directions of the AF spin axes.

To further investigate a possible AF anisotropy and domain structure, we used XMLD - PEEM in the measurement geometry presented in Fig. 2. In the first panel ( $\omega = 0^\circ$ ), a PEEM image recorded with s-polarization is presented. There is clear contrast from different regions, indicative of domains with different AF axis orientation. The domains are irregularly shaped and their size varies between 50 and 500 nm in diameter. Earlier results on similar pseudocubic (001)-oriented films show similar sizes and shapes.<sup>13</sup> In a thin film grown on (001)-oriented SrTiO<sub>3</sub> (STO), the orthorhombic *a* axis is pointing 45° out-of-plane, along the cubic (110) axes ( $[100]_o \parallel [110]_c$ ). The AF easy axis was reported to vary from canting angles of 35° to totally in-plane along the two  $\langle 100 \rangle$  directions.<sup>25,28</sup> If the same crystallographic relation is preserved in a (111)-oriented film, the orthorhombic *a*-axis could either lie in-plane or lie at 55° out-of-plane, aligned with the  $\langle 1\bar{1}0 \rangle$  directions. To investigate if the AF spin axes are mainly in-plane or out-of-plane, we varied the polarization from  $\omega = 0^\circ$  (s-polarization) to  $\omega = 90^\circ$  (p-polarization) in increments of 10°, with incoming light at 16° from the plane of the film. In Fig. 2 the PEEM images recorded for the different polarizations are shown. It is clear that the contrast between the domains decreases as the linear polarization rotates out-of-plane and disappears almost entirely at  $\omega = 90^\circ$ , indicating that the sensitivity to the AF spin axis of these domains is reduced. The difference between the domains gradually decreases, without any domains emerging stronger at specific angles, demonstrating that the AF axes of the domains lie in the film plane. The same experiment was also executed for azimuthal rotation of  $\varphi = 45^\circ$  and  $90^\circ$  (not shown). The results were similar; domain contrast disappears gradually as the polarization is rotated out-of-plane. Hence, we conclude that the domain contrast comes from different in-plane AF spin axes, without any out-of-plane components. This is consistent with data published for (111)-oriented La<sub>0.7</sub>Sr<sub>0.3</sub>FeO<sub>3</sub>/La<sub>0.7</sub>Sr<sub>0.3</sub>MnO<sub>3</sub> superlattices, for which the AF spin axis of La<sub>0.7</sub>Sr<sub>0.3</sub>FeO<sub>3</sub> was found to lie in the film plane for La<sub>0.7</sub>Sr<sub>0.3</sub>FeO<sub>3</sub> layers thicker than 3.6 nm.<sup>29</sup>

For a (001)-oriented LFO/STO film, the orthorhombic *c* axis can orient itself along both the  $[001]_c$  and  $[010]_c$  substrate axes [Fig. 3(a)], resulting in structural twinning domains which are directly coupled to the antiferromagnetic domains that lead to biaxial anisotropy.<sup>13</sup> We have recently shown three structural domain variants in a 20 nm thick (111)-oriented LFO thin film by dark field transmission electron microscopy.<sup>30</sup> The structural domains have irregular shape and diameters ranging from 50 to 300 nm. This is comparable to the antiferromagnetic domain sizes, which have similar irregular shape and with sizes of 50–500 nm. It should be noted that the smallest AF domains approach the resolution of the PEEM images. The structural domains differ by having the orthorhombic *a* or *b*

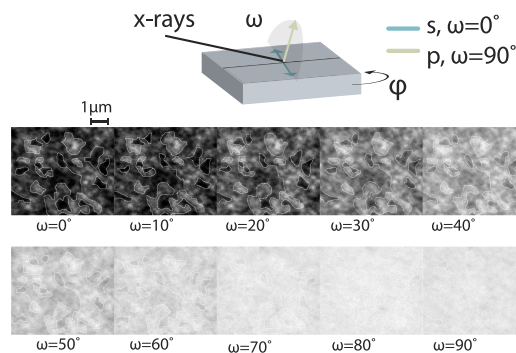


FIG. 2. Schematic of the measurement geometry for PEEM measurements,  $\omega$  is the x-ray polarization angle with the x-ray polarization axis at  $\omega = 0^\circ$  parallel to the sample surface (s-polarization) and  $\varphi$  is the azimuthal sample rotation angle with  $\varphi = 0^\circ$  parallel to the cubic  $[1\bar{1}0]$  substrate crystallographic direction. PEEM images recorded at  $\varphi = 0^\circ$ ,  $\omega = 0^\circ - 90^\circ$  with the outline of some domains drawn in white, showing how the contrast disappears gradually as the polarization is rotated out-of-plane, indicating an in-plane AF spin axis.

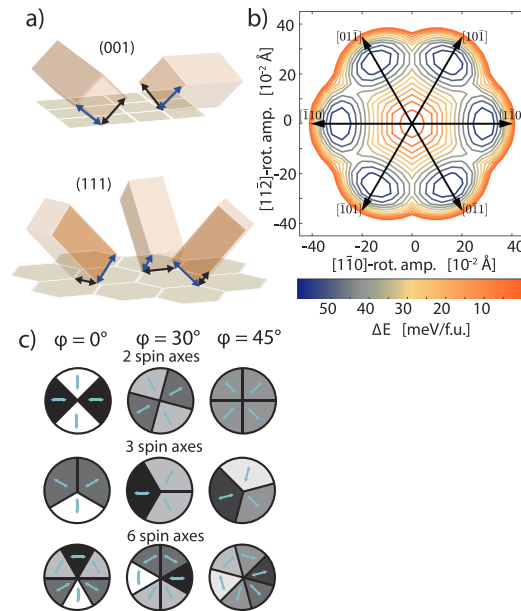


FIG. 3. (a) Schematic of structural domains in the (001) orientation and (111) orientation, with the orthorhombic  $a$  axis in black and the orthorhombic  $b$  axis in blue. (b) Energy contour plot for out-of-phase octahedral rotation mode amplitude from DFT calculations for (111)-oriented LFO/STO, showing six minima corresponding to six possible structural domains. (c) Schematic of how different number of spin axis would result in different number of contrast levels for different azimuthal angles ( $\varphi = 0^\circ$ ,  $30^\circ$ , and  $45^\circ$ ) for polarization parallel to the sample surface ( $\omega = 0^\circ$ ).

lattice parameters oriented parallel to the substrates  $[1\bar{1}0]$ ,  $[\bar{1}01]$ , or  $[0\bar{1}1]$  cubic directions [Fig. 3(a)]. However, as the film is strained to a cubic substrate, it is not possible to distinguish the  $a$  and  $b$  lattice parameters; thus, there are effectively six structural variants with equivalent energies. To test this, DFT calculations of the energy landscape as a function of octahedral rotation pattern when LFO is strained to (111)-oriented STO are shown in Fig. 3(b). Bulk LFO has an  $a^-a^-c^+$  tilt pattern, corresponding to out-of-phase octahedral rotations around the orthorhombic  $a$  and  $b$  axes and in-phase rotation along the  $c$  axis. The contour plot in Fig. 3(b) depicts the out-of-phase octahedral rotation mode amplitude around the in-plane directions of the STO substrates, with a constant in-phase rotation amplitude of  $0.3$  Å. Six discrete energy minima are found, corresponding to out-of-phase octahedral rotation around the  $\langle 1\bar{1}0 \rangle$  directions with an in-phase octahedral rotation around the  $\langle 100 \rangle$  family. Hence, DFT points towards six possible structural variants for the (111)-oriented LFO/STO system.

In Fig. 3(a) the black arrows indicate the bulk AF spin axis, with a 3-fold AF anisotropy, along the  $\langle 1\bar{1}0 \rangle$  crystalline directions, while the blue arrows indicate the  $b$ -axis, which would have an in-plane component along the  $\langle 11\bar{2} \rangle$  crystal directions. To experimentally determine the in-plane directions of the AF spin axes of the epitaxially strained film, the sample was rotated azimuthally around its center position ( $\varphi$ ) and imaged with s-polarized x-rays ( $\omega = 0^\circ$ ). Figure 3(c) depicts a schematic of how different domain structures would look like in PEEM for different azimuthal angles. For (001)-oriented films the AF spin orientation is biaxial, with  $90^\circ$  between the spin axes, resulting in black/white domains at  $\varphi = 0^\circ/90^\circ$  and no domain contrast at  $\varphi = 45^\circ$ , whereas multiple shades of grey are expected for three and six AF spin axes. In Fig. 4, we show corresponding data taken at an azimuthal angle of  $\varphi = 0^\circ$ ,  $45^\circ$ , and  $90^\circ$ . The images are shown at the same contrast settings. A similar domain contrast is observed for  $\varphi = 45^\circ$  as for  $\varphi = 0^\circ$  and  $90^\circ$ , clearly suggesting the presence of more than two spin axes. To establish the spin axes, we follow specific domains at different azimuthal angles ( $\varphi$ ). In Fig. 4, the high-contrast domains at  $\varphi = 0^\circ$  and  $90^\circ$  are clearly visible. For



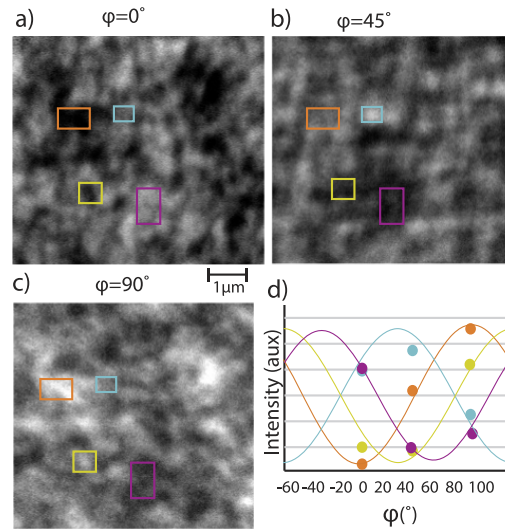


FIG. 4. [(a), (b), and (c)] PEEM images recorded at  $\varphi = 0^\circ$ ,  $45^\circ$ , and  $90^\circ$  and  $\omega = 0^\circ$  where  $\varphi = 0^\circ$  is parallel to the cubic  $[1\bar{1}0]$  substrate crystallographic direction. (d) The average XMLD signal intensity of 4 different domains [indicated in 4(a), (b), and (c) as colored squares] as a function of the azimuthal angle. The expected  $\cos^2 \theta$  dependence is outlined as a guide to the eye.

data taken at  $\varphi = 45^\circ$ , the previous black/white domains become grey, and new domains become evident making it difficult to determine the shape of the domains. Figure 4(d) depicts the variation in signal intensity for four domains which are dark and bright in the PEEM image recorded for  $\varphi = 0^\circ$ . The originally darkest domain in the  $\varphi = 0^\circ$  image (orange square) becomes grey for  $\varphi = 45^\circ$  and bright for  $\varphi = 90^\circ$ , in agreement with the AF axis parallel to  $\varphi = 90^\circ$ . However, for the bright domains in the  $\varphi = 0^\circ$  image (turquoise and purple square), one becomes dark (purple) at  $\varphi = 45^\circ$ , while the other becomes brighter (turquoise), before both domains turn to dark grey in the  $\varphi = 90^\circ$  image. The grey domain in  $\varphi = 0^\circ$  (yellow) continues to be dark grey in  $\varphi = 45^\circ$  and turns bright in  $\varphi = 90^\circ$ . As a guide to the eye, the expected  $\cos^2 \theta$  dependence of AF domains with maximum signal intensity at  $\varphi = 30^\circ$  (turquoise),  $90^\circ$  (orange),  $120^\circ$  (yellow), and  $150^\circ$  (purple) is plotted in Fig. 4(d). Though only three azimuthal angles are probed, the data fit well with this model and point towards the presence of AF domains with their axes oriented along both the in-plane  $\langle 1\bar{1}0 \rangle$  and  $\langle 11\bar{2} \rangle$  crystallographic directions.

To better probe if an AF spin axis can be oriented along the in-plane  $\langle 11\bar{2} \rangle$  direction, a series of images was measured with azimuthal orientation of the sample at  $\varphi = 0^\circ - 132^\circ$ , incremented with  $12^\circ$  per image. The images were then rotated to spatially comply with each other, and principal component analysis (PCA) on the image series was carried out to obtain the azimuthal dependence of the XMLD signal. Different domain categories were defined by having a maximum at a specific angle and a minimum  $90^\circ$  from the maximum, following the  $\cos^2 \theta$  dependence. In Fig. 5(a) the PEEM image recorded for  $\varphi = 0^\circ$  is presented for comparison with the resulting domain categories depicted in different colors in Fig. 5(b). Five different categories are identified, with maxima at  $\varphi = 0^\circ$  (blue),  $30^\circ$  (turquoise),  $60^\circ$  (green),  $90^\circ$  (orange), and  $120^\circ$  (yellow). Categories with maxima in between these angles are colored grey. For the images in Fig. 5(a), the spatial resolution is  $\sim 100$  nm. A good fit between Figs. 5(a) and 5(b) is found with domain features from 100 to 500 nm for all the domain categories. In Fig. 5(c) the mean intensity for the pixels in each category is plotted as a function of azimuthal rotation. A reasonable fit to the expected  $\cos^2 \theta$  dependence is found for all the five domain categories. Hence, we conclude that all five domain categories are present. In Fig. 5(b) it is clear that the domain categories with maxima at  $\varphi = 0^\circ$  (blue),  $60^\circ$  (green), and  $90^\circ$  (orange) are

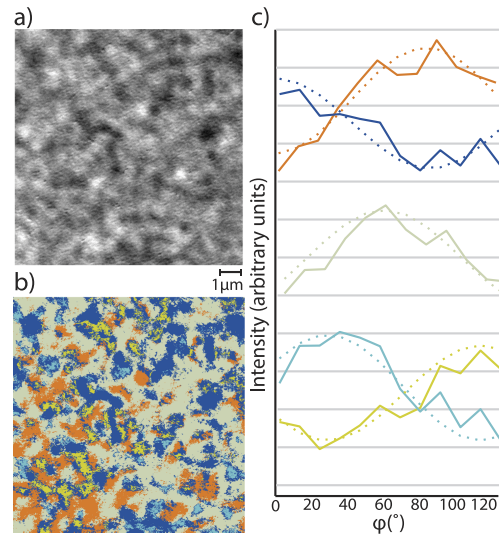


FIG. 5. (a) PEEM image at  $\varphi = 90^\circ$  and  $\omega = 0^\circ$ . (b) A compiled image of the different domain types (colored) found from a stack of PEEM images at  $\varphi = 0^\circ$ – $132^\circ$  and  $\omega = 0^\circ$ , where  $\varphi = 0^\circ$  is parallel to the cubic  $[1\bar{1}0]$  substrate crystallographic direction. (c) The mean intensity of the pixels for each azimuthal angle categorized by domain type, where blue (orange) has a maximum (minimum) at  $\varphi = 0^\circ$ , green has a maximum at  $\varphi = 60^\circ$ , and turquoise (yellow) has a maximum (minimum) at  $\varphi = 30^\circ$ . With fits of  $\cos^2 \theta$  dependence as dotted lines.

more dominant than domain categories with maxima at  $\varphi = 30^\circ$  (turquoise) and  $120^\circ$  (yellow), and no domains are found with maxima at  $\varphi = 150^\circ$  for these images. The orange, turquoise, and missing angle are domains with the AF spin axis along the  $\langle 1\bar{1}0 \rangle$  family of crystallographic directions, while the blue, green, and yellow are along the  $\langle 11\bar{2} \rangle$  family. The difference in dominance does not seem related to crystallographic families and could be due to a random distribution at this specific area of the sample. In Fig. 4 we have indications of domains with maxima at  $\varphi = 30^\circ$  (turquoise),  $90^\circ$  (orange),  $120^\circ$  (yellow), and  $150^\circ$  (purple). Taking the data in Figs. 4 and 5 together clearly suggests six possible AF axes in the sample.

In summary, the data reveal that LFO strained to (111)-oriented STO has six possible structural variants, which couple to the AF domain structure. The AF axis is oriented along the in-plane direction of the film, with an energy degeneracy between the  $\langle 1\bar{1}0 \rangle$  and the  $\langle 11\bar{2} \rangle$  in-plane directions, resulting in six possible AF spin axes in for the LFO/STO (111) epitaxial system. The correlation between the AF and structural twin domains, with the orthorhombic  $a$  and  $b$  axes orienting along the  $\langle 110 \rangle$  cubic substrate axes, opens up the possibility to engineering specific structural domain orientations as a possible avenue to control AF domains in thin films of perovskites.

Part of this work was performed at the SIM beamline of the Swiss Light Source, Paul Scherrer-Institut, Villigen, Switzerland. We thank Michele Buzzi, Dr. Armin Kleibert, and Professor Frithjof Nolting for their assistance with the PEEM experiments. The Advanced Light Source is supported by the Director, Office of Science, Office of Basic Energy Sciences, of the U.S. Department of Energy under Contract No. DE-AC02-05CH11231. Partial funding for these experiments was obtained from Nano-Network under Grant No. 190086/s10 and the Norway America foundation, through Norway House Foundation fund. The Norwegian Metacenter for Computational Science is acknowledged for providing computational resources Uninett Sigma 2, Project No. NN9301K.

<sup>1</sup> T. Jungwirth, X. Marti, P. Wadley, and J. Wunderlich, *Nat. Nanotechnol.* **11**(3), 231 (2016).

<sup>2</sup> V. Baltz, A. Manchon, M. Tsoi, T. Moriyama, T. Ono, and Y. Tserkovnyak, "Antiferromagnetic spintronics," [arXiv:1606.04284](https://arxiv.org/abs/1606.04284) [cond-mat.mtrl-sci].

- <sup>3</sup> X. Martí, I. Fina, and T. Jungwirth, *IEEE Trans. Magn.* **51**(4), 2900104 (2015); E. V. Gomonay and V. M. Loktev, *Low Temp. Phys.* **40**(1), 17 (2014).
- <sup>4</sup> J. Nogués and I. K. Schuller, *J. Magn. Magn. Mater.* **192**(2), 203 (1999); A. Berkowitz and K. Takano, *ibid.* **200**(1), 552 (1999); M. Kiwi, *ibid.* **234**(3), 584 (2001).
- <sup>5</sup> P. Wadley, B. Howells, J. Železný, C. Andrews, V. Hills, R. P. Campion, V. Novák, K. Olejník, F. Maccherozzi, S. S. Dhesi, S. Y. Martin, T. Wagner, J. Wunderlich, F. Freimuth, Y. Mokrousov, J. Kuneš, J. S. Chauhan, M. J. Grzybowski, A. W. Rushforth, K. W. Edmonds, B. L. Gallagher, and T. Jungwirth, *Science* **351**(6273), 587 (2016).
- <sup>6</sup> M. J. Grzybowski, P. Wadley, K. W. Edmonds, R. Beardsley, V. Hills, R. P. Campion, B. L. Gallagher, J. S. Chauhan, V. Novák, T. Jungwirth, F. Maccherozzi, and S. S. Dhesi, *Phys. Rev. Lett.* **118**(5), 057701 (2017).
- <sup>7</sup> K. Olejník, V. Schuler, X. Martí, V. Novák, Z. Kašpar, P. Wadley, R. P. Campion, K. W. Edmonds, B. L. Gallagher, J. Garces, M. Baumgartner, P. Gambardella, and T. Jungwirth, *Nat. Commun.* **8**, 15434 (2017).
- <sup>8</sup> E. G. Tveten, A. Qaiumzadeh, and A. Brataas, *Phys. Rev. Lett.* **112**(14), 147204 (2014).
- <sup>9</sup> A. Scholl, J. Stöhr, J. Lüning, J. W. Seo, J. Fompeyrine, H. Siegwart, J.-P. Locquet, F. Nolting, S. Anders, E. E. Fullerton, M. R. Scheinfein, and H. A. Padmore, *Science* **287**(5455), 1014 (2000).
- <sup>10</sup> H. Y. Hwang, Y. Iwasa, M. Kawasaki, B. Keimer, N. Nagaosa, and Y. Tokura, *Nat. Mater.* **11**(2), 103 (2012).
- <sup>11</sup> E. V. Gomonay and V. M. Loktev, *Low Temp. Phys.* **30**(10), 804 (2004).
- <sup>12</sup> E. Folven, A. Scholl, A. Young, S. T. Retterer, J. E. Boschker, T. Tybell, Y. Takamura, and J. K. Grepstad, *Phys. Rev. B* **84**(22), 220410 (2011).
- <sup>13</sup> J. W. Seo, E. E. Fullerton, F. Nolting, A. Scholl, J. Fompeyrine, and J.-P. Locquet, *J. Phys.: Condens. Matter* **20**(26), 264014 (2008).
- <sup>14</sup> E. Folven, Y. Takamura, and J. K. Grepstad, *J. Electron Spectrosc. Relat. Phenom.* **185**(10), 381 (2012).
- <sup>15</sup> I. Hallsteinsen, E. Folven, F. K. Olsen, R. V. Chopdekar, M. S. Rzechowski, C. B. Eom, J. K. Grepstad, and T. Tybell, *APL Mater.* **3**(6), 062501 (2015).
- <sup>16</sup> X. Liu, S. Middey, Y. Cao, M. Kareev, and J. Chakhalian, *MRS Commun.* **6**, 133 (2016).
- <sup>17</sup> S. M. Griffin, M. Lilienblum, K. T. Delaney, Y. Kumagai, M. Fiebig, and N. A. Spaldin, *Phys. Rev. X* **2**(4), 041022 (2012).
- <sup>18</sup> I. Hallsteinsen, M. Nord, T. Bolstad, P.-E. Vullum, J. E. Boschker, P. Longo, R. Takahashi, R. Holmestad, M. Lippmaa, and T. Tybell, *Cryst. Growth Des.* **16**(4), 2357 (2016).
- <sup>19</sup> I. Hallsteinsen, J. E. Boschker, M. Nord, S. Lee, M. Rzechowski, P. E. Vullum, J. K. Grepstad, R. Holmestad, C. B. Eom, and T. Tybell, *J. Appl. Phys.* **113**(18), 183512 (2013).
- <sup>20</sup> G. Kresse and J. Furthmüller, *Phys. Rev. B* **54**(16), 11169 (1996); G. Kresse and D. Joubert, *ibid.* **59**(3), 1758 (1999).
- <sup>21</sup> J. P. Perdew, A. Ruzsinszky, G. I. Csonka, O. A. Vydrov, G. E. Scuseria, L. A. Constantin, X. Zhou, and K. Burke, *Phys. Rev. Lett.* **100**(13), 136406 (2008).
- <sup>22</sup> S. L. Dudarev, G. A. Botton, S. Y. Savrasov, C. J. Humphreys, and A. P. Sutton, *Phys. Rev. B* **57**(3), 1505 (1998).
- <sup>23</sup> K. Kunc and R. M. Martin, *Phys. Rev. Lett.* **48**(6), 406 (1982).
- <sup>24</sup> M. Moreau, A. Marthinsen, S. M. Selbach, and T. Tybell, *Phys. Rev. B* **95**(6), 064109 (2017); A. Togo and I. Tanaka, *Scr. Mater.* **108**, 1 (2015).
- <sup>25</sup> J. Lüning, F. Nolting, A. Scholl, H. Ohldag, J. W. Seo, J. Fompeyrine, J.-P. Locquet, and J. Stöhr, *Phys. Rev. B* **67**(21), 214433 (2003).
- <sup>26</sup> R. Nakajima, J. Stöhr, and Y. U. Idzerda, *Phys. Rev. B* **59**(9), 6421 (1999).
- <sup>27</sup> E. Arenholz, G. van der Laan, R. V. Chopdekar, and Y. Suzuki, *Phys. Rev. B* **74**(9), 094407 (2006); Y. Takamura, F. Yang, N. Kemik, E. Arenholz, M. D. Biegalski, and H. M. Christen, *ibid.* **80**(18), 180417 (2009).
- <sup>28</sup> E. Folven, T. Tybell, A. Scholl, A. Young, S. T. Retterer, Y. Takamura, and J. K. Grepstad, *Nano Lett.* **10**(11), 4578 (2010); F. Nolting, A. Scholl, J. Stöhr, J. W. Seo, J. Fompeyrine, H. Siegwart, J. P. Locquet, S. Anders, J. Lüning, E. E. Fullerton, M. F. Toney, M. R. Scheinfein, and H. A. Padmore, *Nature* **405**(6788), 767 (2000); S. Czekaj, F. Nolting, L. J. Heyderman, P. R. Willmott, and G. van der Laan, *Phys. Rev. B* **73**(2), 020401 (2006).
- <sup>29</sup> Y. Jia, R. V. Chopdekar, E. Arenholz, A. T. Young, M. A. Marcus, A. Mehta, and Y. Takamura, *Phys. Rev. B* **92**(9), 094407 (2015); Y. Jia, R. V. Chopdekar, E. Arenholz, Z. Liu, M. D. Biegalski, Z. D. Porter, A. Mehta, and Y. Takamura, *ibid.* **93**(10), 104403 (2016).
- <sup>30</sup> E. Christiansen, M. Nord, I. Hallsteinsen, P. E. Vullum, T. Tybell, and R. Holmestad, *J. Phys.: Conf. Ser.* **644**(1), 012002 (2015).

# Octahedral coupling in (111)- and (001)-oriented $\text{La}_{2/3}\text{Sr}_{1/3}\text{MnO}_3$ / $\text{SrTiO}_3$ heterostructures

M. Moreau, S. M. Selbach and T. Tybell

Paper to be submitted



# Octahedral coupling in (111)- and (001)-oriented $\text{La}_{2/3}\text{Sr}_{1/3}\text{MnO}_3/\text{SrTiO}_3$ heterostructures

Magnus Moreau,<sup>1</sup> Sverre M. Selbach,<sup>2</sup> and Thomas Tybell<sup>1,\*</sup>

1) Department of Electronic Systems, NTNU Norwegian University of Science and Technology, 7491 Trondheim, Norway

2) Department of Materials Science and Engineering, NTNU Norwegian University of Science and Technology, 7491 Trondheim, Norway

\*E-mail: [thomas.tybell@iet.ntnu.no](mailto:thomas.tybell@iet.ntnu.no)

## ABSTRACT

The functional properties of perovskites are coupled to the rotations of the oxygen octahedra, affecting properties at epitaxial interfaces. Here we investigate octahedral coupling in  $\text{La}_{2/3}\text{Sr}_{1/3}\text{MnO}_3/\text{SrTiO}_3$  heterostructures by first principles density functional theory (DFT) calculations, emphasizing the important differences between systems oriented perpendicular to the (111)- and (001)-facets. We find that the coupling length of out-of-phase octahedral rotations is independent of the crystalline facet, pointing towards a steric effect. However, the detailed octahedral structure across the interface is significantly different between the (111)- and (001)-orientations. For (001)-oriented interfaces, there is a clear difference whether the rotation axis in  $\text{SrTiO}_3$  is parallel or perpendicular to the interface plane, while for the (111)-interface the different rotations axes in  $\text{SrTiO}_3$  are symmetry equivalent. Finally, we show that octahedral coupling across the interface can be used to control the spatial distribution of the spin density.

## INTRODUCTION

Epitaxial perovskite oxide heterostructures are interesting because their strong structure property coupling can result in novel properties at the interfaces. Central to the properties of these materials are the oxygen octahedral rotations, which can template across an interface to induce properties not found in the bulk material.<sup>1,2</sup> Examples where octahedral coupling at (001)-oriented interfaces have induced different properties include: improper ferroelectricity in PbTiO<sub>3</sub>/SrTiO<sub>3</sub> (STO) superlattices,<sup>3</sup> increased magnetization and electrical conductivity at the interface between La<sub>2/3</sub>Sr<sub>1/3</sub>MnO<sub>3</sub> (LSMO) and (LaAlO<sub>3</sub>)<sub>0.3</sub>(Sr<sub>2</sub>AlTaO<sub>6</sub>)<sub>0.7</sub>,<sup>4</sup> controlled magnetic anisotropy in LSMO on NdGaO<sub>3</sub>,<sup>5</sup> reduced band gap in BiFeO<sub>3</sub> at the interface with LSMO grown on STO,<sup>6</sup> and the ability to switch ferromagnetism on and off in CaMnO<sub>3</sub>/CaRuO<sub>3</sub> superlattices.<sup>7</sup> One central issue is the length scale the octahedral rotations couple across an interface. To this end, He *et al.*<sup>8</sup> used density functional theory (DFT) to calculate the octahedral coupling length from an infinitely rigid (001)-substrate without any chemical discrepancies, and found that the coupling length could be as short as one layer or extend deep into the film. This has later been confirmed experimentally by Aso *et al.*<sup>9</sup> who showed that the coupling length varied between one layer for BaTiO<sub>3</sub> and seven layers for Sr<sub>0.5</sub>Ca<sub>0.5</sub>TiO<sub>3</sub>. Hence the octahedral coupling length may be rationalized based on the size of A-cation.

A good model system to study the effect of octahedral coupling is ferromagnetic LSMO thin films grown on STO. STO is stable in a tetragonal  $I4/mcm$  crystal structure with an  $a^0a^0c^-$  Glazer tilt pattern<sup>10</sup> below 105 K, while above this temperature the cubic  $Pm\bar{3}m$  space group is stable without any octahedral rotations, i.e.  $a^0a^0a^0$  tilt pattern. Hence, possible coupling due to the octahedral rotations can be turned on and off experimentally by cooling below and heating above the transition temperature.<sup>11-16</sup> It has e.g. been found for (001)-oriented LSMO/STO that tetragonal STO can give rise to twinning in the LSMO thin film,<sup>11</sup> alter the coercive field,<sup>12</sup> transport properties,<sup>13</sup> and magnetic anisotropy<sup>14</sup> of LSMO. Furthermore, Segal *et al.*<sup>15</sup> explained changes in LSMO transport properties around the STO transition temperature in terms of phonon coupling across the interface.

Recent experimental advances has enabled growth along other crystalline facets, such as the (111)-facet,<sup>17</sup> a promising route to further develop oxide electronics.<sup>18</sup> The (111)-interface is interesting

because it possesses hexagonal symmetry that opens up for topological properties.<sup>19</sup> Furthermore, strain in the (111)-plane is considerably different than strain in the (001)-plane, and can give rise to structural Goldstone modes.<sup>20,21</sup> It has also been shown that octahedral rotation coupling can induce a net magnetic moment in antiferromagnetic LaFeO<sub>3</sub> without charge transfer.<sup>22</sup> However, a detailed understanding of how the (111)-interface affects the octahedral coupling remains an open question. As shown in Figure 1, the oxygen octahedra couple through three oxygen at the octahedra face at the (111)-interface (Figure 1 a), while at the (001)-interface the octahedra couple through one apex oxygen (Figure 1 b). Thus, a different coupling is expected for the two facets. Furthermore, for the (111)-interface all of the three octahedra rotation axes  $x$ ,  $y$  and  $z$  are equivalent. However, for the (001)-interface the  $x$ - and  $y$ - axes are parallel to the interface plane, while the  $z$ -axis is perpendicular to it. Hence, for the (111)-interface, no difference in the coupling between out-of-plane  $\gamma$ -rotations and in-plane  $\alpha$ - and  $\beta$ -rotations (see Figure 1 for definitions) is expected, in contrast to (001)-oriented interfaces.<sup>8</sup>

In this work we compare octahedral coupling between LSMO thin films and STO substrates by DFT, with focus on the difference between (111)- and (001)-oriented interfaces. We exploit the tilt patterns in the two stable phases of STO (tetragonal and cubic) in order to compare how octahedral rotations in the substrate can affect the film. The paper is structured as follows: First the calculation details are explained. Then different methodologies for modelling the Sr doping in LSMO are compared, before establishing how strain from (111)- and (001)-oriented STO affects the octahedral rotations of LSMO. Finally, we correlate how changes in octahedral rotations in LSMO, due to coupling to STO, with the spatial spin density distribution.

### CALCULATION DETAILS

The DFT calculations were performed with the Vienna Ab-initio Simulation Package (VASP, version 5.3.3)<sup>23,24</sup> employing the projector augmented wave method (PAW).<sup>24,25</sup> The Perdew-Burke-Ernzerhof generalized gradient approximation for solids (PBEsol) was chosen as it has been shown to accurately reproduce the crystal structure and lattice parameters of solids.<sup>26</sup> The recommended PAW potentials supplied with VASP for La, Sr, Mn, Ti and O were used, having electron configurations  $4s^2 4p^6 5d^1 6s^2$ ,  $4s^2 4p^6 5s^2$ ,  $3p^6 3d^5 4s^2$ ,  $3s^2 3p^6 3d^2 4s^2$  and  $2s^2 2p^4$  respectively. To treat the correlated  $d$  and  $f$  electrons of



Mn and La, Hubbard U values of 3 and 10 eV, respectively, were applied to these orbitals using the Dudarev method.<sup>27</sup> These values U have been shown to adequately model perovskite oxides containing Mn and La.<sup>28,29</sup> To include the strain from the substrate, the in-plane lattice vectors were locked to those calculated for cubic SrTiO<sub>3</sub>, while the out-of-plane and atomic coordinates were allowed to relax. For (111)-strain, the in-plane lattice vectors were along  $[1\bar{1}0]$ - and  $[01\bar{1}]$ -pseudocubic directions and the out-of-plane lattice vector was along  $[111]$ -pseudocubic direction, while for (001)-strain the in-plane lattice vectors were along  $[100]$ - and  $[010]$ -pseudocubic directions and the out-of-plane lattice vector was along  $[001]$ -pseudocubic direction. The atomic positions and the free lattice parameters were relaxed until the forces on the atoms were lower than 1 meV/Å, for the bulk and strain calculations. The plane wave cutoff was set to 550 eV, and the calculations of bulk properties were done with LSMO in the bulk  $R\bar{3}c$  in hexagonal setting, which can be considered a  $\sqrt{2} \times \sqrt{2} \times 2\sqrt{3}$  supercell of the aristotype perovskites structure. This cell is oriented such that the  $\mathbf{a}$ ,  $\mathbf{b}$  and  $\mathbf{c}$  lattice vectors are parallel to the  $[1\bar{1}0]$ -,  $[01\bar{1}]$ - and  $[111]$ -pseudocubic directions respectively, hence this cell was also used for calculations of LSMO when strained in the (111)-plane. On the other hand, a  $2 \times 2 \times 2$  supercell was used for the calculations of LSMO under (001)-strain, this cell has the  $\mathbf{a}$ ,  $\mathbf{b}$  and  $\mathbf{c}$  lattice vectors along  $[100]$ -  $[010]$ - and  $[001]$ -pseudocubic directions respectively. A  $5 \times 5 \times 2$  gamma centered k-point mesh was used in the  $\sqrt{2} \times \sqrt{2} \times 2\sqrt{3}$  calculation cells, while a  $4 \times 4 \times 4$  mesh was used for the  $2 \times 2 \times 2$  cells. Corresponding k-point densities were used for the supercells. To model the Sr doping the virtual crystal approximation<sup>30</sup> (VCA) was used by setting the VCA-tag in VASP to create a superposition of the La and Sr PAW-potentials. As VCA has been used to model LSMO mainly with other DFT-codes,<sup>31</sup> test calculations were performed. These tests compared bulk parameters of LSMO with VCA to calculations where the Sr positions are discrete and spread out over the possible A sites in a  $\sqrt{2} \times \sqrt{2} \times 2\sqrt{3}$  supercell containing 30 atoms, and a  $2\sqrt{2} \times 2\sqrt{2} \times 2\sqrt{3}$  containing 120 atoms.

For the calculations of the interfaces  $\sqrt{2} \times \sqrt{2} \times 10\sqrt{3}$  and  $\sqrt{2} \times \sqrt{2} \times 14$  supercells were used for the (111)- and (001)-interface respectively, as illustrated in Figure 2. These cells were terminated with Ti for (111)-interfaces and TiO<sub>2</sub> for (001)-interfaces, as Ti-based terminations are the results of the commonly used substrate preparations for both STO (001) and (111).<sup>32</sup> The (111)-interface calculation

cells have 23.5 layers of LSMO and 6.5 layers of STO, with a layer spacing of  $d_{111} \sim a_{pc} / \sqrt{3}$ , where  $a_{pc}$  is the pseudocubic lattice constant (Figure 2 a), while the (001)-interface calculation cells have 11.5 layers of LSMO and 2.5 layers of STO with a layer spacing of  $d_{001} \sim a_{pc}$  (Figure 2 b). Using selective dynamics, the STO layers away from the interface was locked to have no rotations, equivalent to the cubic phase stable over 105 K, or locked out-of-phase rotations around one of the pseudocubic axis, equivalent to the tetragonal phase stable under 105 K. The atoms in the free STO layer and all of the atoms in LSMO were allowed to relax until the forces on the free atoms were less than 5 meV/Å, see Figure 2. This is a slightly less strict force criterion than for the bulk and strain calculations, but it was found to be sufficient for these larger cells. For the (001)-interface, there are two symmetry equivalent ways to have the out-of-phase rotation axis of the tetragonal STO; it can be either out-of-plane (tilt pattern  $a^0 a^0 c^-$ ) or in-plane (tilt pattern  $a^0 b^- a^0$  equivalent to  $a^- b^0 b^0$ ). While for the (111)-interface, the three different tetragonal STO tilt patterns,  $a^0 a^0 c^-$ ,  $a^0 b^- a^0$  and  $a^- b^0 b^0$ , are all symmetry equivalent. In order to isolate the effect of rotational coupling, from that of the strain, the in-plane lattice parameters of the interface cells were locked to those calculated for cubic STO, while the out-of-plane lattice parameter was locked to the sum of STO and LSMO strained to STO with the given thicknesses. It was also found that the small changes in lattice parameters between cubic and tetragonal STO has little influence on the octahedral rotations of LSMO.<sup>15</sup>

All crystallographic directions are given in the pseudocubic setting unless otherwise specified, and the atomic structure visualizations were done with VESTA.<sup>33</sup>

## RESULTS AND DISCUSSION

### VCA to model bulk LSMO

To test how suitable VCA is for modelling distortions in LSMO we compare results for bulk LSMO calculated with VCA to a supercell approach with different sizes, containing 30 and 120 atoms, in addition to experimental results.<sup>34</sup> As shown in Table I, the lattice parameters and the  $c/\sqrt{6}a$ -ratio are closest to the experimental value for the largest supercell, but still within a satisfactory range for the

calculations by VCA. Importantly, the VCA and the supercell approaches all correctly reproduce the experimental magnetic moment. The average octahedral rotation angles are subtly underestimated in the supercells, while the VCA approach overestimates them. However, in the supercell approach, different Mn atoms have different distance to the Sr atoms, causing the octahedral rotation angles to vary for different octahedra in the supercell. This variation with position is due to the artificial ordering of Sr in the calculations. When studying octahedral coupling, such spread in octahedral rotations will be superimposed on any effects for octahedra coupling across the interface, making such approach less intuitive. To quantify this spread, the standard deviation in octahedral rotation,  $\sigma$ , is given in Table I. As shown,  $\sigma$  is largest in the 120 atom cell and becomes smaller in the 30 atom cell, while it is exactly equal to zero for the VCA approach, as there is no artificial Sr ordering. This makes the VCA approach suitable when comparing octahedral coupling. Table I also shows how the calculated exchange energy depends on Sr doping model, albeit in all cases a ferromagnetic ground state is the most stable. Finally, we note that due to the increased symmetry and reduced cell size (compared to the large supercell) the VCA approach is less CPU expensive than the supercell approaches.

Figure 3 depicts the calculated density of states (DOS) using the VCA and supercell approaches. As shown, the DOSes are quite similar, especially around the Fermi level, and all approaches capture the known half-metallic character of LSMO, with a similar bandwidth of  $\sim 2.95$  eV. Taken together, the results in Table I and Figure 3, show that the VCA approach gives an adequate description of both the structural and electrical properties of LSMO without artificial variations in the rotation angle.

#### Effect of strain on LSMO

The effect of in-plane strain in the (111)- and (001)-plane is different, as earlier reported for  $\text{LaAlO}_3$ ,<sup>20</sup> which has an  $R\bar{3}c$  ground state, same as LSMO. Relying on both VCA and supercell approaches, we find that in agreement with earlier results for (111)-strained  $\text{LaAlO}_3$ , tensile (111)-strain inflicted on LSMO from STO preserves the  $R\bar{3}c$  symmetry with tilt pattern  $a^- a^- a^-$ . The effect of (111)-strain on the octahedral rotations is thus to increase  $\alpha = \beta = \gamma$ , and with the VCA approach the increase is to  $5.50^\circ$  compared the bulk VCA value of  $5.19^\circ$ . On the other hand, (001)-strain from a STO substrate does

not preserve the  $R\bar{3}c$  symmetry. Instead it has been found experimentally that a resulting in-phase rotation is expected.<sup>35,36</sup> However, the exact tilt pattern of LSMO under (001)-strain from a STO substrate is under debate, Boschker et al.<sup>36</sup> finds a  $a^-a^-c^+$  tilt pattern with  $Pnma$  symmetry. In contrast, Vailionis et al.<sup>35</sup> finds a  $a^+a^-c^0$  tilt pattern with space group  $Cmcm$  for LSMO on (001)-oriented STO. Our results with both the supercell approach and VCA agrees with Boschker et al.<sup>36</sup> where an in-phase octahedral rotation is preferred around the out-of-plane axis, giving a  $a^-a^-c^+$  tilt pattern with  $Pnma$  symmetry and  $\alpha = \beta > \gamma$ . The octahedral rotation angles from the VCA approach are:  $\alpha = \beta = 7.48^\circ$  and  $\gamma = 5.23^\circ$ . The result by Vailionis et al.,<sup>35</sup> a  $a^+a^-c^0$  tilt pattern, is due to the assumption that the rotation around the out-of-plane axis,  $\gamma$ , has to be exactly zero under tensile (001)-strain. This assumption is reasonable for insulating oxides such as  $\text{LaAlO}_3$ ,<sup>20,28,37</sup> but for metallic oxides, such as LSMO and  $\text{LaNiO}_3$ , the increased screening results in a non-zero out-of-plane rotation also under tensile strain.<sup>2,38</sup>

#### Octahedral coupling in the (111)-plane

Figure 4 and 5, show the octahedral coupling from the different phases in STO as calculated with VCA and in-plane  $\sqrt{2} \times \sqrt{2}$  supercell to treat the Sr doping, respectively. As shown, the response is similar for both approaches. For the  $a^0a^0a^0$  locked STO, as shown in Figure 4a and 5a, the relaxation occurs almost exclusively in the STO layer closest to the interface (layer 0). Note that all the rotation angles  $\alpha$ ,  $\beta$  and  $\gamma$  in this case behave in the same manner, as there is no breaking of the trigonal symmetry. On the other hand, for the  $a^0a^0c^-$  locked STO (Figure 4b and 5b) the  $\gamma$ -rotation increases above the equilibrium value, denoted  $\gamma_{strain}$ , both in LSMO and STO before it reaches the equilibrium value in LSMO after approximately 7 layers  $\sim 14 \text{ \AA}$ . The same relaxation length is observed for the  $\alpha$  and  $\beta$  rotations, but they approach the equilibrium value, denoted  $\alpha_{strain}$  and  $\beta_{strain}$ , from below. That only the first LSMO layer is slightly affected by the  $a^0a^0a^0$  locked STO, as shown in Figure 4a and 5a implies that the STO is more susceptible to changes in octahedral rotations than LSMO, and that the octahedral rotation pattern would likely propagate further into STO if it had not been fixed in the calculations. That the  $\gamma$ -angle increases above the equilibrium values before it relaxes for the  $a^0a^0c^-$

locked STO (Figure 4b and 5b) is consistent with that it costs less energy to have all rotation angles distorted by a similar amount, instead of having different relaxation lengths for the different rotation axes.

There are two notable differences between the supercell approach and the VCA, they are: (1) due to the discrete doping in the supercell, the rotation angles are not constant in the LSMO far away from the interface ( $\sigma \neq 0$ , Table I). (2) Since the equilibrium rotation angles are different in LSMO calculated with VCA or supercell approach as shown in Table I, the equilibrium rotation angles are slightly different. However, how the rotations couple across the interface is the same. These results show that the both the VCA and supercell approach can be used to model interface effects of LSMO. However, the VCA approach is preferable when assessing properties such as relaxation lengths, as the properties does not depend on the choice of Sr doping positions. Based on this rationale, we will only consider interfaces calculated with the VCA approach in the following.

#### Octahedral coupling in the (001)-plane

The octahedral coupling the (001)-interface between LSMO and STO is shown in Figure 6. As shown, there is a significant difference between the (001)-interface (Figure 6) and the (111)-interface (Figure 4). For the (001)-interface the in-plane ( $\alpha$  and  $\beta$ ) and out-of-plane ( $\gamma$ ) rotations are different, even when the STO is locked in the  $a^0a^0a^0$ -rotation pattern (Figure 6a), in contrast to (111)-interface coupling (Figure 4a). As shown in Figure 6 a), the  $\alpha = \beta$  rotations show an expected gradual increase towards the equilibrium values,  $\alpha_{strain} = \beta_{strain}$ , over 4 LSMO layers  $\sim 14 \text{ \AA}$ . On the other hand, the  $\gamma$ -rotation for  $a^0a^0a^0$ -STO(001), increases above the out-of-phase equilibrium value,  $\alpha_{strain}$ , in the free STO layer (layer 0), then it decreases below its equilibrium value,  $\gamma_{strain}$ , in the 3<sup>rd</sup> LSMO layer, before it reaches  $\gamma_{strain}$  in the 4<sup>th</sup> LSMO layer from the interface, before finally displaying a small dip in the 5<sup>th</sup> the layer. That the rotation pattern first goes down below the equilibrium value in the 3<sup>rd</sup> layer is followed by a change of rotation type. The first two layers has out-of-phase rotation (-), as preferred in STO, and increased out-of-plane lattice parameter  $c_{pc} \approx 3.84 \text{ \AA}$ , while the layers far away from the interface has in-phase rotations (+) and lattice parameter of  $c_{pc} \approx 3.82 \text{ \AA}$  as dictated by the tensile strain from

the (001)-oriented STO substrate. A change of octahedral rotation pattern and increased lattice parameters close to the interface has also been documented for LSMO on STO(001) experimentally.<sup>39</sup> We note that there here are in-phase and out-of-phase octahedral rotations that meet, which for (111)-interfaces gives rise to a rotation mismatch and changed magnetic properties.<sup>22</sup> No such mismatch is expected in this case, as the change of rotation type occurs around the out-of-plane rotation axis.

When STO is locked in a tilt pattern equivalent to the tetragonal state stable below 105 K, there are as mentioned two symmetry inequivalent orientations with respect to the (001)-interface,  $a^0a^0c^-$  and  $a^-b^0b^0$ . The octahedral coupling for these two orientations are shown in Figure 6 b) and c) respectively. For the  $a^0a^0c^-$ -locked STO, shown in figure 6 b), the sense of octahedral coupling is very similar to the coupling for  $a^0a^0a^0$  locked STO, as described above, with only small changes in the absolute rotation amplitude. This is in contrast to the case for  $a^-b^0b^0$ -locked STO as shown in Figure 6 c), where there is an additional difference between the in-plane rotations  $\alpha$  and  $\beta$ . Here the  $\alpha$ -rotation, which is non-zero in STO, increases to the equilibrium value in LSMO,  $\alpha_{strain}$  in the first LSMO layer, similar to what occurred for LSMO on  $a^0a^0a^0$ -locked STO(111) (Figure 4 a). On the other hand,  $\beta$  which is zero in STO (Figure 6c), relaxes to its equilibrium value  $\beta_{strain} = \alpha_{strain}$  over 4 unit cells  $\sim 14 \text{ \AA}$ , which is the same distance shown for LSMO on  $a^0a^0a^0$ - and  $a^0a^0c^-$ -locked STO (001) (Figure 6 a and b). The out-of-plane rotation angle  $\gamma$  is slightly different for  $a^-b^0b^0$ -locked STO (Figure 6 c), compared to  $a^0a^0a^0$ - and  $a^0a^0c^-$ -locked STO (001) (Figure 6 a and b). For  $a^-b^0b^0$ -locked STO (Figure 6 c), the  $\gamma$ -rotation is lower in the first LSMO layers and never exceeds  $\alpha_{strain}$ . Also, in the 3<sup>rd</sup> LSMO layer, the  $\gamma$ -rotation is not reduced as much as for  $a^-b^0b^0$ -locked STO compared to  $a^0a^0a^0$ - and  $a^0a^0c^-$ -locked STO (001). This shows that for (001)-interfaces, the in-plane rotations couple more strongly into the thin film than out-of-plane rotations.

### Octahedral coupling length

As shown in the previous sections, there are both similarities and difference between the octahedral coupling in the (111)- and (001)-plane. For the (111)-interface a coupling length of 7 layers, corresponding to  $\sim 14 \text{ \AA}$  was found. For the (001)-interface the coupling is longer for in-phase out-of-

plane rotations ( $\gamma$ ) than the out-of-phase in-plane rotations ( $\alpha$  and  $\beta$ ). Hence, the total octahedral coupling length is longer for (001)-oriented LSMO compared to the (111)-orientation, as (111) strain does not give rise to in-phase rotations. However, if one only considers the out-of-phase rotations, the coupling length for the (001)-interface is 4 unit-cells which corresponds to a length of  $\sim 14 \text{ \AA}$ , similar to the (111)-case. That the coupling length does not vary with interface facet, indicates that the coupling is a steric effect, in agreement with Aso *et al.*<sup>9</sup>

### Effect on spin densities

In order to elucidate how the rotation pattern of the STO can affect the functional properties of an epitaxial thin film, the spin density difference in LSMO, depending on if STO is locked in a tilt pattern of  $a^0 a^0 c^-$  and a  $a^0 a^0 a^0$ , is calculated and shown in Figure 7. For the (111)-interface all three variations of the  $a^0 a^0 c^-$  tilt pattern is symmetry equivalent, while for the (001)-interface the  $a^0 a^0 c^-$  and  $a^- b^0 b^0$  are inequivalent. The spin density difference is used since it gives information about possible spatial variation of the spin polarized electron density, even though the total moment per Mn site is almost unaffected by the octahedral rotations. That the moment per Mn site is not affected can be rationalized by the large bandwidth of the half-metallic state of LSMO, as shown in Figure 3.<sup>8</sup>

The effect of (111)-oriented STO on the spin density in LSMO, for one condensed  $a^0 a^0 c^-$  tilt pattern, is shown in Figure 7 a). As shown, a change of octahedral tilt pattern in STO below the 105K structural transition has a large effect on the spin density. The change in tilt pattern has a net shift of the spin density along the in-plane  $[1\bar{1}0]$ -direction, as shown in Figure 7 c) by the blue and yellow lobes. The difference is largest at the interface, and it is reduced further into the LSMO (Figure 7a), consistent with the previous finding that the octahedral rotations relaxes towards the same value far away from the interface (Figure 4). That the shift is along the  $[1\bar{1}0]$ -direction can be understood from the fact that it is orthogonal to the locked STO rotation axis, which is around  $[001]$ .

The effect of (001)-oriented STO on the spin density is shown in Figure 7 b), d) and f). As shown for (001)-interface, there is a large difference between the two symmetry inequivalent versions of STO rotations. When the STO is locked in a state with out-of-plane rotations ( $a^0 a^0 c^-$ ) the spin density

difference is almost zero (Figure 7 b). There is only a weak signal in the spin density difference in the 4<sup>th</sup> Mn layer, with a difference along the in-plane  $[\bar{1}10]$ -direction as shown in Figure 7 e). This is again orthogonal to the  $[001]$ , which is the STO rotation axis. This small difference in spin density is related to the relatively low change in the octahedral rotations when the STO layer is locked in a  $a^0a^0a^0$  tilt pattern, compared to  $a^0a^0c^-$  (Figure 6 a and b). On the other hand, when the STO layer is locked with an in-plane tilt pattern, e.g.  $a^-b^0b^0$ , there is a substantial spin density difference as shown in Figure 7 b) and e). Similar to the case for the (111)-interface (Figure 7 a), the spin density difference for STO(001) locked in  $a^-b^0b^0$  tilt pattern (Figure 7c) is largest at the interface and is reduced further into the LSMO as the difference between the tilt patterns is reduced (Figure 6 a and c). Furthermore for the  $a^-b^0b^0$  locked STO(001), the spin density difference is now along  $[011]$  as shown in Figure 7 e). This is again orthogonal to the STO rotation axis  $[100]$ . Hence, in contrast to the (111)-oriented interface, (001)-interfaces can give rise to a spin density difference with an out-of-plane component.

Comparing the absolute values of the spin density shifts we find that the (111)-interface has an absolute difference of  $0.078 \text{ q/\AA}^2$ , while the absolute value the (001)-interface is  $0.092 \text{ q/\AA}^2$  and  $0.022 \text{ q/\AA}^2$  depending on whether the rotations in the STO is in-plane or out-of-plane, respectively. I.e. the absolute shifts for (111) and (001) in-plane rotated STO are similar and considerably larger than (001) with the rotation axis out-of-plane.

The difference in spin density can affect the magnetic properties such as the easy axis and magnetic moment. For thin films, the magnetic easy axis is typically in the film plane,<sup>40</sup> and LSMO on cubic (001)-oriented STO has biaxial anisotropy, with easy axes along the  $\langle 110 \rangle$ -family of in-plane directions.<sup>41</sup> Furthermore, it has been shown that when LSMO on (001)-STO is cooled below the tetragonal transition temperature, one observes an increase in the coercive field which can be controlled by the cooling history.<sup>12</sup> These changes in coercive field can be rationalized in terms of different domains, which have different effects on the spin density. For LSMO on (111)-oriented cubic STO on the other hand, it is found that the magnetic easy axis has a six fold symmetry with easy axes along both the  $\langle 1\bar{1}0 \rangle$ - and  $\langle 11\bar{2} \rangle$ -families of in-plane directions.<sup>42</sup> For a given  $a^0a^0c^-$  condensation, corresponding



to Figure 7 a and c, there is an effective spin accumulation along the  $[1\bar{1}0]$  direction below 105K, as shown in Figure 8. If all three  $a^0a^0c^-$  rotational variances condenses, we predict that the tetragonal transition in STO should lift the degeneracy between the  $\langle 1\bar{1}0 \rangle$ - and  $\langle 11\bar{2} \rangle$ -family of in-plane directions and result in triaxial anisotropy.<sup>43</sup>

### CONCLUSION

The different symmetry between the (111)-interface and the (001)-interface makes the octahedral coupling between LSMO and STO significantly different. However, the coupling length of out-of-phase rotations is the same,  $\sim 14 \text{ \AA}$ , pointing towards octahedral coupling being a steric effect. Furthermore, for the (111)-interface, the  $a^0a^0c^-$  tilt pattern of STO have three symmetry equivalent variances, while for the (001)-interface, the in-phase rotation can be either in-plane or out-of-plane. This difference has been shown to have a large impact on how the octahedra couples. The octahedral coupling furthermore affects the spin density, where the difference is perpendicular to the STO-rotation axis. These results show that one can rely on geometrical lattice engineering and steric effects to control octahedral coupling and anisotropies of functional properties.

### Acknowledgements

The Norwegian Metacenter for Computational Science is acknowledged for providing computational resources, Uninett Sigma 2, Project No. NN9301K. TT acknowledges funding through the Research Council of Norway grant No.231290.

## REFERENCES

- <sup>1</sup> P. Zubko, S. Gariglio, M. Gabay, P. Ghosez, and J. M. Triscone, *Annu Rev Condens Ma P* **2**, 141 (2011); J. Chakhalian, J. W. Freeland, A. J. Millis, C. Panagopoulos, and J. M. Rondinelli, *Rev. Mod. Phys.* **86**, 1189 (2014); J. M. Rondinelli, S. J. May, and J. W. Freeland, *MRS Bulletin* **37**, 261 (2012).
- <sup>2</sup> J. M. Rondinelli and N. A. Spaldin, *Adv. Mat.* **23**, 3363 (2011).
- <sup>3</sup> E. Bousquet, M. Dawber, N. Stucki, C. Lichtensteiger, P. Hermet, S. Gariglio, J. M. Triscone, and P. Ghosez, *Nature* **452**, 732 (2008).
- <sup>4</sup> E. J. Moon, P. V. Balachandran, B. J. Kirby, D. J. Keavney, R. J. Sichel-Tissot, C. M. Schlepütz, E. Karapetrova, X. M. Cheng, J. M. Rondinelli, and S. J. May, *Nano Lett.* **14**, 2509 (2014).
- <sup>5</sup> Z. Liao, M. Huijben, Z. Zhong, N. Gauquelin, S. Macke, R. J. Green, S. Van Aert, J. Verbeeck, G. Van Tendeloo, K. Held *et al.*, *Nat. Mater.* **15**, 425 (2016).
- <sup>6</sup> A. Y. Borisevich, H. J. Chang, M. Huijben, M. P. Oxley, S. Okamoto, M. K. Niranjana, J. D. Burton, E. Y. Tsybmal, Y. H. Chu, P. Yu *et al.*, *Phys. Rev. Lett.* **105**, 087204 (2010).
- <sup>7</sup> A. J. Grutter, A. Vailionis, J. A. Borchers, B. J. Kirby, C. L. Flint, C. H. He, E. Arenholz, and Y. Suzuki, *Nano Lett.* **16**, 5647 (2016).
- <sup>8</sup> J. He, A. Borisevich, S. V. Kalinin, S. J. Pennycook, and S. T. Pantelides, *Phys Rev Lett* **105**, 227203 (2010).
- <sup>9</sup> R. Aso, D. Kan, Y. Shimakawa, and H. Kurata, *Crystal Growth & Design* **14**, 2128 (2014).
- <sup>10</sup> A. M. Glazer, *Acta Crystallogr. Sect. B* **28**, 3384 (1972).
- <sup>11</sup> V. K. Vlasko-Vlasov, Y. K. Lin, D. J. Miller, U. Welp, G. W. Crabtree, and V. I. Nikitenko, *Phys. Rev. Lett.* **84**, 2239 (2000).
- <sup>12</sup> M. Ziese, I. Vrejoiu, A. Setzer, A. Lotnyk, and D. Hesse, *New Journal of Physics* **10**, 063024 (2008).
- <sup>13</sup> M. Egilmez, M. M. Saber, I. Fan, K. H. Chow, and J. Jung, *Phys. Rev. B* **78**, 172405 (2008).
- <sup>14</sup> D. Pesquera, V. Skumryev, F. Sánchez, G. Herranz, and J. Fontcuberta, *Phys. Rev. B* **84**, 184412 (2011).
- <sup>15</sup> Y. Segal, K. F. Garrity, C. A. F. Vaz, J. D. Hoffman, F. J. Walker, S. Ismail-Beigi, and C. H. Ahn, *Phys. Rev. Lett.* **107**, 105501 (2011).
- <sup>16</sup> X. Li, I. Lindfors-Vrejoiu, M. Ziese, A. Gloter, and P. A. van Aken, *Phys. Rev. Lett.* **113**, 046101 (2014).
- <sup>17</sup> I. Hallsteinsen, J. E. Boschker, M. Nord, S. Lee, M. Rzchowski, P. E. Vullum, J. K. Grepstad, R. Holmestad, C. B. Eom, and T. Tybell, *J. Appl. Phys.* **113**, 183512, 183512 (2013).
- <sup>18</sup> J. Chakhalian, A. J. Millis, and J. Rondinelli, *Nat. Mater.* **11**, 92 (2012).
- <sup>19</sup> D. Xiao, W. Zhu, Y. Ran, N. Nagaosa, and S. Okamoto, *Nat. Commun.* **2**, 596 (2011); D. Doennig, S. Baidya, W. E. Pickett, and R. Pentcheva, *Phys. Rev. B* **93**, 165145 (2016); D. Doennig, W. E. Pickett, and R. Pentcheva, *Phys. Rev. Lett.* **111**, 126804 (2013); S. Raghu, X. L. Qi, C. Honerkamp, and S. C. Zhang, *Phys Rev Lett* **100**, 156401 (2008); K.-Y. Yang, W. Zhu, D. Xiao, S. Okamoto, Z. Wang, and Y. Ran, *Phys. Rev. B* **84**, 201104 (2011); K. Yamauchi, P. Barone, T. Shishidou, T. Oguchi, and S. Picozzi, *Phys Rev Lett* **115**, 037602 (2015).
- <sup>20</sup> M. Moreau, A. Marthinsen, S. M. Selbach, and T. Tybell, *Phys. Rev. B* **95**, 064109 (2017).
- <sup>21</sup> A. Marthinsen, S. M. Griffin, M. Moreau, T. Grande, T. Tybell, and S. M. Selbach, *arXiv preprint arXiv:1708.03490* (2017).
- <sup>22</sup> I. Hallsteinsen, M. Moreau, A. Grutter, M. Nord, P. E. Vullum, D. A. Gilbert, T. Bolstad, J. K. Grepstad, R. Holmestad, S. M. Selbach *et al.*, *Phys. Rev. B* **94**, 201115 (2016).
- <sup>23</sup> G. Kresse and J. Furthmuller, *Phys. Rev. B* **54**, 11169 (1996).
- <sup>24</sup> G. Kresse and D. Joubert, *Phys. Rev. B* **59**, 1758 (1999).
- <sup>25</sup> P. E. Blochl, *Phys. Rev. B* **50**, 17953 (1994).
- <sup>26</sup> J. P. Perdew, A. Ruzsinszky, G. I. Csonka, O. A. Vydrov, G. E. Scuseria, L. A. Constantin, X. Zhou, and K. Burke, *Phys. Rev. Lett.* **100**, 136406, 136406 (2008).
- <sup>27</sup> S. L. Dudarev, G. A. Botton, S. Y. Savrasov, C. J. Humphreys, and A. P. Sutton, *Phys. Rev. B* **57**, 1505 (1998).

- <sup>28</sup> R. L. Johnson-Wilke, D. Marincel, S. Zhu, M. P. Warusawithana, A. Hatt, J. Sayre, K. T. Delaney, R. Engel-Herbert, C. M. Schlepuetz, J. W. Kim *et al.*, *Phys. Rev. B* **88**, 174101, 174101 (2013).
- <sup>29</sup> U. Aschauer, N. Vonruti, and N. A. Spaldin, *Phys. Rev. B* **92**, 054103 (2015); M. Nord, P. E. Vullum, M. Moreau, J. E. Boschker, S. M. Selbach, R. Holmestad, and T. Tybell, *Appl. Phys. Lett.* **106**, 041604 (2015).
- <sup>30</sup> L. Bellaiche and D. Vanderbilt, *Phys. Rev. B* **61**, 7877 (2000).
- <sup>31</sup> Z. Fang, I. V. Solovyev, and K. Terakura, *Phys. Rev. Lett.* **84**, 3169 (2000).
- <sup>32</sup> I. Hallsteinsen, M. Nord, T. Bolstad, P.-E. Vullum, J. E. Boschker, P. Longo, R. Takahashi, R. Holmestad, M. Lippmaa, and T. Tybell, *Crystal Growth & Design* **16**, 2357 (2016).
- <sup>33</sup> K. Momma and F. Izumi, *J. Appl. Crystallogr.* **44**, 1272 (2011).
- <sup>34</sup> P. G. Radaelli, G. Iannone, M. Marezio, H. Y. Hwang, S. W. Cheong, J. D. Jorgensen, and D. N. Argyriou, *Phys. Rev. B* **56**, 8265 (1997).
- <sup>35</sup> A. Vailionis, H. Boschker, W. Siemons, E. P. Houwman, D. H. A. Blank, G. Rijnders, and G. Koster, *Phys. Rev. B* **83**, 064101 (2011).
- <sup>36</sup> H. Boschker, M. Huijben, A. Vailionis, J. Verbeeck, S. v. Aert, M. Luysberg, S. Bals, G. v. Tendeloo, E. P. Houwman, G. Koster *et al.*, *Journal of Physics D: Applied Physics* **44**, 205001 (2011).
- <sup>37</sup> A. J. Hatt and N. A. Spaldin, *Phys. Rev. B* **82**, 195402 (2010).
- <sup>38</sup> S. J. May, J. W. Kim, J. M. Rondinelli, E. Karapetrova, N. A. Spaldin, A. Bhattacharya, and P. J. Ryan, *Phys. Rev. B* **82**, 014110 (2010).
- <sup>39</sup> A. Vailionis, H. Boschker, Z. Liao, J. R. A. Smit, G. Rijnders, M. Huijben, and G. Koster, *Appl. Phys. Lett.* **105**, 131906 (2014).
- <sup>40</sup> Y. Suzuki, H. Y. Hwang, S. W. Cheong, and R. B. van Dover, *Appl. Phys. Lett.* **71**, 140 (1997).
- <sup>41</sup> L. M. Berndt, V. Balbarin, and Y. Suzuki, *Appl. Phys. Lett.* **77**, 2903 (2000).
- <sup>42</sup> I. Hallsteinsen, E. Folven, F. K. Olsen, R. V. Chopdekar, M. S. Rzchowski, C. B. Eom, J. K. Grepstad, and T. Tybell, *APL Materials* **3**, 062501 (2015).
- <sup>43</sup> Explicit calculations of the magnetic easy axis requires relativistic spin orbit effects which is not feasible for the interface calculations due to the number of atoms. Even then, one neglects any contributions from shape effects.

## FIGURES AND TABLES

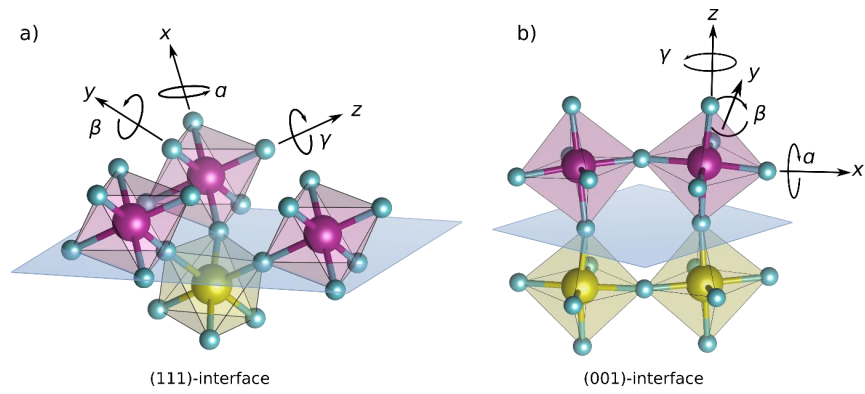


**Figure 1:** Schematics showing the octahedral coupling at the a) (111)-interface and b) (001)-interface. In addition the definitions of the octahedral rotation angles  $\alpha$ ,  $\beta$  and  $\gamma$  the pseudocubic  $x$ -,  $y$ - and  $z$ -directions respectively are shown.

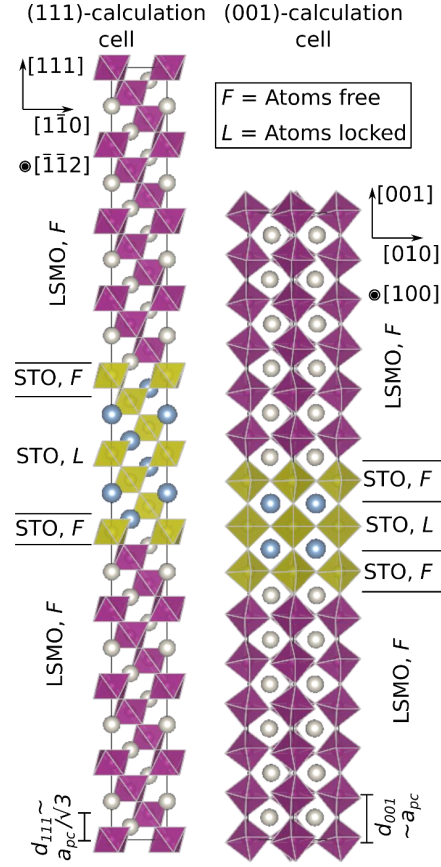


**Figure 2:** The  $\sqrt{2} \times \sqrt{2} \times 10\sqrt{3}$  (left) and  $\sqrt{2} \times \sqrt{2} \times 14$  (right) supercells used for calculating the octahedral response of (111)- and (001)-interfaces respectively. Using selective dynamics the STO layers not at the interface was locked in cubic positions with tilt pattern  $a^0a^0a^0$  or tetragonal with tilt pattern  $a^0a^0c^-$ . Note that for the (001)-interface, the out-of-phase rotation can be either around the out-of-plane axis, i.e.  $a^0a^0c^-$  or around an in plane axis i.e.  $a^-b^0b^0$  equivalent to  $a^0b^-a^0$ . However, for (111)-strain all of these variations are symmetry equivalent.

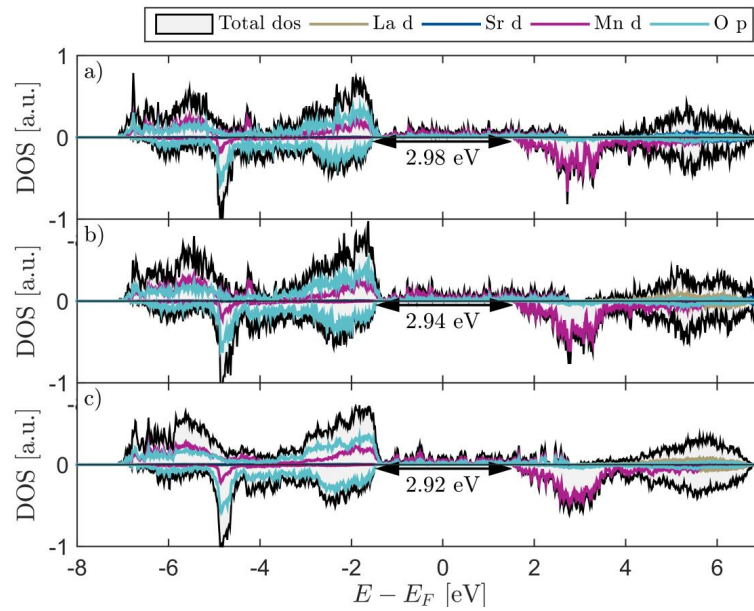


**Figure 3:** Total and orbital projected Density of States (DOS) comparing the different approaches of modelling the Sr Doping in LSMO. a) VCA, b) 30 atom supercell, c) 120 atom supercell. The black arrows indicate the half-metallic bandwidth i.e. the region where there are only spin up states, no spin down states.

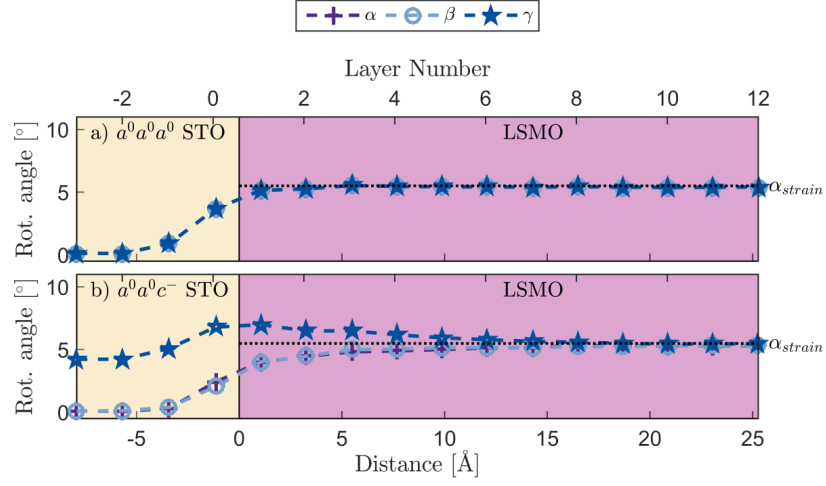


**Figure 4:** Octahedral rotational coupling for at the (111)-interface between LSMO and STO, calculated with the VCA approach. a) shows the results for STO locked in a cubic state without any rotations ( $a^0 a^0 a^0$ ), while b) shows the results if STO is locked in a tetragonal tetragonal state with tiltpattern ( $a^0 a^0 c^-$ ). The STO layer closest to the interface (layer 0) was allowed to relax. The rotation angles  $\alpha$ ,  $\beta$  and  $\gamma$  are defined in Figure 1 a).  $\alpha_{strain} = \beta_{strain} = \gamma_{strain}$  is the rotation angles calculated for LSMO when strained to an (111)-oriented STO substrate.

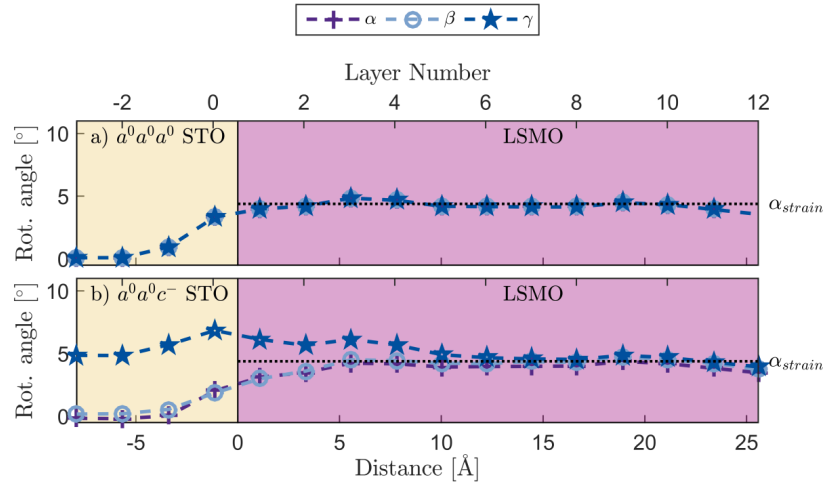


**Figure 5:** Octahedral rotational coupling for at the (111)-interface between LSMO and STO, calculated with in-plane  $\sqrt{2} \times \sqrt{2}$  supercell approach. a) shows the results for STO locked in a cubic state without any rotations ( $a^0 a^0 a^0$ ), while b) shows the results if STO is locked in a tetragonal tetragonal state with tilt pattern ( $a^0 a^0 c^-$ ). The STO layer closest to the interface (layer 0) was allowed to relax. The rotation angles  $\alpha$ ,  $\beta$  and  $\gamma$  are defined in Figure 1 a).  $\alpha_{strain} = \beta_{strain} = \gamma_{strain}$  is the rotation angles calculated for LSMO when strained to an (111)-oriented STO substrate.



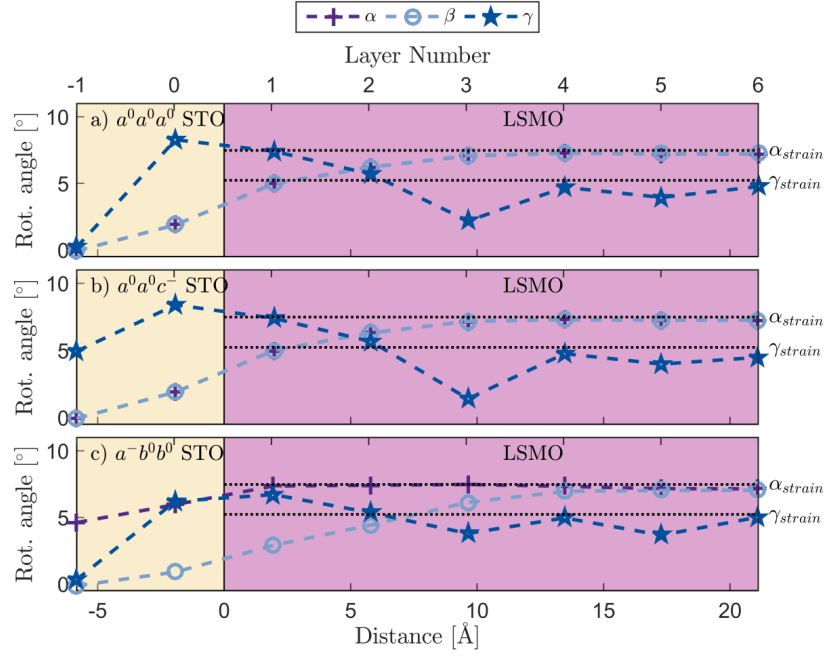


**Figure 6:** Octahedral rotational coupling for at the (001)-interface between LSMO and STO. Calculated with the VCA approach. a) shows the results for STO locked in a cubic state without any rotations ( $a^0 a^0 a^0$ ), while b) and c) show the results if STO is locked in a tetragonal tetragonal state with tilt pattern  $a^0 a^0 c^-$  and  $a^- b^0 b^0$  respectively. Hence, the difference between b) and c) is that the locked rotation axis is around the out-of-plane or the in-plane axis. The STO layer closest to the interface (layer 0) was allowed to relax. The rotation angles  $\alpha$ ,  $\beta$  and  $\gamma$  are defined in Figure 1 b).  $\alpha_{strain} = \beta_{strain} > \gamma_{strain}$  is the rotation angles calculated for LSMO when strained to an (001)-oriented STO substrate.

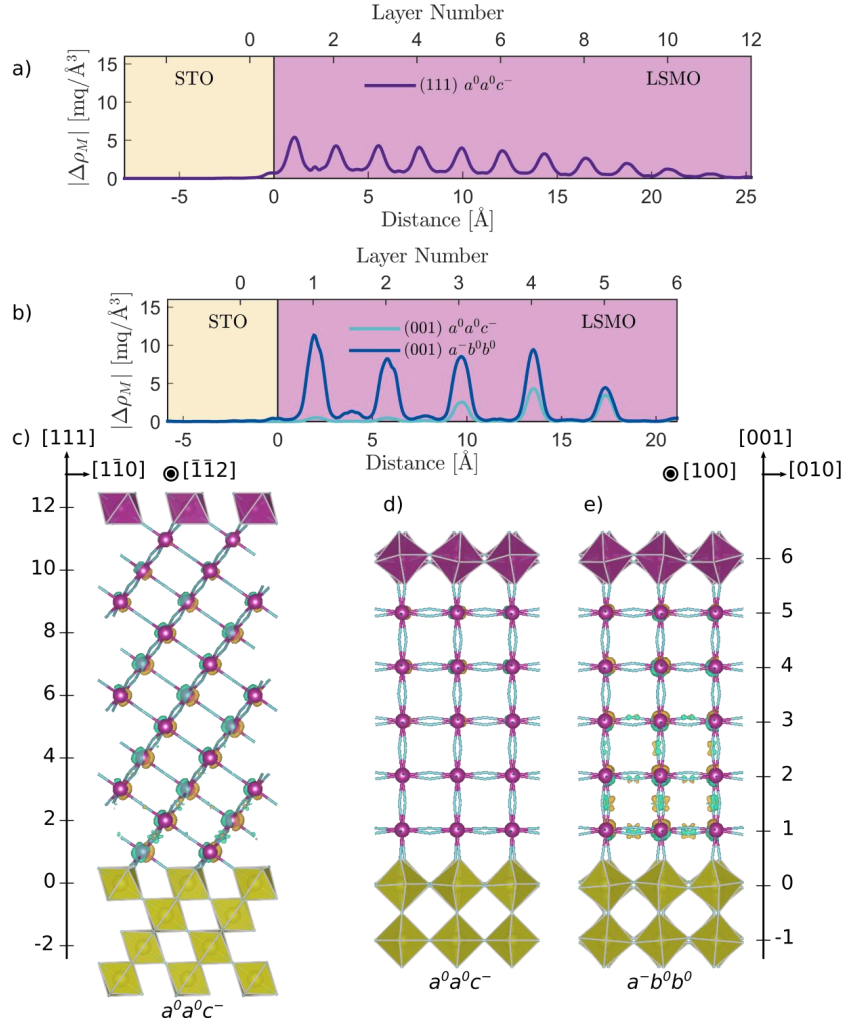


**Figure 7:** Plot of the spin density difference,  $\Delta\rho_M$ , between STO locked in a  $a^0a^0a^0$ -tilt pattern and locked in different tetragonal tilt patterns. a) and b) show as the absolute value of  $\Delta\rho_M$  as a function of distance from the interface for the (111) and (001) interface respectively. c-e) show isosurface plots of the same data, along with the atomic structure, where c)  $a^0a^0c^-$  tilt pattern, (111)-interface, d)  $a^0a^0c^-$  tilt pattern, (001)-interface and e)  $a^-b^0a^0$  tilt pattern, (001)-interface. Positive and negative is colored yellow and blue respectively. The isosurface level is set to 5 mq/Å<sup>3</sup>.

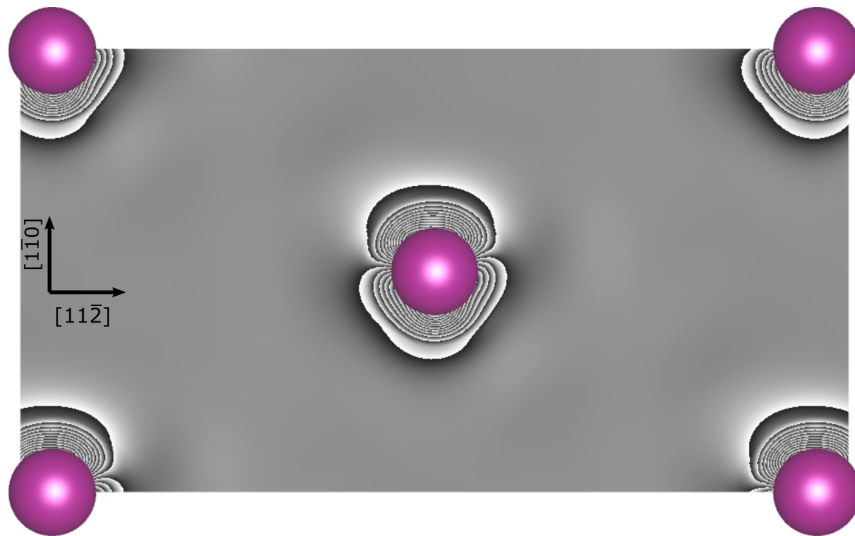


**Figure 8:** Contour plot of the spin density difference in the (111)-plane closest to the interface showing a clear anisotropy between the  $[1\bar{1}0]$ - and  $[11\bar{2}]$ -directions below 105K. The purple balls represents the positions of the Mn atoms.

**TABLE I:** Comparison of bulk parameters calculated for LSMO with VCA,  $\sqrt{2} \times \sqrt{2} \times 2\sqrt{3}$  (30 atoms) and  $2\sqrt{2} \times 2\sqrt{2} \times 2\sqrt{3}$  (120 atoms) supercells of the aristotype perovskite and experimental values.  $a$ ,  $b$  and  $c$  represent the lattice parameters of LSMO in the  $R\bar{3}c$  space group in the hexagonal setting,  $M$  is the saturation magnetism,  $\alpha$ ,  $\beta$  and  $\gamma$  represent the mean octahedral rotations around the pseudocubic axes,  $\sigma$  represents the standard deviation of the octahedral rotations,  $E_{AFM} - E_{FM}$  is the exchange energy, defined as the difference between a G-type antiferromagnetic and a ferromagnetic spin ordering. Experimental data from <sup>34</sup>.

Parameter	VCA	30-atom supercell	120-atom supercell	Experimental
$a = b$ [Å]	5.500	5.510	5.509	5.506
$c$ [Å]	13.214	13.322	13.351	13.356
$\frac{c}{\sqrt{6}a}$	0.981	0.987	0.989	0.990
$M$ [ $\mu_B$ /Mn]	3.67	3.67	3.67	3.67
$\alpha = \beta = \gamma$ [°]	5.19	4.45	4.25	4.48
$\sigma$ [°]	0	0.187	0.310	
$E_{AFM} - E_{FM}$ [eV/f.u.]	0.423	0.386	0.221	
CPU cost [hours/16 cores]	2.7	8.4	177	



---

# Concurrent magnetic and structural reconstructions at the interface of (111)-oriented $\text{La}_{0.7}\text{Sr}_{0.3}\text{MnO}_3$ / $\text{LaFeO}_3$

I. Hallsteinsen, M. Moreau, A. Grutter, M. Nord, P.E. Vullum, D. A. Gilbert, T. Bolstad, J. K. Grepstad, R. Holmestad, S. M. Selbach, A. T. N'Diaye, B. J. Kirby, E. Arenholz and T. Tybell

Published in Physical Review B **94**. 201115(R) (2016)  
DOI: <https://doi.org/10.1103/PhysRevB.94.201115>



### Concurrent magnetic and structural reconstructions at the interface of (111)-oriented $\text{La}_{0.7}\text{Sr}_{0.3}\text{MnO}_3/\text{LaFeO}_3$

I. Hallsteinsen,<sup>1,2</sup> M. Moreau,<sup>1</sup> A. Grutter,<sup>3</sup> M. Nord,<sup>4</sup> P.-E. Vullum,<sup>4,5</sup> D. A. Gilbert,<sup>3</sup> T. Bolstad,<sup>1</sup> J. K. Grepstad,<sup>1</sup> R. Holmestad,<sup>4</sup> S. M. Selbach,<sup>6</sup> A. T. N'Diaye,<sup>2</sup> B. J. Kirby,<sup>3</sup> E. Arenholz,<sup>2</sup> and T. Tybell<sup>1,\*</sup>

<sup>1</sup>Department of Electronics and Telecommunications, NTNU—Norwegian University of Science and Technology, Trondheim 7491, Norway

<sup>2</sup>Advanced Light Source, Lawrence Berkeley National Laboratory, Berkeley, California 94720, USA

<sup>3</sup>Center for Neutron Research, National Institute of Standards and Technology, Gaithersburg, Maryland 20899, USA

<sup>4</sup>Department of Physics, NTNU—Norwegian University of Science and Technology, Trondheim 7491, Norway

<sup>5</sup>SINTEF Materials and Chemistry, Trondheim 7491, Norway

<sup>6</sup>Department of Material Science and Engineering, NTNU—Norwegian University of Science and Technology, Trondheim 7491, Norway

(Received 6 July 2016; published 21 November 2016)

We observe an induced switchable magnetic moment of  $1.6 \pm 0.40 \mu_B/\text{Fe}$  for the nominally antiferromagnetic  $\text{LaFeO}_3$  extending two to four interface layers into the non-charge transfer system  $\text{La}_{0.7}\text{Sr}_{0.3}\text{MnO}_3/\text{LaFeO}_3/\text{SrTiO}_3(111)$ . Simultaneously a mismatch of oxygen octahedra rotations at the interface implies an atomic reconstruction of reduced symmetry at the interface, reaching two to five layers into  $\text{LaFeO}_3$ . Density functional theory of a structure with atomic reconstruction and different correlation strength shows a ferrimagnetic state with a net Fe moment at the interface. Together these results suggest that engineered oxygen octahedra rotations, affecting the local symmetry, affect electron correlations and can be used to promote magnetic properties.

DOI: 10.1103/PhysRevB.94.201115

Interface engineering of oxides is used to promote novel properties such as metallic conduction between two insulators [1,2], and ferromagnetism (FM) between non-FM materials [3,4]. Tailoring magnetic interfaces in a controlled manner is considered a cornerstone of further development of spintronic devices [5]. Until now much attention has been on modified magnetic states due to charge transfer; for example, in superlattices of  $\text{CaRuO}_3/\text{CaMnO}_3$  and  $\text{LaNiO}_3/\text{LaMnO}_3$ , charge transfer results in double exchange between  $\text{Mn}^{3+}/\text{Mn}^{4+}$  and induced FM at the interface [6–8]. In  $(\text{Y}, \text{Ca})\text{Ba}_2\text{Cu}_3\text{O}_7/\text{La}_{0.67}\text{Ca}_{0.33}\text{MnO}_3$  depletion of charge from the Cu-O layers leads to a reconstruction into a FM orbital-ordered system [4]. However, induced FM at Fe has also been observed in nominally nonferromagnetic materials adjacent to  $\text{La}_{0.7}\text{Sr}_{0.3}\text{MnO}_3$  (LSMO) [9,10], even though the  $d^5$  electronic state of  $\text{Fe}^{3+}$  prohibits charge transfer. Atomic reconstructions at interfaces, resulting in novel tilt patterns of the oxygen octahedra, have previously been associated with the emergence of new ferroelectric states [11,12], while the coupling between atomic reconstructions and magnetism is relatively unexplored, despite the importance to spintronic device applications [13,14]. The interface between antiferromagnetic (AF)  $\text{LaFeO}_3$  (LFO) and the half-metal FM LSMO holds promise from an engineering perspective, as charge transfer to the  $d^5\text{Fe}^{3+}$  is prohibited, while atomic reconstructions due to a mismatch in tilt patterns is expected. The tilt patterns of their oxygen octahedra are not directly compatible, with LFO (S.G. 62,  $P6mm$ ) and LSMO (S.G. 167,  $R\bar{3}c$ ) having  $a^-a^-c^+$  and  $a^-a^-a^-$  rotations (Glazer notation), respectively [15]. This mismatch must be accommodated at the interface, likely through atomic reconstructions. In this Rapid Communication, we address how the mismatch in octahedral rotations is accommodated through structural relaxations at

the interface leading to the emergence of FM in LFO, in (111)-oriented LSMO/LFO/ $\text{SrTiO}_3$  (STO) heterostructures. As all the rotation directions of the oxygen octahedra have both in-plane and out-of-plane components at a (111)-oriented interface it is expected that the change from  $a^-a^-c^+$  to  $a^-a^-a^-$  rotation would have a larger impact on the structure than for a (001)-oriented interface. Indeed we show large rotational changes at the LSMO/LFO interface, no substantial charge transfer, and an induced switchable moment at the Fe atoms. The length scale of structural as well as magnetic reconstructions extends three to five layers into LFO, and the induced magnetic moment is an order of magnitude larger than previously reported for LSMO/LFO(001) [9].

Epitaxial heterostructures of LSMO/LFO/STO(111) were deposited by pulsed laser deposition (PLD) with LSMO and LFO thicknesses of 16  $d_{111}$  monolayers (3.6 nm) each, 7.2 nm in total. Deposition parameters are described in Refs. [16–18], resulting in fully strained (111)-oriented films with atomically smooth step-and-terrace surfaces (see the Supplemental Material [19]). The atomic structure was analyzed by scanning transmission electron microscopy (STEM) using high-angle annular dark-field (HAADF), annular bright field (ABF), and electron energy loss spectroscopy (EELS). Scanning distortions were reduced by using nonrigid registration [20] and EELS processing was done using HYPERSPY [19,21]. Density functional theory (DFT) calculations were done with the Vienna *ab initio* simulation package (VASP) using the PBE-sol functional and a plane-wave cutoff energy of 550 eV [22–24]. The projected augmented wave - Perdew Burke Ernzerhof (PAW-PBE) potentials supplied with VASP for La, Sr, Mn, Fe, and O with electron configurations  $4s^24p^65d^16s^2$ ,  $4s^24p^65s^2$ ,  $3d^54s^2$ ,  $3d^64s^2$ , and  $2s^22p^4$  respectively were used and different configurations of La and Sr in LSMO were tested [25]. Hubbard  $U$  of 10 and 3 eV were applied to the La 4*f* and Mn 3*d* orbitals, respectively [26]. Calculations of LFO were done with a 60-atom  $\sqrt{2} \times \sqrt{6} \times 2\sqrt{3}$

\*Corresponding author: thomas.tybell@ntnu.no



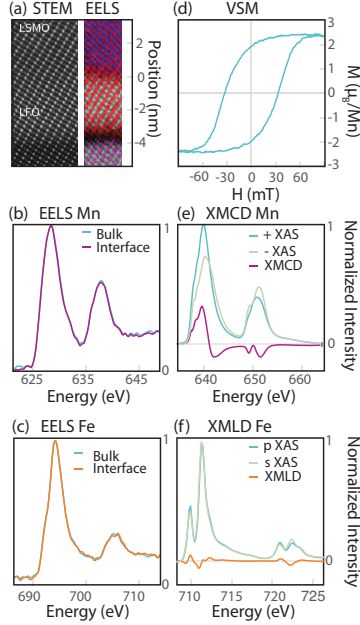
I. HALLSTEINSEN *et al.*PHYSICAL REVIEW B **94**, 201115(R) (2016)

FIG. 1. (a) STEM HAADF image (left) and EELS map (right) colored by element, i.e., La (red), Mn (purple), Fe (turquoise), Sr (pink), and Ti (green). (b,c) show EELS spectra of  $L_{2,3}$  edge of Mn (Fe) at the interface [purple (orange)] and in the center of the layer (turquoise). (d) Hysteresis curve of the bilayer recorded at 50 K. (e,f) XA of different circular (linear) polarization and XMCD (XMLD) spectra of Mn (Fe)  $L$  edge.

supercell, while the interface was modeled with 12/12 (LFO/LSMO) 240-atom  $\sqrt{2} \times \sqrt{6} \times 8\sqrt{3}$  supercells, with corresponding gamma-centered  $k$ -point mesh of  $4 \times 3 \times 2$  and  $4 \times 3 \times 1$ , respectively. The in-plane lattice parameters were locked to the calculated equilibrium value of STO, while the out-of-plane lattice parameter and atomic positions were relaxed until the forces on the ions were below  $0.01 \text{ eV}/\text{\AA}$ .

To investigate charge transfer across the interface, Bader charges [27] were calculated for LSMO/LFO supercells. For Fe, a small change in Bader charge,  $3.03+$  from  $3+$  in bulk, is observed in the unit cell closest to the interface. A small change in Fe valence is expected for Fe-terminated LFO, since this layer effectively corresponds to a mixed LSFO layer, while for the opposite termination the calculations reveal no change in Fe valence. For Mn the Bader charge is increased to  $3.375+$  (from  $3,3+$ ) at the interface, indicating an increased amount of  $\text{Mn}^{4+}$ . Experimental STEM HAADF reveal that the heterostructure is epitaxial, fully strained, and of high crystalline quality and EELS maps reveal a sharp LSMO/LFO interface with no substantial intermixing of cations [Fig. 1(a)], unlike the LFO/STO interface which is intermixed [18,19]. A comparison of EELS spectra at the bulk and at the interface

reveals no change in the Mn and Fe valence state, indicating no charge transfer within the measurement sensitivity [Figs. 1(b) and 1(c)].

The magnetic ground state of the thin films was probed using a vibrating sample magnetometer after a 2 T field cooling to 50 K from room temperature; in Fig. 1(d) a hysteresis at 50 K is shown. The saturation magnetization is  $2.4 \mu_B/\text{Mn}$ , assuming Mn as the only contribution to the magnetic signal and the coercive field is 37.5 mT. The Curie temperature,  $T_c$ , was 275 K [19]. X-ray magnetic circular dichroism (XMCD) and x-ray magnetic linear dichroism (XMLD) spectroscopy were measured at beamline 4.0.2 and 6.3.1 at the Advanced Light Source (ALS) and I1011 at MaxLab II. The spectra shown were measured in total-electron-yield mode by monitoring the sample drain current, with the x rays incident at  $30^\circ$  to the sample surface. Using an eight-pole electromagnet, XMCD was measured with an applied field of  $\pm 0.3 \text{ T}$  parallel to the x-ray beam. For XMLD,  $s$  and  $p$  polarization of the beam was used. Figures 1(e) and 1(f) depict the absorption spectra for the Mn and Fe  $L$  edge, respectively, with spectral shapes in agreement with reported spectra for single-layer films with  $\text{Mn}^{3,3+}$  and  $\text{Fe}^{3+}$  valence state [28,29]. XMCD/XMLD was adopted to probe the element-specific FM/AF; Mn XMCD spectra confirm FM ordering (30% XMCD) and Fe XMLD spectra indicate AF ordering with 5% XMLD (similar to single-layer LFO). LFO in bulk is a  $G$ -type AF, with fully spin polarized (111) planes. The coercive field of the bilayer is increased compared to single layers of LSMO [30]; however, no exchange bias was observed. The dichroism of Fe indicates a canted out-of-plane AF axis, in agreement with (111)  $(\text{La,Sr})\text{FeO}_3$ , which also exhibited no exchange bias [31].

Having established the magnetic states for the individual constituents of the heterostructure we turn to structural effects at the interface, focusing on the LFO. Figure 2(a) shows schematics of the oxygen octahedral rotations for STO ( $a^0a^0a^0$ ), LFO ( $a^-a^-c^+$ ), and LSMO ( $a^-a^-a^-$ ). At the LSMO/LFO interface half of the octahedra match (tilt the same way), while the other half do not (tilt the opposite way). STEM HAADF and ABF imaging along the  $[1\bar{1}0]$ -zone axis were used to probe the atomic positions [Figs. 2(b) and 2(d)]. In Fig. 2(c) the eccentricity (deviation from a circle) of the A-cation columns are plotted as a function of position with respect to the LSMO/LFO interface. In LFO a large eccentricity is expected due to the distortion of the unit cell. As expected, the eccentricity peaks in the center of the LFO layer, and is reduced near both interfaces. However, the change is not abrupt, and two to three layers of LFO close to the LSMO interface have a reduced eccentricity compared to the center of the LFO. Another measure of deviation from the cubic structure is the displacement of the oxygen columns along the  $[100]$  direction, where LFO should have a displacement of 35 pm. In Fig. 2(e) it is clear that the amplitude of the displacements decreases throughout both interfaces, beginning roughly at the second layer of LFO, hence these layers have a reduced displacement. Combining the oxygen displacement and A-cation eccentricity data, the analysis suggests that two to three interface layers of LFO have a reduced distortion compared to bulk. DFT simulations of the octahedral rotation angle along the  $c$  axis ( $\gamma$ ) across the LSMO/LFO interface

CONCURRENT MAGNETIC AND STRUCTURAL ...

PHYSICAL REVIEW B 94, 201115(R) (2016)

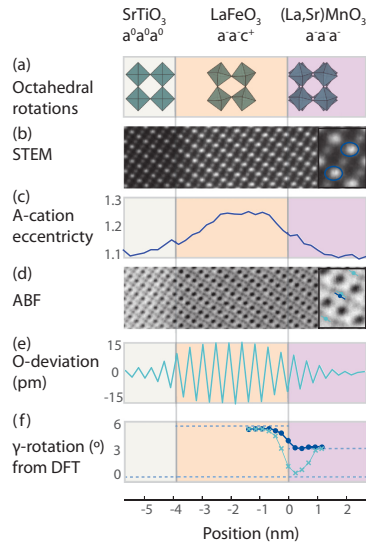


FIG. 2. (a) Schematic of the octahedral rotations in STO ( $a^0a^0a^0$ ), LFO ( $a^-a^-c^+$ ), and LSMO ( $a^-a^-a^-$ ) shown from the [001] direction [33]. (b) STEM-HAADF image. Inset shows the enlarged view of the elliptical form of the La columns in LFO. (c) Plot of the A-cation eccentricity (d) STEM-ABF image. Inset shows an enlarged view of oxygen positions in the layer (turquoise) and the deviation from a cubic structure (blue). (e) Plot of the oxygen column displacement along [100], integrated for monolayers in the [111] direction. (f) Plot of the calculated  $\gamma$  rotation for matched (dark blue) and mismatched (turquoise) octahedra. All plots are shown as a depth profile through the bilayer, and are matched to the TEM images as shown by the gray lines and colored boxes.

are presented in Fig. 2(f), where the matching octahedra (dark blue) and the nonmatching octahedra (light blue) evolve differently. While the rotations of the matched octahedra relax to the bulk value for both materials, the rotation angle of the mismatched octahedra drops toward zero. The tilt pattern at the interface is hence close to the  $a^-a^-c^0$  tilt pattern for half the octahedra. The reduced rotation angle prevails two to four layers into the LFO, in accordance with the experimental data.

To investigate if the observed structural changes at the interface have influence on the magnetic properties, XMCD spectroscopy probing ferromagnetic order was performed at the Fe  $L$  edge [Fig. 3(a)]. We observe a circular dichroism signal of approximately 2% of the Fe  $L3$  normalized absorption peak (XA) signal at 50 K. Measurements were done with alternating polarization of the x rays under a static field and in remanence, as well as with alternating field with a static polarization resulting in the same magnitude and shape of the dichroism signal. Monitoring the field dependence of the Fe and Mn  $L3$  XMCD in hysteresis loops [Fig. 3(c)] reveals that Mn and Fe are antiparallel and with equal coercive fields of

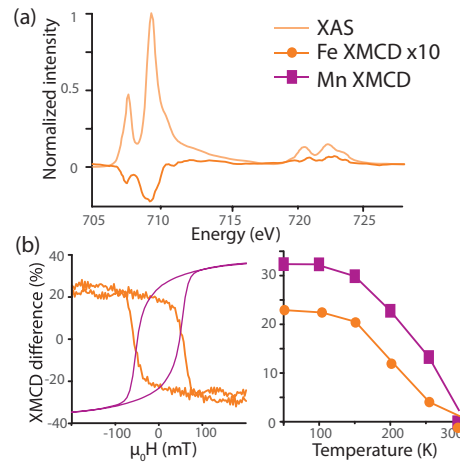


FIG. 3. (a) XA and XMCD spectra at the Fe  $L$  edge. (b) Field (left) and temperature (right) dependence of Fe  $L3$  XMCD (orange) and Mn  $L3$  XMCD (purple).

approximately 70 mT at 50 K. This is in agreement with Bruno *et al.* [9], who demonstrated an induced FM moment in LFO with an antiparallel coupling to LSMO for LSMO/LFO(001). In Fig. 3(d) we have plotted the temperature dependence of the Mn and Fe  $L3$  XMCD. The Fe XMCD signal follows that of Mn, with a comparable  $T_c$ , although the Néel temperature of LFO is much higher (740 K). The similar coercive field and Curie temperature observed for both Mn and Fe strongly suggest that the FM moment of Fe is stabilized by a coupling with the LSMO layer. Although FM systems also have a XMLD response the Fe-XMLD signal is larger than the XMCD signal for Fe, implying a predominantly AF LFO layer.

In order to investigate the depth profile of the magnetic structure we used polarized neutron reflectivity (PNR) performed using the PBR beamline at NIST Center for Neutron Research. Measurements were conducted at 50 K after field cooling in 700 mT, using an in-plane measurement field of 700 mT. The spin of the incident neutrons was polarized parallel or antiparallel to the in-plane magnetic field  $H$ , and the specular reflectivity was measured as a function of wave-vector transfer along the surface normal  $Q_z$ . The model-fitted non-spin-flip reflectivities are depicted in Fig. 4(a). In this scattering geometry the non-spin-flip reflectivity is a function of the nuclear and magnetic scattering length density (SLD) depth profiles, where the magnetic SLD is directly proportional to the magnetization component parallel to  $H$ , and not sensitive to AF ordering. We find a splitting of the two channels, indicating sensitivity to the sample magnetization. The PNR data were modeled using the REFLID software package [32], and the resulting depth profile is shown in Fig. 4(b). It is clear that LSMO is FM with a positive magnetic SLD throughout the film, while at the LFO interface the magnetic SLD is negative for several layers, before relaxing to 0. Hence,

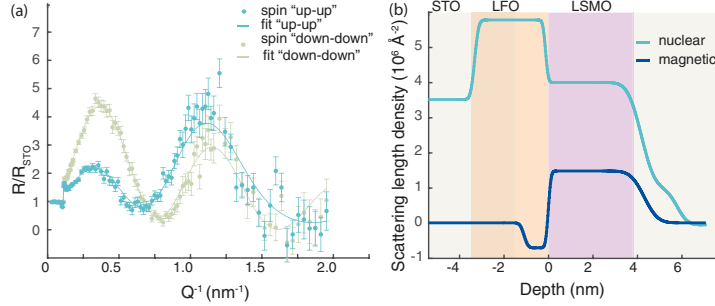
I. HALLSTEINSEN *et al.*PHYSICAL REVIEW B **94**, 201115(R) (2016)

FIG. 4. (a) Neutron reflectivity (crosses) and fits (line) measured in the non-spin-flip geometry, with neutrons polarized with spin up (blue) and spin down (green) with respect to the external field. (b) Magnetic and nuclear depth profile derived from the neutron scattering data.

the LFO has clearly a remanent moment at the interface antiparallel to the LSMO, in agreement with the XMCD measurements. For comparison, we also fit the PNR to a model with zero net magnetization in the LFO layer, which resulted in a significantly poorer fit (see [19]). The fitted PNR model with a 95% confidence interval shows that the induced moment reaches between 0.64 and 1.19 nm (three to five  $d_{111}$  monolayers) into LFO. The FM moment of LSMO was found to be  $3.1 \pm 0.06 \mu_B/\text{Mn}$ , while the LFO moment was found to be  $1.6 \pm 0.40 \mu_B/\text{Fe}$ . However, the value is smaller than the nominal AF moment of  $4.5 \mu_B/\text{Fe}$ , suggesting a canted AF or ferrimagnetic state at the interface.

The length scales of the induced FM moment and the structural reconstruction are both around two to five layers into LFO.  $G$ -type AF order is found to be 313 meV/f.u. lower in energy than FM order from DFT calculations on pure LFO. Although this confirms that  $G$ -type AF is very stable in bulk LFO, a different local symmetry is enforced at the (111)-LFO/LSMO interface, possibly affecting the electron correlations. By taking the Hubbard  $U$  enforced on Fe as a measure of the correlation strength, we compare the energy difference between the FM and AF states for different rotation patterns [Fig. 5(a)]. Interestingly, we find that as  $U_{\text{Fe}}$  approaches zero a FM state is stabilized. This ferromagnetic state is stable for the  $a^-a^-a^0$  rotations resembling the tilt pattern observed at the interface [Fig. 2(e)], but not for the bulk  $a^-a^-c^+$  rotations. For a 12/12 LFO/LSMO superlattice, including the effects of the interface and symmetry mismatch, the lowest energy is still found for the bulk  $G$ -type AF. FM-ordered Fe layers at the interface are metastable with an energy cost of  $\sim 45$  meV/Fe for each FM layer, and the lowest value for parallel Mn and Fe moments. With a nominal  $U_{\text{Mn}}$  of 3 eV, Bader charge analysis revealed that the Mn closest to the LFO has a larger fraction of  $\text{Mn}^{4+}$  compared to the rest of the cell, inconsistent with the EELS measurements. To impose a  $3.3+$  Mn valence increased values of Hubbard  $U$  at the interface ( $U_{\text{Mn},1}$ ) are investigated, which result in an AF ground state with a FM moment at the interface. As seen in Fig. 5(b), the net FM moment for Fe increases with increasing  $U_{\text{Mn},1}$ . For pure LFO a net FM moment was found for decreased  $U_{\text{Fe}}$ ; in Fig. 5(b) we plot the effect of lowering  $U_{\text{Fe}}$  for the

Fe layers closest to the interface ( $U_{\text{Fe},1}$ ), keeping  $U_{\text{Mn}}$  constant at 3 eV. The result is a switchable moment which is increased as  $U_{\text{Fe},1}$  is lowered. In the right panel of Fig. 5(b) these two effects are combined; with the Fe moments as a function of  $U_{\text{Fe},1}$  with  $U_{\text{Mn},1} = 5$  eV. As we reduce the  $U_{\text{Fe},1}$  and increase  $U_{\text{Mn},1}$  we reduce the degree of electron localization of the Fe  $3d$  electrons and obtain a net FM Fe moment. Though the AF structure is not affected by the direction of the Mn, the FM Fe moment is switchable and antiparallel to the Mn moment,

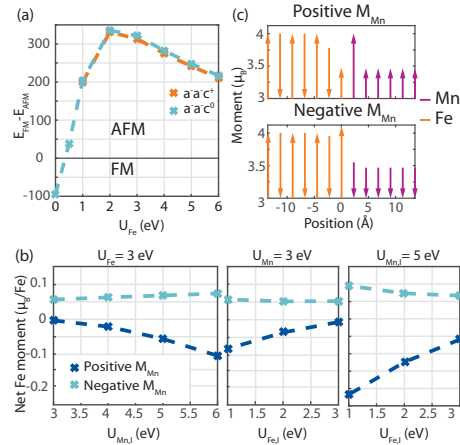


FIG. 5. (a) Energy difference between FM and AF order of LFO as a function of Hubbard  $U$  for different rotation patterns. A positive value means that AF ordering is preferred. Note that the  $a^-a^-c^+$  rotation is not stable for  $U < 1$  eV. (b) Net Fe moment as a function of  $U_{\text{Mn},1}$  and  $U_{\text{Fe},1}$  in the LSMO/LFO supercell. The first panel shows the dependence on  $U_{\text{Mn},1}$  with  $U_{\text{Fe}}$  constant 3 eV, the second panel  $U_{\text{Fe},1}$  with  $U_{\text{Mn}} = 3$  eV, and the third panel  $U_{\text{Fe},1}$  with  $U_{\text{Mn},1} = 5$  eV. (c) Atomic magnetic moments as a function of distance from the LSMO/LFO(111) interface with  $U_{\text{Mn},1} = 5$  eV and  $U_{\text{Fe},1} = 1$  eV.

in agreement with experimental results. The DFT calculations reveal a ferrimagnetic ordering of LFO adjacent to the interface [Fig. 5(c)], where the Fe moment decreases with each layer as we draw nearer to the interface. With  $U_{\text{Mn},1} = 5$  eV and  $U_{\text{Fe},1} = 1$  eV we find a FM moment from  $-0.22 \mu_{\text{B}}/\text{Fe}$  to  $0.09 \mu_{\text{B}}/\text{Fe}$ . As we switch the direction of the Mn moment the effect on the Fe moment is not symmetric; the induced moment is lower when the Mn moment is parallel to the second layer of Fe as compared to the first Fe layer. This can be understood for the reason that the degree of localization is mainly reduced on the Fe layer that matches the Mn moment, and this effect is reduced with the separation from the LSMO interface [19]. The DFT calculations are consistent with a change of the LFO and LSMO symmetry resulting in a ferrimagnetic LFO ground state AF coupled to LSMO, with the magnitude of the moment sensitive to the correlation strength.

In summary, the noncompatible oxygen octahedral rotations of (111)-oriented LFO and LSMO result in atomic reconstructions at the interface, inducing  $a^-a^-c^0$  octahedral rotation symmetry in the last two to four LFO layers near the interface. These reconstructions affect the electron correlations,

as inferred from DFT modeling leading to a ferrimagnetic LFO ground state with AF coupling between the FM Fe and Mn. This finding is supported by XMCD, XMLD, and PNR data. This work shows the importance of structural distortions at epitaxial interfaces in forming magnetic states, and highlights the need to better understand the effect of interfaces on correlation strengths.

T.T. and T.B. acknowledge Research Council of Norway Grant No. 231290. M.N. is supported by the Project NORTEM (Grant No. 197405) within the Programme INFRA- STRUCTURE of the Research Council of Norway. The Norwegian Metacenter for Computational Science (UNINETT Sigma2) was acknowledged for providing computational resources for DFT calculations through Project No. NN9301K. The Advanced Light Source is supported by the Director, Office of Science, Office of Basic Energy Sciences, of the U.S. Department of Energy under Contract No. DE-AC02-05CH11231. Part of this work was performed at the I1011 beamline at MAX II, Sweden, and we thank Gunnar Öhrwall for his assistance at the beamline.

- [1] A. Ohtomo and H. Y. Hwang, *Nature* **427**, 423 (2004).  
 [2] H. Y. Hwang, Y. Iwasa, M. Kawasaki, B. Keimer, N. Nagaosa, and Y. Tokura, *Nat. Mater.* **11**, 103 (2012).  
 [3] A. Brinkman, M. Huijben, M. van Zalk, J. Huijben, U. Zeitler, J. C. Maan, W. G. van der Wiel, G. Rijnders, D. H. A. Blank, and H. Hilgenkamp, *Nat. Mater.* **6**, 493 (2007).  
 [4] J. Chakhalian, J. W. Freeland, G. Srajer, J. Stremper, G. Khaliullin, J. C. Cezar, T. Charlton, R. Dalgliesh, C. Bernhard, G. Cristiani, H.-U. Habermeier, and B. Keimer, *Nat. Phys.* **2**, 244 (2006).  
 [5] M. Gibert, P. Zubko, R. Scherwitzl, J. Íñiguez, and J.-M. Triscone, *Nat. Mater.* **11**, 195 (2012).  
 [6] K. S. Takahashi, M. Kawasaki, and Y. Tokura, *Appl. Phys. Lett.* **79**, 1324 (2001).  
 [7] A. J. Grutter, H. Yang, B. J. Kirby, M. R. Fitzsimmons, J. A. Aguiar, N. D. Browning, C. A. Jenkins, E. Arenholz, V. V. Mehta, U. S. Alaán, and Y. Suzuki, *Phys. Rev. Lett.* **111**, 087202 (2013).  
 [8] M. Gibert, M. Viret, A. Torres-Pardo, C. Piamonteze, P. Zubko, N. Jaouen, J.-M. Tonnerre, A. Mougin, J. Fowlie, S. Catalano, A. Gloter, O. Stéphan, and J.-M. Triscone, *Nano Lett.* **15**, 7355 (2015).  
 [9] F. Y. Bruno, M. N. Grisolia, C. Visani, S. Valencia, M. Varela, R. Abrudan, J. Tornos, A. Rivera-Calzada, A. A. Únal, S. J. Pennycook, Z. Sefrioui, C. Leon, J. E. Villegas, J. Santamaría, A. Barthélémy, and M. Bibes, *Nat. Commun.* **6**, 6306 (2015).  
 [10] P. Yu, J. S. Lee, S. Okamoto, M. D. Rossell, M. Huijben, C. H. Yang, Q. He, J. X. Zhang, S. Y. Yang, M. J. Lee, Q. M. Ramasse, R. Erni, Y. H. Chu, D. A. Arena, C. C. Kao, L. W. Martin, and R. Ramesh, *Phys. Rev. Lett.* **105**, 027201 (2010).  
 [11] H. Wang, J. Wen, D. J. Miller, Q. Zhou, M. Chen, H. N. Lee, K. M. Rabe, and X. Wu, *Phys. Rev. X* **6**, 011027 (2016).  
 [12] E. J. Moon, R. Colby, Q. Wang, E. Karapetrova, C. M. Schlepütz, M. R. Fitzsimmons, and S. J. May, *Nat. Commun.* **5**, 5710 (2014).  
 [13] Z. Liao, M. Huijben, Z. Zhong, N. Gauquelin, S. Macke, R. J. Green, S. Van Aert, J. Verbeeck, G. Van Tendeloo, K. Held, G. A. Sawatzky, G. Koster, and G. Rijnders, *Nat. Mater.* **15**, 425 (2016).  
 [14] A. J. Grutter, A. Vailionis, J. A. Borchers, B. J. Kirby, C. L. Flint, C. He, E. Arenholz, and Y. Suzuki, *Nano Lett.* **16**, 5647 (2016).  
 [15] A. M. Glazer, *Acta Crystallogr., Sect. B* **28**, 3384 (1972).  
 [16] I. Hallsteinsen, J. E. Boschker, M. Nord, S. Lee, M. Rzechowski, P. E. Vullum, J. K. Grepstad, R. Holmestad, C. B. Eom, and T. Tybell, *J. Appl. Phys.* **113**, 183512 (2013).  
 [17] J. E. Boschker, E. Folven, A. F. Monsen, E. Wahlström, J. K. Grepstad, and T. Tybell, *Cryst. Growth Des.* **12**, 562 (2012).  
 [18] I. Hallsteinsen, M. Nord, T. Bolstad, P.-E. Vullum, J. E. Boschker, P. Longo, R. Takahashi, R. Holmestad, M. Lippmaa, and T. Tybell, *Cryst. Growth Des.* **16**, 2357 (2016).  
 [19] See Supplemental Material at <http://link.aps.org/supplemental/10.1103/PhysRevB.94.201115> for more information about deposition, transmission electron microscopy measurements, spin-polarized neutron reflection measurements, and density functional theory calculations.  
 [20] L. Jones, H. Yang, T. J. Pennycook, M. S. J. Marshall, S. Van Aert, N. D. Browning, M. R. Castell, and P. D. Nellist, *Adv. Struct. Chem. Imaging* **1**, 1 (2015).  
 [21] F. de la Peña, P. Burdet, T. Ostasevicius, M. Sarahan, M. Nord, V. T. Fauske, J. Taillon, A. Eljarrat, S. Mazzucco, G. Donval, L. F. Zagonel, M. Walls, and I. Iyengar, *HYPERSPY 0.8.2* (2015).  
 [22] G. Kresse and D. Joubert, *Phys. Rev. B* **59**, 1758 (1999).  
 [23] G. Kresse and J. Furthmüller, *Phys. Rev. B* **54**, 11169 (1996).  
 [24] J. P. Perdew, A. Ruzsinszky, G. I. Csonka, O. A. Vydrov, G. E. Scuseria, L. A. Constantin, X. Zhou, and K. Burke, *Phys. Rev. Lett.* **100**, 136406 (2008).  
 [25] D. S. Mark, M. C. Adam, M. R. James, and J. M. Steven, *J. Phys.: Condens. Matter* **26**, 505502 (2014).  
 [26] S. L. Dudarev, G. A. Botton, S. Y. Savrasov, C. J. Humphreys, and A. P. Sutton, *Phys. Rev. B* **57**, 1505 (1998).

I. HALLSTEINSEN *et al.*

PHYSICAL REVIEW B **94**, 201115(R) (2016)

- [27] G. Henkelman, A. Arnaldsson, and H. Jónsson, *Comput. Mater. Sci.* **36**, 354 (2006).
- [28] J. Lüning, F. Nolting, A. Scholl, H. Ohldag, J. W. Seo, J. Fompeyrine, J. P. Locquet, and J. Stöhr, *Phys. Rev. B* **67**, 214433 (2003).
- [29] Y. Takamura, R. V. Chopdekar, E. Arenholz, and Y. Suzuki, *Appl. Phys. Lett.* **92**, 162504 (2008).
- [30] I. Hallsteinsen, E. Folven, F. K. Olsen, R. V. Chopdekar, M. S. Rzechowski, C. B. Eom, J. K. Grepstad, and T. Tybell, *APL Mater.* **3**, 062501 (2015).
- [31] Y. Jia, R. V. Chopdekar, E. Arenholz, A. T. Young, M. A. Marcus, A. Mehta, and Y. Takamura, *Phys. Rev. B* **92**, 094407 (2015).
- [32] <http://www.ncnr.nist.gov/reflpak>
- [33] K. Momma and F. Izumi, *J. Appl. Crystallogr.* **44**, 1272 (2011).

## Supplementary material

**Concurrent magnetic and structural reconstructions at the interface of (111)-oriented  $\text{La}_{0.7}\text{Sr}_{0.3}\text{MnO}_3/\text{LaFeO}_3$** 

I. Hallsteinsen<sup>1,2</sup>, M. Moreau<sup>1</sup>, A. Grutter<sup>3</sup>, M. Nord<sup>4,5</sup>, P-E. Vullum<sup>5</sup>, D. A. Gilbert<sup>3</sup>, T. Bolstad<sup>1</sup>, F. Olsen<sup>1</sup>, J. K. Grepstad<sup>1</sup>, R. Holmestad<sup>4</sup>, S. M. Selbach<sup>6</sup>, A. T. N'Diaye<sup>2</sup>, B. J. Kirby<sup>3</sup>, E. Arenholz<sup>2</sup> and T. Tybell<sup>1a)</sup>

<sup>1</sup>Department of Electronics and Telecommunications, NTNU - Norwegian University of Science and Technology, Trondheim, 7491, Norway

<sup>2</sup>Advanced Light Source, Lawrence Berkeley National Laboratory, Berkeley, California 94720, USA

<sup>3</sup>Center for Neutron Research, National Institute of Standards and Technology, Gaithersburg, Maryland 20899

<sup>4</sup>Department of Physics, NTNU - Norwegian University of Science and Technology, Trondheim, 7491, Norway

<sup>5</sup>SINTEF Materials and Chemistry, 7491, Norway

<sup>6</sup>Department of Material Science, NTNU - Norwegian University of Science and Technology, Trondheim, 7491, Norway

*I: Thin film synthesis and macroscopic magnetic data*

The films were deposited at 540° C, 0.35 mbar oxygen pressure and 45mm target-substrate distance to obtain thermal mode growth with subsequent cooling in 100mbar oxygen pressure.

A KrF excimer laser ( $\lambda=248$  nm) with a fluency of  $\sim 2$  Jcm<sup>-2</sup> and repetition rate 1 Hz was employed, impinging on a stoichiometric targets. The 0.05° miscut STO(111) substrates were pretreated with buffered hydrogenfluoride and subsequently annealed at 1050° C in oxygen flow. The growth was monitored with RHEED, showing periodic oscillations characteristic of layer-by-layer growth, see Fig S1a). Cu Ka<sub>1</sub> x-ray diffraction, using a diffractometer equipped with a Göbel mirror, V-groove beam compressor and 0.2 mm detector slits, shows lattice constants consistent with fully strained (111)-oriented films, with out-of-plane  $d_{111}$  constants of 0.228 nm for LFO and 0.223 nm for LSMO i.e., compared to 0.225nm for STO. Fig S1b) shows a reflectometry plot is shown and in Fig S1c) a theta- 2theta diffraction plot of the (111) peak, which are both consistent with a total film thickness of 7.5 nm. Tapping mode atomic force microscopy revealed atomically smooth step-and-terrace surfaces, with steps of single  $d_{111}$  atomic layer height and a roughness of 0.10 nm on the plateaus as shown in Fig S1d). The macroscopic magnetic measurements were done with a vibrating sample magnetometer. In Fig S1e) the temperature dependence of the magnetic moment after 2T field cooling is plotted. No significant change was found for zero field cooling with similar samples.

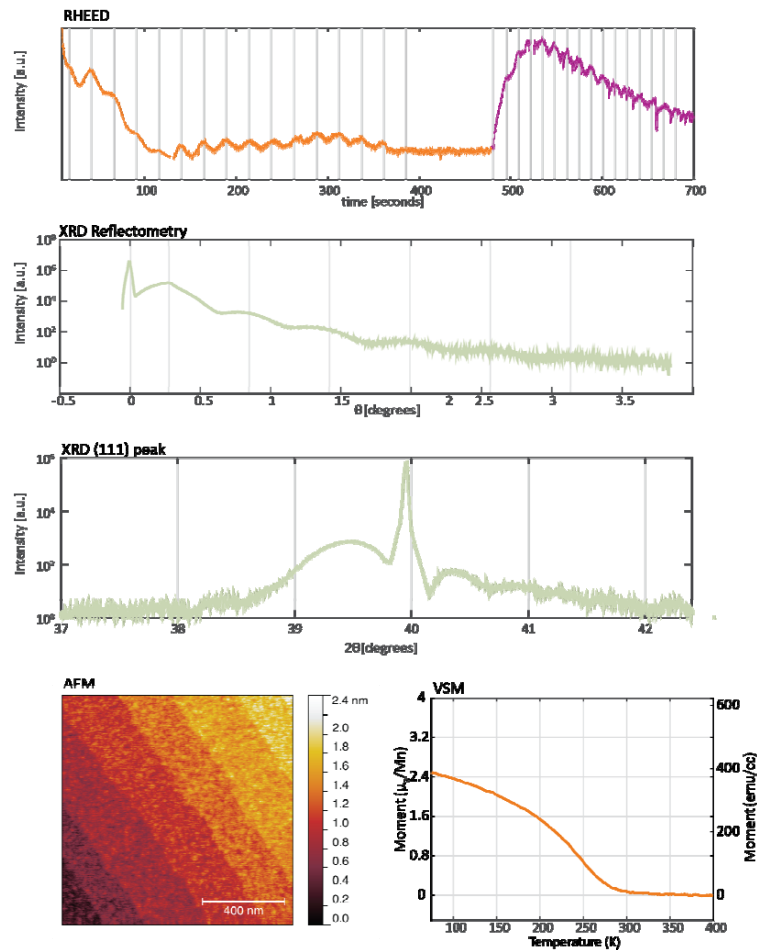


Fig S1:

- RHEED oscillations during growth, plotted as intensity vs time. The plot line is colored orange during LFO growth, and purple during LSMO growth. The oscillation period is denoted by grey lines.
- XRD reflectometry
- XRD theta-2theta plot of the (111) peak
- AFM image of  $1\mu\text{m} \times 1\mu\text{m}$  of the heterostructure after growth and cool down
- Temperature dependence of the magnetic moment of the heterostructure measured by VSM

*II: STEM and EELS investigations*

The atomic structure was analyzed by scanning transmission electron microscopy (STEM) using high-angle annular dark field (HAADF), annular bright field (ABF) and electron energy loss spectroscopy (EELS).

STEM-HAADF and -ABF data were acquired simultaneously, using detector collection semi-angles from 73 to about 200 milliradians (HAADF) and 11.7 to 22.7 milliradians (ABF). The convergence semi-angle of the electron beam was 20.4 milliradians. To reduce the effects of scanning distortions the data was acquired as image stacks with a pixel time of 2.0  $\mu$ s, resulting in two one-image stacks for the ABF and one image stack for the HAADF. The HAADF image stack was processed using SmartAlign [1] resulting in an HAADF data with reduced scanning distortions. Next, the ABF image stack was processed relying on the same distortion corrections as obtained for the HAADF data. The end result is scanning distorted corrected HAADF and ABF images.

The STEM-EELS data was acquired with a convergence semi-angle of 27.4 milliradians, a collection semi-angle of 33.2 milliradians. To obtain elemental maps, such as in Fig1a of the main manuscript, a power-law background subtracted and the response of the respective EELS edges: Ti-L23, Mn-L23, Fe-L23, La-M54 and Sr-L23 were depicted. The dark layer at the LaFeO<sub>3</sub>/SrTiO<sub>3</sub>-interface is due to interdiffusion, as discussed in Ref [2]. All EELS processing was done using HyperSpy [3]. The spatial resolution of the EELS signal is determined to be 0.15 nm by the width of fitted gaussian for the atomically resolved EELS map. The interface widths were defined by the decline from 75% to 25% of the elemental signal, for different processing: raw data, fitting to an arctan and a smoothing with a gaussian of FWHM of 0.4 nm, as shown in Fig S2. For all fits, the LSMO/LFO interface has a narrower interface width than the LFO/STO interface. The maximum interface length for LSMO/LFO is 0.6 nm, corresponding to one layer of each material.

To estimate the amount of structural distortions, two different measures were used: ellipticity of the A-cation columns and oxygen column superstructures in the (100)-direction. To determine the position and shape of the atomic columns, 2-D Gaussian fits were made to each atomic column. The A- and B-cation columns were fitted using the HAADF data, whilst the oxygen columns were fitted using the ABF image.

The ellipticity was found by using non-symmetric 2-D Gaussian fit with rotation, allowing for two different sigmas (x and y) that can rotate for the two Gaussians. To obtain a measure of the ellipticity the largest obtained sigma was divided with the smallest. This measure of ellipticity gives a measure on how much the A-cations “zig-zag” in the direction parallel to the electron beam. For a perfect cubic structure this value would be 1. However, we note that in the cubic SrTiO<sub>3</sub> substrate the ellipticity averaged to about 1.15 due to a range of factors: sample drift, non-perfect correction of astigmatism and residual effects of the scanning distortions. However, the increased ellipticity observed in the LaFeO<sub>3</sub> film is substantially larger compared to the noise level measured in the SrTiO<sub>3</sub>.

The oxygen column superstructures was calculated by estimating the distance between a given oxygen column, and the next oxygen column in the (100)-direction, subtracting to the distance between the oxygen columns and the previous one. By dividing this number by 4 gives one gets a measure of how much the oxygen column position deviates from a perovskite



oxide with no oxygen octahedral tilting, or a octahedral tilting pattern not observable in this TEM-projection. Hence, for a cubic material, such as SrTiO<sub>3</sub> substrate this value is 0 pm, and for bulk LaFeO<sub>3</sub> 39.3 pm. We note that this approach results in a measure oscillating between positive and negative values.

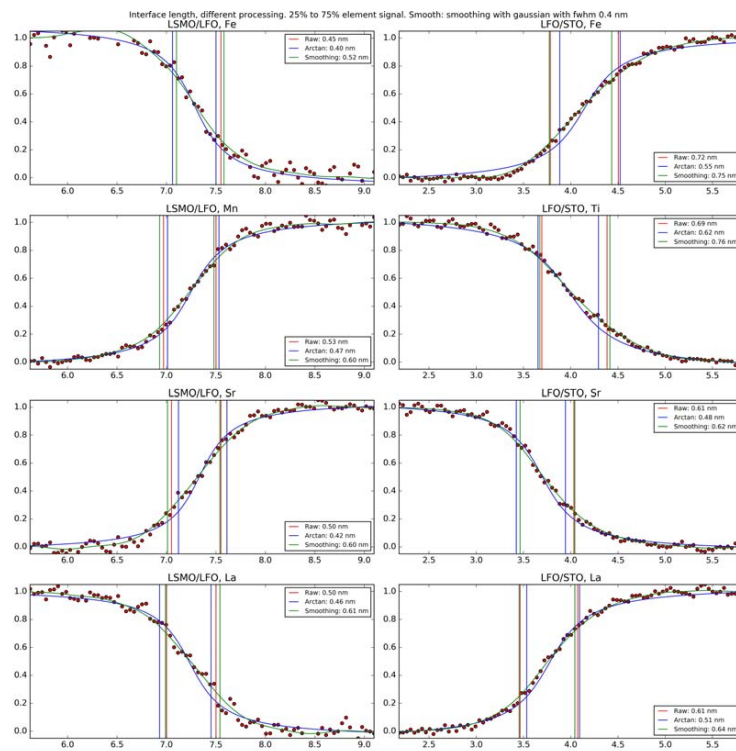


Fig S2:

Estimated width of the chemical interface (75-25% decline) by using the raw data (red), an arctan fit (blue) and a smoothed curve (green) for the different elements on the two interfaces in the heterostructure.

III: Neutron reflectivity fits

The structure and magnetization has also been refined through fitting a model which is identical except that the magnetization within the LFO layer is constrained to be zero. After optimization, we find an increase in the reduced Chi-squared from 1.121 in the case of magnetic LFO at the interface to 1.368 without an interfacial LFO moment. This increase of 22% originates in the fact that the spin “up-up” channel is undershot by the fit in the range of  $Qz = 0.75-1.2 \text{ nm}^{-1}$  and the spin “down-down” channel is undershot from  $Qz = 0.075-0.9 \text{ nm}^{-1}$ . As expected, the interface effect is quite subtle. However, the statistical significance of the difference is more than sufficient to establish an antiparallel magnetization in the interfacial LFO.

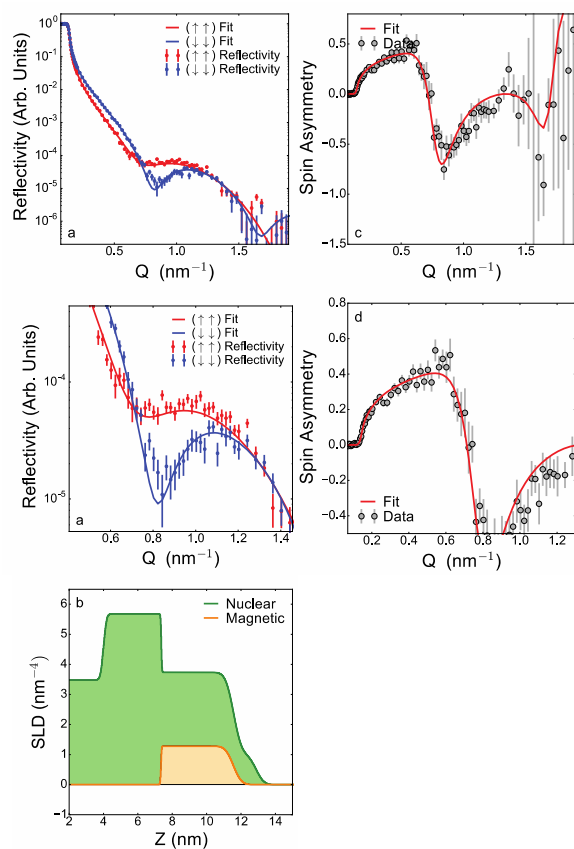


Fig S3:

*Fits of the neutron reflectivity data and spin asymmetry without any induced ferromagnetism at LFO, as shown in the depth profile at the bottom of the figure.*

*III: DFT-investigations of the non-symmetric response of the Fe moments*

The response of the Fe-moment were shown in Fig 5 b) of the main manuscript to not be symmetric with respect to the direction of the Mn-moment at the interface. In Fig S1 we show how the details of the spin structure changes when changing the Hubbard U-values of the Fe closest to the interface,  $U_{\text{Fe}}$ , when the  $U_{\text{Mn}} = 3$  and 5 eV. By reducing the U-values on Fe the reduction of Fe moment happens mainly at the closest Fe moment that has the spin direction parallel to the Mn spin direction. As shown, this effect is stronger when it is the first Fe-layer from the interface that is parallel to the spin direction of LSMO, as compared to the second Fe-layer. This can be seen by observing which arrows are reduced in Fig S4. When the manganese moment is positive (up) it is the first Fe layer from the interface that has the largest reduction of moment if having a positive (up) magnetization. When the manganese moment is negative (down) in Fig. S4, the reduction is largest in the second Fe-layer from the interface, which also has a negative moment (down). However, this reduction of moment in the second Fe-layer from the interface is not as large as the reduction for the first Fe-layer when the manganese moment is positive (up). We attribute the observed asymmetry to a proximity effect, where the distance to the LSMO is important due to reduced overlap of the wave functions.

The effect of reduced localization of the electrons on Fe can be further understood by considering the spin and layer resolved density of states (DOS), as shown in Fig. S5 and S6. Figure S5 shows the spin and layer resolved DOS for the case of a positive Mn moment and  $U_{\text{Fe}} = 1$  eV and  $U_{\text{Mn}} = 5$  eV at the layers closest to the interface. The Fe layer closest to the interface is then clearly metallic. In Fig S6 we show spin and layer resolved DOS for the same U-values, but with a negative Mn moment. Here we observe that there is some Fe states close to the Fermi level both in the layer closest to the interface and in the second Fe-layer from the interface, indicating a reduced localization in both layers.

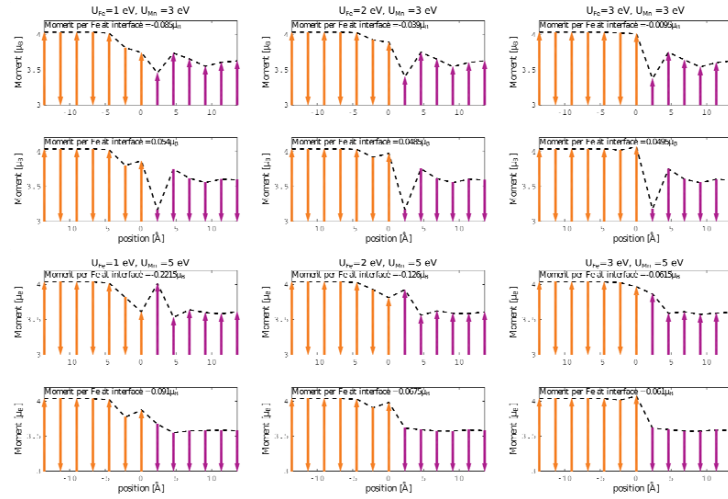


Figure S4, magnetic moment as a function of distance from the interface for different  $U_{Fe}$  and  $U_{Mn}$  at the interface and different alignment of the Mn moment, with respect to the Fe moments.

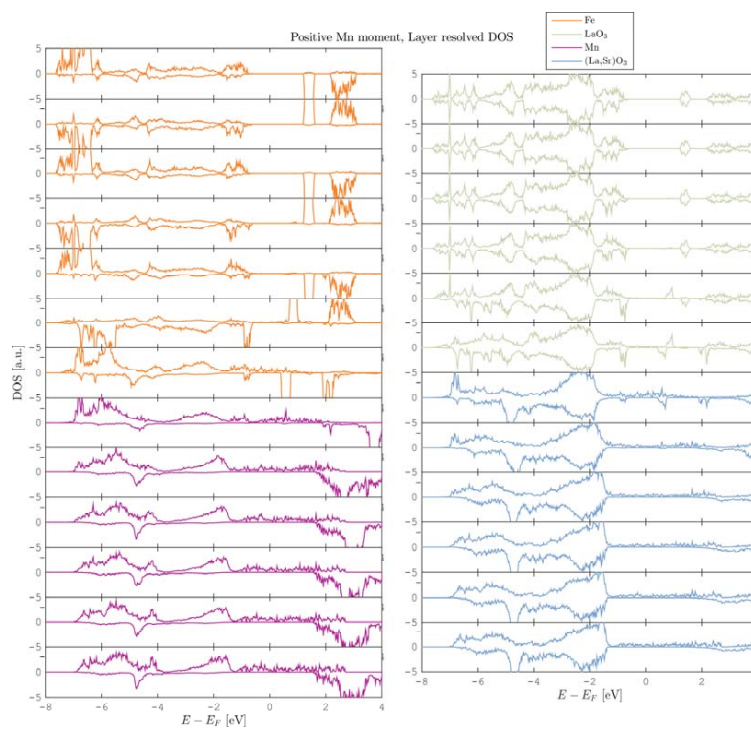


Figure S5, spin and layer resolved density of states for positive Mn moment and  $U_{Fe} = 1$  eV and  $U_{Mn} = 5$  eV at the interface. Spin up states are plotted on the positive  $y$ -axis while spin down are plotted on the negative  $y$ -axis. The different panels show the projection of the density of states for each  $d_{111}$  layer, as one crosses the interface in the  $[111]$ -direction.

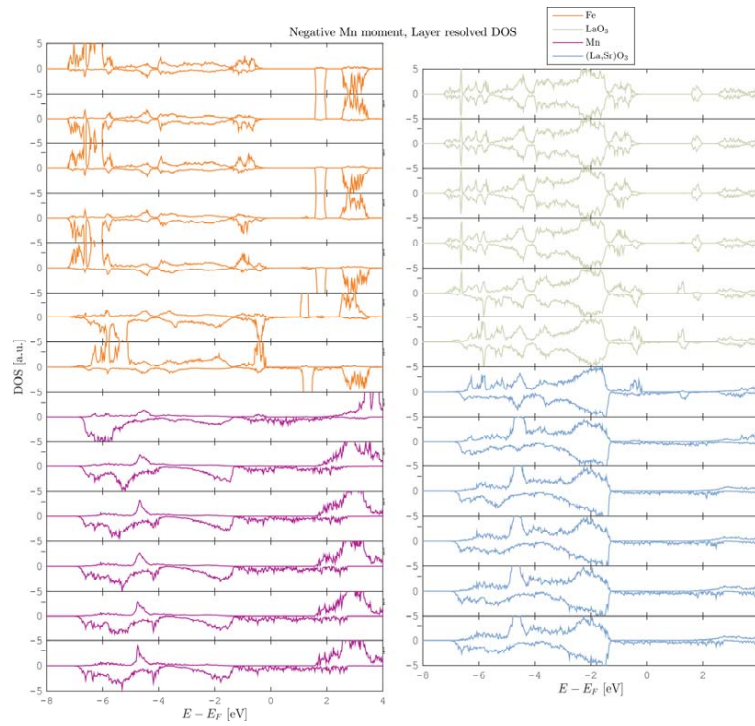


Figure S6, Spin and Layer resolved density of states for negative Mn moment and  $U_{\text{Fe}} = 1$  eV and  $U_{\text{Mn}} = 5$  eV at the interface. Spin up states are plotted on the positive  $y$ -axis while spin down are plotted on the negative  $y$ -axis. The different panels show the projection of the density of states for each  $d_{111}$  layer, as one crosses the interface in the  $[111]$ -direction.

- [1] L. Jones, H. Yang, T. J. Pennycook, M. S. J. Marshall, S. Van Aert, N. D. Browning, M. R. Castell, and P. D. Nellist, *Adv struct chem imaging* **1**, 1 (2015).
- [2] I. Hallsteinsen *et al.*, *Crystal Growth & Design* (2016).
- [3] F. d. l. Peña *et al.*, *hyperspy: HyperSpy 0.8.2*.

## **Part III**

# **Conclusion and Outlook**





---

## Conclusion

*“After a year’s research, one realizes that it could have been done in a week.”*

– Sir William Henry Bragg

In this work, DFT has been used to study functional oxides for thin film applications. Two main routes for controlling their structure have been investigated. These routes have been ordered oxygen vacancies, and the effect of the (111)-orientation on the thin film. The effects of the (111)-interface are further divided into the effects of strain and octahedral coupling. During this work, DFT has been established as a valuable tool to study thin film phenomena in the Oxide Electronics group at NTNU. Our most prominent findings are listed in the following.

For ordered oxygen vacancies in  $(\text{La,Sr})\text{MnO}_{3-\delta}$  it is found that:

- The out-of-plane lattice expansion close to the  $(\text{La,Sr})\text{MnO}_3/\text{SrTiO}_3$  interface can be explained by a large number of oxygen vacancies which are initially disordered.
- As ordered oxygen vacancies have a lower energy compared to disordered, and the oxygen mobility is large, these vacancies will over time order in a brownmillerite structure.
- In the brownmillerite family of ordered vacancy structures, different magnetic sublattices in the octahedral and tetrahedral layers are possible. The preferred spin ordering consists of parallel spins in the octahedral layers and antiparallel spins in the tetrahedral layers.
- There is a large band gap in the tetrahedral layers, while in the octahedral layers there is either a small or no band gap, depending on the oxygen

stoichiometry. In addition, the band structure has a large dispersion parallel to the layers, in contrast to almost no dispersion perpendicular to the layers.

Together, these results show that the ordered oxygen vacancies in  $(\text{La,Sr})\text{MnO}_{3-\delta}$  can result in spatially confined spin polarized electronic conduction. Furthermore, these results demonstrate that anion defect engineering is a viable route to control functional properties in oxide thin films.

For strain in the (111)-plane it is found that:

- Out-of-phase octahedral rotation and polar displacements are split into two orthogonal in-plane modes and one out-of-plane mode. The in-plane axes are found to be along  $[\bar{1}\bar{1}0]$  and  $[11\bar{2}]$ , while the out-of-plane axis is along  $[111]$ . On the other hand, the in-phase octahedral rotations are not split under (111)-strain, in contrast to (001)-strain.
- How the frequencies of in-plane and out-of-plane modes change under (111)-strain depends on the tolerance factor and oxidation states of the A- and B-cations. Under (001)-strain, these modes are always affected in a similar manner.
- There is no preferred in-plane octahedral rotation direction for  $\text{LaAlO}_3$  under compressive (111)-strain. This gives rise to Goldstone-like modes.
- For  $\text{LaFeO}_3$  strained to  $\text{SrTiO}_3(111)$ , the coupling between out-of-phase and in-phase rotations gives rise to six discrete energy minima which can explain the antiferromagnetic domain structure.

Together, these results show the complexities, but also the possibilities by considering strain in other planes than the (001)-plane. The additional control parameters given by the tolerance factor and the oxidation states give further possibilities in order to engineer *materials by design*. Furthermore, the induced Goldstone-like modes in a crystalline solid are interesting, also outside the scope of condensed-matter physics.

When studying octahedral coupling effects at the (111)-interface it is found that:

- The octahedral coupling length is a steric effect, and does not depend on the interface facet. However, the detailed octahedral structure at the interface does depend on whether the interface is (001)- or (111)-oriented.
- The octahedral coupling between (111)-oriented  $(\text{La,Sr})\text{MnO}_3$  with tilt pattern  $a^-a^-a^-$  and  $\text{LaFeO}_3$  with tilt pattern  $a^-a^-c^+$  gives rise to an octahedral mismatch due to the change from in-phase to out-of-phase rotations.

To accommodate this mismatch, large structural reconstructions have to occur.

- Concurrent with this octahedral mismatch is an induced ferromagnetic moment in  $\text{LaFeO}_3$ . This ferromagnetic moment in  $\text{LaFeO}_3$ , can further be explained by changes in correlation strength due to the structural reconstructions.

Together, these results show that the type of octahedral coupling is affected by the interface orientation. Furthermore, they reveal that the (111)-interface can induce and enhance functional properties in oxide thin films.

Overall, these findings demonstrate that manipulating oxide thin films, through either ordered oxygen vacancies or different interface facets, have a large potential in the post-silicon world of electronics. In addition, they provide pieces in the overarching dream of one day creating *materials by design*, not through serendipity, as is often the case today.



---

## Outlook

*“Gödel proved that the world of pure mathematics is inexhaustible; no finite set of axioms and rules of inference can ever encompass the whole of mathematics; given any finite set of axioms, we can find meaningful mathematical questions which the axioms leave unanswered. I hope that an analogous situation exists in the physical world. If my view of the future is correct, it means that the world of physics and astronomy is also inexhaustible; no matter how far we go into the future, there will always be new things happening, new information coming in, new worlds to explore, a constantly expanding domain of life, consciousness, and memory.”*

– Freeman Dyson

Engineering of oxide thin films has revealed emergent properties, such as superconductivity at the interface between two bands insulators. In this work, we have investigated further control mechanisms in order to make oxides viable for post-silicon electronics, with the overarching dream of one day achieve *materials by design*. Still, there are many long- and short-term research problems that needs to be solved. On the long-term, progress is needed both in terms of integrating oxides in electronic devices, and on the computer modelling level. However, in this chapter the focus is on short-term prospects which are directly related to, and can enhance this work.

For the ordered oxygen vacancy structures in  $(\text{La,Sr})\text{MnO}_{3-\delta}$  it would be interesting to probe the effect changing the chemistry, e.g. by changing the the Sr/La ratio. This is interesting as the Sr/La ratio, along with the concentration oxygen vacancies, determines the oxidation state of Mn shifting the balance between super and double-exchange. In this work, it is found that  $\text{Mn}^{3+}$  is preferred in the tetrahedral layers, while the remaining  $\text{Mn}^{3+}$  and  $\text{Mn}^{4+}$  are evenly distributed in

the octahedral layers. Hence, by controlling the Sr/La ratio, further control of the magnetic and electronic properties should be possible. Furthermore, ordered A-cations in the Ruddlesden-Popper family can induce improper ferroelectricity [86]; it would be interesting to study if the same is possible in the brownmillerites. In addition, experimental realizations of the different anion ordered structures, measuring the magnetic and electronic transport properties would greatly enhance this work. When realizing this experimentally, one could also study if the electric field control, achieved by Lu et al. [100] for  $\text{SrCoO}_{3-\delta}$ , could be advanced in Mn based systems.

For further studies of (111)-oriented oxides, one interesting avenue is to investigate the effects of non-quadratic strain. This will make the  $[\bar{1}\bar{1}0]$ -,  $[0\bar{1}\bar{1}]$ - and  $[\bar{1}0\bar{1}]$ -directions inequivalent and lift the trigonal symmetry, possibly enhancing the induced physical properties. Non-quadratic strain will be the result when e.g. an orthorhombic material is used as a substrate. Since most perovskites are orthorhombic, non-quadratic strain will often be the experimental situation, and preliminary experimental data is already available in our group. Furthermore, experimental realizations of the Goldstone-like modes predicted under (111)-strain would be interesting, e.g. because Goldstone modes could be a model system for high-energy physics, similar to the hexagonal manganites [222]. It would also be interesting to further study other materials with other numbers of  $d$ -electrons, e.g.  $d^1$  and  $d^7$  systems will be more directly be affected by the different crystal field splitting for the (111)-interface than e.g.  $d^5$  systems. Finally, combining strain-phonon and octahedral coupling in (111)-interfaces with elements displaying large spin-orbit effects, will have prospects of engineering novel topological phases.

The final possible avenue we will mention here is one that combines ordered oxygen vacancies with different interface facets. In general, this can be used to create novel ordering schemes, which can result in completely new structural phases. A more concrete suggestion would be to combine ordered oxygen vacancies and different crystalline facets to enable eutactic growth of oxides with non-isostructural lattices, by the means of a bridging structure [223]. This possibility has recently been demonstrated by O'Sullivan et al. [224], where they achieved a coherent lattice between a fluorite structure ( $\text{AO}_{2-\delta}$ ) on a (001)-oriented perovskite ( $\text{ABO}_3$ ), by using a pyrochlore ( $\text{A}_2\text{B}_2\text{O}_7$ ) as a bridge. Here the pyrochlore can be considered an oxygen deficient fluorite. The combination of different non-isostructural oxides is interesting because the two phases can host synergistic effects, e.g. combining the ferroic properties of the spinel and perovskite structures. The bridging layer in itself is also interesting, as it is unlikely to be a thermodynamic stable phase, and has a broken inversion symmetry. Hence, it may be host to unique properties of its own. Thus, utilizing DFT to study ordered oxygen vacancies with different interface facets, one can predict general rules for when a bridging structure is

likely to occur and calculate its properties.

Overall, we hope that the current work inspires further work within ordered anion vacancies and engineering of interfaces using non-traditional crystalline facets.





---

## Bibliography

- [1] J. Bardeen and W. Brattain. *Three-electrode circuit element utilizing semiconductive materials*. 1950. URL: <https://www.google.no/patents/US2524035> (cit. on p. 3).
- [2] J. Kilby. *Miniature semiconductor integrated circuit*. 1963. URL: <https://www.google.no/patents/US3115581> (cit. on p. 3).
- [3] G. E. Moore. "Cramming more components onto integrated circuits". In: *Electronics* 38.8 (1965), p. 114. DOI: 10.1109/N-SSC.2006.4785860 (cit. on p. 3).
- [4] IBM. *IBM Research Alliance Produces Industry's First 7nm Node Test Chips*. 2015. URL: <https://www-03.ibm.com/press/us/en/pressrelease/47301.wss> (cit. on p. 3).
- [5] Gallup. *Americans Split on How Often They Upgrade Their Smartphones*. 2015. URL: [http://www.gallup.com/poll/184043/americans-split-often-upgrade-smartphones.aspx?utm\\_source=Economy&utm\\_medium=newsfeed&utm\\_campaign=tiles](http://www.gallup.com/poll/184043/americans-split-often-upgrade-smartphones.aspx?utm_source=Economy&utm_medium=newsfeed&utm_campaign=tiles) (cit. on pp. 3, 4).
- [6] P. Gargini. "The International Technology Roadmap for Semiconductors (ITRS): "Past, present and future"". In: *GaAs IC Symposium. IEEE Gallium Arsenide Integrated Circuits Symposium. 22nd Annual Technical Digest 2000. (Cat. No.00CH37084)*. 2000, pp. 3–5. DOI: 10.1109/GAAS.2000.906261 (cit. on p. 4).
- [7] T. N. Theis and P. M. Solomon. "It's time to reinvent the transistor!" In: *Science* 327.5973 (2010), pp. 1600–1. DOI: 10.1126/science.1187597 (cit. on p. 4).

- [8] Y. Sun, S. E. Thompson, and T. Nishida. “Physics of strain effects in semiconductors and metal-oxide-semiconductor field-effect transistors”. In: *Journal of Applied Physics* 101.10 (2007), p. 104503. DOI: 10.1063/1.2730561 (cit. on pp. 4, 23).
- [9] Y.-K. Choi, T. King, and C. Hu. “Nanoscale CMOS spacer FinFET for the terabit era”. In: *IEEE Electron Device Letters* 23.1 (2002), pp. 25–27. DOI: 10.1109/55.974801 (cit. on p. 4).
- [10] R. R. Schaller. “Moore’s Law: Past, present, and future”. In: *IEEE Spectrum* 34.6 (1997), pp. 52–+. DOI: 10.1109/6.591665 (cit. on p. 4).
- [11] Samsung. *Samsung Starts Industry’s First Mass Production of System-on-Chip with 10-Nanometer FinFET Technology*. 2016. URL: <https://news.samsung.com/global/samsung-starts-industrys-first-mass-production-of-system-on-chip-with-10-nanometer-finfet-technology> (cit. on p. 4).
- [12] M. M. Waldrop. “More than moore”. In: *Nature* 530.7589 (2016), p. 144. DOI: 10.1038/530144a (cit. on p. 4).
- [13] ITRS. *IEEE Rebooting Computing Supports National Strategic Computing Initiative*. 2015. URL: <http://www.businesswire.com/news/home/20150901006390/en#.VeX0cnv7uYU> (cit. on p. 4).
- [14] J. Mannhart and D. G. Schlom. “Oxide interfaces—an opportunity for electronics”. In: *Science* 327.5973 (2010), pp. 1607–11. DOI: 10.1126/science.1181862 (cit. on p. 4).
- [15] H. Takagi and H. Y. Hwang. “An emergent change of phase for electronics”. In: *Science* 327.5973 (2010), pp. 1601–2. DOI: 10.1126/science.1182541 (cit. on p. 4).
- [16] P. Zubko, S. Gariglio, M. Gabay, P. Ghosez, and J. M. Triscone. “Interface Physics in Complex Oxide Heterostructures”. In: *Annual Review of Condensed Matter Physics, Vol 2* 2.1 (2011), pp. 141–165. DOI: 10.1146/annurev-conmatphys-062910-140445 (cit. on pp. 4, 5, 29).
- [17] A. Ohtomo and H. Y. Hwang. “A high-mobility electron gas at the LaAlO<sub>3</sub>/SrTiO<sub>3</sub> heterointerface”. In: *Nature* 427.6973 (2004), pp. 423–426. DOI: 10.1038/nature02308 (cit. on pp. 4, 27).
- [18] N. Reyren et al. “Superconducting interfaces between insulating oxides”. In: *Science* 317.5842 (2007), pp. 1196–9. DOI: 10.1126/science.1146006 (cit. on pp. 4, 27).
- [19] M. Lorenz et al. “The 2016 oxide electronic materials and oxide interfaces roadmap”. In: *Journal of Physics D-Applied Physics* 49.43 (2016), p. 433001. DOI: 10.1088/0022-3727/49/43/433001 (cit. on pp. 4, 5, 18, 32).

- [20] J. M. Rondinelli and N. A. Spaldin. “Structure and properties of functional oxide thin films: insights from electronic-structure calculations”. In: *Advanced Materials* 23.30 (2011), pp. 3363–81. DOI: 10.1002/adma.201101152 (cit. on pp. 5, 23, 29, 44, 46).
- [21] R. E. Cohen. “Origin of Ferroelectricity in Perovskite Oxides”. In: *Nature* 358.6382 (1992), pp. 136–138. DOI: 10.1038/358136a0 (cit. on pp. 5, 13, 14).
- [22] R. E. Cohen and H. Krakauer. “Electronic-Structure Studies of the Differences in Ferroelectric Behavior of BaTiO<sub>3</sub> and PbTiO<sub>3</sub>”. In: *Ferroelectrics* 136.1-4 (1992), pp. 65–83. DOI: 10.1080/00150199208016067 (cit. on pp. 5, 13, 14).
- [23] E. Bousquet, M. Dawber, N. Stucki, C. Lichtensteiger, P. Hermet, S. Gariglio, J. M. Triscone, and P. Ghosez. “Improper ferroelectricity in perovskite oxide artificial superlattices”. In: *Nature* 452.7188 (2008), pp. 732–6. DOI: 10.1038/nature06817 (cit. on pp. 5, 14).
- [24] T. H. Kim et al. “Polar metals by geometric design”. In: *Nature* 533.7601 (2016), pp. 68–72. DOI: 10.1038/nature17628 (cit. on pp. 5, 26, 34, 54).
- [25] C. Becher et al. “Strain-induced coupling of electrical polarization and structural defects in SrMnO<sub>3</sub> films”. In: *Nature Nanotechnology* 10.8 (2015), pp. 661–5. DOI: 10.1038/nnano.2015.108 (cit. on p. 5).
- [26] K. Lejaeghere et al. “Reproducibility in density functional theory calculations of solids”. In: *Science* 351.6280 (2016), aad3000. DOI: 10.1126/science.aad3000 (cit. on p. 6).
- [27] J. P. Perdew, K. Burke, and M. Ernzerhof. “Generalized gradient approximation made simple”. In: *Physical Review Letters* 77.18 (1996), pp. 3865–3868. DOI: 10.1103/PhysRevLett.77.3865 (cit. on pp. 6, 41, 52).
- [28] K. Burke. “Perspective on density functional theory”. In: *The Journal of chemical physics* 136.15 (2012), p. 150901. DOI: 10.1063/1.4704546 (cit. on pp. 6, 37).
- [29] K. Kim and K. D. Jordan. “Comparison of Density-Functional and Mp2 Calculations on the Water Monomer and Dimer”. In: *Journal of Physical Chemistry* 98.40 (1994), pp. 10089–10094. DOI: 10.1021/j100091a024 (cit. on p. 6).
- [30] P. J. Stephens, F. J. Devlin, C. F. Chabalowski, and M. J. Frisch. “Ab-Initio Calculation of Vibrational Absorption and Circular-Dichroism Spectra Using Density-Functional Force-Fields”. In: *Journal of Physical Chemistry* 98.45 (1994), pp. 11623–11627. DOI: 10.1021/j100096a001 (cit. on p. 6).

- [31] S. V. Kalinin, A. Borisevich, and D. Fong. “Beyond condensed matter physics on the nanoscale: the role of ionic and electrochemical phenomena in the physical functionalities of oxide materials”. In: *ACS Nano* 6.12 (2012), pp. 10423–37. DOI: 10.1021/nn304930x (cit. on pp. 7, 18).
- [32] S. V. Kalinin and N. A. Spaldin. “Materials science. Functional ion defects in transition metal oxides”. In: *Science* 341.6148 (2013), pp. 858–9. DOI: 10.1126/science.1243098 (cit. on pp. 7, 18).
- [33] J. Chakhalian, A. J. Millis, and J. Rondinelli. “Whither the oxide interface”. In: *Nature Materials* 11.2 (2012), pp. 92–4. DOI: 10.1038/nmat3225 (cit. on pp. 7, 32).
- [34] K. Momma and F. Izumi. “VESTA 3 for three-dimensional visualization of crystal, volumetric and morphology data”. In: *Journal of Applied Crystallography* 44 (2011), pp. 1272–1276. DOI: 10.1107/S0021889811038970 (cit. on pp. 8, 55).
- [35] C. N. R. Rao and J. Gopalakrishnan. *New directions in solid state chemistry. Edition en anglais*. Cambridge University Press, 1997. DOI: 10.1017/CB09780511623141 (cit. on pp. 10, 18, 22).
- [36] J. B. Goodenough. “Electronic and ionic transport properties and other physical aspects of perovskites”. In: *Reports on Progress in Physics* 67.11 (2004), pp. 1915–1993. DOI: 10.1088/0034-4885/67/11/R01 (cit. on pp. 10, 18).
- [37] V. M. Goldschmidt. “Die Gesetze der Krystallochemie”. In: *Die Naturwissenschaften* 14.21 (1926), pp. 477–485. DOI: 10.1007/bf01507527 (cit. on p. 10).
- [38] T. Negas and R. S. Roth. “The system  $\text{SrMnO}_{3-x}$ ”. In: *Journal of Solid State Chemistry* 1.3-4 (1970), pp. 409–418. DOI: 10.1016/0022-4596(70)90123-4 (cit. on pp. 10, 20).
- [39] K. Uusi-Esko and M. Karppinen. “Extensive Series of Hexagonal and Orthorhombic  $\text{RMnO}_3$  (R = Y, La, Sm, Tb, Yb, Lu) Thin Films by Atomic Layer Deposition”. In: *Chemistry of Materials* 23.7 (2011), pp. 1835–1840. DOI: 10.1021/cm103480d (cit. on p. 10).
- [40] R. N. Song, M. H. Hu, X. R. Chen, and J. D. Guo. “Epitaxial growth and thermostability of cubic and hexagonal  $\text{SrMnO}_3$  films on  $\text{SrTiO}_3(111)$ ”. In: *Frontiers of Physics* 10.3 (2015), pp. 321–326. DOI: 10.1007/s11467-015-0467-z (cit. on p. 10).
- [41] C. J. Howard and H. T. Stokes. “Group-theoretical analysis of octahedral tilting in perovskites”. In: *Acta Crystallographica Section B-Structural Science* 54.6 (1998), pp. 782–789. DOI: 10.1107/S0108768198004200 (cit. on pp. 11, 12).

- [42] A. M. Glazer. “The classification of tilted octahedra in perovskites”. In: *Acta Crystallographica Section B* 28.11 (1972), pp. 3384–3392. DOI: 10.1107/s0567740872007976 (cit. on p. 11).
- [43] A. M. Glazer. “Simple Ways of Determining Perovskite Structures”. In: *Acta Crystallographica Section A* 31.Nov1 (1975), pp. 756–762. DOI: 10.1107/S0567739475001635 (cit. on p. 11).
- [44] P. M. Woodward. “Octahedral Tilting in Perovskites. I. Geometrical Considerations”. In: *Acta Crystallographica Section B Structural Science* 53.1 (1997), pp. 32–43. DOI: 10.1107/s0108768196010713 (cit. on p. 12).
- [45] P. M. Woodward. “Octahedral Tilting in Perovskites. II. Structure Stabilizing Forces”. In: *Acta Crystallographica Section B Structural Science* 53.1 (1997), pp. 44–66. DOI: 10.1107/s0108768196012050 (cit. on p. 12).
- [46] J. Young and J. M. Rondinelli. “Octahedral Rotation Preferences in Perovskite Iodides and Bromides”. In: *Journal of Physical Chemistry Letters* 7.5 (2016), pp. 918–22. DOI: 10.1021/acs.jpcllett.6b00094 (cit. on p. 12).
- [47] M. Avdeev, E. N. Caspi, and S. Yakovlev. “On the polyhedral volume ratios  $V_A/V_B$  in perovskites  $ABX_3$ ”. In: *Acta Crystallographica Section B* 63.Pt 3 (2007), pp. 363–72. DOI: 10.1107/S0108768107001140 (cit. on pp. 12, 13).
- [48] *Tolerance Factor Calculator*. URL: <http://www.me.utexas.edu/~benedekgroup/ToleranceFactorCalculator/> (cit. on p. 12).
- [49] C. Michel, J.-M. Moreau, G. D. Achenbach, R. Gerson, and W. James. “The atomic structure of  $\text{BiFeO}_3$ ”. In: *Solid State Communications* 7.9 (1969), pp. 701–704. DOI: 10.1016/0038-1098(69)90597-3 (cit. on pp. 12, 14).
- [50] N. W. Thomas. “The compositional dependence of octahedral tilting in orthorhombic and tetragonal perovskites”. In: *Acta Crystallographica Section B-Structural Science* 52.1 (1996), pp. 16–31. DOI: 10.1107/S0108768195006100 (cit. on p. 13).
- [51] N. W. Thomas. “A re-examination of the relationship between lattice strain, octahedral tilt angle and octahedral strain in rhombohedral perovskites”. In: *Acta Crystallographica Section B-Structural Science* 52.6 (1996), pp. 954–960. DOI: 10.1107/S0108768196009214 (cit. on p. 13).
- [52] A. Cammarata and J. M. Rondinelli. “Covalent dependence of octahedral rotations in orthorhombic perovskite oxides”. In: *Journal of Chemical Physics* 141.11 (2014), p. 114704. DOI: 10.1063/1.4895967 (cit. on p. 13).

- [53] E. Mamontov, T. Egami, W. Dmowski, T. Gog, and C. Venkataraman. “Anisotropic covalent bonds in  $\text{KNbO}_3$  observed by resonant x-ray scattering”. In: *Physical Review B* 66.22 (2002), p. 224105. DOI: 10.1103/PhysRevB.66.224105 (cit. on p. 14).
- [54] J. Harada, T. Pedersen, and Z. Barnea. “X-Ray and Neutron Diffraction Study of Tetragonal Barium Titanate”. In: *Acta Crystallographica Section a-Crystal Physics Diffraction Theoretical and General Crystallography A* 26.3 (1970), pp. 336–&. DOI: 10.1107/S0567739470000815 (cit. on p. 14).
- [55] G. Shirane, R. Pepinsky, and B. C. Frazer. “X-ray and neutron diffraction study of ferroelectric  $\text{PbTiO}_3$ ”. In: *Acta Crystallographica* 9.2 (1956), pp. 131–140. DOI: 10.1107/s0365110x56000309 (cit. on p. 14).
- [56] K. A. Müller and H. Burkard. “ $\text{SrTiO}_3$ : An intrinsic quantum paraelectric below 4 K”. In: *Physical Review B* 19.7 (1979), pp. 3593–3602. DOI: 10.1103/PhysRevB.19.3593 (cit. on p. 14).
- [57] V. Železný, E. Cockayne, J. Petzelt, M. F. Limonov, D. E. Usvyat, V. V. Lemanov, and A. A. Volkov. “Temperature dependence of infrared-active phonons in  $\text{CaTiO}_3$ : A combined spectroscopic and first-principles study”. In: *Physical Review B* 66.22 (2002), p. 224303. DOI: 10.1103/PhysRevB.66.224303 (cit. on p. 14).
- [58] C. Ang, A. S. Bhalla, and L. E. Cross. “Dielectric behavior of paraelectric  $\text{KTaO}_3$ ,  $\text{CaTiO}_3$ , and  $(\text{Ln}_{1/2}\text{Na}_{1/2})\text{TiO}_3$  under a dc electric field”. In: *Physical Review B* 64.18 (2001), p. 184104. DOI: 10.1103/PhysRevB.64.184104 (cit. on p. 14).
- [59] C. H. Perry and T. F. McNelly. “Ferroelectric “Soft” Mode in  $\text{KTaO}_3$ ”. In: *Physical Review* 154.2 (1967), pp. 456–458. DOI: 10.1103/PhysRev.154.456 (cit. on p. 14).
- [60] G. A. Samara and B. Morosin. “Anharmonic Effects in  $\text{KTaO}_3$ : Ferroelectric Mode, Thermal Expansion, and Compressibility”. In: *Physical Review B* 8.3 (1973), pp. 1256–1264. DOI: 10.1103/PhysRevB.8.1256 (cit. on p. 14).
- [61] W. Zhong and D. Vanderbilt. “Competing structural instabilities in cubic perovskites”. In: *Physical Review Letters* 74.13 (1995), pp. 2587–2590. DOI: 10.1103/PhysRevLett.74.2587 (cit. on p. 14).
- [62] N. Sai and D. Vanderbilt. “First-principles study of ferroelectric and antiferrodistortive instabilities in tetragonal  $\text{SrTiO}_3$ ”. In: *Physical Review B* 62.21 (2000), pp. 13942–13950. DOI: 10.1103/PhysRevB.62.13942 (cit. on p. 14).
- [63] C. H. Lin, C. M. Huang, and G. Y. Guo. “Systematic ab initio study of the phase diagram of epitaxially strained  $\text{SrTiO}_3$ ”. In: *Journal of Applied Physics* 100.8 (2006), p. 084104. DOI: 10.1063/1.2358305 (cit. on p. 14).

- [64] J. M. Rondinelli and C. J. Fennie. “Octahedral rotation-induced ferroelectricity in cation ordered perovskites”. In: *Advanced Materials* 24.15 (2012), pp. 1961–8. DOI: 10.1002/adma.201104674 (cit. on p. 14).
- [65] A. P. Levanyuk and G. S. Daniil. “Improper ferroelectrics”. In: *Soviet Physics Uspekhi* 17.2 (1974), p. 199. DOI: 10.1070/PU1974v017n02ABEH004336 (cit. on p. 14).
- [66] D. I. Khomskii. *Transition Metal Compounds*. Cambridge University Press, 2014. DOI: 10.1017/CB09781139096782 (cit. on pp. 14, 26).
- [67] C. Zener. “Interaction between the  $d$ -Shells in the Transition Metals. II. Ferromagnetic Compounds of Manganese with Perovskite Structure”. In: *Physical Review* 82.3 (1951), pp. 403–405. DOI: 10.1103/PhysRev.82.403 (cit. on p. 16).
- [68] P. W. Anderson. “Antiferromagnetism - Theory of Superexchange Interaction”. In: *Physical Review* 79.2 (1950), pp. 350–356. DOI: 10.1103/PhysRev.79.350 (cit. on p. 16).
- [69] J. B. Goodenough. “Theory of the Role of Covalence in the Perovskite-Type Manganites  $[\text{La}, M(\text{II})]\text{MnO}_3$ ”. In: *Physical Review* 100.2 (1955), pp. 564–573. DOI: 10.1103/PhysRev.100.564 (cit. on pp. 16, 18).
- [70] I. S. Lyubutin, T. V. Dmitrieva, and A. S. Stepin. “Dependence of exchange interactions on chemical bond angle in a structural series: cubic perovskite-rhombic orthoferrite-rhombohedral hematite”. In: *Journal of Experimental and Theoretical Physics* 88.3 (1999), pp. 590–597. DOI: 10.1134/1.558833 (cit. on p. 18).
- [71] J. B. Goodenough. “An interpretation of the magnetic properties of the perovskite-type mixed crystals  $\text{La}_{1-x}\text{Sr}_x\text{CoO}_{3-\lambda}$ ”. In: *Journal of Physics and Chemistry of Solids* 6.2-3 (1958), pp. 287–297. DOI: 10.1016/0022-3697(58)90107-0 (cit. on p. 18).
- [72] J. Goodenough. *Magnetism and the chemical bond*. Interscience Publishers, 1963. URL: <https://books.google.co.in/books?id=ljtRAAAAMAAJ> (cit. on p. 18).
- [73] J. Kanamori. “Superexchange Interaction and Symmetry Properties of Electron Orbitals”. In: *Journal of Physics and Chemistry of Solids* 10.2-3 (1959), pp. 87–98. DOI: 10.1016/0022-3697(59)90061-7 (cit. on pp. 18, 32).
- [74] A. M. Haghiri-Gosnet and J. P. Renard. “CMR manganites: physics, thin films and devices”. In: *Journal of Physics D-Applied Physics* 36.8 (2003), R127–R150. DOI: 10.1088/0022-3727/36/8/201 (cit. on p. 18).



- [75] A. Marthinsen, C. Faber, U. Aschauer, N. A. Spaldin, and S. M. Selbach. “Coupling and competition between ferroelectricity, magnetism, strain, and oxygen vacancies in AMnO<sub>3</sub> perovskites”. In: *MRS Communications* 6.03 (2016), pp. 182–191. DOI: 10.1557/mrc.2016.30 (cit. on pp. 18–20).
- [76] F. Kröger and H. Vink. “Relations between the Concentrations of Imperfections in Crystalline Solids”. In: *Solid State Physics* 3 (1956), pp. 307–435. DOI: 10.1016/S0081-1947(08)60135-6 (cit. on p. 18).
- [77] P. Kofstad. “Defects and transport properties of metal oxides”. In: *Oxidation of Metals* 44.1 (1995), pp. 3–27. DOI: 10.1007/BF01046721 (cit. on p. 19).
- [78] S. B. Adler. “Chemical expansivity of electrochemical ceramics”. In: *Journal of the American Ceramic Society* 84.9 (2001), pp. 2117–2119. DOI: 10.1111/j.1151-2916.2001.tb00968.x (cit. on p. 20).
- [79] Chen, Yu, and S. B. Adler. “Thermal and Chemical Expansion of Sr-Doped Lanthanum Cobalt Oxide (La<sub>1-x</sub>Sr<sub>x</sub>CoO<sub>3-δ</sub>)”. In: *Chemistry of Materials* 17.17 (2005), pp. 4537–4546. DOI: 10.1021/cm050905h (cit. on p. 20).
- [80] T. Grande, J. R. Tolchard, and S. M. Selbach. “Anisotropic Thermal and Chemical Expansion in Sr-Substituted LaMnO<sub>3-δ</sub>: Implications for Chemical Strain Relaxation”. In: *Chemistry of Materials* 24.2 (2012), pp. 338–345. DOI: 10.1021/cm2030608 (cit. on p. 20).
- [81] H. L. Tuller and S. R. Bishop. “Point Defects in Oxides: Tailoring Materials Through Defect Engineering”. In: *Annual Review of Materials Research, Vol 41* 41 (2011), pp. 369–398. DOI: 10.1146/annurev-matsci-062910-100442 (cit. on p. 20).
- [82] W. Li et al. “Oxygen-vacancy-induced antiferromagnetism to ferromagnetism transformation in Eu<sub>0.5</sub>Ba<sub>0.5</sub>TiO<sub>3-δ</sub> multiferroic thin films”. In: *Scientific Reports* 3 (2013), p. 2618. DOI: 10.1038/srep02618 (cit. on p. 20).
- [83] C. H. Park and D. J. Chadi. “Microscopic study of oxygen-vacancy defects in ferroelectric perovskites”. In: *Physical Review B* 57.22 (1998), R13961–R13964. DOI: 10.1103/PhysRevB.57.R13961 (cit. on p. 20).
- [84] J. F. Scott and M. Dawber. “Oxygen-vacancy ordering as a fatigue mechanism in perovskite ferroelectrics”. In: *Applied Physics Letters* 76.25 (2000), pp. 3801–3803. DOI: 10.1063/1.126786 (cit. on p. 20).
- [85] P. V. Balachandran and J. M. Rondinelli. “Massive band gap variation in layered oxides through cation ordering”. In: *Nature Communications* 6 (2015), p. 6191. DOI: 10.1038/ncomms7191 (cit. on p. 20).

- [86] A. T. Mulder, N. A. Benedek, J. M. Rondinelli, and C. J. Fennie. “Turning  $\text{ABO}_3$  Antiferroelectrics into Ferroelectrics: Design Rules for Practical Rotation-Driven Ferroelectricity in Double Perovskites and  $\text{A}_3\text{B}_2\text{O}_7$  Ruddlesden-Popper Compounds”. In: *Advanced Functional Materials* 23.38 (2013), pp. 4810–4820. DOI: 10.1002/adfm.201300210 (cit. on pp. 20, 200).
- [87] X. Z. Lu and J. M. Rondinelli. “Epitaxial-strain-induced polar-to-nonpolar transitions in layered oxides”. In: *Nature Materials* 15.9 (2016), pp. 951–5. DOI: 10.1038/nmat4664 (cit. on p. 20).
- [88] S. N. Ruddlesden and P. Popper. “New compounds of the  $\text{K}_2\text{NIF}_4$  type”. In: *Acta Crystallographica* 10.8 (1957), pp. 538–539. DOI: 10.1107/s0365110x57001929 (cit. on p. 21).
- [89] B. Aurivillius. “Mixed bismuth oxides with layer lattices. 2. Structure of  $\text{Bi}_4\text{Ti}_3\text{O}_{12}$ ”. In: *Arkiv for kemi* 1.6 (1950), pp. 499–512 (cit. on p. 21).
- [90] M. Dion, M. Ganne, and M. Tournoux. “Nouvelles familles de phases  $\text{M}^I\text{M}_2^I\text{Nb}_3\text{O}_{10}$  a feuillets “perovskites””. In: *Materials Research Bulletin* 16.11 (1981), pp. 1429–1435. DOI: 10.1016/0025-5408(81)90063-5 (cit. on p. 21).
- [91] A. J. Jacobson, J. W. Johnson, and J. T. Lewandowski. “Interlayer chemistry between thick transition-metal oxide layers: synthesis and intercalation reactions of  $\text{K}[\text{Ca}_2\text{Na}_{n-3}\text{Nb}_n\text{O}_{3n+1}]$  ( $3 \leq n \leq 7$ )”. In: *Inorganic Chemistry* 24.23 (1985), pp. 3727–3729. DOI: 10.1021/ic00217a006 (cit. on p. 21).
- [92] J.-C. Grenier, J. Darriet, M. Pouchard, and P. Hagenmuller. “Mise en evidence d’une nouvelle famille de phases de type perovskite lacunaire ordonnee de formule  $\text{A}_3\text{M}_3\text{O}_8$  ( $\text{AMO}_{2,67}$ )”. In: *Materials Research Bulletin* 11.10 (1976), pp. 1219–1225. DOI: 10.1016/0025-5408(76)90024-6 (cit. on pp. 21, 22).
- [93] A. F. Sammells, R. L. Cook, J. H. White, J. J. Osborne, and R. C. MacDuff. “Rational selection of advanced solid electrolytes for intermediate temperature fuel cells”. In: *Solid State Ionics* 52.1 (1992), pp. 111–123. DOI: 10.1016/0167-2738(92)90097-9 (cit. on pp. 21, 34).
- [94] S. B. Adler. “Factors Governing Oxygen Reduction in Solid Oxide Fuel Cell Cathodes”. In: *Chemical Reviews* 104.10 (2004), pp. 4791–4844. DOI: 10.1021/cr020724o (cit. on pp. 21, 34).
- [95] Y. M. Kim, J. He, M. D. Biegalski, H. Ambaye, V. Lauter, H. M. Christen, S. T. Pantelides, S. J. Pennycook, S. V. Kalinin, and A. Y. Borisevich. “Probing oxygen vacancy concentration and homogeneity in solid-oxide fuel-cell cathode materials on the subunit-cell level”. In: *Nature Materials* 11.10 (2012), pp. 888–94. DOI: 10.1038/nmat3393 (cit. on pp. 21, 34).

- [96] J.-C. Grenier, G. Schiffmacher, P. Caro, M. Pouchard, and P. Hagemuller. “Etude par diffraction X et microscopie electronique du système  $\text{CaTiO}_3\text{Ca}_2\text{Fe}_2\text{O}_5$ ”. In: *Journal of Solid State Chemistry* 20.4 (1977), pp. 365–379. DOI: 10.1016/0022-4596(77)90174-8 (cit. on p. 22).
- [97] G. B. Zhang and D. M. Smyth. “Defects and transport of the brownmillerite oxides with high oxygen ion conductivity -  $\text{Ba}_2\text{In}_2\text{O}_5$ ”. In: *Solid State Ionics* 82.3-4 (1995), pp. 161–172. DOI: 10.1016/0167-2738(95)00196-2 (cit. on p. 22).
- [98] J. D. Ferguson, Y. Kim, L. F. Kourkoutis, A. Vodnick, A. R. Woll, D. A. Muller, and J. D. Brock. “Epitaxial oxygen getter for a brownmillerite phase transformation in manganite films”. In: *Advanced Materials* 23.10 (2011), pp. 1226–30. DOI: 10.1002/adma.201003581 (cit. on pp. 22, 25).
- [99] L. Yao, S. Inkinen, and S. van Dijken. “Direct observation of oxygen vacancy-driven structural and resistive phase transitions in  $\text{La}_{2/3}\text{Sr}_{1/3}\text{MnO}_3$ ”. In: *Nature Communications* 8 (2017), p. 14544. DOI: 10.1038/ncomms14544 (cit. on pp. 22, 25).
- [100] N. Lu et al. “Electric-field control of tri-state phase transformation with a selective dual-ion switch”. In: *Nature* 546.7656 (2017), 124+. DOI: {10.1038/nature22389} (cit. on pp. 22, 200).
- [101] C. G. Granqvist. “Electrochromics for smart windows: Oxide-based thin films and devices”. In: *Thin Solid Films* 564 (2014), pp. 1–38. DOI: 10.1016/j.tsf.2014.02.002 (cit. on p. 22).
- [102] E. Tsymbal, E. Dagotto, C. B. Eom, and R. Ramesh. *Multifunctional oxide heterostructures*. Oxford University Press, 2012. DOI: 10.1093/acprof:oso/9780199584123.001.0001 (cit. on pp. 23, 45).
- [103] N. A. Pertsev, A. G. Zembilgotov, and A. K. Tagantsev. “Effect of mechanical boundary conditions on phase diagrams of epitaxial ferroelectric thin films”. In: *Physical Review Letters* 80.9 (1998), pp. 1988–1991. DOI: 10.1103/PhysRevLett.80.1988 (cit. on p. 23).
- [104] N. A. Pertsev, A. K. Tagantsev, and N. Setter. “Phase transitions and strain-induced ferroelectricity in  $\text{SrTiO}_3$  epitaxial thin films”. In: *Physical Review B* 61.2 (2000), R825–R829. DOI: 10.1103/PhysRevB.61.R825 (cit. on p. 23).
- [105] K. J. Choi et al. “Enhancement of ferroelectricity in strained  $\text{BaTiO}_3$  thin films”. In: *Science* 306.5698 (2004), pp. 1005–9. DOI: 10.1126/science.1103218 (cit. on p. 24).
- [106] J. H. Haeni et al. “Room-temperature ferroelectricity in strained  $\text{SrTiO}_3$ ”. In: *Nature* 430.7001 (2004), pp. 758–61. DOI: 10.1038/nature02773 (cit. on p. 24).

- [107] A. J. Hatt and N. A. Spaldin. “Structural phases of strained  $\text{LaAlO}_3$  driven by octahedral tilt instabilities”. In: *Physical Review B* 82.19 (2010), p. 195402. DOI: 10.1103/PhysRevB.82.195402 (cit. on p. 25).
- [108] S. J. May, J. W. Kim, J. M. Rondinelli, E. Karapetrova, N. A. Spaldin, A. Bhattacharya, and P. J. Ryan. “Quantifying octahedral rotations in strained perovskite oxide films”. In: *Physical Review B* 82.1 (2010), p. 014110. DOI: 10.1103/PhysRevB.82.014110 (cit. on p. 25).
- [109] R. L. Johnson-Wilke et al. “Quantification of octahedral rotations in strained  $\text{LaAlO}_3$  films via synchrotron x-ray diffraction”. In: *Physical Review B* 88.17 (2013), p. 174101. DOI: 10.1103/PhysRevB.88.174101 (cit. on pp. 25, 52).
- [110] A. T. Zayak, X. Huang, J. B. Neaton, and K. M. Rabe. “Structural, electronic, and magnetic properties of  $\text{SrRuO}_3$  under epitaxial strain”. In: *Physical Review B* 74.9 (2006), p. 094104. DOI: 10.1103/PhysRevB.74.094104 (cit. on pp. 25, 44, 53).
- [111] C. J. Eklund, C. J. Fennie, and K. M. Rabe. “Strain-induced ferroelectricity in orthorhombic  $\text{CaTiO}_3$  from first principles”. In: *Physical Review B* 79.22 (2009), p. 220101. DOI: 10.1103/PhysRevB.79.220101 (cit. on p. 25).
- [112] U. Aschauer, R. Pfenninger, S. M. Selbach, T. Grande, and N. A. Spaldin. “Strain-controlled oxygen vacancy formation and ordering in  $\text{CaMnO}_3$ ”. In: *Physical Review B* 88.5 (2013), p. 054111. DOI: 10.1103/PhysRevB.88.054111 (cit. on p. 25).
- [113] U. Aschauer, N. Vonruti, and N. A. Spaldin. “Effect of epitaxial strain on cation and anion vacancy formation in  $\text{MnO}$ ”. In: *Physical Review B* 92.5 (2015), p. 054103. DOI: 10.1103/PhysRevB.92.054103 (cit. on p. 25).
- [114] R. U. Chandrasena et al. “Strain-Engineered Oxygen Vacancies in  $\text{CaMnO}_3$  Thin Films”. In: *Nano Letters* 17.2 (2017), pp. 794–799. DOI: 10.1021/acs.nanolett.6b03986 (cit. on p. 25).
- [115] L. Yao, S. Majumdar, L. Akaslopolo, S. Inkinen, Q. H. Qin, and S. van Dijken. “Electron-beam-induced Perovskite-Brownmillerite-Perovskite structural phase transitions in epitaxial  $\text{La}_{2/3}\text{Sr}_{1/3}\text{MnO}_3$  films”. In: *Advanced Materials* 26.18 (2014), pp. 2789–93. DOI: 10.1002/adma.201305656 (cit. on p. 25).
- [116] J. Young and J. M. Rondinelli. “Crystal structure and electronic properties of bulk and thin film brownmillerite oxides”. In: *Physical Review B* 92.17 (2015), p. 174111. DOI: 10.1103/PhysRevB.92.174111 (cit. on p. 25).

- [117] J. F. Li, J. L. Wang, M. Wuttig, R. Ramesh, N. Wang, B. Ruetter, A. P. Pyatakov, A. K. Zvezdin, and D. Viehland. “Dramatically enhanced polarization in (001), (101), and (111) BiFeO<sub>3</sub> thin films due to epitaxial-induced transitions”. In: *Applied Physics Letters* 84.25 (2004), pp. 5261–5263. DOI: 10.1063/1.1764944 (cit. on p. 26).
- [118] Y. B. Xu, Y. L. Tang, Y. L. Zhu, Y. Liu, S. Li, S. R. Zhang, and X. L. Ma. “Misfit Strain Relaxation of Ferroelectric PbTiO<sub>3</sub>/LaAlO<sub>3</sub> (111) Thin Film System”. In: *Scientific Reports* 6 (2016), p. 35172. DOI: 10.1038/srep35172 (cit. on p. 26).
- [119] R. Oja, K. Johnston, J. Frantti, and R. M. Nieminen. “Computational study of (111) epitaxially strained ferroelectric perovskites BaTiO<sub>3</sub> and PbTiO<sub>3</sub>”. In: *Physical Review B* 78.9 (2008), p. 094102. DOI: 10.1103/PhysRevB.78.094102 (cit. on pp. 26, 34).
- [120] A. Raeliarijaona and H. X. Fu. “Various evidences for the unusual polarization behaviors in epitaxially strained (111) BaTiO<sub>3</sub>”. In: *Journal of Applied Physics* 115.5 (2014), p. 054105. DOI: 10.1063/1.4864218 (cit. on pp. 26, 34).
- [121] Y. Konishi, Z. Fang, M. Izumi, T. Manako, M. Kasai, H. Kuwahara, M. Kawasaki, K. Terakura, and Y. Tokura. “Orbital-state-mediated phase-control of manganites”. In: *Journal of the Physical Society of Japan* 68.12 (1999), pp. 3790–3793. DOI: 10.1143/Jpsj.68.3790 (cit. on p. 26).
- [122] H. Yamada, M. Kawasaki, T. Lottermoser, T. Arima, and Y. Tokura. “LaMnO<sub>3</sub>/SrMnO<sub>3</sub> interfaces with coupled charge-spin-orbital modulation”. In: *Applied Physics Letters* 89.5 (2006), p. 052506. DOI: 10.1063/1.2266863 (cit. on p. 26).
- [123] B. R. K. Nanda and S. Satpathy. “Effects of strain on orbital ordering and magnetism at perovskite oxide interfaces:LaMnO<sub>3</sub>/SrMnO<sub>3</sub>”. In: *Physical Review B* 78.5 (2008), p. 12. DOI: 10.1103/PhysRevB.78.054427 (cit. on p. 26).
- [124] D. Xiao, W. Zhu, Y. Ran, N. Nagaosa, and S. Okamoto. “Interface engineering of quantum Hall effects in digital transition metal oxide heterostructures”. In: *Nature Communications* 2 (2011), p. 596. DOI: 10.1038/ncomms1602 (cit. on p. 27).
- [125] D. Doennig, W. E. Pickett, and R. Pentcheva. “Massive symmetry breaking in LaAlO<sub>3</sub>/SrTiO<sub>3</sub>(111) quantum wells: a three-orbital strongly correlated generalization of graphene”. In: *Physical Review Letters* 111.12 (2013), p. 126804. DOI: 10.1103/PhysRevLett.111.126804 (cit. on pp. 27, 32).

- [126] I. Hallsteinsen, J. E. Boschker, M. Nord, S. Lee, M. Rzechowski, P. E. Vullum, J. K. Grepstad, R. Holmestad, C. B. Eom, and T. Tybell. “Surface stability of epitaxial  $\text{La}_{0.7}\text{Sr}_{0.3}\text{MnO}_3$  thin films on (111)-oriented  $\text{SrTiO}_3$ ”. In: *Journal of Applied Physics* 113.18 (2013), p. 183512. DOI: 10.1063/1.4804312 (cit. on pp. 28, 32).
- [127] I. Hallsteinsen, M. Nord, T. Bolstad, P.-E. Vullum, J. E. Boschker, P. Longo, R. Takahashi, R. Holmestad, M. Lippmaa, and T. Tybell. “Effect of Polar (111)-Oriented  $\text{SrTiO}_3$  on Initial Perovskite Growth”. In: *Crystal Growth & Design* 16.4 (2016), pp. 2357–2362. DOI: 10.1021/acs.cgd.6b00143 (cit. on p. 28).
- [128] H. Chen, A. J. Millis, and C. A. Marianetti. “Engineering Correlation Effects via Artificially Designed Oxide Superlattices”. In: *Physical Review Letters* 111.11 (2013), p. 116403. DOI: 10.1103/PhysRevLett.111.116403 (cit. on p. 28).
- [129] J. E. Kleibeuker et al. “Electronic Reconstruction at the Isopolar  $\text{LaTiO}_3/\text{LaFeO}_3$  Interface: An X-Ray Photoemission and Density-Functional Theory Study”. In: *Physical Review Letters* 113.23 (2014), p. 237402. DOI: 10.1103/PhysRevLett.113.237402 (cit. on p. 28).
- [130] A. Bhattacharya and S. J. May. “Magnetic Oxide Heterostructures”. In: *Annual Review of Materials Research, Vol 44* 44.1 (2014), pp. 65–90. DOI: 10.1146/annurev-matsci-070813-113447 (cit. on p. 28).
- [131] C. W. Lin, S. Okamoto, and A. J. Millis. “Dynamical mean-field study of model double-exchange superlattices”. In: *Physical Review B* 73.4 (2006), p. 041104. DOI: 10.1103/PhysRevB.73.041104 (cit. on p. 28).
- [132] K. S. Takahashi, M. Kawasaki, and Y. Tokura. “Interface ferromagnetism in oxide superlattices of  $\text{CaMnO}_3/\text{CaRuO}_3$ ”. In: *Applied Physics Letters* 79.9 (2001), pp. 1324–1326. DOI: 10.1063/1.1398331 (cit. on pp. 28, 31).
- [133] S. J. May, A. B. Shah, S. G. E. te Velthuis, M. R. Fitzsimmons, J. M. Zuo, X. Zhai, J. N. Eckstein, S. D. Bader, and A. Bhattacharya. “Magnetically asymmetric interfaces in a  $\text{LaMnO}_3/\text{SrMnO}_3$  superlattice due to structural asymmetries”. In: *Physical Review B* 77.17 (2008), p. 174409. DOI: 10.1103/PhysRevB.77.174409 (cit. on p. 28).
- [134] B. R. K. Nanda, S. Satpathy, and M. S. Springborg. “Electron Leakage and Double-Exchange Ferromagnetism at the Interface between a Metal and an Antiferromagnetic Insulator:  $\text{CaRuO}_3/\text{CaMnO}_3$ ”. In: *Physical Review Letters* 98.21 (2007), p. 216804. DOI: 10.1103/PhysRevLett.98.216804 (cit. on pp. 28, 31).

- [135] B. R. K. Nanda and S. Satpathy. “Spin-polarized two-dimensional electron gas at oxide interfaces”. In: *Physical Review Letters* 101.12 (2008), p. 127201. DOI: 10.1103/PhysRevLett.101.127201 (cit. on p. 28).
- [136] J. Chakhalian et al. “Magnetism at the interface between ferromagnetic and superconducting oxides”. In: *Nature Physics* 2.4 (2006), pp. 244–248. DOI: 10.1038/nphys272 (cit. on p. 29).
- [137] R. Aso, D. Kan, Y. Shimakawa, and H. Kurata. “Atomic level observation of octahedral distortions at the perovskite oxide heterointerface”. In: *Sci Rep* 3 (2013), p. 2214. DOI: 10.1038/srep02214 (cit. on p. 29).
- [138] R. Aso, D. Kan, Y. Shimakawa, and H. Kurata. “Octahedral Tilt Propagation Controlled by A-Site Cation Size at Perovskite Oxide Heterointerfaces”. In: *Crystal Growth & Design* 14.5 (2014), pp. 2128–2132. DOI: 10.1021/cg500285m (cit. on pp. 29, 30).
- [139] J. M. Rondinelli and N. A. Spaldin. “Substrate coherency driven octahedral rotations in perovskite oxide films”. In: *Physical Review B* 82.11 (2010), p. 113402. DOI: 10.1103/PhysRevB.82.113402 (cit. on p. 29).
- [140] J. He, A. Borisevich, S. V. Kalinin, S. J. Pennycook, and S. T. Pantelides. “Control of octahedral tilts and magnetic properties of perovskite oxide heterostructures by substrate symmetry”. In: *Physical Review Letters* 105.22 (2010), p. 227203. DOI: 10.1103/PhysRevLett.105.227203 (cit. on p. 29).
- [141] L. Qiao et al. “Dimensionality Controlled Octahedral Symmetry-Mismatch and Functionalities in Epitaxial  $\text{LaCoO}_3/\text{SrTiO}_3$  Heterostructures”. In: *Nano Letters* 15.7 (2015), pp. 4677–84. DOI: 10.1021/acs.nanolett.5b01471 (cit. on pp. 29, 52).
- [142] Z. Liao et al. “Controlled lateral anisotropy in correlated manganite heterostructures by interface-engineered oxygen octahedral coupling”. In: *Nature Materials* 15.4 (2016), pp. 425–31. DOI: 10.1038/nmat4579 (cit. on pp. 30, 31).
- [143] A. J. Grutter, A. Vailionis, J. A. Borchers, B. J. Kirby, C. L. Flint, C. He, E. Arenholz, and Y. Suzuki. “Interfacial Symmetry Control of Emergent Ferromagnetism at the Nanoscale”. In: *Nano Letters* 16.9 (2016), pp. 5647–51. DOI: 10.1021/acs.nanolett.6b02255 (cit. on p. 31).
- [144] K. Ueda, H. Tabata, and T. Kawai. “Ferromagnetism in  $\text{LaFeO}_3\text{-LaCrO}_3$  Superlattices”. In: *Science* 280.5366 (1998), pp. 1064–1066. DOI: 10.1126/science.280.5366.1064 (cit. on p. 32).
- [145] K. Ueda, H. Tabata, and T. Kawai. “Atomic arrangement and magnetic properties of  $\text{LaFeO}_3\text{-LaMnO}_3$  artificial superlattices”. In: *Physical Review B* 60.18 (1999), R12561–R12564 (cit. on p. 32).

- [146] K. Ueda, H. Tabata, and T. Kawai. “Control of magnetic properties in  $\text{LaCrO}_3\text{--LaFeO}_3$  artificial superlattice”. In: *Journal of Applied Physics* 89.5 (2001), pp. 2847–2851. DOI: 10.1063/1.1327287 (cit. on p. 32).
- [147] W. E. Pickett. “Spin-density-functional-based search for half-metallic anti-ferromagnets”. In: *Physical Review B* 57.17 (1998), pp. 10613–10619. DOI: 10.1103/PhysRevB.57.10613 (cit. on p. 32).
- [148] S. Chakraverty et al. “Ferrimagnetism and spontaneous ordering of transition metals in double perovskite  $\text{La}_2\text{CrFeO}_6$  films”. In: *Physical Review B* 84.6 (2011), p. 064436. DOI: 10.1103/PhysRevB.84.064436 (cit. on p. 32).
- [149] B. Gray, H. N. Lee, J. Liu, J. Chakhalian, and J. W. Freeland. “Local electronic and magnetic studies of an artificial  $\text{La}_2\text{FeCrO}_6$  double perovskite”. In: *Applied Physics Letters* 97.1 (2010), p. 013105. DOI: 10.1063/1.3455323 (cit. on p. 32).
- [150] K. Yoshimatsu, K. Nogami, K. Watarai, K. Horiba, H. Kumigashira, O. Sakata, T. Oshima, and A. Ohtomo. “Synthesis and magnetic properties of double-perovskite oxide  $\text{La}_2\text{MnFeO}_6$  thin films”. In: *Physical Review B* 91.5 (2015), p. 054421. DOI: 10.1103/PhysRevB.91.054421 (cit. on p. 32).
- [151] M. Gibert, P. Zubko, R. Scherwitzl, J. Iniguez, and J. M. Triscone. “Exchange bias in  $\text{LaNiO}_3\text{--LaMnO}_3$  superlattices”. In: *Nature Materials* 11.3 (2012), pp. 195–8. DOI: 10.1038/nmat3224 (cit. on p. 32).
- [152] Y. Jia, R. V. Chopdekar, E. Arenholz, A. T. Young, M. A. Marcus, A. Mehta, and Y. Takamura. “Exchange coupling in (111)-oriented  $\text{La}_{0.7}\text{Sr}_{0.3}\text{MnO}_3/\text{La}_{0.7}\text{Sr}_{0.3}\text{FeO}_3$  superlattices”. In: *Physical Review B* 92.9 (2015), p. 094407. DOI: 10.1103/PhysRevB.92.094407 (cit. on p. 32).
- [153] Y. Jia, R. V. Chopdekar, E. Arenholz, Z. Q. Liu, M. D. Biegalski, Z. D. Porter, A. Mehta, and Y. Takamura. “Thickness dependence of exchange coupling in (111)-oriented perovskite oxide superlattices”. In: *Physical Review B* 93.10 (2016), p. 104403. DOI: 10.1103/PhysRevB.93.104403 (cit. on p. 32).
- [154] G. Herranz, F. Sanchez, N. Dix, M. Scigaj, and J. Fontcuberta. “High mobility conduction at (110) and (111)  $\text{LaAlO}_3/\text{SrTiO}_3$  interfaces”. In: *Scientific Reports* 2 (2012), p. 758. DOI: 10.1038/srep00758 (cit. on p. 32).
- [155] F. D. M. Haldane. “Model for a Quantum Hall-Effect without Landau-Levels - Condensed-Matter Realization of the Parity Anomaly”. In: *Physical Review Letters* 61.18 (1988), pp. 2015–2018. DOI: 10.1103/PhysRevLett.61.2015 (cit. on p. 32).



- [156] M. Z. Hasan and C. L. Kane. “Colloquium: Topological insulators”. In: *Reviews of Modern Physics* 82.4 (2010), pp. 3045–3067. DOI: 10.1103/RevModPhys.82.3045 (cit. on p. 32).
- [157] S. Raghu, X. L. Qi, C. Honerkamp, and S. C. Zhang. “Topological Mott insulators”. In: *Physical Review Letters* 100.15 (2008), p. 156401. DOI: 10.1103/PhysRevLett.100.156401 (cit. on p. 32).
- [158] A. Ruegg and G. A. Fiete. “Topological insulators from complex orbital order in transition-metal oxides heterostructures”. In: *Physical Review B* 84.20 (2011), p. 201103. DOI: 10.1103/PhysRevB.84.201103 (cit. on p. 32).
- [159] K.-Y. Yang, W. Zhu, D. Xiao, S. Okamoto, Z. Wang, and Y. Ran. “Possible interaction-driven topological phases in (111) bilayers of  $\text{LaNiO}_3$ ”. In: *Physical Review B* 84.20 (2011), p. 201104. DOI: 10.1103/PhysRevB.84.201104 (cit. on p. 32).
- [160] D. Doennig, W. E. Pickett, and R. Pentcheva. “Confinement-driven transitions between topological and Mott phases in  $(\text{LaNiO}_3)_N/(\text{LaAlO}_3)_M(111)$  superlattices”. In: *Physical Review B* 89.12 (2014), p. 121110. DOI: 10.1103/PhysRevB.89.121110 (cit. on p. 32).
- [161] D. Doennig, S. Baidya, W. E. Pickett, and R. Pentcheva. “Design of Chern and Mott insulators in buckled 3d oxide honeycomb lattices”. In: *Physical Review B* 93.16 (2016), p. 165145 (cit. on p. 32).
- [162] K. Yamauchi, P. Barone, T. Shishidou, T. Oguchi, and S. Picozzi. “Coupling Ferroelectricity with Spin-Valley Physics in Oxide-Based Heterostructures”. In: *Physical Review Letters* 115.3 (2015), p. 037602. DOI: 10.1103/PhysRevLett.115.037602 (cit. on p. 32).
- [163] K. Yamauchi, P. Barone, and S. Picozzi. “Topological phase transition coupled with spin-valley physics in ferroelectric oxide heterostructures”. In: *Physical Review B* 95.3 (2017), p. 035146. DOI: 10.1103/PhysRevB.95.035146 (cit. on p. 32).
- [164] T. J. Anderson, S. Ryu, H. Zhou, L. Xie, J. P. Podkaminer, Y. Ma, J. Irwin, X. Q. Pan, M. S. Rzchowski, and C. B. Eom. “Metastable honeycomb  $\text{SrTiO}_3/\text{SrIrO}_3$  heterostructures”. In: *Applied Physics Letters* 108.15 (2016), p. 151604. DOI: 10.1063/1.4947006 (cit. on p. 32).
- [165] S. Middey, D. Meyers, M. Kareev, E. J. Moon, B. A. Gray, X. Liu, J. W. Freeland, and J. Chakhalian. “Epitaxial growth of (111)-oriented  $\text{LaAlO}_3/\text{LaNiO}_3$  ultra-thin superlattices”. In: *Applied Physics Letters* 101.26 (2012), p. 261602. DOI: 10.1063/1.4773375 (cit. on p. 33).

- [166] D. Hirai, J. Matsuno, and H. Takagi. “Fabrication of (111)-oriented  $\text{Ca}_{0.5}\text{Sr}_{0.5}\text{IrO}_3/\text{SrTiO}_3$  superlattices—A designed playground for honeycomb physics”. In: *APL Materials* 3.4 (2015), p. 041508. DOI: 10.1063/1.4913389 (cit. on p. 33).
- [167] S. Middey et al. “Mott Electrons in an Artificial Graphenelike Crystal of Rare-Earth Nickelate”. In: *Physical Review Letters* 116.5 (2016), p. 056801. DOI: 10.1103/PhysRevLett.116.056801 (cit. on p. 33).
- [168] M. Fiebig, T. Lottermoser, D. Frohlich, A. V. Goltsev, and R. V. Pisarev. “Observation of coupled magnetic and electric domains”. In: *Nature* 419.6909 (2002), pp. 818–820. DOI: 10.1038/nature01077 (cit. on p. 33).
- [169] B. B. Van Aken, T. T. M. Palstra, A. Filippetti, and N. A. Spaldin. “The origin of ferroelectricity in magnetoelectric  $\text{YMnO}_3$ ”. In: *Nature Materials* 3.3 (2004), pp. 164–170. DOI: 10.1038/nmat1080 (cit. on p. 33).
- [170] D. S. Sholl and J. A. Steckel. *Density functional theory: a practical introduction*. Hoboken, N.J.: Wiley, 2009, XII, 238 s. : ill. DOI: 10.1002/9780470447710 (cit. on p. 37).
- [171] K. Burke and L. O. Wagner. “DFT in a nutshell”. In: *International Journal of Quantum Chemistry* 113.2 (2013), pp. 96–101. DOI: 10.1002/qua.24259 (cit. on p. 37).
- [172] K. Burke. “The abc of dft”. In: *Department of Chemistry, University of California* (2007) (cit. on p. 37).
- [173] P. J. Hasnip, K. Refson, M. I. Probert, J. R. Yates, S. J. Clark, and C. J. Pickard. “Density functional theory in the solid state”. In: *Philos Trans A Math Phys Eng Sci* 372.2011 (2014), p. 20130270. DOI: 10.1098/rsta.2013.0270 (cit. on p. 37).
- [174] R. M. Martin. *Electronic structure: basic theory and practical methods*. Cambridge university press, 2004. DOI: 10.1017/CB09780511805769 (cit. on pp. 37, 41, 44).
- [175] W. Koch and M. C. Holthausen. *A chemist’s guide to density functional theory*. John Wiley & Sons, 2001. DOI: 10.1002/3527600043 (cit. on p. 37).
- [176] R. O. Jones. “Density functional theory: Its origins, rise to prominence, and future”. In: *Reviews of Modern Physics* 87.3 (2015), pp. 897–923. DOI: 10.1103/RevModPhys.87.897 (cit. on p. 37).
- [177] A. D. Becke. “Perspective: Fifty years of density-functional theory in chemical physics”. In: *The Journal of Chemical Physics* 140.18 (2014), 18A301. DOI: 10.1063/1.4869598 (cit. on p. 37).

- [178] A. J. Cohen, P. Mori-Sanchez, and W. Yang. “Challenges for density functional theory”. In: *Chem Rev* 112.1 (2012), pp. 289–320. DOI: 10.1021/cr200107z (cit. on p. 37).
- [179] P. Hohenberg and W. Kohn. “Inhomogeneous Electron Gas”. In: *Physical Review B* 136.3b (1964), B864–+. DOI: 10.1103/PhysRev.136.B864 (cit. on p. 39).
- [180] W. Kohn and L. J. Sham. “Self-Consistent Equations Including Exchange and Correlation Effects”. In: *Physical Review* 140.4a (1965), pp. 1133–&. DOI: 10.1103/PhysRev.140.A1133 (cit. on p. 39).
- [181] D. M. Ceperley and B. J. Alder. “Ground-State of the Electron-Gas by a Stochastic Method”. In: *Physical Review Letters* 45.7 (1980), pp. 566–569. DOI: 10.1103/PhysRevLett.45.566 (cit. on p. 41).
- [182] J. P. Perdew, A. Ruzsinszky, J. Tao, V. N. Staroverov, G. E. Scuseria, and G. I. Csonka. “Prescription for the design and selection of density functional approximations: more constraint satisfaction with fewer fits”. In: *The Journal of Chemical Physics* 123.6 (2005), p. 62201. DOI: 10.1063/1.1904565 (cit. on pp. 41, 42).
- [183] J. P. Perdew and K. Schmidt. “Jacob’s ladder of density functional approximations for the exchange-correlation energy”. In: *Density Functional Theory and Its Application to Materials* 577.1 (2001), pp. 1–20. DOI: 10.1063/1.1390175 (cit. on p. 41).
- [184] V. I. Anisimov, J. Zaanen, and O. K. Andersen. “Band Theory and Mott Insulators - Hubbard-U Instead of Stoner-I”. In: *Physical Review B* 44.3 (1991), pp. 943–954. DOI: 10.1103/PhysRevB.44.943 (cit. on p. 41).
- [185] S. Satpathy, Z. S. Popović, and F. R. Vukajlović. “Electronic Structure of the Perovskite Oxides:  $\text{La}_{1-x}\text{Ca}_x\text{MnO}_3$ ”. In: *Physical Review Letters* 76.6 (1996), pp. 960–963. DOI: 10.1103/PhysRevLett.76.960 (cit. on p. 41).
- [186] J. Hong, A. Stroppa, J. Íñiguez, S. Picozzi, and D. Vanderbilt. “Spin-phonon coupling effects in transition-metal perovskites: A DFT + U and hybrid-functional study”. In: *Physical Review B* 85.5 (2012), p. 054417. DOI: PhysRevB.85.054417 (cit. on p. 42).
- [187] M. Chandrima, S. F. Randy, O. Satoshi, L. Ho Nyung, and A. R. Fernando. “Ground-State and Spin-Wave Dynamics in Brownmillerite  $\text{SrCoO}_{2.5}$  – a Combined Hybrid Functional and LSDA + U Study”. In: *Journal of Physics: Condensed Matter* 26.3 (2014), p. 036004. DOI: 10.1088/0953-8984/26/3/036004 (cit. on p. 42).
- [188] H. J. Monkhorst and J. D. Pack. “Special Points for Brillouin-Zone Integrations”. In: *Physical Review B* 13.12 (1976), pp. 5188–5192. DOI: 10.1103/PhysRevB.13.5188 (cit. on p. 43).

- [189] D. R. Hamann, M. Schluter, and C. Chiang. “Norm-Conserving Pseudopotentials”. In: *Physical Review Letters* 43.20 (1979), pp. 1494–1497. DOI: 10.1103/PhysRevLett.43.1494 (cit. on p. 44).
- [190] D. Vanderbilt. “Soft self-consistent pseudopotentials in a generalized eigenvalue formalism”. In: *Physical Review B* 41.11 (1990), pp. 7892–7895. DOI: 10.1103/PhysRevB.41.7892 (cit. on p. 44).
- [191] P. E. Blochl. “Projector augmented-wave method”. In: *Physical Review B* 50.24 (1994), pp. 17953–17979. DOI: 10.1103/PhysRevB.50.17953 (cit. on pp. 44, 50).
- [192] G. Kresse and D. Joubert. “From ultrasoft pseudopotentials to the projector augmented-wave method”. In: *Physical Review B* 59.3 (1999), pp. 1758–1775. DOI: 10.1103/PhysRevB.59.1758 (cit. on pp. 44, 50).
- [193] H. Chen. “A First-Principles Study on Oxide Interfaces”. 2012 (cit. on p. 47).
- [194] W. Cochran. “Crystal Stability and the Theory of Ferroelectricity”. In: *Physical Review Letters* 3.9 (1959), pp. 412–414. DOI: 10.1103/PhysRevLett.3.412 (cit. on p. 48).
- [195] E. Bousquet. “First-Principles study of ferroelectric oxide nanostructures”. 2009 (cit. on pp. 48, 49, 54).
- [196] R. M. Pick, M. H. Cohen, and R. M. Martin. “Microscopic Theory of Force Constants in the Adiabatic Approximation”. In: *Physical Review B* 1.2 (1970), pp. 910–920 (cit. on p. 48).
- [197] G. Kresse and J. Hafner. “Ab initiomolecular dynamics for liquid metals”. In: *Physical Review B* 47.1 (1993), pp. 558–561. DOI: 10.1103/PhysRevB.47.558 (cit. on p. 50).
- [198] G. Kresse and J. Hafner. “Ab initio molecular-dynamics simulation of the liquid-metal-amorphous-semiconductor transition in germanium”. In: *Physical Review B* 49.20 (1994), pp. 14251–14269. DOI: 10.1103/PhysRevB.49.14251 (cit. on p. 50).
- [199] G. Kresse and J. Furthmuller. “Efficiency of ab-initio total energy calculations for metals and semiconductors using a plane-wave basis set”. In: *Computational Materials Science* 6.1 (1996), pp. 15–50. DOI: 10.1016/0927-0256(96)00008-0 (cit. on p. 50).
- [200] G. Kresse and J. Furthmuller. “Efficient iterative schemes for ab initio total-energy calculations using a plane-wave basis set”. In: *Physical Review B* 54.16 (1996), pp. 11169–11186. DOI: 10.1103/PhysRevB.54.11169 (cit. on p. 50).

- [201] G. Kresse, M. Marsman, and J. Furthmüller. *VASP manual*. URL: <https://cms.mpi.univie.ac.at/vasp/vasp/vasp.html> (cit. on pp. 50–52, 55).
- [202] L. Bellaïche and D. Vanderbilt. “Virtual crystal approximation revisited: Application to dielectric and piezoelectric properties of perovskites”. In: *Physical Review B* 61.12 (2000), pp. 7877–7882 (cit. on p. 50).
- [203] Z. Fang, I. V. Solovyev, and K. Terakura. “Phase Diagram of Tetragonal Manganites”. In: *Physical Review Letters* 84.14 (2000), pp. 3169–3172 (cit. on p. 50).
- [204] J. P. Perdew, A. Ruzsinszky, G. I. Csonka, O. A. Vydrov, G. E. Scuseria, L. A. Constantin, X. Zhou, and K. Burke. “Restoring the density-gradient expansion for exchange in solids and surfaces”. In: *Physical Review Letters* 100.13 (2008), p. 136406. DOI: 10.1103/PhysRevLett.100.136406 (cit. on p. 52).
- [205] S. L. Dudarev, G. A. Botton, S. Y. Savrasov, C. J. Humphreys, and A. P. Sutton. “Electron-energy-loss spectra and the structural stability of nickel oxide: An LSDA+U study”. In: *Physical Review B* 57.3 (1998), pp. 1505–1509. DOI: 10.1103/PhysRevB.57.1505 (cit. on p. 52).
- [206] L. Schimka, J. Harl, and G. Kresse. “Improved hybrid functional for solids: the HSEsol functional”. In: *The Journal of Chemical Physics* 134.2 (2011), p. 024116. DOI: 10.1063/1.3524336 (cit. on p. 52).
- [207] W. H. Press, B. P. Flannery, S. A. Teukolsky, and W. T. Vetterling. *Numerical Recipes: the art of scientific computing*. 1986 (cit. on p. 52).
- [208] P. Pulay. “Convergence Acceleration of Iterative Sequences - the Case of Scf Iteration”. In: *Chemical Physics Letters* 73.2 (1980), pp. 393–398. DOI: 10.1016/0009-2614(80)80396-4 (cit. on p. 52).
- [209] H. Hellmann. “Zur Rolle der kinetischen Elektronenenergie für die zwischenatomaren Kräfte”. In: *Zeitschrift für Physik* 85.3 (1933), pp. 180–190. DOI: 10.1007/bf01342053 (cit. on p. 52).
- [210] R. P. Feynman. “Forces in Molecules”. In: *Physical Review* 56.4 (1939), pp. 340–343. DOI: 10.1103/PhysRev.56.340 (cit. on p. 52).
- [211] G. P. Francis and M. C. Payne. “Finite Basis Set Corrections to Total Energy Pseudopotential Calculations”. In: *Journal of Physics-Condensed Matter* 2.19 (1990), pp. 4395–4404. DOI: 10.1088/0953-8984/2/19/007 (cit. on p. 52).

- [212] K. Kunc and R. M. Martin. “Ab Initio Force Constants of GaAs: A New Approach to Calculation of Phonons and Dielectric Properties”. In: *Physical Review Letters* 48.6 (1982), pp. 406–409. DOI: 10.1103/PhysRevLett.48.406 (cit. on p. 53).
- [213] A. Togo and I. Tanaka. “First principles phonon calculations in materials science”. In: *Scripta Materialia* 108 (2015), pp. 1–5. DOI: 10.1016/j.scriptamat.2015.07.021 (cit. on p. 53).
- [214] K. Parlinski, Z. Q. Li, and Y. Kawazoe. “First-Principles Determination of the Soft Mode in Cubic ZrO<sub>2</sub>”. In: *Physical Review Letters* 78.21 (1997), pp. 4063–4066. DOI: 10.1103/PhysRevLett.78.4063 (cit. on p. 53).
- [215] L. Chaput, A. Togo, I. Tanaka, and G. Hug. “Phonon-phonon interactions in transition metals”. In: *Physical Review B* 84.9 (2011), p. 094302. DOI: 10.1103/PhysRevB.84.094302 (cit. on p. 53).
- [216] N. Marzari and D. Vanderbilt. “Maximally localized generalized Wannier functions for composite energy bands”. In: *Physical Review B* 56.20 (1997), pp. 12847–12865. DOI: 10.1103/PhysRevB.56.12847 (cit. on p. 55).
- [217] I. Souza, N. Marzari, and D. Vanderbilt. “Maximally Localized Wannier Functions for Entangled Energy Bands”. In: *Physical Review B* 65.3 (2001), p. 035109. DOI: 10.1103/PhysRevB.65.035109 (cit. on p. 55).
- [218] A. A. Mostofi, J. R. Yates, Y. S. Lee, I. Souza, D. Vanderbilt, and N. Marzari. “WANNIER90: A tool for obtaining maximally-localised Wannier functions”. In: *Computer Physics Communications* 178.9 (2008), pp. 685–699. DOI: 10.1016/j.cpc.2007.11.016 (cit. on p. 55).
- [219] R. F. W. Bader. “A Quantum-Theory of Molecular-Structure and Its Applications”. In: *Chemical Reviews* 91.5 (1991), pp. 893–928. DOI: 10.1021/cr00005a013 (cit. on p. 55).
- [220] G. Henkelman, A. Arnaldsson, and H. Jonsson. “A fast and robust algorithm for Bader decomposition of charge density”. In: *Computational Materials Science* 36.3 (2006), pp. 354–360. DOI: 10.1016/j.commatsci.2005.04.010 (cit. on p. 55).
- [221] W. Tang, E. Sanville, and G. Henkelman. “A grid-based Bader analysis algorithm without lattice bias”. In: *Journal of Physics-Condensed Matter* 21.8 (2009), p. 084204. DOI: 10.1088/0953-8984/21/8/084204 (cit. on p. 55).
- [222] S. M. Griffin, M. Lilienblum, K. T. Delaney, Y. Kumagai, M. Fiebig, and N. A. Spaldin. “Scaling Behavior and Beyond Equilibrium in the Hexagonal Manganites”. In: *Physical Review X* 2 (4 2012), p. 041022. DOI: 10.1103/PhysRevX.2.041022 (cit. on p. 200).

- [223] K. R. Poeppelmeier and J. M. Rondinelli. “Oxide interfaces: Mismatched lattices patched up”. In: *Nature Chemistry* 8.4 (2016), pp. 292–294. DOI: 10.1038/nchem.2477 (cit. on p. 200).
- [224] M. O’Sullivan, J. Hadermann, M. S. Dyer, S. Turner, J. Alaria, T. D. Manning, A. M. Abakumov, J. B. Claridge, and M. J. Rosseinsky. “Interface control by chemical and dimensional matching in an oxide heterostructure”. In: *Nature Chemistry* 8.4 (2016), pp. 347–353. DOI: 10.1038/nchem.2441 (cit. on p. 200).

